

Electrical Stimulation of the Human Left Ventricle

Zur Erlangung des akademischen Grades eines

DOKTOR-INGENIEURS

von der Fakultät für
Elektrotechnik und Informationstechnik
der Universität Fredericiana Karlsruhe

genehmigte

DISSERTATION

von

Dipl. Phys. Iulia-Mihaela Graf
aus Bistrița
Rumänien

Hauptreferent: Prof. Dr. rer. nat. O. Dössel

Korreferent: Prof. Alexander Panfilov

Aknowledgements

Many people deserve my gratitude for their support and assistance though contributing to this work. Particularly, I would like to thank to Prof. Dr. Olaf Dössel who provided me an excellent research platform and introduced me to the interesting mysteries of biomedical engineering. Special thanks to Gunnar Seemann for his good advices and numerous comments. To Matthias Mohr I would also like to thank for creating a very good working atmosphere. I'd like to extend my gratitude to Rotraut Frech without whom my work would not have been possible.

I am deeply grateful to my parents, Mihail and Iuliana Popp, who did always their best in helping me. My kindest thanks to Nicolae Feier for the offered spiritual support. Finally, a great merci is for Christian who encouraged me in the best possible way and permanently sustained me from the scientific point of view.

This work was financially supported by the Research Training Group 786 'Mixed Fields and Nonlinear Interactions' of the German Research Foundation (DFG).

Contents

1	Introduction	1
1.1	Motivation	1
1.2	Objectives	3
1.3	Organization	3
2	Mathematical and Technical Basics	5
2.1	Physical Laws of Electromagnetism	5
2.1.1	Maxwell's Equations	5
2.1.2	Poisson's Equation for Stationary Electrical Fields	7
2.2	Numerical Methods	7
2.2.1	Numerics for Systems of Linear Equations	7
2.2.2	Numerics of Partial Differential Equations	8
3	Anatomy and Function of the Heart	13
3.1	Structure of the heart in connection with the blood flow	13
3.2	Excitation initiation and conduction system	17
4	Cardiac Electrophysiology	19
4.1	Transport Mechanisms in Cell Membrane	19
4.2	Electrical Modeling of Cell Membranes	21
4.2.1	Resistor-Capacitor Cell Membrane	21
4.2.2	Stokes-Einstein equation	22
4.2.3	Nernst Equation	23
4.2.4	Goldman-Hodgkin-Katz Equation	24
4.3	Action Potentials	25
4.3.1	Resting Phase	25
4.3.2	Depolarisation Phase	26
4.3.3	Early Repolarisation Phase	27
4.3.4	Plateau Phase	27
4.3.5	Repolarisation Phase	27
4.4	Electrophysiological Cardiac Cell Models	27
4.4.1	Priebe-Beuckelmann Model	28
4.4.2	Ten Tusscher-Noble-Noble-Panfilov Model	31
4.5	Electrocardiogram	35
4.6	Excitation Propagation	38
4.6.1	Gap Junctions	39
4.6.2	Models of the Electrical Flow	39
4.6.3	The Bidomain Reaction Diffusion Model	40

4.7	Cardiac Pathologies	42
4.7.1	Arrhythmias	42
4.7.2	Flutter and Fibrillation	44
4.7.3	Myocardial Infarction	47
4.7.4	Hypertrophy Patterns	47
4.7.5	Heart Block	47
4.7.6	Pre-excitation Syndromes	48
4.7.7	Long QT interval Romano-Ward Syndrome	48
4.7.8	Brugada Syndrome	48
5	Defibrillators	49
5.1	Constructional Aspects	49
5.2	Research Aspects	53
5.2.1	Experimental Research	53
5.2.2	Weiss-Lapicque Law	54
5.2.3	Blair Law	55
5.2.4	Theoretical Research	56
6	Features of a Human Ventricular Myocardial Model	59
6.1	Geometry	60
6.1.1	Parallelepipedic Myocardial Preparation	61
6.1.2	Large Virtual Section of Human Myocardium	65
6.1.3	Curved Segment of Human Myocardium	66
6.2	Electrophysiological Heterogeneity	69
6.3	Myocardial Fiber Orientation	79
6.4	Tissue-Bath Volumes Ratio	83
6.5	Cardiac Microstructure-Cleavage Planes	88
6.6	Inferences	92
7	Influence of Electrical Stimulation Characteristics	95
7.1	Features of the Electrical Stimuli	95
7.1.1	Microscopic Level	95
7.1.2	Macroscopic Level	108
7.2	Electrode Characteristics	119
7.3	New Defibrillation Procedure: Electrodes Array	124
7.4	Electrical Stimulation Moment	129
7.5	Inferences	134
8	Factors Modifying the Vulnerability to Electrical Shocks	137
8.1	Electroporating Membrane	137
8.1.1	Physical Properties of Electroporation	138
8.1.2	Application of the Electroporation Formalism to a Specific Electrophysiological Cell Model	146
8.2	Heart Failure	149
8.3	Inferences	157
9	Summary and Conclusions	159

Bibliography	161
---------------------	------------

Curriculum Vitae	173
-------------------------	------------

List of Figures

2.1	Examples of finite differences meshes	10
2.2	Example of numbering the node points in two-dimensional, rectangular, equidistant mesh	11
3.1	Anatomy of the heart with blood vessels	14
3.2	Blood flow in the heart	15
3.3	Cardiac fiber orientation	16
3.4	The transmural orientation of cleavage planes in a rat heart . . .	16
3.5	The electrical system of the heart	17
4.1	Schematic representation of the cell membrane	20
4.2	Schematic representation of the transport mechanisms in the cell membrane	21
4.3	Schematic representation of the resistor-capacitor model of the cell membrane	22
4.4	Schematic representation of cell membrane according to Nernst formalism	24
4.5	Schematic representation of cell membrane according to Goldman-Hodgkin-Katz formalism	25
4.6	The phases of an action potential in a human ventricular myocyte	26
4.7	Schematic representation of Priebe-Beuckelmann cell model . . .	30
4.8	Schematic representation of the ten Tusscher-Noble-Noble-Panfilov Model	33
4.9	Steady state curves describing the gating of the fast Na current .	34
4.10	Schematic representation of ECG formation	35
4.11	Einthoven Triangle	36
4.12	Schematic representation of myocardium according to the bidomain model	40
4.13	ECG changes during flutter and fibrillation.	44
4.14	Relationship between stimulation and fibrillation threshold . . .	46
5.1	Diagram of an automatic external defibrillator	50
5.2	Examples of different defibrillation wave forms	51
5.3	Schematic representation of the location of an implantable cardioverter defibrillator and its electrodes	52
5.4	The representation of Weiss-Lapicque law	54
5.5	Simplified model, the defibrillator and the living body according to the electrical properties	57

6.1	Truncated ellipsoid representation of ventricular geometry.	60
6.2	Different geometrical types of myocardial wedges.	61
6.3	The position and the geometrical characteristics of the paddles utilized for stimulating the tissue.	62
6.4	V_m distribution in a parallelepipedic myocardial preparation. . .	63
6.5	Φ_e distribution in a parallelepipedic myocardial preparation. . . .	64
6.6	V_m distribution in a large myocardial slice.	66
6.7	V_m spatial distribution in a curved myocardial preparation stim- ulated by various electrodes.	67
6.8	Φ_e distribution in a curved myocardial preparation.	68
6.9	V_m spatio-temporal distribution in a curved myocardial prepa- ration.	69
6.10	Transmural variation of the physiological parameters.	71
6.11	The action potential of isolated subendocardial, M and subepi- cardial human left ventricular myocytes.	72
6.12	Distribution of APD along the Z-axis in an electrophysiologically homogeneous and heterogeneous myocardial preparations.	72
6.13	The simulated transmural ECG specific to an electrophysiologi- cally homogeneous and a heterogeneous myocardial preparation.	73
6.14	The position and the geometrical characteristics of the needle electrodes utilized for stimulating the tissue.	74
6.15	Distribution of V_m in NM and HM after monophasic external electrical stimulation.	76
6.16	Distribution of V_m in NM and HM after biphasic external elec- trical stimulation.	77
6.17	Distribution of V_m in NM and HM after monophasic internal electrical stimulation.	78
6.18	Fiber Orientation	79
6.19	Configuration used for the study of the influence of fiber orien- tation on a two dimensional myocardial preparation.	80
6.20	Formation of virtual electrodes in 2D myocardium with various fiber angles.	81
6.21	Distribution of V_m in two-dimensional sheets with various fiber orientation	82
6.22	3D myocardium with realistic fiber orientation immersed in bath	83
6.23	3D myocardium with 70° fiber orientation immersed in bath . . .	84
6.24	V_m in a section through the model, composed of a medium sized myocardium incorporated in bath, stimulated by rectan- gular paddles	85
6.25	V_m in a section through the model, which contains a very small myocardial volume incorporated in bath, stimulated by rectan- gular paddles	86
6.26	V_m in a section through the model, which contains a medium sized myocardium incorporated in bath, stimulated by needle electrodes	87

6.27	The formation of secondary electrical sources, due to tissue inhomogeneities, e.g. cleavage planes, according to the bidomain formalism	89
6.28	Electrically stimulated resting myocardium with cleavage planes.	93
6.29	Arrhythmic myocardium fragmented by cleavage planes.	94
7.1	Wave forms utilized for stimulating the cell	96
7.2	The excitation thresholds for a 10 ms long biphasic 100 Hz cellular stimulation	97
7.3	V_m profile during a successful excitation with a biphasic 100 Hz and 10 ms long stimulus	97
7.4	The gate variables for I_{Na} during a successful excitation with a biphasic 100 Hz and 10 ms long stimulus	98
7.5	Excitation threshold of myocytes for 500 Hz and 1 kHz of biphasic stimulation	99
7.6	Excitation threshold of myocytes for 2 and 4 kHz of biphasic stimulation	100
7.7	AP profile during and after a successful excitation with a 2 kHz and 5 ms long biphasic stimulus	101
7.8	AP profile during and after a failing excitation with a 2 kHz and 5 ms long biphasic stimulus	101
7.9	The gate variables for I_{Na} after a successful excitation with a 2 kHz and 5 ms long biphasic stimulus	102
7.10	The gate variables for I_{Na} after a failing excitation with a 2 kHz and 5 ms long biphasic stimulus	103
7.11	Excitation threshold of myocytes for various frequencies of the monophasic stimulation	105
7.12	V_m and the gate variables for I_{Na} after a successful excitation with a 2 kHz and 5 ms long monophasic stimulus	106
7.13	Comparison between monophasic and biphasic cellular stimulation.	107
7.14	Comparison between monophasic rectangular and truncated exponential stimulation wave forms	107
7.15	Excitation thresholds of monophasic rectangular and truncated exponential stimuli fitted by Weiss-Lapique and Blair laws . . .	108
7.16	Biphasic stimulation of a continuous wedge of myocardium . . .	109
7.17	Excitation thresholds for biphasic stimulation of a continuous wedge of myocardium corresponding to 500 Hz and 1 kHz	110
7.18	Excitation thresholds for biphasic stimulation of a continuous wedge of myocardium corresponding to 2 kHz and 4 kHz	111
7.19	Biphasic stimulation of a fragmented wedge of myocardium . .	112
7.20	Excitation thresholds for biphasic stimulation of a fragmented wedge of myocardium corresponding to 500 Hz and 1 kHz	113
7.21	Excitation thresholds for monophasic stimulation of a continuous wedge of myocardium corresponding to 500 Hz and 1 kHz	114
7.22	Excitation thresholds for monophasic stimulation of a continuous wedge of myocardium corresponding to 2 kHz and b) 4 kHz . . .	115

7.23	Excitation thresholds for monophasic transversal and longitudinal stimulation of a continuous wedge of myocardium	116
7.24	Monophasic stimulation of a fragmentized wedge of myocardium	117
7.25	Comparison between excitation thresholds of 5 ms long biphasic stimulations (rheobases) of different frequencies for a continuous wedge of myocardium	117
7.26	Models of the chosen configurations of electrodes for the study.	121
7.27	Schematic representation of the displacement of the area most affected in the 7th electrical configuration	121
7.28	Displacement of the most affected area in the 5th electrical configuration	122
7.29	Distribution of the transmembrane voltage in an heterogeneous left ventricle myocardium beneath the electrodes oriented perpendicular on endo- and epicardial surfaces.	122
7.30	Excitation thresholds corresponding to 1 and 2 kHz stimulation for stimulation applied along and across the fibers.	123
7.31	Electrodes array configuration	125
7.32	V_m spatio-temporal evolution in a human myocardium after excitation through a couple of 3 electrodes arrays	126
7.33	V_m spatio-temporal evolution in a myocardium incorporated in blood, after excitation through a couple of 3 electrodes arrays .	127
7.34	V_m spatio-temporal evolution in a human myocardium after excitation through a couple of 49 electrodes arrays	128
7.35	V_m spatio-temporal evolution in a myocardium incorporated in blood, after excitation through a couple of 49 electrodes arrays .	129
7.36	Variation of excitation threshold with the number of electrodes .	130
7.37	The placement of defibrillation paddles	130
7.38	The simulated ECG of the fibrillating human ventricular myocardium	131
7.39	Variation of transmembrane voltage in a continuous myocardium defibrillated at 450 ms	131
7.40	Variation of transmembrane voltage in a myocardium fragmentized by 3 cleavage planes and defibrillated at 450 ms	132
7.41	Variation of transmembrane voltage in a continuous myocardium after an unsuccessful defibrillation applied at 500 ms	132
8.1	The bipolar molecule is rotating under the influence of external electrical fields	139
8.2	The work done by the tension $\Gamma(r)$ per unit time is dissipating radially around each pore of increasing radius $r(t)$	142
8.3	The work done by the tension $\Gamma(r)$ per unit time dissipates in the surrounding fluid	144
8.4	The closing of small pores simultaneous with the expansion of large pores	145
8.5	Final closure of the pores	146
8.6	The variation of transmembrane voltage after electroporation of the membrane	147

8.7	The distribution of isopotential surfaces after an electrical stimulation of 5 ms, applied through needle electrodes. The pictures illustrate the data obtained with a model, which does not contain electroporation.	148
8.8	The distribution of isopotential surfaces after an electrical stimulation of 5 ms, applied through needle electrodes. The results were delivered by the model including the mathematical formalism of electroporation.	149
8.9	Comparison between simulated APDs of healthy and failing heart with normal electrical conductivities	151
8.10	Temporal evolution of V_m in the heart failing models with normal electrical conductivities after 10 ms long monophasic stimulation	152
8.11	Temporal evolution of V_m in the heart failing models with reduced electrical conductivities after 10 ms long monophasic stimulation	153
8.12	ECG comparison between healthy and failing heart	154
8.13	Temporal evolution of V_m in the heart failing models with normal electrical conductivities after 10 ms long biphasic stimulation . .	155

List of Tables

4.1	List of ionic currents in Priebe-Beuckelmann cell model. The variation of each term produces a modification of V_m value. . . .	29
4.2	The list of ionic currents, composing I_{ion} in the ten Tusscher-Noble-Noble-Panfilov cell model. The variation of each term produces a modification of V_m	32
6.1	List of the normal values of the electrical conductivities.	65
6.2	List of the electrical stimulation configurations utilized in the study of electrophysiological heterogeneity.	75
7.1	Configurations used in the investigation of electrode characteristics	120
7.2	The reaction of human ventricular myocardium (continuous model/ fragmented model) to defibrillation.	133
8.1	The description of the myocardial preparations constructed for the investigation of heart failure.	150

1 Introduction

1.1 Motivation

Nearly a quarter of humanity suffers of cardiovascular diseases. Ventricular fibrillation is the most dangerous one. It starts from a single or several tornado-like sources of electrical activity, disorderly propagating throughout the heart and rapidly breaking up into numerous wavelets. The cardiac fibers excite without synchrony leading to cessation of the blood flow. As a result of the scientific research done, we presently know that death is imminent within minutes unless a shock therapy is applied.

The history of fibrillation and defibrillation goes back to the pioneering work of Carl Ludwig (1816-1895), distinguished professor of Physiology. He developed in 1847 the so-called kymograph to register changes in arterial pressure and a flowmeter to measure flow through arteries and veins. During his research a perfused animal heart was for the first time maintained in vitro in a beating state. In 1849, Ludwig's student, M. Hoffa was the first to witness and, most importantly, to document the onset of ventricular fibrillation, induced by an external electrical stimulus.

In the second half of the 19th century many investigators attempted to describe the physics of cardiac arrhythmia. Originally, most of the physiologists favored neurogenic theory of fibrillation, suggesting irregular contractions of the heart muscle produced by an abnormal impulse generation and conduction within the nerve fiber network. The Swiss physiologist, A. Vulpian focused his research on myocardial diseases. Starting from the existing observations he was the first to suggest the myogenic theory of fibrillation [1].

The heart muscle itself sustains the irregular propagation of impulses, resulting in mechanical disarray. In order to emphasize the myogenic nature of the observed arrhythmia the process was termed fibrillation (*'mouvement fibrillaire'*). The observations of A. Vulpian were independently confirmed by the British physiologist John A. MacWilliam, who arrived at similar conclusions regarding the myogenic nature of fibrillation [2].

Numerous conclusions drawn by MacWilliam became a part of the commonly accepted paradigm. The investigations indicated that ventricular fibrillation and atrial fibrillation are different phenomena, distinctively inducible by stimulating the ventricles or atria. As A. Vulpian and MacWilliam concluded that fibrillation has myogenic nature and it is not due to injury or irritation of nerves that are propagated over the ventricles.

Further experiments with "faradization" of the heart were conducted by two physiologists from the University of Geneva, Switzerland, J. L. Prevost and F.

Batelli. In 1899, they discovered that, while a weak stimulus can produce fibrillation, a stimulus of higher strength applied to the heart could arrest ventricular fibrillation and restore normal sinus rhythm. At the end of 19th century, in contrast to the discovery of the electrocardiogram, defibrillation did not raise much attention.

After the turn of the century, as medicine advanced and people lived longer, heart disease became a leading cause of death. These new circumstances caused scientists to focus their attention on the therapies of the cardiac arrhythmias.

The discovery of Prevost and Batelli was confirmed and advanced by the subsequent work in many groups, most prominently by the research laboratory of Carl J. Wiggers from Western Reserve University in Cleveland, Ohio. Using the state of the art of experimental methodology of his time, the cinematograph, Carl Wiggers was able to advance original observations of Vulpian, describing several stages of ventricular fibrillation produced by a stimulus, known as Wiggers stage I, Wiggers stage II, etc. Carl Wiggers provided the first mechanistic explanation of the induction of ventricular fibrillation within the framework of the concept of vulnerable window. He also perfected defibrillation procedure in an animal model of defibrillation. The work of Carl J. Wiggers was well known to the thoracic surgeon Claude S. Beck from the University Hospitals in Cleveland, adjacent to the Western Reserve University. In 1947, Dr. Beck successfully applied defibrillation therapy and saved the first human life by this method [3]. His success triggered a wide acceptance of this method by the clinical community and started a wide front of basic and clinical research of fibrillation and defibrillation.

The work of Prevost and Batelli was independently continued by the Russian physiologists N. A. Negovsky and N. L. Gurvich in Moscow. N. L. Gurvich was trained by the director of the Institute of Physiology in Moscow L.S. Schtern, who graduated from the University of Geneva and was an associate of J. L. Prevost for many years. Naum L. Gurvich made many important discoveries and advancements in defibrillation, including an advent of the biphasic waveform, use of a capacitor for shock delivery and the introduction of the stimulatory theory of defibrillation.

The development of technology enlarged the possibilities of researching the electrical activity of the heart. In the last decades new insights in the function and structure of the cardiac tissues were gained by the use of new measurement techniques. These information were further used to describe mathematically the properties and the behavior of the heart. In this way arose the possibility of reconstructing previously performed measurements and prediction of yet unknown phenomena.

The topic of this work is the mathematical modeling of the electrical behavior of the human ventricular myocardium. A detailed information of phenomena on both microscopic and macroscopic levels needed to understand the ideas behind the model is presented.

1.2 Objectives

The focus of this work is set on the mathematical modeling of the electrical behavior of the human left ventricle and to identify the effects of the therapeutic shocks with time. In order to achieve quantitative simulations in the scope of this focus, existing models are enhanced and new models are developed. A main objective of this thesis is to reconstruct human electrical heterogeneity in schematic and realistic anatomical models. These inhomogeneous and anisotropic anatomical models are used to simulate the excitation propagation in the human heart. The influence of these structures on the effect of electric stimulation is investigated.

The physiologic and pathologic heterogeneity is reconstructed implementing new models and adapting existing ones. The cleavage planes are included in the virtual preparation for observing the effects of the muscle lamination. A new electroporation formalism is developed for simulating the reaction of the cardiomyocytes to strong electrical shocks.

The designed anatomical and electrophysiological models are used to simulate and investigate the interplay for either physiological or pathological cases. The results help to gain new insights into the insufficiently elaborated functions of the human heart or to support the understanding of pathologies e.g. cardiac arrhythmias.

1.3 Organization

The thesis is divided into three parts. First it describes the methodology, in the following part is summarized the state of the art and in the last three chapters are presented the results of the work.

The mathematical and the numerical methods of this work are described in chapter 2. These include ordinary and partial differential equations and their solution methods as well as minimization approaches and basic knowledge about the theory of electrical fields that are important for the methodology of this work.

Chapter 3 presents the anatomy of the heart. The anatomical structure of the heart is illustrated in connection with its main function, the blood pumping. Furthermore, the excitation initiation and the propagation of the depolarization is described.

The electrophysiological properties in cardiac cells are detailed in chapter 4. First are described different involved membrane proteins and the membrane modeling. Furthermore, the ventricular electrophysiology is illustrated. The following section sums up the transfer of electrophysiology and excitation propagation into mathematical models. The electrocardiogram is also explained in chapter 4. In the last section are presented the cardiac pathologies, with the focus on fluttering and fibrillation.

Chapter 5 starts with the constructional aspect of defibrillators. Furthermore, it illustrates the experimental and theoretical investigations of defibrillation phenomena.

In chapter 6 the characteristics of the human left myocardium which can be included in a virtual preparation are described. The influence of each feature is presented in detail. The chapter mainly addresses the theoretical researcher.

Chapter 7 illustrates how the characteristics of the electrical stimulation affect the human myocardium. The results include views on both the cellular and tissue level. Furthermore, it presents a new defibrillation procedure: the electrodes array. The chapter gives information for the defibrillator producers and experimenters.

In chapter 8 are included the research of two factors modifying the vulnerability to electrical shocks: electroporation and heart failing conditions. The results are of interest for both theoretical researchers and medical doctors.

The last chapter of this thesis discusses the results and gives an outlook on possible further research.

2 Mathematical and Technical Basics

Theoretical research reveals new aspects of the cardiological phenomena with the aid of numerical methods and computer systems. This type of investigation of the electrical behavior of the human heart requires knowledge about several mathematical and numerical methods. The chapter presents a summary of the physical formalisms used to model the anatomical, electrophysiological and excitation diffusion properties of the heart as well as the mathematics necessary to understand the results achieved with the simulations.

The time dependent biophysical processes are given by the numerical solution of ordinary differential equations describing the properties of the cells. The theory of differential equations is presented together with numerical methods appropriate for solving large coupled systems of equations. The efficiency of the numerical treatment strongly depends on the selected method. Coupling of several cells into a net describing the tissue as an electrically coupled system requires knowledge about the theory of electrical fields and the electrical properties of the tissue. The bidomain model, which is used in this work to describe the electrical coupling of cells, is based on the generalized Poisson equation for stationary electrical fields. This kind of approach yields partial differential equations for the excitation propagation.

A succinct description of a numerical solver for the partial differential equations describing the electrical activity of the cells in combination with the conduction of excitation is included in this chapter. The focus of the description is set on Finite Difference Method.

2.1 Physical Laws of Electromagnetism

2.1.1 Maxwell's Equations

The theoretical foundation of electromagnetism is comprised in the Maxwell's equations together with the three medium dependent equations. The modeling of electromagnetic processes typical to biological tissues plays an important role in the application of Maxwell's equations. Commonly material properties are nonlinear and anisotropic, due to the characteristic microscopical organization of the tissue. The utilization of tensor algebra allows an efficient treatment both from a theoretical and a numerical point of view.

The Maxwell's equations describe the connection between the electrical field E , the electric flux density D , the electric current density J , the electric charge

density ρ_v , the magnetic field \mathbf{H} and the magnetic induction \mathbf{B} . In the generalized differential form the Maxwell's equations include the variation with time:

$$\nabla \cdot \mathbf{D} = \rho_v \quad (2.1)$$

$$\nabla \cdot \mathbf{B} = 0 \quad (2.2)$$

$$\nabla \times \mathbf{E} = -\frac{\partial \mathbf{B}}{\partial t} \quad (2.3)$$

$$\nabla \times \mathbf{H} = \mathbf{J} + \frac{\partial \mathbf{D}}{\partial t} \quad (2.4)$$

For the stationary case, Maxwell's equations read:

$$\nabla \cdot \mathbf{D} = \rho_v \quad (2.5)$$

$$\nabla \cdot \mathbf{B} = 0 \quad (2.6)$$

$$\nabla \times \mathbf{E} = 0 \quad (2.7)$$

$$\nabla \times \mathbf{H} = \mathbf{J} \quad (2.8)$$

The interaction between the field and matter is given by the three medium-dependent equations:

$$\mathbf{D} = \epsilon_0 \mathbf{E} + \mathbf{P} \quad (2.9)$$

where \mathbf{P} represents the electric polarization and ϵ_0 the permittivity in vacuum.

$$\mathbf{B} = \mu_0(\mathbf{H} + \mathbf{M}) \quad (2.10)$$

with \mathbf{M} denoting the magnetic moment and μ_0 the permeability of vacuum.

$$\mathbf{J} = \sigma \mathbf{E} + \mathbf{J}_s \quad (2.11)$$

where the parameter σ gives the electrical conductivity. These are called constitutive relations for the medium in which the electromagnetic fields exist. The fields are assumed to be single valued, bounded and continuous functions in space and time with continuous derivatives.

The continuity equation expresses the conservation of electric charge:

$$\nabla \cdot \mathbf{J} = -\frac{\partial \rho_v}{\partial t} \quad (2.12)$$

2.1.2 Poisson's Equation for Stationary Electrical Fields

The flow of electrical currents in an electrically conducting medium can be described with the Poisson's equation for stationary electrical fields:

$$\nabla \cdot (\sigma \nabla \phi) + f = 0 \quad (2.13)$$

f is the source current density, σ the electrical conductivity, and ϕ the scalar electrical potential function. This equation is derived from the second Maxwell's equation:

$$\nabla \cdot \mathbf{J} = \nabla \cdot (\nabla \times \mathbf{H}) = 0$$

since the divergence of the curl operator is zero. The overall current density $\mathbf{J} = \mathbf{J}_s + \mathbf{J}_o$ is the sum of the electric current density resulting from local sources \mathbf{J}_s and the ohmic current density \mathbf{J}_o . The relation between the electrical field \mathbf{E} and the potential function ϕ is given by:

$$\mathbf{E} = -\nabla \phi$$

From the above equation and $\mathbf{J} = \sigma \mathbf{E}$ is deduced the Poisson's equation:

$$\nabla \mathbf{J}_s = \nabla \sigma \mathbf{E} = -\nabla \cdot (\sigma \nabla \phi) = f$$

The conductivity tensor σ in the Poisson's equation is describing the electrical properties of the underlying material. In biological tissues, as cardiac media, the conductivity is anisotropic and heterogeneously distributed over the space. This has to be considered when solving the Poisson's equation.

The following sections describe how to handle numerically the partial differential equations subsequent to the Poisson's equation in order to achieve linear equation systems and how these linear equation systems are solved.

2.2 Numerical Methods

2.2.1 Numerics for Systems of Linear Equations

A system of linear equations can be written as:

$$\sum_{j=1}^N a_{ij} x_j + b_i = 0 \quad (2.14)$$

or

$$\mathbf{A} \cdot \mathbf{x} + \mathbf{b} = \mathbf{0} \quad (2.15)$$

The coefficients a_{ij} and b_i are known a-priori and x_j constitute the unknowns. In the matrix formulation are used: $\mathbf{A} = [a_{ij}]$, $\mathbf{b} = [b_i]$ and $\mathbf{x} = [x_j]$.

Direct and iterative methods can be utilized for solving the system of linear equations. Direct methods are based on successive elimination of the unknown, e.g. with Gauss and Cholesky algorithm. Iterative methods use an iterative refinement of approximative solutions. Representatives of iterative methods are Gauss-Seidel, Jacobi, successive overrelaxation and multigrid methods.

Gauss-Seidel Method The Gauss-Seidel Method converges if the matrix \mathbf{A} is diagonally dominant. The technique is performed by decomposition of the matrix \mathbf{A} into the sum of the lower triangular matrix \mathbf{L} , the diagonal matrix \mathbf{D} and the upper triangular matrix \mathbf{U} :

$$\mathbf{A} = \mathbf{L} + \mathbf{D} + \mathbf{U} \quad (2.16)$$

The matrix decomposition is given by:

$$(\mathbf{L} + \mathbf{D}) \cdot \mathbf{x}^{(k)} = -\mathbf{U} \cdot \mathbf{x}^{(k-1)} + \mathbf{b} \quad (2.17)$$

In the k -th step of the summation formulation the new coefficients $x_i^{(k)}$ are determined by:

$$x_i^{(k)} = -\frac{1}{a_{ii}} \left(b_i + \sum_{j=1}^{i-1} a_{ij} x_j^{(k)} + \sum_{j>i}^{n-1} a_{ij} x_j^{(k-1)} \right) \quad (2.18)$$

Gauss-Seidel technique requires only the most recent values for the calculation and not all, as is necessary in the Jacobi method. The difference implies a faster convergence of the Gauss-Seidel technique, although for dense matrices it is inherently sequential. Another advantage of the method is that the new and previous solution can share their storage.

2.2.2 Numerics of Partial Differential Equations

In mathematical terms, a partial differential equation (PDE) is any formula involving a function of more than one independent variable and at least one partial derivative of that function. The order n of a PDE is equal to the highest order derivative that appears in the equation. The principal part of a PDE is the collection of the terms containing derivatives of the highest order.

Exemplary, a second order linear differential equation in the region $\Omega \subset \mathfrak{R}$ is given by:

$$\begin{aligned} A(x_1, x_2) \frac{\partial^2 f}{\partial x_1^2} + 2B(x_1, x_2) \frac{\partial^2 f}{\partial x_1 \partial x_2} + C(x_1, x_2) \frac{\partial^2 f}{\partial x_2^2} + \\ + D(x_1, x_2) \frac{\partial f}{\partial x_1} + E(x_1, x_2) \frac{\partial f}{\partial x_2} + F(x_1, x_2) f = G(x_1, x_2) \end{aligned} \quad (2.19)$$

with the functions A , B , C , D , E , F and G known. Depending on the value of these functions and assuming that $A^2 + B^2 + C^2 \neq 0$ in Ω , this equation can be classified in three types:

- $AC - B^2 > 0$: elliptic
- $AC - B^2 < 0$: hyperbolic
- $AC - B^2 = 0$: parabolic

The classification influences the selection of numerical treatment of the partial differential equation. A representative of an elliptic differential equation is the so-called Poisson equation, described by:

$$\frac{\partial^2 f}{\partial x_1^2} + \frac{\partial^2 f}{\partial x_2^2} = G(x_1, x_2) \quad (2.20)$$

If the right hand side of the equation is equal to zero we obtain the Laplace equation. Both Poisson and Laplace equation are frequently used for describing stationary and quasi-stationary physical phenomena.

2.2.2.1 Initial Values and Boundary Conditions

Initial values can be set everywhere in the region Ω and its boundary region Γ . Different types of boundary conditions can be defined. A Dirichlet condition specifies the value at the boundary $\Gamma_D \subset \Gamma$ with the function Φ :

$$f(x) = \Phi(x) \quad \text{for } x \in \Gamma_D.$$

A Neumann condition defines the values of gradient in normal direction \mathbf{n} to the boundary $\Gamma_N \subset \Gamma$ with the function γ :

$$\frac{\partial f}{\partial \mathbf{n}}(x) = \gamma(x) \quad \text{for } x \in \Gamma_N.$$

A Cauchy condition is the general formulation of the boundary conditions:

$$\frac{\partial f}{\partial \mathbf{n}}(x)\alpha(x)f(x) = \beta(x) \quad \text{for } x \in \Gamma_C.$$

The functions α and β are defined at the partial boundary $\Gamma_C \subset \Gamma$.

Some partial differential equations do not have an analytical solution. For these cases an approximative solution can be found using numerical methods. Such a complex problem is constituted by the system of nonlinear equations describing the cardiac electrical activity. In this direction Finite-Element Method ([4], [5], [6], [7]), Finite-Difference Method ([8], [9], [10]) and Boundary Element Method ([11], [4], [12], [13]) were implemented.

2.2.2.2 Finite Difference Method

The finite difference method (FDM) was first developed by A. Thom [14] in the 1920s under the title "method of squares" to solve nonlinear hydrodynamic equations. Since that time, the method has found applications in solving different field problems. The finite difference techniques are based on approximations done by replacing the differential equations with difference equations. FDM can be subdivided into a sequence of five steps.

Discretization of the Spatial Domain Rectangular, isotropic and equidistant lattices are applied in the spatial domain (Fig. 2.1). The node points, x_i are located at the vertices. The regularity of the nodes simplifies the discretization of the partial differential equations.

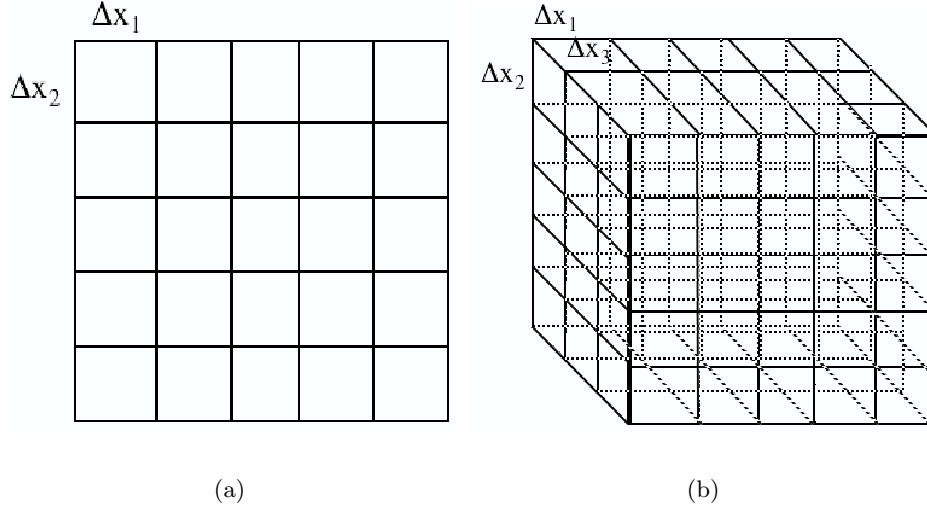


Figure 2.1: Examples of finite differences meshes in (a) two and (b) three dimensions.

Determination of Node Equations An approximation of the first order spatial derivative in a one-dimensional domain at the node point x_i can be achieved with various schemes. The used formalisms are named: central, forward and backward difference. The mathematical equations describing them are:

$$\frac{\partial f(x_i)}{\partial x} \simeq \frac{f_{i+1} - f_{i-1}}{2\Delta x} \quad \text{for central} \quad (2.21)$$

$$\frac{\partial f(x_i)}{\partial x} \simeq \frac{f_{i+1} - f_i}{\Delta x} \quad \text{for forward} \quad (2.22)$$

$$\frac{\partial f(x_i)}{\partial x} \simeq \frac{f_i - f_{i-1}}{\Delta x} \quad \text{for backward} \quad (2.23)$$

$$(2.24)$$

The functions f_{i-1} , f_i and f_{i+1} correspond to the node points x_{i-1} , x_i and x_{i+1} , respectively. Using two-fold central differences the second order derivative at the node point x_i is described by:

$$\frac{\partial^2 f(x_i)}{\partial x^2} \simeq \frac{f_{i+1} - 2f_i + f_{i-1}}{\Delta x^2} \quad (2.25)$$

For applying the method to a space and time dependent function, $\Phi(x, t)$, the solution region must be divided in the $x - t$ plane into equal rectangles or meshes of sides Δx and Δt .

The coordinates can be than written as:

$$x = i \cdot \Delta x, i = 0, 1, 2, \dots \quad (2.26)$$

$$t = j \cdot \Delta t, j = 0, 1, 2, \dots \quad (2.27)$$

The first and second order time derivatives can be obtained using the schemes presented for spatial approximations.

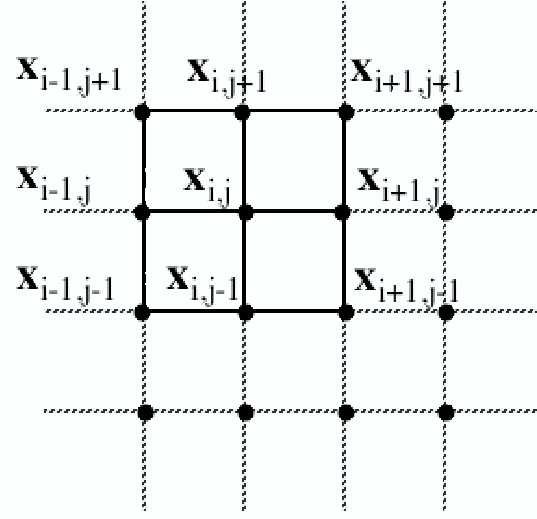


Figure 2.2: Example for numbering the node points in a two-dimensional, rectangular, equidistant mesh.

The relations corresponding to a node $x_{i,j}$ included in a two-dimensional spatial domain are:

$$\frac{\partial f(x_{i,j})}{\partial x_1} \simeq \frac{f_{i+1,j} - f_{i-1,j}}{2\Delta x_1} \quad (2.28)$$

$$\frac{\partial f(x_{i,j})}{\partial x_2} \simeq \frac{f_{i,j+1} - f_{i,j-1}}{2\Delta x_2} \quad (2.29)$$

The two-dimensional Poisson equation can be approximated in an equidistant, isotropic lattice by substituting the second order derivatives. At the point $x_{i,j}$, the Poisson equation reads:

$$\frac{\partial^2 f(x_{i,j})}{\partial x_1^2} + \frac{\partial^2 f(x_{i,j})}{\partial x_2^2} = G(x_{i,j}) \quad (2.30)$$

With finite difference approximation, one finds:

$$\frac{-4f_{i,j} + f_{i+1,j} + f_{i-1,j} + f_{i,j+1} + f_{i,j-1}}{\Delta x^2} = G(x_{i,j}) \quad (2.31)$$

The errors generated by finite difference method can be estimated by using the Taylor series expansion.

$$f(x_0 + \Delta x) = f(x_0) + \Delta x f'(x_0) + \frac{1}{2!}(\Delta x)^2 f''(x_0) + \frac{1}{3!}(\Delta x)^3 f'''(x_0) + \dots \quad (2.32)$$

and

$$f(x_0 - \Delta x) = f(x_0) - \Delta x f'(x_0) + \frac{1}{2!}(\Delta x)^2 f''(x_0) - \frac{1}{3!}(\Delta x)^3 f'''(x_0) + \dots \quad (2.33)$$

The coupling of the last two expressions gives:

$$f(x_0 + \Delta x) + f(x_0 - \Delta x) = 2f(x_0) + (\Delta x)^2 f''(x_0) + O(\Delta x)^4 \quad (2.34)$$

where $O(\Delta x)^4$ is the Landau notation, showing that terms of order higher than 4 are neglected. The first and the second derivatives are then equal to:

$$f''(x_0) \simeq \frac{f(x_0 + \Delta x) + f(x_0 - \Delta x) - 2f(x_0)}{(\Delta x)^2} \quad (2.35)$$

$$f'(x_0) \simeq \frac{f(x_0 + \Delta x) - f(x_0 - \Delta x)}{2\Delta x} \quad (2.36)$$

The truncation error can be cubically reduced regarding the distance Δx . Alternatively, the error can be decreased by introduction of higher order terms in the approximation schemes.

Assembling of System Equations The element matrices and vectors are assembled to generate the system of equations describing the entire domain. These equations are commonly linear and they incorporate the system matrix \mathbf{A} and the system vector \mathbf{b} .

$$\mathbf{A} \cdot \mathbf{f} + \mathbf{b} = \mathbf{0} \quad (2.37)$$

The values of the node variables f_i represent the solution function f and are a-priori unknown. The system matrix \mathbf{A} and the system vector \mathbf{b} result from a collection of sorted vectors \mathbf{a}_i and coefficients b_i , corresponding to a node variable:

$$\mathbf{A} = \begin{pmatrix} a_1^T \\ \vdots \\ a_N^T \end{pmatrix}, \mathbf{b} = \begin{pmatrix} b_1^T \\ \vdots \\ b_N^T \end{pmatrix}.$$

The properties of the system matrix depend on the characteristics of the element matrices. E.g. the assembling of symmetric, positive-definite element matrices leads to a symmetric, positive-definite system matrix. The system matrix \mathbf{A} consists commonly of diagonal blocks, which can be efficiently stored.

Incorporation of Boundary Conditions The incorporation of boundary conditions can be performed on element or system level by modification of the corresponding equation systems. If the differential equation is described by a system of linear equations, boundary conditions can be introduced by reducing the dimensions or replacing coefficients of the system matrix \mathbf{A} and system vector \mathbf{b} .

Solution of System Equations Depending on the type of differential equation, different sorts of equation systems exist. Stationary problems, as the ones based on Poisson equation, commonly deliver a system of linear equations, which can be solved with special numerical methods, like Gauss-Seidel technique. The symmetry, positive-definiteness and sparsity of the system matrix are of advantage on behalf of the performance of solution and feasibility of numerical methods.

3 Anatomy and Function of the Heart

The human heart is a muscular organ with a weight of 230 to 350 *g* and the size of a fist [15, 16, 17]. It is situated in between the two lungs in the mediastinum of the thorax and is surrounded by the pericardium, a closed fibrosic sac. The main axis of the heart is normally oriented from back-top-right to front-bottom-left with the base at the upper and the apex at the lower end. The function of the heart is to maintain the blood flow through the vessels by periodic contractions and relaxations. In this way the body is supplied with oxygen and nutrients. Also, the end products of the metabolism are carried away from the cells.

3.1 Structure of the heart in connection with the blood flow

Every living cell needs oxygen in order to function. The cardiovascular system, which is constituted from the heart and the blood vessels, has the task to deliver oxygen-rich blood to every cell in the body. The arteries are the passageways through which the blood is delivered. The largest artery is the aorta, branching off the heart and then dividing into many smaller arteries. The veins carry the deoxygenated blood back to the lungs to pick up more oxygen, and then back to the heart once again. Blood flows continuously through the circulatory system being coordinated by the heart that works both as a pump and blood reservoir.

The heart, just like all other muscles in the body, needs its own supply of oxygen in order to function properly. Although its chambers contain blood, it receives no nourishment from the blood inside the chambers. The heart gets its blood supply from the coronary arteries. The two major coronary arteries (the right coronary artery and the left main coronary artery) branch off the aorta, and then divide into many smaller arteries lying in the heart muscle and feeding the heart. The attachment of blood vessels is species dependent and interindividual variations are reported [19].

The anatomy of the heart can be described from different points of view, e.g. geometric, electrophysiologic and embryologic. From a macroscopic spatial point of view a mammalian heart, has a trapezoidal silhouette and is located inside the thorax and near to the lungs. It is embedded by the pericardial sac. The heart is divided in two functionally and anatomical similar structures. The right and the left halves represent the partition of the blood circulation system in two different sections. The right half collects the deoxygenated blood from the body and pumps it to the lungs. The left one collects the oxygenated

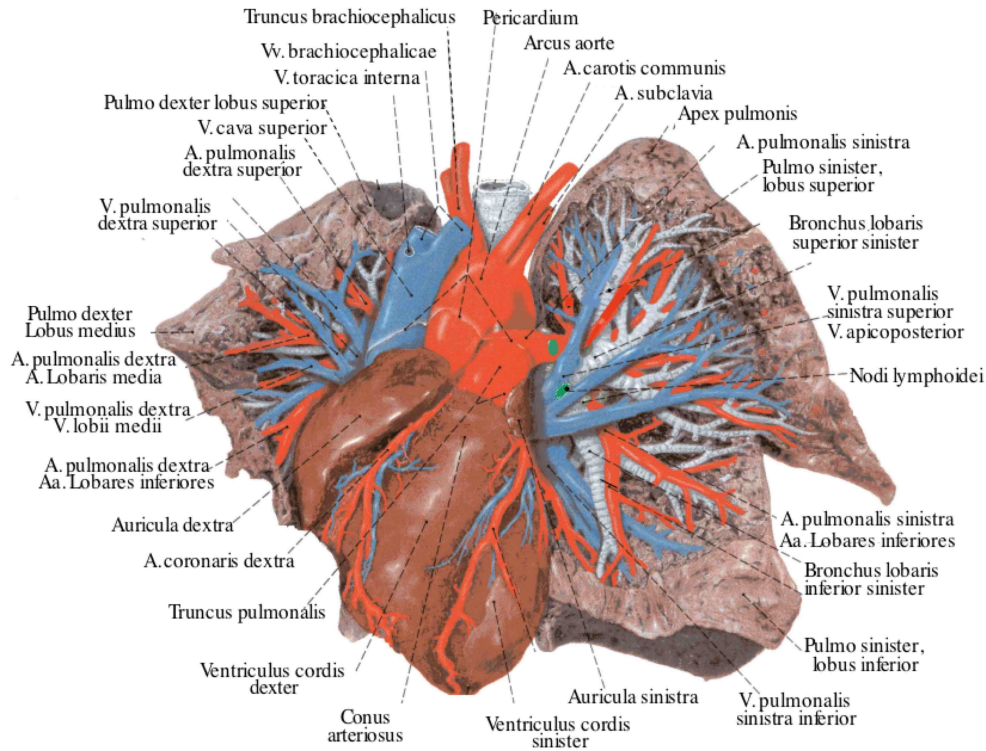


Figure 3.1: Detailed anatomy of the heart with blood vessels. Fig. adapted from [18].

blood from the lungs to deliver it to the body. Because of its function the left half is the larger one. A further division of the halves in lower and upper parts is marking the atria and the ventricles. Therefore, a mammalian heart is composed out of four chambers. The atria collects the incoming blood, transported afterwards to the ventricles. From these the blood is moved to supply the body and the heart itself. Since the ventricles are the primary generator of power, they are described by relatively large muscular structures. The atria and the ventricles are composed of walls, surrounding a blood medium. The walls consist primarily of a muscle structure, the myocardium, covered by endocardium on the inside and epicardium outside. The atria and the ventricles are connected through blood vessels. Ostia are the major points of attachment. The left ventricle contains the mitral and the aortic ostium. The right ventricle has the tricuspid and the pulmonary ostium. Between the atria and the ventricles resides the atrioventricular septum, consisting of fibrous connective tissue. The His bundle is punctuating the atrioventricular septum. The blood is transferred between the upper and the lower chambers through atrioventricular valves. Attached to the wall are intracaval structures, i.e. the papillary muscles and trabeculae. The papillary muscle can be compared to pillars basing with one end in the wall. At the other end they are connected with tendons leading to the atrioventricular valves. The trabeculae are composed of branching small muscle bundles, pervading the ventricular cavities similar to a mesh.

The working myocardium of the ventricles is characterized by an oriented and laminated structure ([22], [23], [24]). The orientation of myocytes in the

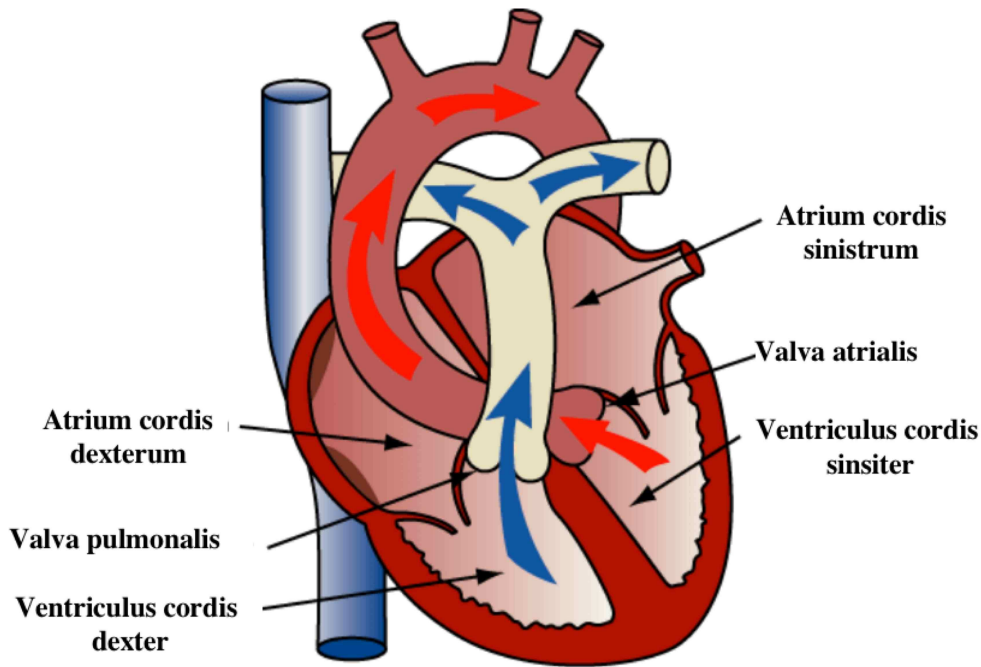


Figure 3.2: Geometry of the heart and blood flow. The right and the left atrium are located at the upper part of the heart. At the lower part, the two ventricles are visible. Deoxygenated blood reaches the right atrium through the V. cava superior and inferior. Oxygenated blood flows through the four pulmonary veins into the left atrium. During the contraction of the atria, the blood is transported through the tricuspid and the bicuspid valve into the right and the left ventricle, respectively. During the next contraction of the ventricles the blood is pumped from the right ventricle through the pulmonary valve into the lung circulation and from the left ventricle through the aortis valve into the body circulation. Fig. adapted from [20].

ventricular wall is dependent on the depth. The orientation can be quantitatively described by the helix angle of a fiber path through the myocardium parallel to the local epicardium. For being able to describe the variation of the fiber orientation from the quantitatively point of view a local system of coordinates must be introduced. The orthogonal local coordinate system is constructed by a vector parallel to the principal axis of the ellipsoid and a second vector, perpendicular on the principal axis and on the normal of the surface. In human left ventricular myocardium an angle of -75° was measured epicardially, 70° endocardially and 0° in the midwall. Commonly a continuous variation of the angle from epicardial to endocardial region is measured. In the apex cordis the orientation leads to two vortices, one for each ventricle.

The lamination of the myocardium results from the grouping of myocytes. The grouping is caused by the enveloping of groups of myocytes by the perimysal collagenous network. In the papillary muscles a lamination was nowhere observed in anatomical studies.

The orientation of myocytes in the mammal atria reflects the configuration of the muscle bundles ([25], [26], [27]). Circumferential orientation exists in the mitral and tricuspidal ostia and at the atriocaval junction of the pulmonary

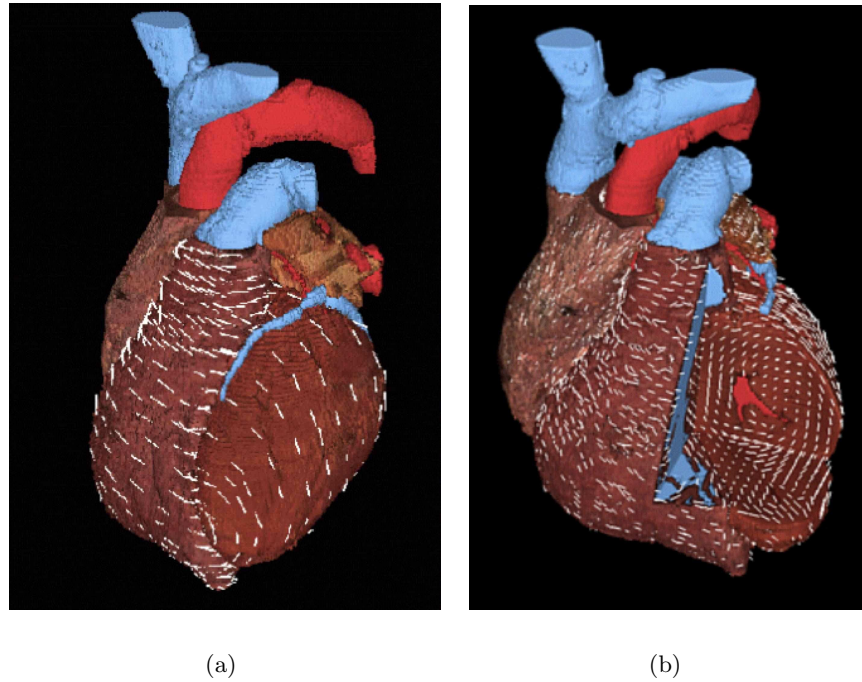


Figure 3.3: Fiber orientation a) on the epicardial surface and b) across the heart.

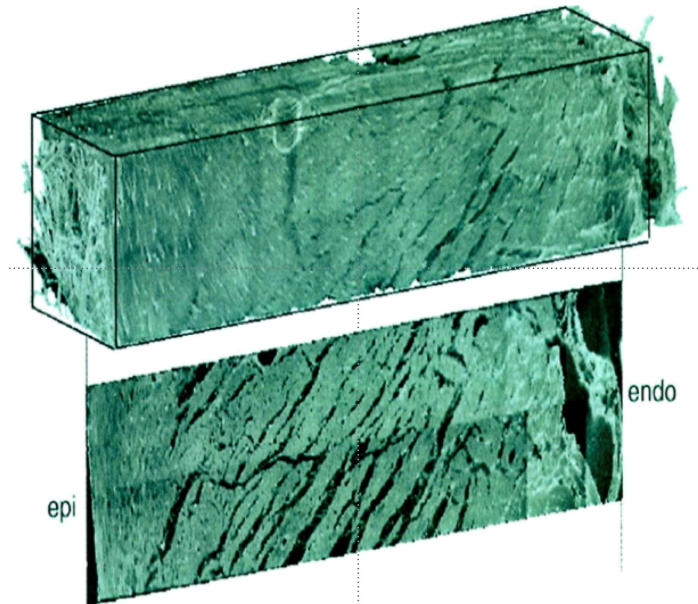


Figure 3.4: Micrograph of fiber orientation and lamination in a wedge of the rat left ventricular myocardium. Myocardial sheets are surrounded by connective tissue covering the capillaries. Fig. adapted from [21].

veins. Longitudinal orientation is present in the venae cavae, in the crista terminalis and in the Bachmann bundle. A lamination of the myocardium is not specific to the atrial region.

3.2 Excitation initiation and conduction system

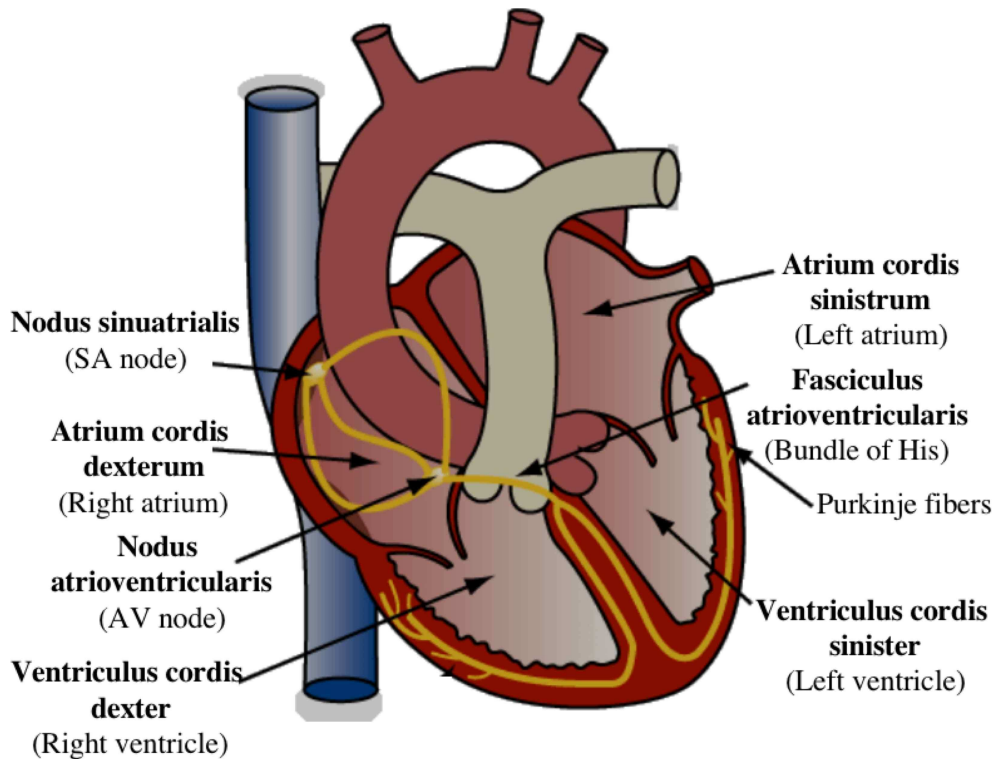


Figure 3.5: The electrical system of the heart. The primary pacemaker is the sinoatrial node. From there the excitation spreads along the crista terminalis, pectinate muscles and along internodal bundles towards the AV node. During this phase, the working myocardium of the right atrium gets directly excited, while the left atrium gets activated by the interatrial bundles (Bachmann bundle and connection located by the coronary sinus). The excitation spreads from the AV node only along the His bundle towards the ventricles. The excitation is further conducted by the Tawara branches into the Purkinje fibers, spreading network-like into the subendocardial myocardium. Example from Heart Rhythm Society.

The complex system of cardiac muscles is creating what can be, in the simplest terms called, a hydrodynamical pump. The electric control of the heart for pumping comes from an intrinsic electrical conduction system.

An electrical stimulus is generated by the sinoatrial (SA) node (Keith-Flackscher node), a small mass of specialized tissue located in the right atrium (right upper chamber) of the heart. The SA node generates an electrical stimulus periodically (60 to 100 times per minute under normal conditions). The excitation travels through the conduction pathways and causes the heart's chambers to contract and pump out blood. The right and left atria are stimulated first and contract a short period of time before the right and left ventricles. The electrical impulse travels from the SA node to the atrioventricular (AV) node (Aschoff-Tawara node), where it stops for a very short period, then continues down the conduction pathways via the bundle of His into the ventricles. The

bundle of His divides into right and left pathways to provide electrical stimulation to both ventricles.

Normally, as the electrical impulse moves through the heart, the heart contracts. The regular mechanical activities correspond to the heartbeats. The atria contracts a fraction of a second before the ventricles so their blood empties into the ventricles before the ventricles contract.

4 Cardiac Electrophysiology

The myocardium consists of several different types of cardiomyocytes. A classification of the cardiomyocytes can be done by considering their electrophysiological characteristics. A part of the cells is mainly responsible for the initiation of the electrical activity, while the rest is responsible for the conduction of excitation. The phenomena of cell activation and spreading of excitation is based on ionic flow through the cell membrane and between adjacent cells. The processes corresponding to the cellular membrane are described in the first part of the chapter. After the description of the membrane functions, the methods used in their modeling are summed up. By passage of specific ions in a suitably temporal sequence through the cell membrane the characteristic course of action potential of cardiomyocytes is achieved. The formation of the action potential is described in detail in the following part of this chapter. The rich experimental investigation of the cellular electrophysiology helped in the development of cell models. In this chapter two models of the human ventricular myocytes are presented in detail.

Section 4.5 includes information about the ECG. A part of the cardiac pathologies can be identified by reading the ECG recordings. The section 4.7 contains a succinct description of the causes and effects of the cardiac pathologies. The focus is on flutter and fibrillation, which are extremely dangerous arrhythmias related to a modification of the electrophysiology and the excitation propagation.

4.1 Transport Mechanisms in Cell Membrane

Cardiac electrical activity is determined by the transmembrane voltage (V_m), equal to the difference between the electrical potentials of the intracellular and extracellular environment. V_m can only have a nonzero value because of the selectively-permeable cardiac cell membrane. The membrane is composed of a number of proteins which are similar to shifting tiles (Fig. 4.1). The spaces between the tiles are filled with fluid-like phospholipids. The phospholipid consists of hydrophilic heads and tails. The hydrophilic heads point towards the extracellular medium and the cytoplasm. The hydrophobic tails repel the water and point in. Thus, the phospholipids form a bilayer that acts like a barrier between the cell and the environment. The phospholipid bilayer also contains cholesterol, making the bilayer stronger, more flexible and more permeable.

The purpose of the membrane is to control the transport of substances in and out of the cell. The ions can flow between intra- and extracellular media or between neighboring cells. The proteins composing the bilayer are recep-

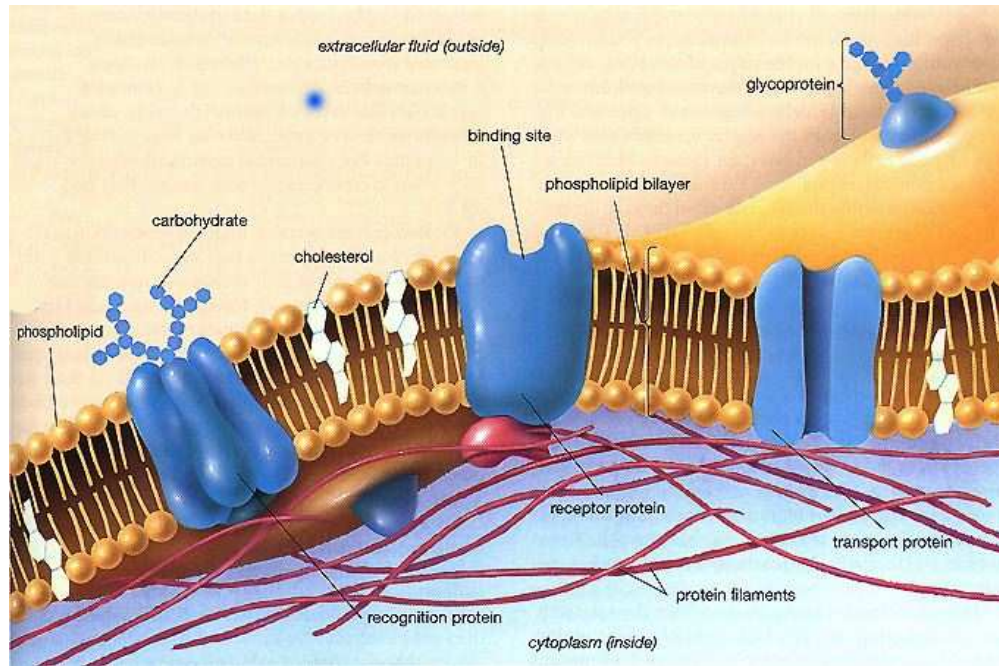


Figure 4.1: Schematic representation of the cell membrane and its components. Fig. from [28].

tor proteins, dealing with communication, recognition proteins and transport proteins controlling the movement of water and soluble molecules through the membrane. In order to regulate the transport of molecules, there are two types of proteins in the cell: carrier proteins and transport proteins. The transport is either active or passive (Fig. 4.2).

The active transport is moving molecules against the concentration gradient and energy is required in the form of ATP. Ions are actively transported with the aid of pumps and co-transporters. The function of ionic pumps is to set up an electrochemical gradient. The input energy for the process is derived from hydrolysis of ATP. During the co-transport process in the cell membrane, two molecules travel together. One is named driver, while the other molecule is termed the passenger. The driver diffuses through the membrane due to electrochemical gradient, but this function can only be fulfilled together with a passenger-molecule. ATP is not directly involved, but it sets up the electrochemical gradient utilized to propel the driver-molecule. Two types of coupled transport exist: symport, the process in which the driver and the passenger are transported in the same direction and antiport, where two molecules are transported in opposite directions.

For passive transport no energy is required because molecules move in the direction of concentration gradient. Passive transport is divided in two types: simple diffusion and facilitated diffusion. Through simple diffusion nonpolar molecules can cross the membrane. Such a phenomenon is the osmosis, representing the diffusion of water molecules. The net movement of water toward the ion-rich solution builds up hydrostatic pressure, called osmotic pressure,

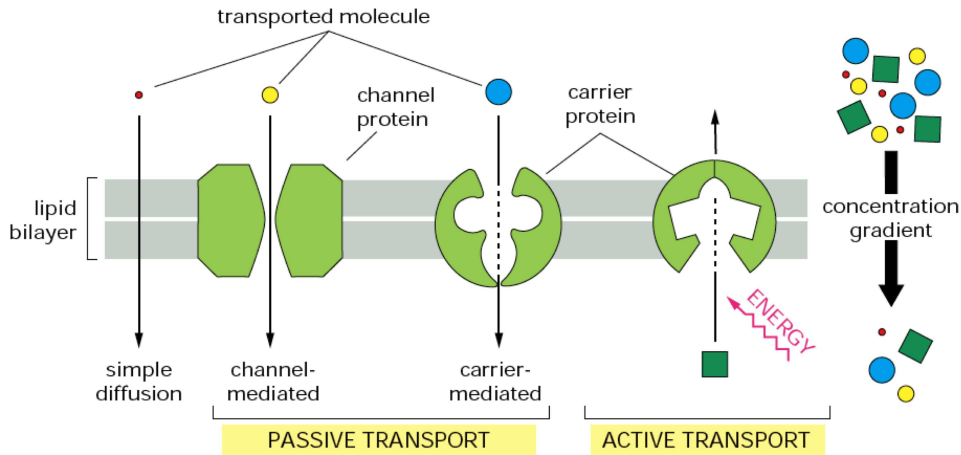


Figure 4.2: Schematic representation of the transport mechanisms in the cell membrane. Except during diffusion, the molecules are transported through the membrane with the aid of membrane proteins parted in carrier and transport types. The transport can be either active or passive.

counteracting at some point the attraction of the ions.

The kinetics of facilitated transport are different from those of simple diffusion. The rate of diffusion in simple transport is directly proportional with the concentration of diffusing molecules. The diffusion rate in facilitated transport is limited by the number of ionic channels and permeases (carrier proteins). Each membrane channel is rather selective for its particular ion (Na^+ , K^+ , Ca^{2+}). The ionic current passing through its corresponding channel at a time depends on the strength of the driving force (proportional with the potential difference for that ion) and how readily the channel will allow the ion passage. Once all the helpers are saturated, the increasing concentration of diffusing molecules will only prolong the waiting queue for the helper and without influencing the transport rate.

Another role of the cell membrane is that it produces various types of connections between cells. Desmosomes attach cells together like "glue". A tight junction is fusing the cells together. The gap junction consists of fused pairs of channels.

4.2 Electrical Modeling of Cell Membranes

4.2.1 Resistor-Capacitor Cell Membrane

The electrical behaviour of a cell membrane can be approximated by a resistor-capacitor circuit, with the nonlinear resistor R_m . The membrane capacity, C_m can be expressed as a function of the electrical charge, q and transmembrane voltage, V_m :

$$C_m = \frac{q}{V_m} \quad (4.1)$$

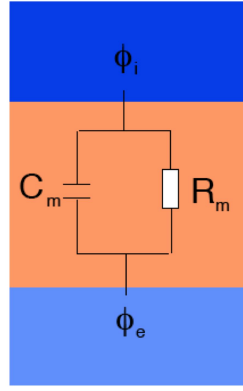


Figure 4.3: Schematic representation of the resistor-capacitor model of the cell membrane. The circuit consists of a nonlinear resistor R_m , and a constant capacitor C_m . The voltage over the membrane V_m is defined as the difference between the extracellular potential Φ_e and the intracellular potential Φ_i .

where $V_m = \Phi_i - \Phi_e$. Considering that V_m is a function of time and C_m is constant, equation (4.1) can be rewritten as:

$$\frac{dV_m}{dt} = \frac{1}{C_m} \frac{dq}{dt} \quad (4.2)$$

The capacity of sarcolemma is depending on its surface. A specific capacitance of approximately $1 \mu\text{F}/\text{cm}^2$ is found in biological cells. The resistor R_m is responsible for the discharge of the membrane by the current I_C . The resistance of the membrane, R_m can be determined applying Ohm law:

$$R_m = -\frac{V_m}{I_C} \quad (4.3)$$

The description of the cell membrane as resistor-capacitor circuit neglects the dependence between V_m and the ionic concentration in the intra- and extracellular media. The ionic diffusion through membrane is described by Stokes-Einstein equation, Nernst equation and Goldman-Hodgkin-Katz equation.

4.2.2 Stokes-Einstein equation

The diffusion of ions through cell membrane during passive transport can be evaluated with Stokes-Einstein equation. The movement of an ion through a solution, in the presence of an external electrical field depends on the gradient of the electrical potential, on the total ionic concentration and on the electrophoretic effect. The ion moves at a constant rate determined by a balance of these forces. This leads to the definition of mobility u_x of the ion x . The relationship between the diffusion constant, D and mobility is expressed in the Einstein equation by:

$$D = \frac{u_x RT}{z_x F} \quad (4.4)$$

where R is the molar gas constant, z_x defines the atomic number, F is the Faraday's constant and T represents the temperature (in K). The diffusion

constant may be related to the viscosity by the Stokes-Einstein equation:

$$D = \frac{RT}{6\pi r_x \eta} \quad (4.5)$$

where r_x is the radius of the solvated ion and η is the viscosity of the fluid. We consider two chambers a and b containing gases of concentrations C_a and C_b respectively. The two chambers are separated by a semipermeable membrane, with the surface S and the thickness d . The concentration difference $\Delta C = C_a - C_b$ will induce the diffusion of the gases. The diffusion rate, J_{diff} is given by:

$$J_{\text{diff}} = S D \frac{\Delta C}{d} \quad (4.6)$$

The electrochemical effects of the ions diffusion can be described with Nernst formalism.

4.2.3 Nernst Equation

Nernst equation extends the formalism describing the process of ionic diffusion including the chemical reactions. The physical system associated with the formalism was termed galvanic cell.

Walther H. Nernst (1864-1941) received the Nobel prize in 1920 in recognition of his work in thermochemistry. His contribution to chemical thermodynamics led to the well known equation correlating chemical energy and the electric potential of a galvanic cell or battery.

Electric Work and Gibbs Free Energy Energy induces the appearance of all physical processes including chemical reactions. In a redox reaction, the energy released during the process due to movement of charged particles gives rise to a potential difference. The maximum potential difference is called the electromotive force, (EMF). The maximum electric work, W is the product between the total charge q and the potential difference, ΔE . The value of ΔE is determined by the nature of the reactants and electrolytes, not by the size of the cell or amounts of material in it. The amount of reactants is proportional to the charge and available energy of the galvanic cell.

The Gibb's free energy, ΔG is the negative value of maximum electric work,

$$\Delta G = -W = -q\Delta E$$

A redox (oxidation-reduction) involves the transfer of n electron moles from one atom to another. Knowing the charge of one electron mole, termed Faraday's constant, F being equal to 96485 C the total charge can be written as:

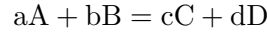
$$q = n \cdot F$$

and

$$\Delta G = -nF\Delta E.$$

At standard conditions, $\Delta G^\circ = -nF\Delta E^\circ$.

The General Nernst Equation The general Nernst equation correlates the Gibb's Free Energy ΔG and the EMF of a galvanic cell. For the reaction



and

$$Q = \frac{[C]^c [D]^d}{[A]^a [B]^b},$$

it has been shown that:

$$\Delta G = \Delta G^\circ + RT \cdot \ln Q.$$

Therefore

$$-nF\Delta E = -nF\Delta E^\circ + RT \cdot \ln Q$$

where R, T, Q and F are the gas constant, temperature (in K), reaction quotient and Faraday constant respectively. Thus, we have

$$\Delta E = \Delta E^\circ - \frac{RT}{nF} \ln \frac{[C]^c [D]^d}{[A]^a [B]^b} \quad (4.7)$$

The relation is known as the Nernst equation. The formula allows us to calculate the cell potential of any galvanic cell for any concentration.

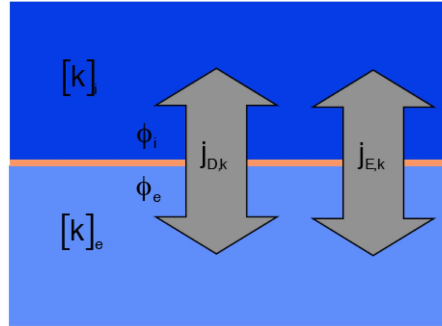


Figure 4.4: Schematic representation of cell membrane according to Nernst formalism.

When a system is at equilibrium, $\Delta E = 0$, and $Q_{eq} = K$. For the equilibrium concentration follows:

$$\Delta E^\circ = -\frac{RT}{nF} \ln \frac{[C]^c [D]^d}{[A]^a [B]^b} \quad (4.8)$$

4.2.4 Goldman-Hodgkin-Katz Equation

The Goldman-Hodgkin-Katz equation was developed to describe the equilibrium voltage of a cellular membrane separating the intra- and extracellular space. The equation extends the Nernst equation by including multiple kinds of ions, that play an important role in cellular electrophysiology. In the formalism a concentration for each kind of ions is assigned to the intra- and extracellular

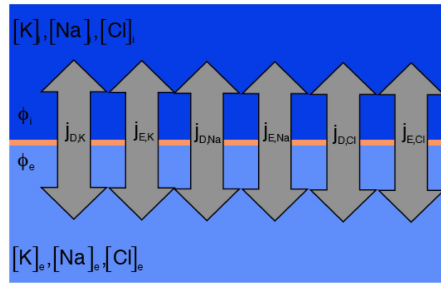


Figure 4.5: Schematic representation of cell membrane according to Goldman-Hodgkin-Katz formalism.

space. The equation expresses the ionic flow through the membrane caused by diffusion and electrical forces.

With the Goldman-Hodgkin-Katz equation the equilibrium voltage is determined from:

$$\Delta E^\circ = -\frac{RT}{nF} \ln \frac{P_K[K^+]_i + P_{Na}[Na^+]_i + P_{Cl}[Cl^-]_o}{P_K[K^+]_o + P_{Na}[Na^+]_o + P_{Cl}[Cl^-]_i} \quad (4.9)$$

from intra- and extracellular ionic concentrations, ionic permeabilities and absolute temperature T . The permeability of the membrane for the K^+ , Na^+ and Cl^- ions is given by the terms P_K , P_{Na} and P_{Cl} , respectively. The mathematical relation, which describes the permeability of an ion x is:

$$P_x = \frac{D_x \beta_x}{h}$$

with the membrane thickness h , the diffusion coefficient D_x and the water membrane partition coefficient β_x . A restriction of the Goldman-Hodgkin-Katz equation is that the membrane is presumed to be homogeneous, planar and infinite and the distribution of the ionic concentration is homogeneous. Further assumptions are that the electric field in the membrane is constant and the ions pass through the membrane independently.

4.3 Action Potentials

The standard model used to understand the electrical behavior of a cardiac cell is the action potential (AP) of the ventricular myocyte. As long as the cell is not being electrically stimulated V_m is remaining constant. Once the cell is excited, it begins a sequence of actions involving the influx and efflux of multiple cations and anions that together produce the action potential of the cell, propagating the electrical stimulation to the cells that lie adjacent to it. We can determine the phase of the AP according to the ionic modifications and the value of V_m (Fig. 4.6).

4.3.1 Resting Phase

The resting phase corresponds to the state, in which the cell remains until it is excited by an external electrical stimulus (that typically occurs from an adjacent

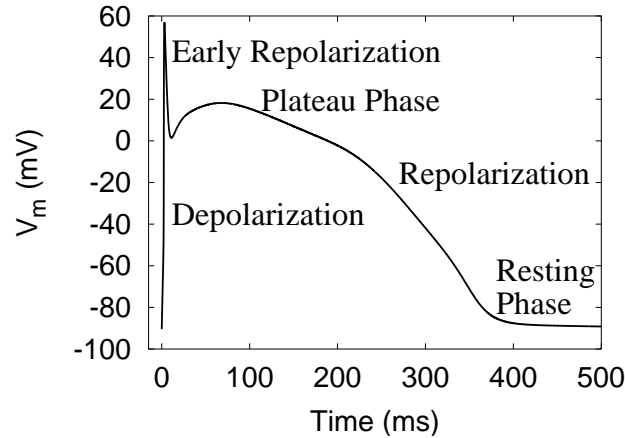


Figure 4.6: The action potential of a human ventricular myocyte generated with Priebe-Beuckelmann cell model. All phases of the action potential are shown in the picture.

cell). This phase of the AP is associated with diastole of the chamber of the heart.

Certain cells of the heart have the ability to undergo spontaneous depolarisation, in which an action potential is generated without any influence from nearby cells. The phenomenon is known as automaticity. The cells that can undergo spontaneous depolarisation are the primary cardiac pacemakers and set the heart rate. Usually, these are cells in the SA node of the heart. Electrical activity that originates from the SA node is propagated to the rest of the heart. The fastest conduction of the electrical activity is via the cardiac electrical conduction system.

In cases of heart block, when the activity of the primary pacemaker does not propagate to the rest of the heart, a latent pacemaker (also termed escape pacemaker) will undergo spontaneous depolarisation and create an action potential.

depolarisation of SA and AV nodal cells largely depend on a net increase in intracellular positive charge. Mechanisms include a decrease in the net K^+ outward flow, and a time-dependant increase inflow of Na^+ and Ca^{2+} ions.

4.3.2 Depolarisation Phase

The slope of the rapid depolarisation phase is determined by the parameters of the electrical stimulation. This phase is due to opening of the fast Na^+ channels and the subsequent rapid increase in the membrane conductance to Na^+ (g_{Na}) and a rapid influx of ionic current in the form of Na^+ ions (I_{Na}) into the cell.

The ability of the cell to open the fast Na^+ channels during depolarisation phase is related to V_m at the moment of excitation. If V_m is at the baseline (about -85 mV), all the fast Na^+ channels are closed. Excitation will open them, causing a large influx of Na^+ ions.

The fast sodium channel contains three gates, the m, the h and the j gate. It is the interaction of these gates that enables the transport of Na^+ through

the membrane. In the resting state, the m gate is closed and the h and j gates are opened. Upon electrical stimulation of the cell, the m gate opens quickly while simultaneously the h and j gates close slowly. For a brief period of time, all three gates are open and Na^+ can flow in the cell across the electrochemical gradient.

4.3.3 Early Repolarisation Phase

The early repolarisation phase is due to closure of the fast Na^+ channels, causing an abrupt end to the depolarisation of the cell. The transient net outward current is due to the movement of K^+ and Cl^- ions. During this phase, V_m decreases fast in a short time interval.

4.3.4 Plateau Phase

The term plateau phase of the action potential indicates the relatively small change in V_m compared to the other phases. Even though V_m is maintained almost at a constant value, many ionic shifts occur during this period of the action potential.

Ca^{2+} and K^+ are the principle ions that are transported across the cell membrane in the course of the plateau phase. The Ca^{2+} channel is activated at a V_m of -35 to -45 mV, causing an influx of Ca^{2+} into the cell. The Ca^{2+} channels activate and inactivate much slower than the fast Na^+ channels. This makes the calcium current, I_{Ca} slower and of longer duration than the fast Na^+ channel.

A second, slow Na^+ channel is also involved in the formation of the plateau phase.

The slow influx of Ca^{2+} is balanced by the outward K^+ current, caused by the activity of multiple K^+ channels. The K^+ current gradually increases during the plateau phase, causing an increasing net loss of positive charge from the cell (reducing the value of V_m).

4.3.5 Repolarisation Phase

During the repolarisation phase the K^+ channels are still open, allowing more K^+ ions to leave the cell and to accumulate in the extracellular space. This net loss of positive charge causes the cell to repolarize. The K^+ channels close when V_m is restored to -80 mV.

4.4 Electrophysiological Cardiac Cell Models

The theoretical research of the excitable cells began more than 50 years ago. With the enhancement of the techniques used for measuring the membrane protein properties the cellular models became more accurate. The model of Beeler and Reuter (1977) [29] as well as the one of Luo and Rudy (1991) [30] were the most important approaches until the mid 90s. Most of the recently developed human cardiac electrophysiological models are based on these two models.

The newer models consist of up to approximately 60 equations describing the properties of the cell membrane, ionic concentrations, intracellular structures like the sarcoplasmic reticulum, and calcium buffering mechanisms and also consider the effects of mechanical stretch to the cell.

Presently exist several models describing human electrophysiological characteristics. The Courtemanche et al. model (1998) [31] and the Nygren et al. model (1998) [32] are for atrial activity. The Priebe and Beuckelmann (1998) [33], Bernus et al. (2002) [34], Ten Tusscher et al. (2004) [35], and Iyer et al. (2004) [36] describe the ventricular activity.

During the research presented in this thesis the electrophysiological model of Priebe-Beuckelmann (PB model) and ten Tusscher-Noble-Noble-Panfilov (TNNP model) were used. Both models are described in the following sections.

4.4.1 Priebe-Beuckelmann Model

Starting from Luo-Rudy model [30] and using data obtained with voltage-clamp technique Priebe and Beuckelmann created a model describing the behavior of human ventricular myocytes [33]. The major ionic currents, I_{Ca} , I_{to} , I_K with its two components (I_{Kr} and I_{Ks}), and I_{K1} , are computed based on human cell data. In addition, the $[Ca^{2+}]_i$ transients in human myocytes and their alterations in failing myocytes observed experimentally can be simulated by this model (Fig. 4.7). The other currents included into the model, I_{Na} , I_{NaCa} , and I_{NaK} , were adopted from Luo-Rudy model and modulated in such a way that simulations are widely consistent with available human data.

The differential equation describing the time-dependent changes in transmembrane voltage in space-clamp conditions is:

$$\frac{\partial V_m}{\partial t} = -\frac{1}{C_m}(\sum I_{mem} - I_{inter}) \quad (4.10)$$

where C_m is the membrane capacity, I_{inter} is the intercellular source current and $\sum I_{mem}$ represents the total transmembrane current. In PB model it is equal to:

$$\begin{aligned} \sum I_{mem} = & I_{Na} + I_{K1} + I_{to} + I_{Kr} + I_{Ks} + I_{Ca} \\ & + I_{NaK} + I_{NaCa} + I_{Na,b} + I_{Ca,b} \end{aligned} \quad (4.11)$$

The meaning of each ionic current is illustrated in the table 4.1. Extracellular concentration of ions is maintained constant. The modification of the value of ionic currents produces a variation of the intracellular concentration of Ca^{2+} .

The cell membrane is a bilipid layer, containing a large number of specific ionic channels and ionic pumps. Ion channels, like many other proteins, have moving parts that perform useful functions. The channel proteins contain an aqueous, ion-selective pore that crosses the plasma membrane and they use a number of distinct gating mechanisms to open and close this pore in response to biological stimuli such as the binding of a ligand or a change in the transmembrane voltage. The activity of the cell membrane was first described by

	Notation	Definition
Natrium currents	I_{Na}	fast Natrium current
	$I_{Na,b}$	basic Natrium current
Potassium currents	I_{K1}	time independent Potassium current
	I_{Kr}	rapid activating Potassium current
	I_{Ks}	slowly activating Potassium current
	I_{to}	transient outward Potassium current
Calcium currents	I_{Ca}	slow Calcium current
	$I_{Ca,b}$	basic Calcium current
Mixed currents	I_{NaK}	the current of the Natrium-Potassium pump
	I_{NaCa}	the current of the Natrium-Calcium pump

Table 4.1: List of ionic currents in Priebe-Beuckelmann cell model. The variation of each term produces a modification of V_m value.

Hodgkin and Huxley [37]. In the formulation gating is treated as a stochastic process. The state of the ionic channels is indicated by the gate variables, which can take the values 0 or 1. If the number of opened channels is equal to n , the number of closed channels must be $(1-n)$. The dynamic response of the currents is controlled by voltage dependent rate constants α and β .



If the maximum whole-cell conductance to ions X is equal to \bar{I}_x , the ionic current, effectively passing through the opened channel is I_x . The mathematical relation, expressing the value of I_x for n opened channels is:

$$I_x = n \cdot \bar{I}_x. \quad (4.13)$$

In the previous example we considered the ion channel having a single gate. For a single type of gate we have:

$$\frac{dn}{dt} = \alpha(1-n) - \beta n. \quad (4.14)$$

In the steady state, the mean number of opened channels is constant. Therefore,

$$\alpha(1-n_\infty) - \beta n_\infty = 0 \quad (4.15)$$

$$\frac{\alpha}{\alpha + \beta} = n_\infty \quad (4.16)$$

where n_∞ represents the mean number of opened channels in the steady state. If we rewrite (4.14) by including n_∞ from 4.16 we obtain:

$$\frac{dn}{dt} = \frac{n_\infty - n}{\tau}, \quad (4.17)$$

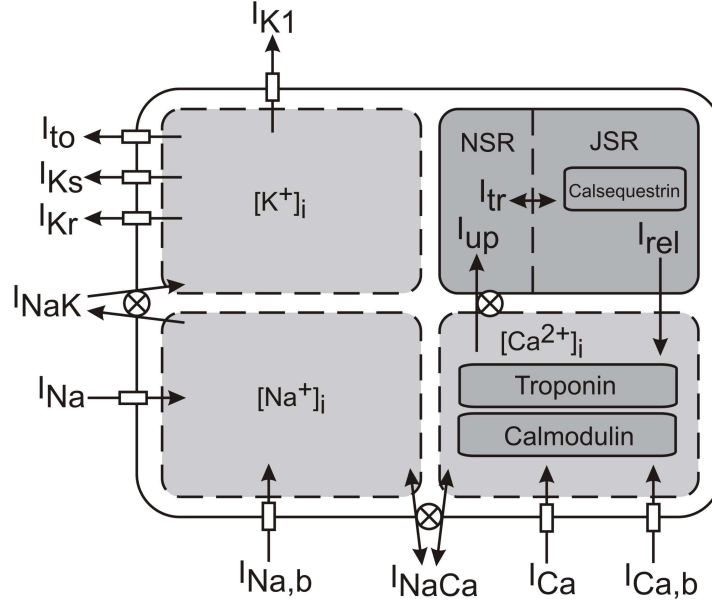


Figure 4.7: Schematic representation of Priebe-Beuckelmann cell model. NSR denotes the network sarcoplasmic reticulum and JSR is the junctional sarcoplasmic reticulum. The arrows indicate the direction, in which the ionic currents can flow through the ionic channels and pumps. The model has dynamic ionic concentration handling.

where

$$\tau = \frac{1}{\alpha + \beta}. \quad (4.18)$$

The parameter τ depends on the rate constants α and β , therefore it is time and voltage dependent. By integration n is obtained as a function of time:

$$n(t) = n_{\infty} - (n_{\infty} - n_0) e^{-\left(\frac{t}{\tau}\right)} \quad (4.19)$$

where $n_0 = n(t=0)$. If many gates are involved in one channel the open probability of all these gates have to be multiplied. The rate constants in Priebe-Beuckelmann cell model have the following form:

$$F_i = A e^{[B(V_m + C) + D]} + E \quad (4.20)$$

All ionic currents were computed for 1 pF cell membrane capacitance. The experiments determined that the inactivation of I_{Ca} is $[Ca^{2+}]$ dependent [38]. This feature was integrated in the model with the inclusion of a proportional factor $f_{Ca} = [1 + ([Ca^{2+}]_i/600\text{nmol/L})]^{-1}$.

$$I_{Ca}(V_m, t) = g_{Ca, \max} \cdot d \cdot f \cdot f_{Ca} \cdot (V_m - E_{Ca}) \quad (4.21)$$

The parameter $g_{Ca, \max}$ is the maximum conductivity for I_{Ca} , d and f are the activation and respectively the inactivation gates for I_{Ca} and E_{Ca} is the equilibrium potential for $[Ca^{2+}]$.

The steady states activation and inactivation curves of I_{to} were obtained from fitting the experimental data produced in 1996 by Naebauer et al. [38] with Boltzman distribution. Mathematically, I_{to} is expressed by:

$$I_{to}(V_m, t) = g_{to,max} (V_m - E_{to}) \cdot r \cdot t \quad (4.22)$$

where $g_{to,max}$ is the maximum conductivity for I_{to} , r and t are the activation and respectively the inactivation gates for I_{to} . E_{to} is the equilibrium potential for I_{to} .

I_{K1} is predominantly carried by K^+ ions in human ventricular myocytes. Therefore the reversal potential of I_{K1} is calculated by Nernst's equation for K^+ . I_{K1} is defined by:

$$I_{K1}(V_m) = g_{K1,max} \cdot (V_m - E_{K1}) \cdot X_{K1} \quad (4.23)$$

where $g_{K1,max}$ is the maximum conductivity, X_{K1} is the inactivation gate and E_{K1} is the equilibrium potential for I_{K1} .

The existence of two components of the delayed rectifier, a slowly activating component I_{Ks} and a rapidly activating component I_{Kr} was documented in 1996 by Li et al. [39]. Both currents were incorporated into the model on the basis of their data set. In the model they are defined as:

$$I_{Ks}(V_m, t) = g_{Ks,max} \cdot (V_m - E_{Ks}) \cdot X_s^2 \quad (4.24)$$

where $g_{Ks,max}$ is the maximum conductivity for I_{Ks} , X_s is the activation gate for I_{Ks} and E_{Ks} is the equilibrium potential for I_{Ks} .

$$I_{Kr}(V_m, t) = g_{Kr,max} \cdot \frac{1}{F_{C,IKr}} \cdot (V_m - E_{Kr}) \cdot X_r \quad (4.25)$$

where $g_{Kr,max}$ is the maximum conductivity for I_{Kr} , X_r is the activation gate for I_{Kr} , $F_{C,IKr}$ is the inward rectifier factor for I_{Kr} and E_{Kr} is the equilibrium potential for I_{Kr} .

4.4.2 Ten Tusscher-Noble-Noble-Panfilov Model

In 2004 Ten-Tusscher et al. [35] proposed a new electrophysiological model (TNNP model) for human ventricular myocytes.

The mathematical construction is based on experimental data on most of the major ionic currents: the fast sodium, L-type calcium, transient outward, rapid and slow delayed rectifier, and inward rectifier currents. The inclusion of basic calcium dynamics, allows the existence of a realistic modeling of calcium transients, calcium current inactivation, and the contraction staircase. Through transient outward and slow delayed rectifier currents the human epicardial, endocardial, and M cell specific action potentials were reproduced. Another unique feature of the model is the broad conduction velocity restitution, bringing a good agreement with available data.

	Notation	Definition
Natrium currents	I_{Na}	fast Natrium current
	I_{bNa}	basic Natrium current
Potassium currents	I_{K1}	time independent Potassium current
	I_{Kr}	rapid activating Potassium current
	I_{Ks}	slowly activating Potassium current
	I_{pK}	plateau Potassium current
	I_{to}	transient outward Potassium current
Calcium currents	I_{CaL}	slow Calcium current
	I_{bCa}	basic Calcium current
	I_{pCa}	plateau Calcium current
Mixed currents	I_{NaK}	the current of the Natrium-Potassium pump
	I_{NaCa}	the current of the Natrium-Calcium pump

Table 4.2: The list of ionic currents, composing I_{ion} in the ten Tusscher-Noble-Noble-Panfilov cell model. The variation of each term produces a modification of V_m .

The transmembrane voltage, as a function of the membrane currents is expressed in TNNP model as:

$$\frac{dV_m}{dt} = -\frac{1}{C_m}(I_{Na} + I_{CaL} + I_{to} + I_{Kr} + I_{Ks} + I_{K1} + I_{NaCa} + I_{NaK} + I_{bNa} + I_{bCa} + I_{pK} + I_{pK} + I_{inter}) \quad (4.26)$$

where C_m is the membrane capacity and I_{inter} is the intercellular source current. The rest of the currents are explained in table 4.2 and illustrated in Fig. 4.8.

The representation of the fast Na^+ current, mainly responsible for depolarisation, is based on three gate formulations, first introduced by Beeler and Reuter [29]:

$$I_{Na}(V_m, t) = g_{Na} \cdot m^3 \cdot h \cdot j \cdot (V_m - E_{Na}), \quad (4.27)$$

where E_{Na} denotes the equilibrium potential for I_{Na} , g_{Na} is the maximum conductivity, m , h and j are the voltage-dependent activation and respectively fast and slow inactivation gates. Each of these gates is governed by Hodgking-Huxley-type equations for gating variables. They are characterized by a steady state value (m_∞ , h_∞ and j_∞) and a corresponding time constant (τ_m , τ_h and τ_j).

The steady state activation value is:

$$m_\infty = \frac{1}{[1 + e^{\frac{-56.86 - V_m}{9.03}}]^2} \quad (4.28)$$

The steady state activation curve (m_∞^3), illustrated in Fig. 4.9 a, was fitted to data on steady state activation of wild type human Na^{2+} channels expressed in HEK-293 cells [40].

The rate constants of the m gate are:

$$\alpha_m = \frac{1}{1 + e^{\frac{-60 - V_m}{5}}}, \quad (4.29)$$

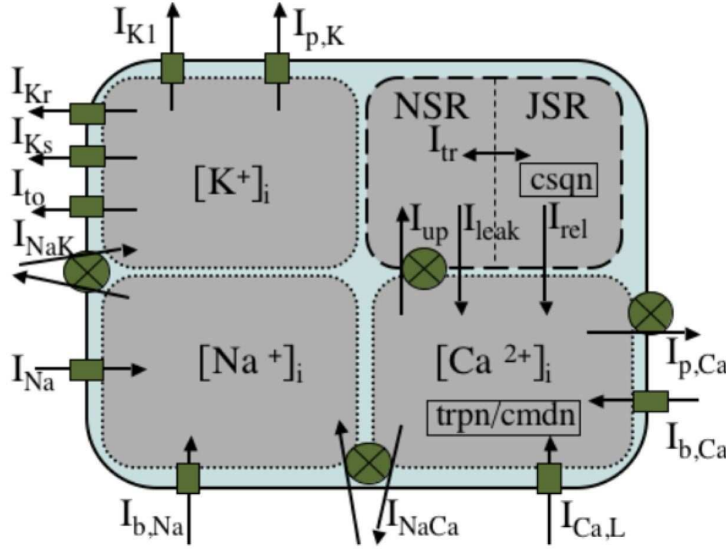


Figure 4.8: Schematic representation of the ten Tusscher-Noble-Noble-Panfilov Model. The arrows indicate the direction, in which the ionic currents can flow through the ionic channels represented by rectangles and pumps, illustrated as crossed circles.

$$\beta_m = \frac{0.1}{1 + e^{\frac{V_m + 35}{5}}} + \frac{0.1}{1 + e^{\frac{V_m - 50}{200}}}. \quad (4.30)$$

The time constant of the m gate is defined as:

$$\tau_m = \alpha_m \cdot \beta_m. \quad (4.31)$$

The derivation of the m gate variable with respect to time is:

$$\frac{dm}{dt} = \alpha_m \cdot (1 - m) - \beta_m \cdot m \quad (4.32)$$

The steady state fast and slow inactivation values are:

$$h_\infty = j_\infty = \frac{1}{[1 + e^{\frac{V_m + 71.55}{7.43}}]^2} \quad (4.33)$$

The rate constants of h and j follow different mathematical rules, all of them presenting modifications at $V_m = -40$ mV.

Also the steady state inactivation curve (Fig. 4.9 b) was fitted to experimental data measured by Nagumo et al. [40].

The L-type I_{Ca} is described by the following equation:

$$I_{CaL}(V_m, t) = g_{CaL} \cdot d \cdot f \cdot f_{Ca} \cdot 4 \frac{V(F)^2}{RT} \frac{[Ca]_i \cdot e^{\frac{2VF}{RT}} - 0.341 \cdot [Ca]_o}{e^{\frac{2VF}{RT}} - 1.0} \quad (4.34)$$

where, with respect to I_{CaL} , g_{CaL} is the maximum conductivity, d and f are the voltage-dependent activation and respectively the inactivation gates and

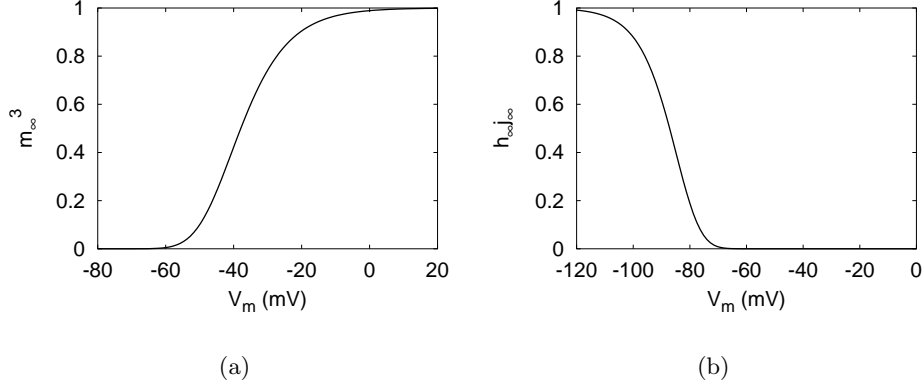


Figure 4.9: Steady state a) activation and b) inactivation curves describing the gating of the fast Na current.

f_{Ca} is an intracellular calcium-dependent inactivation gate. The driving force is modeled with a Goldman-Hodgkin-Katz equation.

Mathematically, I_{to} is expressed by:

$$I_{to}(V_m, t) = g_{to,max} (V_m - E_{to}) \cdot r \cdot s \quad (4.35)$$

where $g_{to,max}$ is the maximum conductivity for I_{to} , r and s are the voltage-dependent activation and respectively, inactivation gates for I_{to} and E_{to} is the equilibrium potential for I_{to} . The parameter $g_{to,max}$ was fitted to experimental data obtained by Naebauer et al. [38].

I_{K1} is predominantly carried by K^+ ions in human ventricular myocytes. Therefore the reversal potential of I_{K1} is calculated by Nernst's equation for K^+ . I_{K1} is defined by:

$$I_{K1}(V_m) = g_{K1,max} \cdot \sqrt{\frac{[K]_o}{5.4}} \cdot (V_m - E_{K1}) \cdot X_{K1} \quad (4.36)$$

where $g_{K1,max}$ is the maximum conductivity for I_{K1} , X_{K1} is the inactivation gate for I_{K1} and E_{K1} is the equilibrium potential for I_{K1} . Because no data is available on the extracellular potassium concentration $[K]_o$ dependence on I_{K1} , a similar dependence as implemented for animal myocytes was assumed.

The existence of two components of the delayed rectifier, a slowly activating component I_{Ks} and a rapidly activating component I_{Kr} was documented in 1996 by Li et al. [39]. Both currents were incorporated into the model on the basis of the experimental data set. In the model the two currents are defined as:

$$I_{Ks}(V_m, t) = g_{Ks,max} \cdot (V_m - E_{Ks}) \cdot X_s^2 \quad (4.37)$$

where $g_{Ks,max}$ is the maximum conductivity for I_{Ks} , X_s is the activation gate for I_{Ks} and E_{Ks} is the equilibrium potential for I_{Ks} . The rapid delayed rectifier current is described by:

$$I_{Kr}(V_m, t) = g_{Kr,max} \cdot \sqrt{\frac{[K]_o}{5.4}} \cdot (V_m - E_{Kr}) \cdot X_{r1} \cdot X_{r2} \quad (4.38)$$

where $g_{K_r, \max}$ is the maximum conductivity for I_{K_r} . X_{r1} and X_{r2} are the activation and respectively the inactivation gates for I_{K_r} . E_{K_r} is the equilibrium potential for I_{K_r} .

4.5 Electrocardiogram

Definition In 1893 the Dutch physiologist Willem Einthoven introduced at a meeting of the Dutch Medical Association the term 'electrocardiogram' (ECG or EKG) for naming a new noninvasive method for cardiac investigations. The data delivered by the electrocardiograph indicate the temporal electrical activity of the heart. A typical ECG tracing of a normal heartbeat consists of a p wave, a QRS complex and a T wave. The names were established by Willem Einthoven.

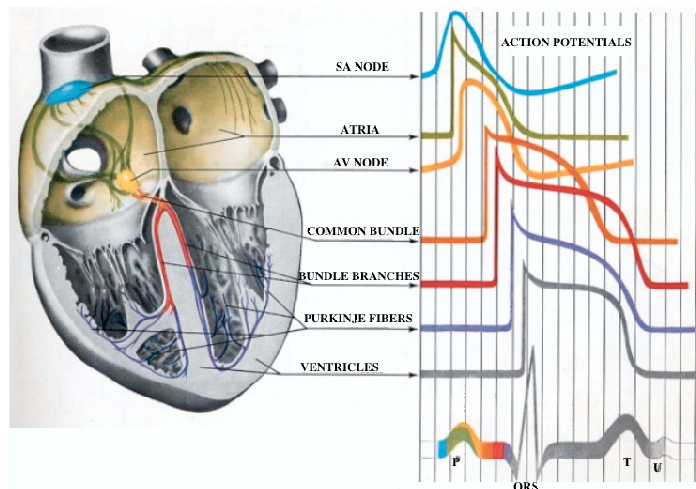


Figure 4.10: The AP corresponding to each type of cardiomyocyte and the ECG formation. Fig. adapted from [20].

The four deflections prior to the correction formula were labelled ABCD and the 5 derived deflections were labelled PQRST. The choice of P is a mathematical convention by using letters from the second half of the alphabet. N has other meanings in mathematics and O is used for the origin of the Cartesian coordinates. In fact Einthoven used O X to mark the timeline on his diagrams. A lot of work had been undertaken to reveal the true electrical waveform of the ECG by eliminating the damping effect of the moving parts in the amplifiers and using correction formulae. The image of the PQRST diagram may have been striking enough to have been adopted by the researchers as a true representation of the underlying form. The naming convention was maintained when the more advanced string galvanometer started creating electrocardiograms a few years later.

The P wave is the electrical signature of the current that causes atrial contraction. Both the left and right atria contract simultaneously. The QRS complex corresponds to the current causing the contraction of the ventricles, being more forceful than that of the atria and involves more muscle area, thus resulting in a much greater ECG deflection. The QRS complex contains the atrial

repolarisation. The T wave represents the repolarisation of the ventricles.

In Einthoven's electrocardiographic model the cardiac source is a two-dimensional dipole in a fixed location within a volume conductor that is either infinite and homogeneous or a homogeneous sphere with the dipole source at its center. Einthoven assumed that the functional position of the measurement sites of the right and left arm and the left leg corresponded to points on the torso which, in turn, bore a geometric relationship approximating the apices of an equilateral triangle. The location of the heart dipole relative to the leads was chosen, for simplicity, to be at the center of the equilateral triangle (Fig. 4.11).

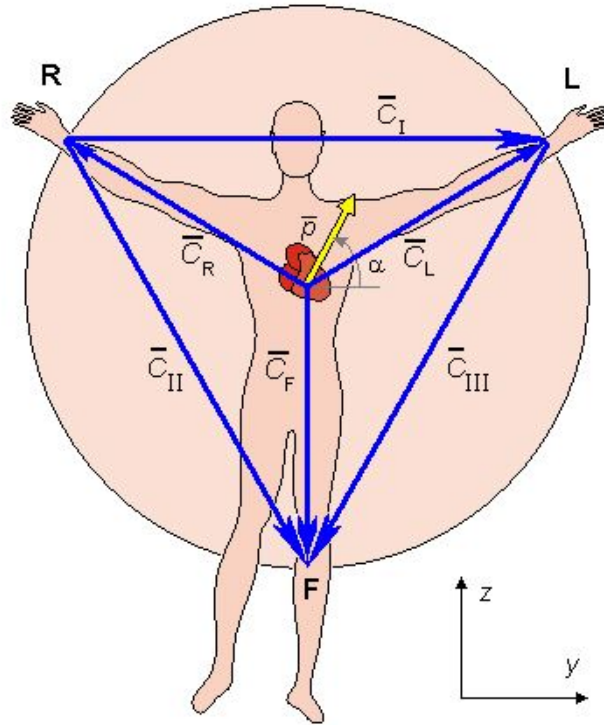


Figure 4.11: Einthoven triangle. The vectors \vec{c}_R , \vec{c}_L , and \vec{c}_F indicate the distance between the measurement points and the heart. The vectors \vec{c}_I , \vec{c}_{II} , and \vec{c}_{III} illustrate the points utilized in the calculation of the fundamental lead voltages. Fig. from [41].

The right and left arms and left foot were denoted by R, L, and F, respectively. The three corresponding lead vectors \vec{c}_R , \vec{c}_L , and \vec{c}_F are the radius vectors between the origin and the corresponding points on the equilateral triangle. The potentials at these points are:

$$\begin{aligned} F_R &= \vec{c}_R \cdot \vec{p} \\ F_L &= \vec{c}_L \cdot \vec{p} \\ F_F &= \vec{c}_F \cdot \vec{p} \end{aligned} \tag{4.39}$$

Einthoven defined the potential differences between the three pairs of these three points to constitute the fundamental lead voltages in electrocardiography. These are designated V_I , V_{II} , and V_{III} and are given by:

$$\begin{aligned}V_I &= F_L - F_R \\V_{II} &= F_L - F_R \\V_{III} &= F_L - F_R\end{aligned}\tag{4.40}$$

Einthoven did not consider the effect of the volume conductor on the lead vectors. The effect of the body surface on the limb leads was published by Ernest Frank (1954), and the effect of the internal inhomogeneities was studied by Burger and van Milaan (1946). The corresponding lead vector triangles are called Frank triangle and Burger triangle.

Presently, a typical ECG report shows the cardiac cycle from 12 different voltage points.

- The inferior leads are II, III and aVF, the lateral leads are I and aVL.
- The chest, or anterior leads are V1 through V6.
- aVR is rarely used for diagnostic information, but indicates if the ECG leads were placed correctly on the patient.

Inferior, lateral and anterior refer to specific sections of the heart. The inferior leads record events from the apex of the left ventricle. The lateral and anterior leads record events from the left wall and front walls of the left ventricle, respectively. The right ventricle has a smaller muscle mass than the left ventricle. It leaves only a small imprint on the ECG, making it more difficult to diagnose the changes in the right ventricle. The finest ECG produced at present is generated by a 256 leads system.

Information Provided by ECG On ECG the following cardiac characteristics can be measured or detected:

- The underlying rate and rhythm mechanism of the heart.
- The orientation of the heart in the chest cavity.
- Evidence of hypertrophy of the heart muscle.
- Evidence of damage of various parts of the heart muscle.
- Evidence of acutely impaired blood flow to the heart muscle (ischemia).
- Patterns of abnormal electrical activity that may predispose the patient to abnormal cardiac rhythm disturbances.

With the use of ECG the following conditions may be diagnosed:

- Abnormally fast or irregular heart rhythms.

- Abnormally slow heart rhythms.
- Abnormal conduction of cardiac impulses, which may suggest underlying cardiac or metabolic disorders.
- Evidence of the occurrence of a prior heart attack (myocardial infarction).
- Evidence of an evolving, acute heart attack.
- Evidence of an acute impairment to blood flow to the heart during an episode of a threatened heart attack (unstable angina).
- Adverse effects on the heart from various heart diseases or systemic diseases (such as high blood pressure, thyroid conditions, etc.).
- Adverse effects on the heart from certain lung conditions (such as emphysema, pulmonary embolus, etc.).
- Certain congenital heart abnormalities.
- Evidence of abnormal blood electrolytes (potassium, calcium, magnesium).
- Evidence of inflammation of the heart or its lining (myocarditis, pericarditis).

Limitations of the ECG The ECG is a static picture and may not reflect severe underlying heart problems at a time when the patient is not having any symptoms. The most common example is of a patient with a history of intermittent chest pain due to severe underlying coronary artery disease. This patient may have an entirely normal ECG at a time when he is not experiencing any symptoms. In such instances, the ECG as recorded during an exercise stress test may reflect an underlying abnormality while the ECG taken at rest may be normal.

Many abnormal patterns on an ECG may be non-specific, meaning that they may be observed with a variety of different conditions. They may even be a normal variant and not reflect any abnormality at all. These conditions can often be sorted out by a physician with a detailed examination, and occasionally other cardiac tests (e.g. echocardiogram, exercise stress test).

In some instances, the ECG may be entirely normal despite the presence of an underlying cardiac condition that normally would be reflected in the ECG. The reasons for this are largely unknown, but it is important to remember that a normal ECG does not necessarily exclude the possibility of underlying heart disease. Furthermore, a patient with heart symptoms should frequently require additional examination.

4.6 Excitation Propagation

The myocardium is build of discrete cardiomyocytes. These myocytes are surrounded by the extracellular space. The discrete structure influences e.g. the

electrophysiological properties of the tissue [42, 43]. The propagation of excitation is driven by electrical coupling of the cardiomyocytes. If one cell is depolarized, V_m rises and a voltage gradient between adjacent cells can be measured. Then the electrical current flows through gap junctions and through the extracellular space into the neighboring resting cell and this cell gets activated. The intercellular electrical coupling leads to a functional electrical syncytium of the myocardium. Since the conductivity of the gap junctions is larger than the conductivity between adjacent cells via the extracellular space, the activation sequence is mainly influenced by the anisotropic electrical properties of the gap junctions.

4.6.1 Gap Junctions

Gap junctions behave primarily like low resistance ohmic resistors, which vary the conductivity depending on the trans-junctional voltage [44, 45]. In contrast to membrane channels they do not show ion selectivity, but allow passage of both cations and anions with a slightly preference for cations. They also provide intercellular metabolic coupling [46].

The conductance of a gap junction depends on ionic factors such as the intracellular concentrations of H^+ , Ca^{2+} , Na^+ , and Mg^{2+} [47]. Thus, gap junction conductance is influenced by application of drugs, which alters the concentration of these ions. Pathologies like myocardial ischemia varies gap junction conductance, because the pH value of the extracellular fluid is changed and that influences the concentration of intracellular H^+ .

Alteration of gap junctional conductance effects the overall electrical interaction between cardiac myocytes. Because connexins form the gap junction, they are important determinants of myocardial coupling properties. Changing genetic expression of connexins causes changes in the overall electrical conductance. Computer simulations and experimental studies showed that a reduction in gap junctional conductance results in reduced excitation propagation velocity [48]. Measurements quantified that the density of gap junctions of the SA node and of the AV node is less than in atrial and ventricular tissue [49].

4.6.2 Models of the Electrical Flow

Modeling of excitation propagation with simplified reaction-diffusion systems describes the physiological and pathological excitation on organ level [50, 51, 52]. The reaction-diffusion systems include two components. One represents the membrane activity termed the reaction part. The other describes the electrical interaction of the tissue and is called the diffusion part. An early representative is the two state Fitz-Hugh-Nagumo model [53]:

$$\frac{\partial u}{\partial t} = \frac{u - \frac{u^3}{3} - v}{\epsilon} + D\nabla^2 u, \quad \frac{\partial v}{\partial t} = \epsilon(u + \beta - \gamma v) \quad (4.41)$$

with the state variables u and v for the activation and inactivation of V_m . The diffusion term is formulated for isotropic media with the scalar diffusion coefficient D . The parameters β , γ , and ϵ are the so-called membrane parameters

and are influencing the course of the AP. The diffusion coefficient and the membrane parameters are time dependent.

A modification of the FitzHugh-Nagumo equations allows a more realistic description of the propagation in the myocardium [6, 54]. This model considers the anisotropic features of the tissue by using a diffusion tensor. It includes more membrane parameters to adapt the AP course to measured data and achieves more realistic results.

The most common approach to reproduce the activity of cardiac tissue consists of a model describing the anisotropic excitation propagation in combination with an electrophysiologically accurate ionic model. The excitation propagation model could be either based on resistor networks or can consider the electrical flow of ions between adjacent cells using Poisson's equation. The advantage of resistor networks to describe electrical coupling of cardiac cells is the lower computational cost compared to approaches based on Poisson's equation. The main disadvantage is that varying anisotropic conductivities in the tissue are not reproducible with the resistor network methods.

A further distinction is made between models considering the extracellular space to be on constant potential and thus calculating the current flow through the intracellular space and through gap junctions (monodomain model) and approaches taking the current flow in intra- and extracellular space as well as through gap junctions into account (bidomain model). Both, monodomain and bidomain model can be represented by resistor network or Poisson's equation based approaches. The implemented method in this work is based on the calculation of Poisson's equation.

4.6.3 The Bidomain Reaction Diffusion Model

The bidomain reaction diffusion model is an experimentally confirmed mathematical tool used in the description of the electrical propagation in the cardiac tissue [55]. In 1978, L. Tung proposed the method, replacing the cardiac tissue by intra- and extracellular continua, each filling the space occupied by the actual myocardium. The representation of bidomain model is illustrated in Fig. 4.12

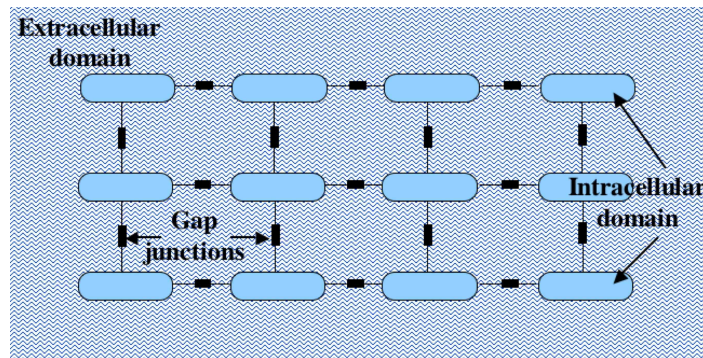


Figure 4.12: Schematic representation of myocardium according to the bidomain model. The method is replacing the cardiac tissue by intra- and extracellular continua, each filling the space occupied by the actual myocardium.

The bidomain model describes a material incorporating the electrical prop-

erties of two distinct, continuous spaces. A material, such as blood or fatty tissue, containing no continuous intracellular space will be referred to as a monodomain. A monodomain can be thought of as a bidomain with a nonconductive intracellular space.

Cardiac tissue consists of cells tightly coupled by intercellular junctions, which connect the intracellular space of one cell to the intracellular space of the surrounding cells. The junctions are characterized by a higher resistivity than the rest of the intracellular space.

Muscle fibers can be represented by a cable model. The fiber is separated into regions of intracellular space, extracellular space, and the separating membrane. Both the junctional resistance and the intracellular conductivity are included in this model by an averaged intracellular conductivity, representing a macroscopic equivalent to these microscopic quantities. The cable model can be extended to two or three dimensions.

The governing equations for the bidomain model are Poisson's equation written in each region with the source term being the source current density (unit A/m³) through the membrane (I_m):

$$\nabla(\sigma_e \nabla \Phi_e) = -I_m \quad (4.42)$$

$$\nabla(\sigma_i \nabla \Phi_i) = I_m \quad (4.43)$$

In these equations, Φ_i (unit V) is the potential in the intracellular space and Φ_e (unit V) is the potential in the extracellular space. The macroscopic conductivities are denoted by the tensors σ_i and σ_e (unit S/cm) and often describe a tissue that is anisotropic. For a passive membrane, the transmembrane current is given by a combination of resistive and capacitive currents,

$$I_m = \beta \left(C_m \frac{\partial \Phi_m}{\partial t} + G_m \Phi_m \right) \quad (4.44)$$

where β (unit m⁻¹) is the membrane surface to volume ratio of the bidomain space, C_m (unit F/m²) is the membrane capacitance, G_m (unit S/m²) is the membrane conductance. The transmembrane voltage is defined as: $V_m = \Phi_i - \Phi_e$. Having these relations, the bidomain system of equations can be expressed by:

$$\nabla((\sigma_i + \sigma_e) \nabla \Phi_e) + \nabla(\sigma_i \nabla V_m) = 0 \quad (4.45)$$

$$\nabla(\sigma_i \nabla V_m) + \nabla(\sigma_i \nabla \Phi_e) = -I_{\text{inter}}. \quad (4.46)$$

Physically, the extracellular space of a cardiac cell on the boundary of a tissue in a surrounding bath is in contact with the monodomain bath region. In the bidomain formulation this contact is defined by the boundary conditions of a bidomain tissue. These conditions state that:

- At the boundary the normal component of current between a bidomain and monodomain tissue is continuous in the extracellular space.
- The normal component of current between a bidomain and monodomain tissue is zero in the intracellular space.
- The extracellular potential and the monodomain potential are continuous.

$$\frac{\sigma_e \partial \Phi_e}{\partial \vec{n}} = \frac{\sigma_{\text{mono}} \partial \Phi_{\text{mono}}}{\partial \vec{n}} \quad (4.47)$$

$$\frac{\sigma_i \partial \Phi_i}{\partial \vec{n}} = 0 \quad (4.48)$$

$$\Phi_e = \Phi_{\text{mono}} \quad (4.49)$$

In this system of equations, \vec{n} is the unit vector showing the normal direction to the boundary between a bidomain region, with potentials Φ_e and Φ_i , and a monodomain region, with potential Φ_{mono} .

Accordingly, the current density in the intracellular domain, \vec{J}_i , is given by:

$$\vec{J}_i = -[\sigma_{ix}^b \frac{\partial \Phi_i}{\partial x} \vec{i} + \sigma_{iy}^b \frac{\partial \Phi_i}{\partial x} \vec{j} + \sigma_{iz}^b \frac{\partial \Phi_i}{\partial x} \vec{k}] \quad (4.50)$$

where σ_{ix}^b , σ_{iy}^b and σ_{iz}^b are the bidomain conductivities in the x, y and z directions and \vec{i} , \vec{j} and \vec{k} are the unit vectors in x, y and z directions. By integration over an homogeneous region with conductivity σ we obtain the electrical potential being equal to:

$$\Phi_{Pi}(x', y', z') = -\frac{1}{4\pi\sigma} \int_v \frac{\nabla \cdot \vec{J}_i}{r} dv \quad (4.51)$$

where r is the distance from a field point $P(x', y', z')$ to an element of source at $dv(x, y, z)$. In the extracellular domain, the current density, \vec{J}_e , is equal to:

$$\vec{J}_e = -[\sigma_{ex}^b \frac{\partial \Phi_e}{\partial x} \vec{i} + \sigma_{ey}^b \frac{\partial \Phi_e}{\partial x} \vec{j} + \sigma_{ez}^b \frac{\partial \Phi_e}{\partial x} \vec{k}] \quad (4.52)$$

$$-\nabla \vec{J}_i = \nabla \vec{J}_e = I_m, \quad (4.53)$$

where I_m is the transmembrane current per unit volume.

Commonly the Poisson equations are solved with finite-difference or finite element method, while Euler or Runge-Kutta are used to solve the underlying ordinary differential equations (Sect. 2).

4.7 Cardiac Pathologies

4.7.1 Arrhythmias

Arrhythmia (or dysrhythmia) is a problem that affects the electrical system of the heart muscle, producing abnormal heart rhythms. It can cause the heart to pump less effectively. An arrhythmia occurs when the heart's natural behavior is disrupted by a certain factor as discussed below.

Normal or Abnormal Impulse Initiation The working myocardium is not automatically active. As outlined in Sect. 4.3, the action potentials of the myocytes are generated by a spread of excitation. In all cardiac cells that are capable of autorhythmicity, depolarisation towards the threshold occurs spontaneously. Normally only a few cells in the SA node are in fact responsible for timing the contraction of the heart. All the other cells in the specialized tissue are excited in the same way as the working musculature. As long as there is no electrical stimulus these cells are in the resting phase. But the stability of the resting potential can be lost under various conditions associated with partial depolarisation of the membrane (hypokalemia, stretching, etc.). Then the affected cells can develop diastolic depolarisations, similar to those produced by pacemakers. In some circumstances the secondary depolarisation fronts can interfere with the primary one and modify the normal heart rhythm. A source of excitation apart from the regular pacemaker tissue is called an ectopic center or ectopic focus.

The heart contracts as the electrical impulse moves through it. This normally occurs 60 to 80 times a minute when a person is at rest. The atria contract a split-second before the ventricles. This lets the atria empty their blood into the ventricles before the ventricles contract. A heart rate of less than 60 beats per minute is called bradycardia. A serious bradycardia is correlated to insufficient blood flow to the brain. Rapid heart beating, called tachycardia or tachyarrhythmia, can produce palpitations, rapid heart action, chest pain, dizziness, lightheadedness, fainting or near fainting if the heart beats too fast to circulate blood effectively. Heartbeats may be either regular or irregular in rhythm.

When rapid heart beating starts in the ventricles, called ventricular tachycardia, it can interfere with the heart's ability to pump enough blood to the brain and other vital organs. This dangerous arrhythmia can change without warning into the most serious heart rhythm disturbance: ventricular fibrillation. In this, the lower chambers quiver and the heart cannot pump any blood. Collapse and sudden cardiac death follow unless medical help is provided immediately.

If treated in time, ventricular tachycardia and ventricular fibrillation can be converted into a normal rhythm with electrical shocks. Rapid heart beating can be controlled with medications or by identifying and destroying the focus of rhythm disturbances. One effective way to correct these life-threatening rhythms is by using an electronic device called an implantable cardioverter (defibrillator).

In atrial fibrillation the atria quiver instead of beating effectively. Blood is not pumped out efficiently and blood clots can be formed. If a part of a blood clot formed in the atria leaves the heart and lodges through an artery in the brain a stroke results.

Abnormalities of Impulse Generation A change of normal automaticity can be induced by normal sinus node pacemaker failure, appearing in disease states or if the normal SA node is excessively rapid due to sympathetic nerve

stimulation.

The arrhythmia can also be correlated to the pacemaker in His Bundle-Purkinje system, normally controlling the cardiac rhythm as escape pacemaker or when sympathetic activity is increased. Such an event can be initiated during sinus bradycardia or AV block of atrial impulses, characterized by a rate lower than the intrinsic rate of His-Purkinje pacemaker. Another possibility occurs if abnormal conditions like ischemia or medication treatment increases the rate of firing of His-Purkinje system pacemaker to overcome the sinus node rate.

The abnormal automaticity in Purkinje cells, involved in a heart attack with ischemic fibers (reduced oxygen) can also trigger dysrhythmias.

The myocytes can produce rapid firing during the repolarisation phase due to premature beats, increased calcium blood levels, increased adrenaline levels or digitalis toxicity.

Abnormalities of Impulse Conduction The abnormalities of impulse conduction are manifested through the existence of supplementary depolarisation fronts and ordered or random reentries. Such cardiac activities can be manifested due to the lowering of the electrical conductivity in a part of the myocardium or by anomalous AV connections, causing a short PR and a wide QRS interval. The additional, anomalous electrical path promotes rapid heart beats called supraventricular tachycardia. When the abnormal electrical path is destroyed tachycardia does not reoccur.

4.7.2 Flutter and Fibrillation

Flutter and fibrillation are arrhythmias resulting from an abnormal spread of excitation, causing parts of the myocardium to contract while other regions of the cardiac muscle are relaxing. The functional fragmentation can be both localized in atria and in ventricles. Ventricular flutter is reflected in ECG by waves with high frequency and large amplitude (Fig. 4.13 a). If flutter persists for several minutes it changes into fibrillation. The fluctuation associated to ventricular fibrillation are very irregular, changing rapidly in frequency, shape and amplitude (Fig. 4.13 b).



Figure 4.13: ECG changes during a) flutter and b) fibrillation. The arrow indicates the initiation of arrhythmias.

Mechanisms of Flutter and Fibrillation There are two alternative concepts for describing mechanisms underlying flutter and fibrillation. In 1875 En-

gelmann presented a theory, assuming ectopic automaticity as the main cause of fibrillation [56]. This hypothesis states that there are one or more ectopic foci, firing at high rates. By this, the regular excitation and conduction of impulses is disrupted. In 1914 Mines and Garrey postulated that circulating excitation waves (reentry) are responsible for fibrillatory arrhythmia [56]. According to the second theory, fibrillation is attributed to a primary disturbance in the spread of depolarisation, in which excitatory waves circulate throughout more or less extended regions of the heart.

At the moment it cannot be decided under which conditions either of the two mechanisms operate. However, most of the phenomena that accompany initiation of fibrillation can be convincingly explained with the theory of reentry. In 1973 Allesie et al. presented direct evidence in favor of this hypothesis for isolated rabbit atria [56]. The concept is also sustained by experiments involving left ventricles [57] and by theoretical research [58], [51].

A fundamental requirement for the appearance of reentries is the existence of interconnected pathways along which excitation can proceed continuously. Experiments indicated that in atria the regions surrounding the ostia of the great veins can constitute pathways for reentry [59]. Allesie et al. (1977) demonstrated that reentry may occur in a flat sheet of myocardial, without macroscopically visible circuit pathways, due to electrophysiological differences between the myocytes. Thus a refractory zone may simulate a nonexcitable anatomical obstacle around which reentry can occur.

In a myocardial fiber assumed to be infinite in length, excitation would proceed in a wavelike fashion. The distance between the excited and the recovered parts is about 0.3 m. The value can be calculated by multiplying the conduction velocity (approximately 1.0 m/s) with the action potential duration (higher than 0.3 s). It is obvious that under normal conditions, such a long excitation wave cannot induce a reentry in the human heart. Thus a reentry is exclusively correlated to the shortening of the excitation wave, induced by decreasing the velocity of conduction and shortening of the refractory period. The alteration degree until reentry occurs, strongly depends on the size of the possible pathways.

The relationship between heart size and probability of fibrillation was an early finding of Garrey [60], who introduced the notion of the critical myocardium mass for reentry to occur. Furthermore, the theory explains the experimentally observed fact that fibrillation is more likely to develop in large hearts, while small hearts tend to defibrillate spontaneously.

Vulnerable Period Atrial or ventricular fibrillation can be induced by electrical stimulation applied during the late systole, interval termed vulnerable period. The term was introduced by Wiggers and Wegria (1939) to express the fact that the susceptibility of the heart to ventricular fibrillation is more or less confined to a certain phase of cardiac cycle [56].

In the ventricles the nonuniformity in recovery of excitability is maximal preceding the apex of the T wave of the ECG. In this period, fully recovered (resting phase), partly recovered (end of repolarisation phase) or absolutely

refractory (an additional stimulus would not modify the value of V_m) myocytes coexist in the tissue. The normal heart is susceptible to fibrillation only during this phase. At other moments an extra electrical stimulus would not produce a fibrillation. Under certain conditions, as it is during ischemia, the vulnerable window may extend even beyond the T wave.

In addition to the induction of fibrillation by electrical stimulation, a spontaneously generated extrasystole that occurs during a highly nonuniform phase of recovery may also induce fibrillation. The event is termed R-on-T phenomenon in the ECG and it is considered a preliminary symptom of imminent fibrillation.

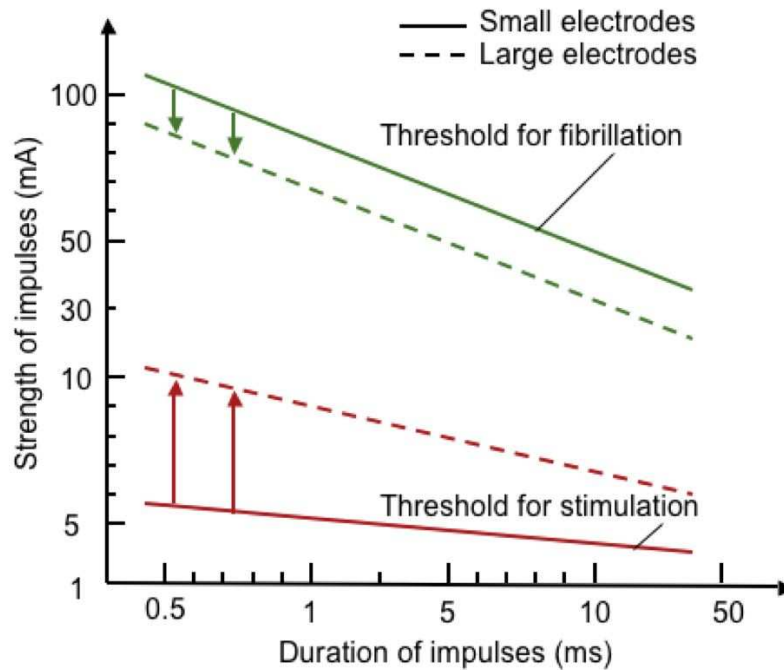


Figure 4.14: Relationship between stimulation and fibrillation threshold in the isolated heart of guinea pig for rectangular pulses [61]. The electrical stimuli were applied through large electrodes with a surface of 0.7 cm^2 or through small electrodes (0.05 cm^2).

The Threshold for Fibrillation The fibrillation threshold is defined as the minimal current intensity required to initiate this arrhythmia. This can be considered as an index of the extra amount of nonuniformity in excitability that must be added to the myocardium for creating a fibrillatory condition. Between the nonuniformity degree of the myocardium and the strength of the electrical stimulation necessary to produce fibrillation is an indirect dependence. Thus diseased hearts may be more susceptible to arrhythmias induced by electrical shocks than healthy ones.

The absolute value of fibrillation threshold also depends on the size and position of the electrodes, the current waveform, the duration of current flow and the transition resistance. Only if these characteristics are maintained constant can relative changes in the fibrillation threshold be attributed to changes of

vulnerability of the heart.

Fig. 4.14 depicts the threshold curves for fibrillation and stimulation, corresponding to an isolated whole heart of a guinea pig. The results were gathered after applying rectangular pulses with duration of 0.5-50 ms [61].

4.7.3 Myocardial Infarction

Ischemic heart disease, commonly named also coronary artery disease is a condition in which fatty deposits (atheroma) accumulate in the cells lining the wall of the coronary arteries. These fatty deposits build up gradually and irregularly in the large branches of the two main coronary arteries encircling the heart being the main source of its blood supply. The process called atherosclerosis leads to the narrowing or hardening of the blood vessels supplying blood to the heart muscle (the coronary arteries). The following effect is occurrence of ischemia (inability to provide adequate oxygen) in the heart and it may damage the myocardium. Complete occlusion of the blood vessel leads to a heart attack (myocardial infarction). According to its location, different types of heart attacks were registered: acute inferior myocardial infarction, acute anterior myocardial infarction, acute posterior myocardial infarction, old inferior myocardial infarction and acute myocardial infarction in the presence of left bundle branch block.

4.7.4 Hypertrophy Patterns

Chronic elevation of myocardial stress due to pressure overload, as in hypertension or aortic stenosis, causes cardiac muscle (ventricular and atrial) to hypertrophy with a resulting increase in myocardial thickness. There is normally little or no change in overall cardiac size, therefore the wall thickening occurs at the expense of the cavity. Systolic function tends to remain normal in the presence of hypertrophy, but diastolic filling patterns are altered. Severe pressure overload eventually leads to impairment of systolic function and finally to left ventricular failure. As systolic function deteriorates, the cavity enlarges, but the walls tend to remain thick. This is in contrast to the dilated cardiomyopathy of ischemic origin.

4.7.5 Heart Block

Congenital heart block is known also as Adams-Stokes syndrome as well as atrioventricular block. It is characterized by interference with the transfer of electrical impulses that regulate the normal rhythmic pumping activity of the heart muscle (heart block). The severity of such conduction abnormalities may vary among affected individuals.

In the mild form of heart block (First Degree), the two upper chambers of the heart (atria) beat normally, but the contractions of the two lower chambers (ventricles) slightly lag behind. In the more severe forms (Second Degree), only a half to a quarter of the atrial beats are conducted to the ventricles. In complete heart block (Third Degree), the atria and ventricles beat independently.

In most cases, infants with First or Second Degree experience no symptoms (asymptomatic).

Another similar pathology is the bundle branch block. Normally, the electrical impulse travels down both the right and left branches at the same speed. Thus, both ventricles contract at the same time. Occasionally, there's a block in one of the branches, and electrical impulses are slowed or blocked as they travel through His bundles.

4.7.6 Pre-excitation Syndromes

If there is an extra conduction pathway, like left lateral and anteroseptal pathway, the electrical signal may arrive at the ventricles too soon. This condition is called Wolff-Parkinson-White syndrome.

Lown-Ganong-Levine Syndrome is a form of pre-excitation characterized by a short PR interval associated with a normal QRS complex.

The existence of pre-excitation syndromes in a heart increases the chance of tachycardia apparition.

4.7.7 Long QT interval Romano-Ward Syndrome

Long Q-T syndrome is an infrequent, hereditary disorder of the heart's electrical rhythm that can occur in otherwise-healthy people. It usually affects children or young adults. It can be identified with the ECG, presenting a prolonged Q-T interval. People with this syndrome are susceptible to an abnormally rapid heart rhythm (arrhythmia) called "Torsade des pointes". When it occurs, the heart muscle cannot contract effectively. The effect is that the normal volume of blood, meant to supply the body and the brain is reduced. If the brain is starved of oxygen, the person faints within seconds. If the heart cannot regain its normal rhythm, it may go into spasms that lead to ventricular fibrillation.

4.7.8 Brugada Syndrome

In 1992 Brugada et al. described a novel clinical entity, which is now frequently called "Brugada syndrome" (BrS) [62]. It is an inherited form of cardiac arrhythmia, presenting with a typical electrocardiographic pattern of ST segment elevation in leads V_I to V_{III} , and incomplete or complete right bundle branch block. In approximately 20% of cases, the underlying cause of BrS is a genetic defect in the SCN5A gene, which encodes the sodium channel controlling the depolarisation phase of the cardiac action potential.

Since no cardiac structural abnormalities are usually found in BrS patients, the disease may be defined as a "pure" electrical abnormality of myocardial cells within an otherwise normal heart. Syncope, typically occurring at rest or during sleep is a common presentation of BrS, and it is caused by fast polymorphic ventricular tachycardia. When tachycardia does not terminate spontaneously or if resuscitation maneuvers are not promptly carried out, it may degenerate into ventricular fibrillation and lead to sudden death.

5 Defibrillators

In present, electrical defibrillation is the only known therapy, that can end a fibrillation. The devices used for this treatment can be external or internal and basically they function in the same way, being generators of electrical impulses, delivered to the heart through electrodes. The constructional aspects are described in detail in the first section of this chapter. Due to the fact that a ventricular fibrillation is an extremely dangerous arrhythmia and because the presently used therapies are not always effective, the phenomenon is intensively investigated both experimentally and theoretically. The state of the art of the research is presented in this chapter in separate sections for the experimental and for the theoretical study. Based on the experimental data was formulated the Weiss-Lapicque law, which is taken into consideration in constructing the defibrillators and can be used as a link between theory and practice. Weiss-Lapicque Law is described in detail in section 5.2.2.

5.1 Constructional Aspects

Development of practical defibrillators began in the 1920s with funding from Consolidated Edison of New York in response to an increasing number of electric shock accidents and deaths. In 1947, Beck et al performed the first successful human defibrillation using specially designed internal cardiac paddles. He used two 110V, 1.5 A, alternative current shocks to resuscitate a 14-year-old boy who had become pulseless during elective chest surgery. In 1956, Zoll et al performed the first successful human external defibrillation using a 15 A AC current that produced 710 V applied across the chest for 0.15 s. In 1961, Alexander, Kleiger and Lown first described the use of AC current for terminating ventricular tachycardia (VT). Work by Lown et al in the early 1960s demonstrated the superiority and safety of DC over AC for defibrillation. Currently two basic types of defibrillators are used: external and internal.

Fig. 5.1 presents the diagram of an automatic external defibrillator. Early models of external defibrillators (ED) required inserting an oral/epigastric electrode and placing a second electrode on the chest. EDs today require the placement of pads on epiderma, at the right sternal border and at the cardiac apex. The geometrical form of the electrodes can be either rectangular or circular. Between the surface of the electrodes and skin a high electrical conductive solution must be applied, for substituting the capacitive medium with a galvanic one. The treatment protects the skin of the defibrillated patient from burning. The electrodes serve to monitor and to defibrillate. EDs also can inform the user when lead contact is poor, when the machine is preparing to defibrillate,

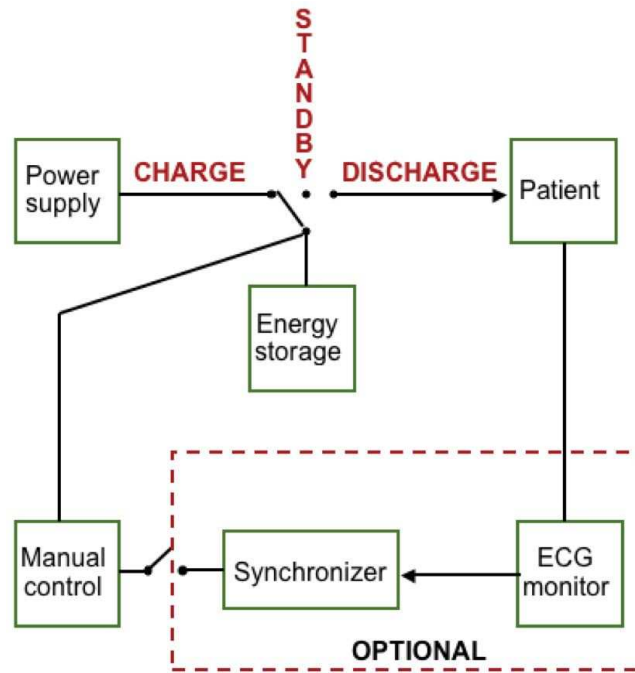


Figure 5.1: Diagram of an automatic external defibrillator.

when to check for a pulse, when a nonshockable rhythm is present, or when motion is detected.

Fully automatic EDs shock at preprogrammed levels once ventricular fibrillation (VF) or VT is sensed. Electrodes are placed in position and the ED is turned on after confirming that the patient is in cardiac arrest. The only way to prevent firing once the machine is committed to discharge is by turning off the ED.

Semiautomatic models inform the user when VF or VT is sensed, then advise defibrillation. The operator must press a button to deliver the shock. The user has the option to discharge the unit, even if the ED is not advising so. Many models allow the operator to override the ED.

Early EDs were designed to respond primarily to a heart rate greater than 150 electrical complexes per minute and an electrocardiographic wave (QRS) amplitude greater than 0.15 mm. Presently, the ECG rhythm is analyzed via a combination of several methods. In addition to rate and amplitude criteria, the QRS is analyzed as to its slope, morphology, power spectrum density, and time away from the isoelectric baseline for preset levels defined as abnormal. Checks are made in 2 to 4 s intervals. In general, if abnormal complexes are detected for more than double the frequency of any other QRS for 3 consecutive checks, the ED will be primed to deliver a shock.

Presently, many defibrillation producers exist. Each has developed his own defibrillation wave form, which has been optimized in time (Fig. 5.2). The optimum defibrillation pulse was defined by Irnich to be characterized by the lowest necessary energy [63]. The most common defibrillation wave form is of the biphasic type. When such a defibrillation shock is delivered, the polarity

of the electrodes is inverted during the second phase of the procedure. The shock-to-shock cycle time is typically less than 20 seconds.

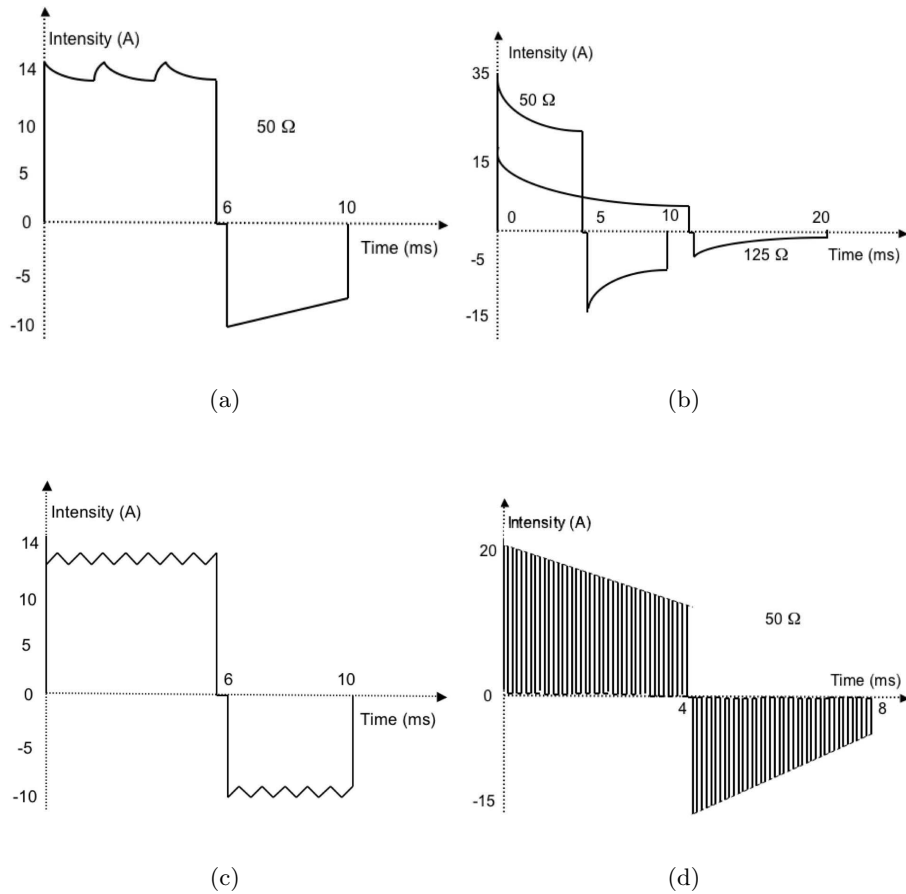


Figure 5.2: Examples of different defibrillation wave forms presently used by a) Zoll, Siemens, b) Philips, c) Metrax and d) Schiller.

The EDs are programmed such that the waveform parameters are adjusted as a function of patient impedance (Fig. 5.2 b). The value of the patient impedance can be measured directly or it can be determined from the slope of the voltage time curve. With the presently in use capacitor discharge approach, the energy required for defibrillation is a primary factor that dictates capacitor size and hence the size of the device. As a result the energy has become a usual gauge for judging defibrillation, even though early and more recent studies indicate that time averaged current is more closely related to defibrillation efficacy.

According to the defibrillators design principles, the patients are divided in two groups: adults and infants. To each class corresponds a certain amount of defibrillation energy and a set of electrode sizes. For example, Philips constructed defibrillators, which deliver in a single output 150 J into a 50 Ω load for adults and 50 J into a 50 Ω load for infants. The surface of the adult pads developed by Philips is equal to 137.1 cm² and for infants is 101.6 cm².

Some defibrillators also include the option of event data transmission to a computer using an infrared protocol. The data including parts of the ECG and analysis decisions can also be stored by the defibrillator.

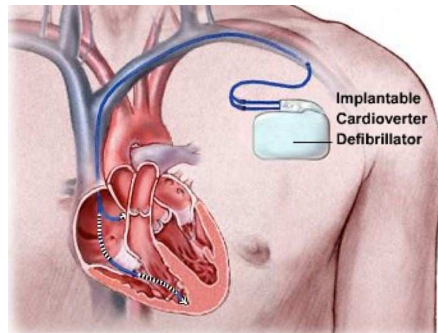


Figure 5.3: Schematic representation of the location of an implantable cardioverter defibrillator and its electrodes. Fig. from [64].

Patients who have had spontaneous and/or inducible life-threatening ventricular arrhythmias and those who are at high risk for developing such arrhythmias can obtain an implantable cardioverter defibrillator (ICDs). In addition, these devices are indicated for prophylactic treatment of patients with a prior myocardial infarction.

An implantable cardioverter-defibrillator (ICD) is a device designed to quickly detect an abnormal heart rhythm (arrhythmia) and suppress it immediately. The ICD can convert the arrhythmia back to normal rhythm by delivering an electrical shock to the heart. This way the ICD can effectively prevent sudden death.

An ICD is a minicomputer with a volume approximately equal to 10 cm^3 . It consists of: a pulse generator with batteries and a capacitor that can send a powerful shock to the heart, an electronic logic circuit to tell the ICD when to discharge and lead electrodes to sense the cardiac rhythm and deliver the shock to the heart muscle. During the implantation of an ICD, electrodes are inserted through the veins into the heart, and the pulse generator is surgically buried under the skin of the chest, generally below the left collarbone.

Modern ICDs also include pacing capabilities so that the device can act as a pacemaker. Pacing may be necessary to support the heart in some instances (for example, after a shock) or as a method to terminate certain arrhythmias. The ICD permanently tests the heartbeats for regularity, but remains inactive until it senses a rhythm deemed life-threatening. Then, the ICD delivers a powerful electric shock to the heart. Each shock uses energy from the generator, transformed before the shock to a capacitor. The ICD batteries are designed to last 5 to 8 years. New defibrillation techniques with smaller amount of necessary energy are searched for increasing the patient comfort and for prolonging the ICD life.

5.2 Research Aspects

5.2.1 Experimental Research

Despite extensive investigation, defibrillation mechanisms continue to be debated. A part of the researchers involved in the study of defibrillation phenomena are using experimental methods for gathering the results. The defibrillation shocks can be applied to living animals, presenting ongoing arrhythmias, to perfused hearts or slices of myocardium. The experimental data are conventionally gathered using measurements via 2 to 10 electrodes. More elaborate experiments add the technique of optical recording with voltage-sensitive dyes or the electrical mapping.

Optical recording using voltage-sensitive dyes has been used to investigate the mechanisms of defibrillation because it (1) is immune to the artifacts produced by high-voltage shocks, (2) provides the time course of the membrane action potential, and (3) can be used to make simultaneous recordings at many sites. The researchers may use the laser scanning technique to record optically action potentials from several sites with high temporal resolution (order of ms) on the surface of the isolated, perfused heart during defibrillation [65]. The data are typically analyzed by constructing maps of impulse propagation and examining individual recordings from sites of interest.

Optical imaging of cardiac transmembrane voltage in dye-stained tissue is an emerging technique in cardiac electrophysiology. Despite its widespread application to studies of isolated hearts, it has been used traditionally to record only a single view that presents the potential distribution of a fraction of the cardiac surface. This poses a significant limitation in studying whole heart electrophysiology, particularly when large-scale phenomena such as fibrillation and defibrillation are topic of the study.

Of high interest in the defibrillation research is the time interval, following the initiation of the electrical stimulation. Whole-heart electrical mapping of defibrillation in animals has shown that after shocks near the defibrillation threshold (DFT) in strength, the immediate postshock activation pattern is mainly focal and is similar for both successful (SDF) and failed (FDF) defibrillation episodes. The similarity of the first postshock activations suggests that the immediate myocardial responses to the shock alone may not determine defibrillation success but rather that the first several postshock cycles may influence shock outcome. Electrical mapping, however, cannot detect activation for up to tens of milliseconds after the shock and provides no direct measure of repolarisation after the shock.

Optical mapping does not have these limitations. Citation of studies in isolated rabbit hearts have reported that reentry caused by unidirectional propagation of activation immediately after the shock is responsible for FDF. SDF has been proposed to occur when a shock sufficiently prolongs and synchronizes repolarisation, decreasing the dispersion of repolarisation and thus preventing conduction block, which can lead to reentry and ventricular fibrillation (VF). These results, however, were obtained from a relatively small epicardial region with shocks well below the DFT.

One of the drawbacks of conventional optical mapping procedure is the fact that it delivers information only from the surface of the heart. The electrical mapping presents an advantage from this point of view. Three-dimensional electrical mapping is possible by inserting very thin (diameter of the order of 100 μm) fiberglass needles in the myocardium. Each of the needles can incorporate several electrodes. The data obtained with electrical mapping is restricted to a certain part of the transmural wall.

Presently, the research group of Arkady Pertsov is using a newly developed experimental technique, termed transillumination method [66]. The electrophysiological mechanisms of polymorphic ventricular tachycardia and fibrillation are analyzed using newly developed experimental tools for three-dimensional (3D) visualization of the electrical activity in the thickness of myocardial wall. The surface manifestations as well as limited 3D information obtained using intramural plunge electrodes, suggested 3D vortex-like reentry (scroll waves) as a mechanism of these arrhythmias. The new experimental method (transillumination) significantly enhances the ability to study 3D reentrant activity via visualization of its organizing center - filament.

5.2.2 Weiss-Lapicque Law

During the 19th century considerable research was done to determine the effect of electricity on various animal tissue structures. The main aim was the formulation of a universal law for electrical stimulation. To sum up the results of his study, Weiss formulated a law, stating that the minimum current required above a certain threshold for stimulation, is inversely proportional to the duration of the electrical stimulation.

$$I = \frac{B}{t} + R \quad (5.1)$$

The term I denotes the threshold current, B is the charge at electrode-myocardial interface, t is the duration of the stimulation current and R represents the minimum stimulation independent of duration of the stimulus.

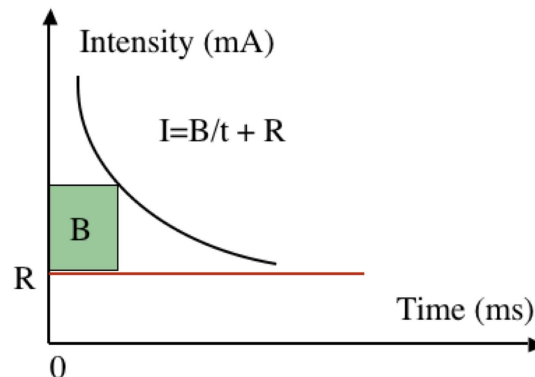


Figure 5.4: The representation of Weiss-Lapicque law.

Lapicque experimented with muscles of various invertebrates by measur-

ing the stimulation thresholds for varying directions. He concluded that by changing the time scale and normalizing the threshold at a point independent of time, the stimulation curves of different tissues from various invertebrates overlap. Consequently Lapicque introduced two new terms to define the tissue stimulation threshold:

1. rheobase - the stimulation threshold independent of the duration of the stimulus;
2. chronaxie - the time at which the minimum threshold is double the rheobase. He called this the measure of excitability of the tissue.

The variation of the threshold current with time, according to Weiss-Lapicque law is illustrated in Fig. 5.4. All implantable defibrillators deliver voltage through a capacitor discharge, resulting in exponentially declining pulses. Early studies in animals suggested that the strength-duration relationship for such pulses was similar to the Weiss-Lapicque relationship for stimulation of cardiac tissue with rectangular shaped pulses.

Weiss-Lapicque relationship predicts a rheobase or minimum mean current for defibrillation and a chronaxie, the pulse width requiring twice the rheobase current. This results in a U-shaped curve for energy or peak voltage as a function of pulse width. For defibrillation pulses, the optimal pulse width is believed to correspond to tilts of 60%. Very long duration or untruncated pulses were ineffective in part because they resulted in refrillation of the heart. Accordingly, all implantable devices are programmed to truncate monophasic defibrillation pulses or the first phase of a biphasic pulse close to a 60% tilt.

5.2.3 Blair Law

Weiss-Lapicque law does not fit perfectly the experimental data. Therefore, several alternative models have been proposed to describe the relationship between pulse width and defibrillation efficacy. One of the most known theories was formulated by Blair in 1932 [67].

The two terms introduced with Weiss-Lapicque formalism, the rheobase and the chronaxie were maintained by Blair. The main difference between the two models is the expression of the time dependence. The formula proposed by Blair, giving the excitation threshold as function of the applied voltage (V) reads:

$$\log \frac{V}{V - R} = k \cdot t + C \quad (5.2)$$

The term R denotes the rheobase, k measures the rate of decay of excitatory process, t is the duration of the electrical stimulus and C is a constant.

Rearranging the equation 5.2 we obtain:

$$V = \frac{R}{e^{k \cdot t + C} - 1} + R \quad (5.3)$$

Considering Ohm's law the voltage can be substituted by the current:

$$I = \frac{R_0}{e^{k \cdot t + C} - 1} + R_0 \quad (5.4)$$

where R_0 represents the rheobase divided by the membrane resistance.

In his formalism Blair defined the chronaxie as:

$$\tau = \frac{1}{k}(\log 2 + C) \quad (5.5)$$

From equations (5.6) and (5.5) the relation for intensity as function of impulse duration, rheobase and chronaxie reads:

$$I = \frac{R_0}{e^{\frac{t \cdot (\log 2 + C)}{\tau} + C} - 1} + R_0 \quad (5.6)$$

Even though Blair's formalism is more complex than the one presented by Weiss-Lapicque it is not valid for long duration stimulations, neither for cases in which the intensity of the electrical impulse is slowly increasing or it oscillates in time. In 1933 W. Rushton published an article presenting in detail the limitations of Blair's model [68].

5.2.4 Theoretical Research

Many studies have been performed on animal hearts ranging from mouse, rat, guinea pig, rabbit, dog and pig heart. However, the phenomena observed in animal hearts are not necessarily the same as those, occurring in humans. For example, the frequency of ventricular fibrillation in a human heart is about 5 Hz [69], whereas in the pig heart it is in the interval 10-14 Hz [70], although they have comparable sizes. Another major limitation of experimental studies is that patterns of excitation can be recorded with reasonable resolution only from limited parts of the heart volume and mainly from the surface, whereas the underlying excitation patterns are three-dimensional.

Computer modeling, especially simulations of human cardiac behavior can play an important role in overcoming these types of limitations. In a simplified model, the defibrillator and the living body can be represented by an electrical circuit (Fig. 5.5). The generator of the electrical shocks comprises a power supply and a RLC circuit, varying from one device to another according to the programmed waveform. The skin and the medium between the electrodes and the heart are represented by resistances: R_s and R_i respectively. The myocardial fiber that follows in the scheme, differentiates the intracellular medium from the extracellular one. The resistances of the myocardium are selected in such a way that the velocity of the excitation propagation is correctly described, both in intra- and the extracellular medium. Even though such a schematic representation can be used for certain studies, it lacks many important features of the heart, like the electrophysiological properties, fiber orientation, representation of the geometry, etc.. The bidomain model permits the inclusion of cardiac characteristics. Therefore most of the present simulations of the electrical behavior of the heart are based on electrophysiological models and bidomain technique.

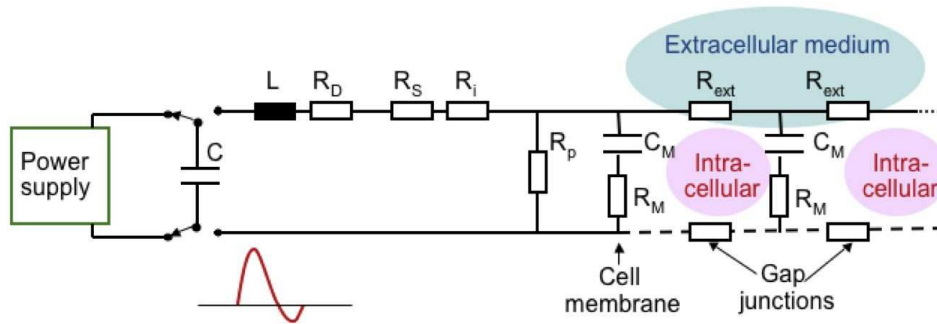


Figure 5.5: Simplified model of the defibrillator and the living body from the view point of electrical properties.

Due to the limited availability of human cardiomyocytes for experimental research, most detailed electrophysiological models have been formulated for animal cells (e.g. Noble model describes guinea pig ventricular cells [71], Luo-Rudy models are for mammalian ventricular cardiomyocytes [30], etc.).

Utilizing electrophysiological models that describe the activity of animal's myocytes many important features of defibrillation phenomena were discovered. The research group of N. Trayanova, used mostly Luo-Rudy and Beeler-Reuter electrophysiological models, presented new insights into defibrillation process. They have been able to identify how some features of the architectural structure, of the electrophysiology and of the electrical propagation influence the response to electrical shocks. For example, they observed that success of defibrillation depends on special electric field pattern in the heart called virtual electrodes and they found that the formation of virtual electrodes far away from the primary electrical sources strongly depends on the fiber orientation [72].

An important part of defibrillation studies is to understand effects of electrical shocks on cardiac cells and tissues. The research group of I. Efimov, investigated the phenomena both experimentally and theoretically. In 2004, it was observed that the stimulation of the myocardium with high electrical shocks destroys gap junctions in certain regions inducing a strong modification of the response of the tissue [73]. The phenomenon was termed cell-uncoupling effect.

In recent years more and more data on human cardiac electrophysiology has been gathered. In 1998 Priebe and Beuckelmann published the first model of human ventricular myocytes [33], which was largely based on Luo-Rudy phase 2 model. In 2000, Bernus optimized the electrophysiological model presented by Priebe and Beuckelmann. In 2004 a new model for human ventricular myocytes by Ten Tusscher, Noble, Noble and Panfilov (TNNP model) appeared [35]. This model uses new formulations for all major ionic currents based on a now much wider experimental data set.

Despite the fact that human electrophysiological cell models exist, not many researchers study defibrillation by means of virtual human myocardium.

6 Features of a Human Ventricular Myocardial Model

Theoretical investigations of the interaction between a myocardium and an electrical field is only possible if a virtual cardiac wedge is predefined. The virtual myocardium can produce various reactions depending on the features included in the preparation and on the characteristics of the electrical field.

This chapter is focused on the study of the influence on the response to electrical stimulation of each feature of the myocardial model. In each subchapter is treated a cardiac characteristic that can be included in a human left ventricular preparation. The studies present corresponding selection criteria and comparisons with experimental data.

One of the first steps in the modeling of the myocardial tissue is the selection of the geometrical features corresponding to micro- and macroscopic levels. The shape and the sizes of the myocytes and of the tissue are generally selected according to computation considerations. An introduction of the selection criteria and of the influence of the geometry is presented in the first section of this chapter.

In the following section is proved the necessity of a correct implementation of the electrophysiological variation of cell model across the human transmural wall.

A key role in a realistic simulation of the path of the electrical current inside the myocardium is played by the anisotropy of the electrical conductivity together with the fiber orientation (Sect. 6.3). The unequal distribution of the intra- and extracellular electrical conductivities corresponding to longitudinal and transversal directions is due to microscopic properties. On a macroscopic level, the anisotropic electrical conductivity is caused by directional differences in cell-to-cell coupling.

Cleavage planes and a blood pool may also be incorporated in the myocardial preparation. Both the region of the blood and of the fragmentizing clefts exclusively comprise nonexcitable cells. The electrical current, passing from the monodomain region into the myocardium is distributed between the intra- and the extracellular domain. The redistribution of the electrical current may induce the occurrence of secondary electrical sources as shown in Sect. 6.4, 6.5. If the excitation spreads from the formed secondary electrical sources, the spatio-temporal distribution of V_m is modified. The corresponding changes are described in detail.

The chapter closes with the summation of the inferences drawn from the presented results.

6.1 Geometry

Depending on the geometrical characteristics, the virtual myocardial preparations used in theoretical studies of cardiological phenomena can be classified as one-, two- and three-dimensional models.

The one-dimensional model represents a straight fibre. Presently, it is rarely used, because of the high restrictions connected with the dimension.

A two-dimensional model is used in general when high computation speed is requested. In the two-dimensional myocardial sheet the fibres can be straight or curved, the electrical unequal anisotropy ratio can be partially incorporated, electrophysiological heterogeneity can be included and the tissue can be immersed in bath.

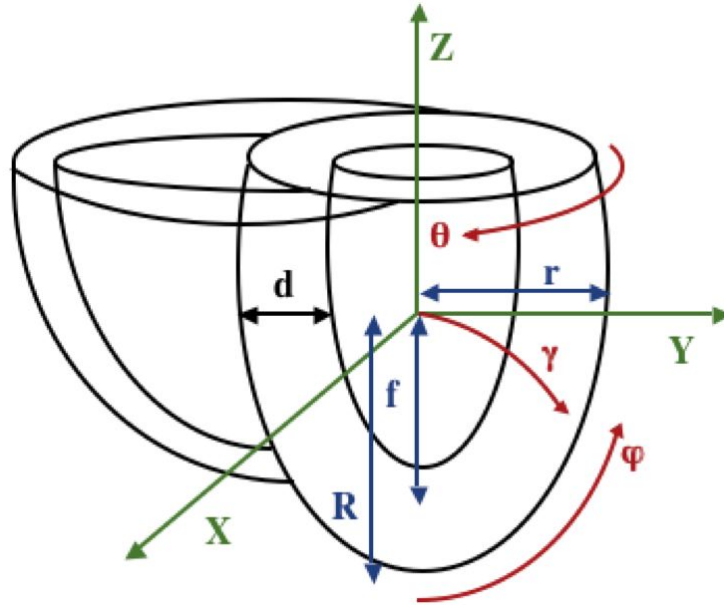


Figure 6.1: Truncated ellipsoid representation of ventricular geometry. The labels show the major left ventricular radius (R), minor radius (r), focal length (f), Cartesian coordinates (X, Y, Z) and prolate spheroidal coordinates (ϕ, γ, θ)

Three dimensional models usually present a high degree of complexity, classifying them as the best representation of the real ventricular myocardium. The left ventricle can be modeled by an ellipsoid of revolution truncated at the base (Fig. 6.1). The crescentic right ventricle wraps circumferentially about 180° around the heart wall and it extends longitudinally about two-thirds of the distance from the base to the apex. In Fig. 6.1 R and r are the principle axes of the epicardium. With d was denoted the thickness of the myocardium. The focal length, f is defined by: $f^2 = R^2 - r^2$.

For describing mathematically a curved model of the myocardium, prolate spheroidal coordinates are introduced.

$$x = f \cdot \cosh(\gamma)\cos(\phi)$$

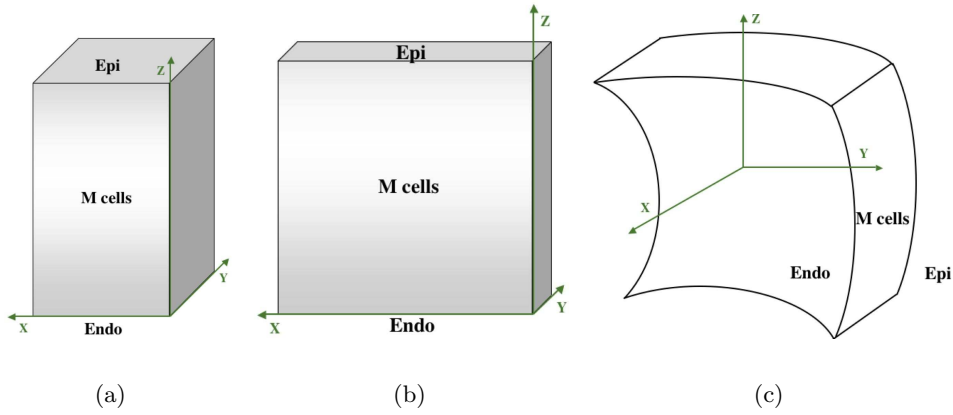


Figure 6.2: Different geometrical types of myocardial wedges. a) A parallelepipedic section through the virtual myocardium that is commonly used for studying fundamental phenomena of electrical stimulation. b) A thin slice of the virtual myocardium, containing two large sides. This geometrical configuration is generally utilized for simulating arrhythmic cardiac behaviors. c) A curved section of the myocardium, often used for studying phenomena in which the curvature of the tissue is very important.

$$\begin{aligned} y &= f \cdot \sinh(\gamma) \sin(\phi) \cos(\theta) \\ z &= f \cdot \sinh(\gamma) \sin(\phi) \sin(\theta) \end{aligned} \quad (6.1)$$

The disadvantage of the truncated ellipsoidal models is the corresponding long computation time. Usually, in theoretical studies of the human myocardium sections of the ellipsoidal model are utilized (Fig. 6.2).

With a parallelepipedic section of the virtual myocardium (Fig. 6.2 a) the transmural heterogeneous cardiac characteristics can be investigated. The geometrical construction is also appropriate for the research of fundamental processes that involve propagation across the transmural wall. The longest axis of the parallelepipedic model is the one perpendicular to endo- and epicardial surfaces. The realistic dimension of the longest side of the parallelepipedic model has the order of cm.

Self maintaining arrhythmic human cardiac behaviors, like fibrillation and flutter are simulated in large models (Fig. 6.2 b). Two sides of the virtual myocardium are a few cm long. Considering the geometry of the human left ventricle in a realistic simulation the third dimension is decreased to a value below one cm.

The curved section of the myocardium (6.2 c) is a finer description of the myocardium than the parallelepipedic models. The construction can include the realistic variation of the tissue curvature and of the wall thickness. The curved virtual myocardium is appropriate for the research of internal defibrillation.

6.1.1 Parallelepipedic Myocardial Preparation

In the study presented in this section was considered a parallelepipedic myocardial preparation, with the size $1 \times 1 \times 2 \text{ cm}^3$, totally resting before the

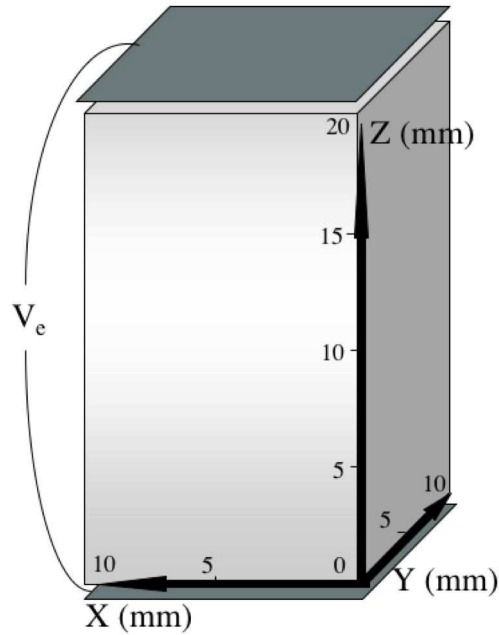


Figure 6.3: The position and the geometrical characteristics of the paddles utilized for stimulating the tissue.

electrical stimulus was applied. The electrophysiology was described by the Priebe-Beuckelmann cell model (Sect. 4.4.1). The myocytes were arranged in fibers, characterized by realistic orientation and the electrical conductivity of the media was set to be anisotropic (Table 6.1). The myocardium was excited with a monophasic shock with the absolute value of 1 V, and a duration of 1 ms [74]. The characteristics of the electrodes is illustrated in Fig. 6.3. After the initiation of excitation, the myocardium went through the following phases:

- hyperpolarization near the anode and depolarisation near the cathode (Fig. 6.4 a);
- spread of excitation from the depolarized region all over the tissue (Fig. 6.4 b);
- isopotential state followed by the repolarisation of the myocytes (Fig. 6.4 c, d).

Due to the selected configuration the results presented symmetry with respect to X and Y axis. Therefore the illustrated data are shown only for XZ plane (Fig. 6.5, 6.4).

During the first phase, the results indicated an exponential decay of V_m with the distance along the fiber. The myocardial layer beneath the anode presented a reduced V_m indicating the hyperpolarization. The cells incorporated in the first plane next to the cathode presented a positive V_m marking the depolarisation (Fig. 6.4 a). The V_m value of the myocardial area neighboring the hyperpolarized cells was higher than the one specific to the resting state. Very

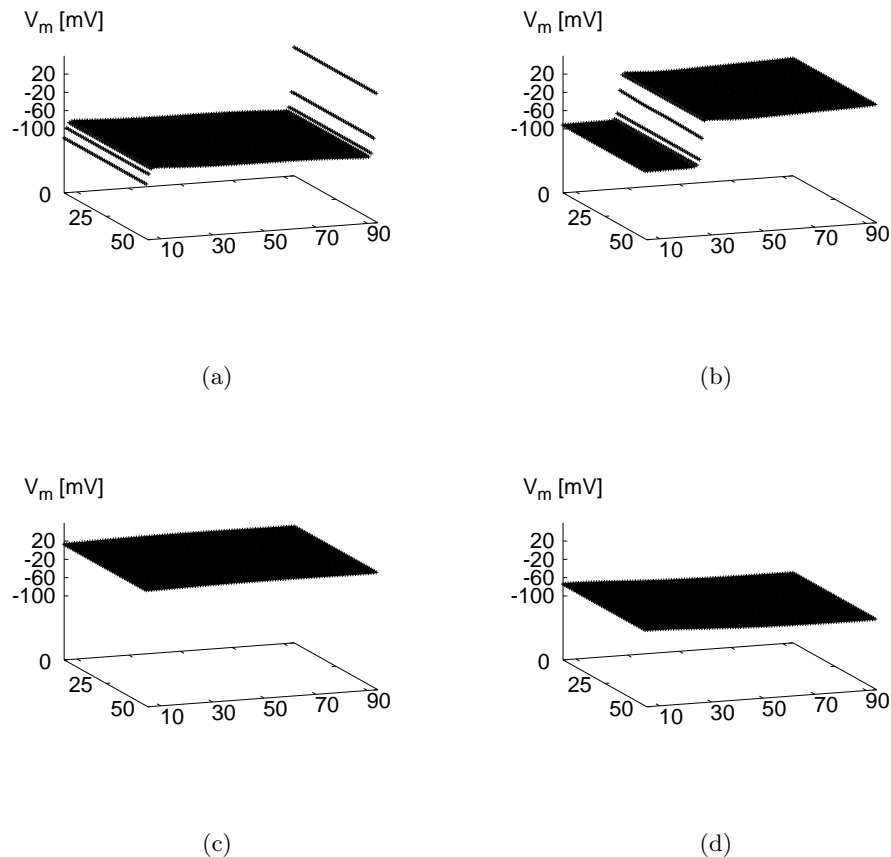


Figure 6.4: Temporal evolution of V_m , as a function of X and Z , measured in voxels, in a virtual section of human myocardium, with realistic fiber orientation, at different time steps: a) 1 ms, b) 30 ms, c) 50 ms, d) 390 ms, after 1ms long monophasic electrical stimulation with the amplitude of 1V. The pictures illustrate the typical post-stimulation phases of a parallelepipedic myocardial preparation.

strong hyperpolarization can induce a depolarisation in these areas. The phenomenon was termed virtual electrode. The appearance of secondary electrical sources depends on many factors and not only on the strength of the electrical shock (Sect. 6.1.3, 6.3).

During the propagation of the depolarisation front V_m presented two values: a positive one corresponding to the excited myocytes and a negative one characteristic to the resting tissue.

The time passing before complete depolarisation is reached depends on the velocity of excitation propagation and on the length of the fiber. The depolarisation phase of the myocardium corresponds to the QRS interval of the recorded ECG. For the chosen configuration the duration of the depolarisation phase was 50 ms.

While the myocytes were in the plateau phase the tissue was in the isopotential state. The repolarisation velocity depends on electrophysiological char-

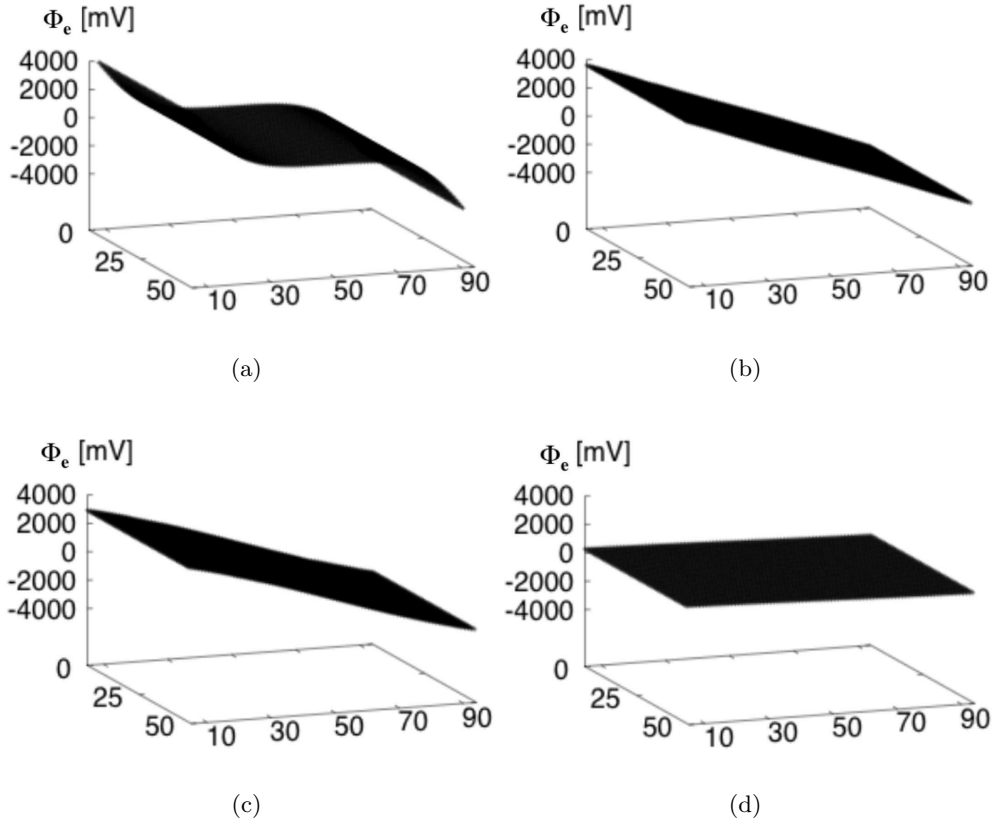


Figure 6.5: Extracellular potential as a function of X and Z, measured in voxels, in a virtual section of human myocardium, with realistic fiber orientation, at different time steps: a) 1 ms, b) 5 ms, c) 10 ms, d) 50 ms, after 1ms long monophasic electrical stimulation with the amplitude of 1V.

acteristics (Sect. 6.2). 390 ms from the initiation of the electrical stimulation, the entire myocardium was completely repolarized.

Another parameter whose evolution can be observed in a myocardial preparation post stimulation is the extracellular potential. 1 ms after the electrical stimulation, Φ_e presented an exponential variation along the fiber, near the electrodes (Fig. 6.5 a). The space constant for Φ_e was bigger than the one characteristic to V_m (Fig. 6.4 a). The modification of Φ_e was extended along a total distance of 1 cm. At the same moment, V_m had a value different from the one specific to the resting phase along a total distance of 0.012 cm. Due to the symmetry of the system, Φ_e and V_m were spatially constant across the XY plane.

Analyzing the time history of Φ_e it was observed that the exponential variation was transformed in 5 ms in a linear dependence on spatial dimension (Fig. 6.5 b). The angle formed by the spatial variation of Φ_e and the Z axis decreased with time (Fig. 6.5 c). At the end of depolarisation phase the value of the angle of Φ_e was reduced to 0° . From the moment in which the myocardium was completely depolarized Φ_e remained constant at 0 V (Fig. 6.4 d).

Parameter	Definition	Value (mS/cm)
σ_{il}	longitudinal conductivity in the intracellular domain	2.13
σ_{it}	transversal conductivity in the intracellular domain	12.87
σ_{el}	longitudinal conductivity in the extracellular domain	4.72
σ_{et}	transversal conductivity in the extracellular domain	5.35

Table 6.1: List of the normal values of the electrical conductivities.

In conclusion, the temporal variation of Φ_e along the myocardium only presents information about the initiation of excitation in the cardiac muscle and the moment in which the entire muscle is depolarized. In contrast, V_m provides a complete set of information about the spatio-temporal evolution of the myocardium. Thus, V_m generally constitutes the parameter of interest, both experimentally and theoretically. The variation of V_m calculated with the bidomain model is in agreement with the experimental data [75].

Due to the fact that the longest side of the tissue was only 2 cm long and the action potential duration of the human ventricular myocytes is around 350 ms, in the myocardial preparation the totally refractory did not coexist with the partially refractory and the excitable state.

6.1.2 Large Virtual Section of Human Myocardium

For the study of large parallelepipedic myocardial slices a 3D preparation with the size of $4 \times 0.5 \times 4 \text{ cm}^3$ was utilized ([76], [77]). The electrophysiology was described by the Priebe-Beuckelmann cell model (Sect. 4.4.1). The myocardial fibers had realistic orientation.

The resting myocardium was initially stimulated with a monophasic shock delivered through a pair of electrodes placed near the tissue, perpendicular on Z axis (see system of coordinates in Fig. 6.2 b). The electrodes had an area of $4 \times 0.5 \text{ cm}^2$, equal to the sides of the myocardium, parallel to the paddles. The electrical shock had a duration of 1 ms and a strength of 1 V. The induced base-line depolarisation was similar to the one described for the smaller parallelepipedic tissue. The difference between the responses of the two myocardial preparations was the time necessary to complete the excitation of the myocardium. The prolongation of the depolarisation phase was induced by the geometrical modification. For the present configuration the tissue was completely depolarized 83 ms after the excitation initiation.

The repolarisation phase comprised a temporal interval, in which in the myocardial wedge coexisted refractory with partly refractory and excitable myocytes (Fig. 6.6 b). The period with these characteristics is termed vulnerable window. Its length increases with the size of the tissue (Sect. 4.7.2). The electrical stimulation of the myocardium during the vulnerable interval can produce

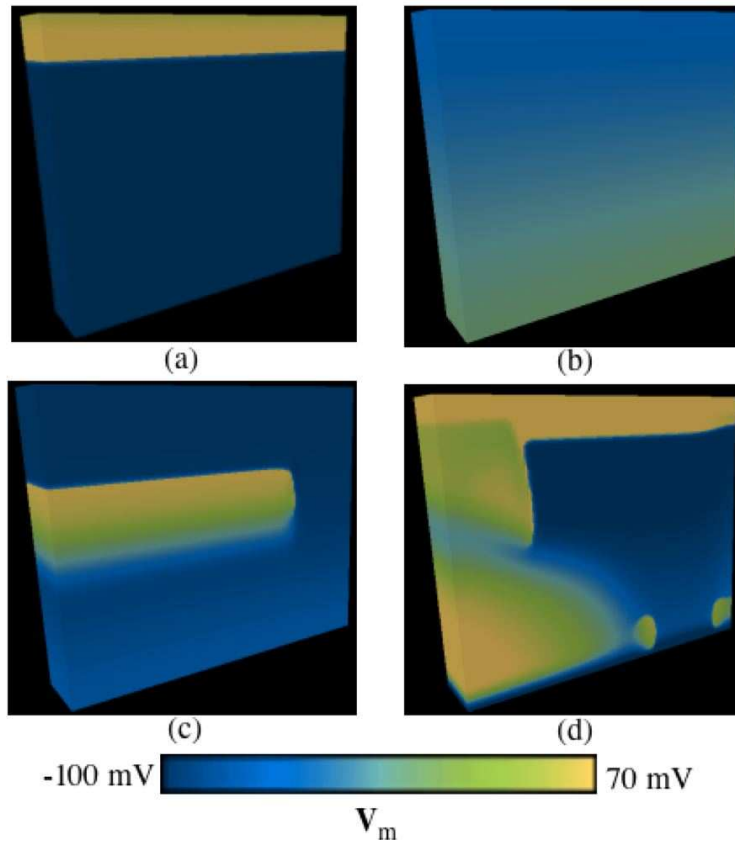


Figure 6.6: Temporal distribution of V_m in a large virtual section of human myocardium, with realistic fiber orientation, at different time steps: a) 20 ms, b) 320 ms, after 1ms long monophasic electrical stimulation with the amplitude of 1V. The rectangular electrodes were placed outside the myocardium, near the ends of the longest side. A second stimulus applied in the center of the tissue during the vulnerable window c) 375 ms from the initiation of the simulation produces an abnormal depolarisation, which can develop in an arrhythmic behavior d) 790 ms from the initiation of the simulation.

arrhythmic behaviors (Fig. 6.6 c, d, section 7.4). Therefore, such types of myocardial preparations can be used for studying the effects of electrical shocks on arrhythmic human hearts.

6.1.3 Curved Segment of Human Myocardium

For studying the reaction of a curved section of human myocardium a 3D preparation electrophysiologically based on the Tusscher-Noble-Noble-Panfilov model (Sect. 4.4.2) was used. The realistic myocardial fiber twist and electrical anisotropy were incorporated in the used configuration. A specific feature of the model was the varying curvature and thickness. The maximum thickness (at the top) was equal to 24 mm and the minimum thickness was 20 mm. The height and the width were chosen equal to 30 mm. The endocardial and epicardial surfaces were bordered by blood.

The utilized electrical impulse was characterized by a duration of 5 ms and

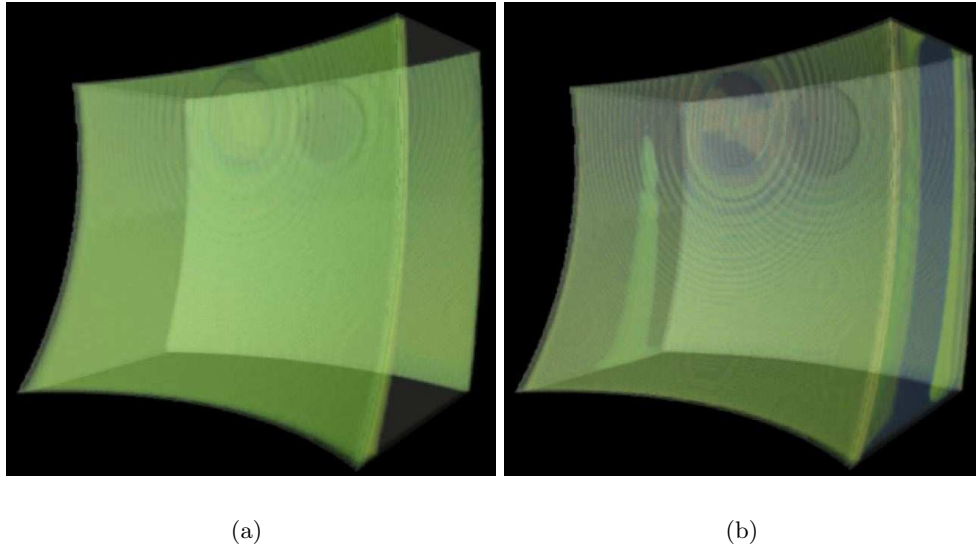


Figure 6.7: Spatial distribution of V_m immediately after a monophasic electrical stimulation with the duration of 1 ms and amplitude of 1 V. a) Electrodes were oriented parallel to the endo- and epicardial surfaces. b) Large electrodes were placed perpendicular to the endo- and epicardial surfaces. Same color code as in Fig. 6.6.

an amplitude of 1V. The stimulation through electrodes parallel to the endo- and epicardial surfaces produced in the curved tissue a different reaction than the parallelepipedic preparations. Each stimulus, which induced a primary excitation of the myocardium induced the occurrence of additional secondary electrical sources with sufficient strength to depolarize the tissue. After the electrical stimulation of the virtual wedge, depolarisation fronts were initialized in subendocardial and subepicardial areas (Fig. 6.7 a).

The positioning of the electrodes perpendicular on endo- and epicardial surfaces and between the two regions also induced the occurrence of secondary electrical sources (Fig. 6.7 b). Another aspect related to the placement of the electrodes orthogonal on endo- and epicardial surfaces was the formation of both hyperpolarization and depolarisation beneath the electrodes, as both a cathode and an anode would have been placed there. The depolarisation of the myocardium, beneath the anode is termed occurrence of virtual electrode or secondary electrical sources. The notion of secondary electrical sources is more often used for denoting the depolarisation during the stimulation of a section of myocardium far away from the electrodes.

The center of the region beneath the cathode was depolarized and the extremes were hyperpolarized. The myocardial layer bordering the anode presented an inverted reaction (Fig. 6.7 b). The phenomenon was also observed experimentally by Knisley et al. [78].

The excitation propagation from the subendocardial and subepicardial surfaces can be observed by measuring the spatio-temporal distribution of Φ_e or V_m . In the configurations, with paddles parallel to endo- and epicardium, the

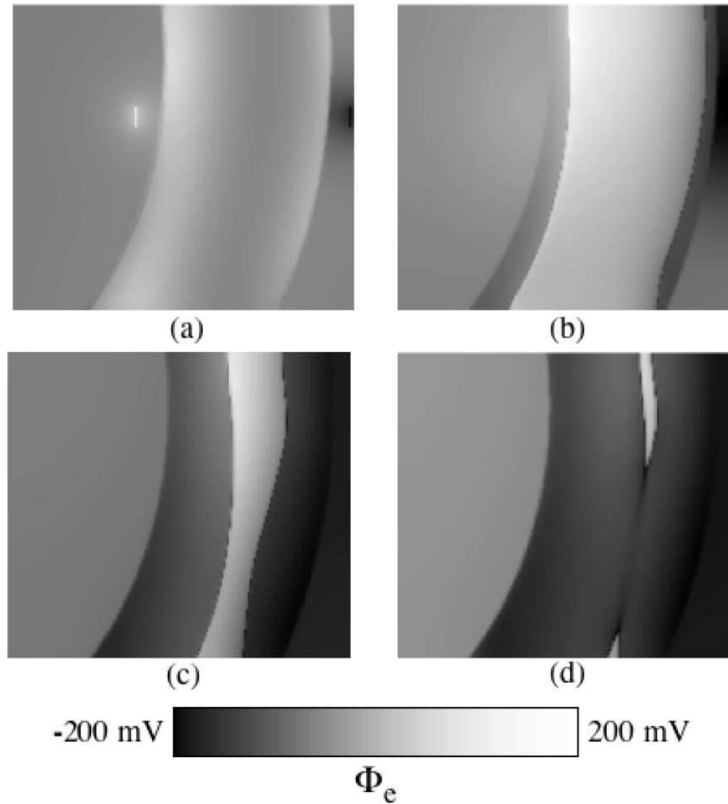


Figure 6.8: The distribution of Φ_e in a section through the curved myocardium in the XZ plane. The resting tissue was excited by a monophasic electrical stimulus characterized by a duration of 5 ms and an amplitude of 1V. The response of the myocardium a) 1 ms, b) 15 ms, c) 55 ms, d) 65 ms after the initiation of the electrical stimulation. The visualization of Φ_e , clearly indicated the characteristics of the used electrical shock, together with the positions and the dimensions of the electrodes. The initiation of excitation is not clearly defined, but once the stimulation ends the depolarisation fronts can be observed until the entire tissue is depolarized.

system presents a symmetry with respect to Y (Fig. 6.8 a). For such cases, for presenting the results can be used a section through the tissue in the XZ plane. The evolution of Φ_e in the curved preparation, as a difference to a parallelepipedic myocardial wedge, indicates the depolarisation fronts simultaneous with V_m (Fig. 6.8, 6.9). The tissue was completely depolarized in 65 ms and it regained the complete resting state 405 ms after the initiation of excitation.

The results indicate that the inclusion of the curvature in the model modified the response of the myocardium to electrical stimulation. Therefore, for the research of the internal defibrillation the curvature must be included in the models.

Discussion The calculation of bidomain equations presents the temporal evolution of Φ_e and V_m . In a parallelepipedic myocardial preparation Φ_e indicates the moment of the complete depolarisation of the tissue. In the curved myocardial model the variation of Φ_e indicates both the depolarisation front and

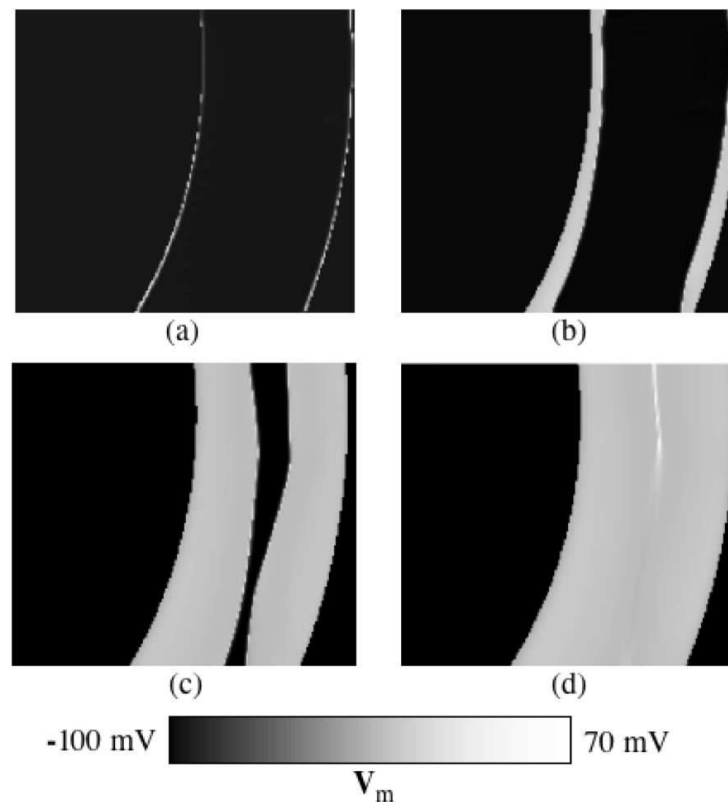


Figure 6.9: The distribution of V_m in a section through the curved myocardium in the XZ plane. The resting tissue was excited by a monophasic electrical stimulus characterized by a duration of 5 ms and an amplitude of 1V. The response of the myocardium a) 1 ms, b) 15 ms, c) 55 ms, d) 65 ms after the initiation of the electrical stimulation. The results indicate the occurrence of virtual electrodes in subepicardial and subendocardial regions. The depolarisation fronts propagate from both directions and meet in the middle of the myocardium.

the moment corresponding to complete tissue depolarisation. Invariant to the geometry of the tissue, Φ_e does not give any information about the state of the tissue after the depolarisation is complete. In contrast to Φ_e , the variation of V_m conveys information about the reaction of the myocardium from the start of the excitation until complete repolarisation. Generally only the value of V_m is presented for indicating the state of the myocardium.

6.2 Electrophysiological Heterogeneity

Experiments have shown that a regional electrophysiological heterogeneity exists across the myocardium. Even though cardiac electrophysiology has been intensively investigated, the underlying theoretical aspects are not completely understood.

Subendocardial, subepicardial and midmyocardial (M) cells elicit different action potential (AP) profiles and durations. Recent research identified the electrophysiological characteristics inducing the differences among the cells in-

corporated in the ventricular myocardium. Experiments and theory showed that mainly responsible for the transmural variance are: the transient outward potassium current (I_{to}) [79], the slow delayed rectifier potassium current (I_{Ks}) [80], the fast sodium current (I_{Na}) [81] and calcium channels [82], [83].

One aim of this work was to identify the influence of the transmural electrophysiological variation on the fundamental reaction of the myocardium to electrical stimulation. Simulations were performed on two types of myocardial preparations: a control electrophysiologically homogeneous and an electrophysiological heterogeneous human heart. The myocardial preparations were excited by different electrical stimuli.

Constructional aspects of the myocardial preparations The cellular electrophysiology of the cardiac preparations used in the study, was described by the ten Tusscher-Noble-Noble-Panfilov model of a human ventricular myocyte (Sect. 4.4.2). The main distinction between the two myocardial preparations is constituted by the description of the electrophysiology. The control model, denoted by NM, comprised a homogeneous distribution of the electrophysiological properties. The model including the transmural electrophysiological heterogeneity was denoted by HM.

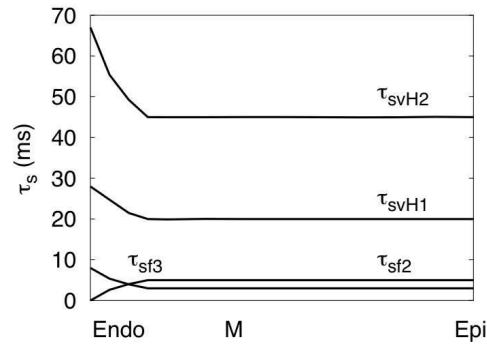
The distinctive cell types comprising the HM wall were modelled by the variation of I_{to} and I_{Ks} (Fig. 6.10). The heterogeneity in AP morphology is prominent for isolated myocytes (Fig. 6.11). Subepicardial cells produce an AP with a spike-and-dome profile, containing a deep notch. Subendocardial cells display a longer plateau with a small notch. M cells develop the longest APD.

The components of the used electrical conductivities for intra- and extracellular space correspond to the measured experimental values. The orientation of myocardial fibers was adapted to measurements of human ventricular cells. The geometry of the virtual cardiac wedges is shown in Fig. 6.2a. The size of the preparations was 10 mm x 10 mm x 20 mm. The grid was composed of cubic voxels with a side length of 0.2 mm.

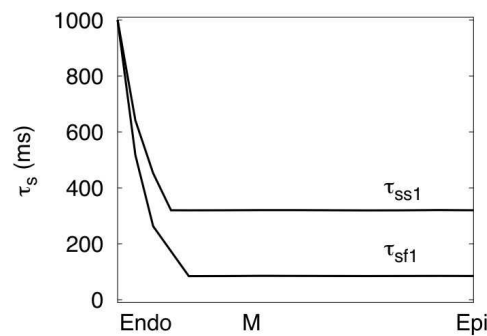
Due to the constructional features, the APD and ECG profiles differ between the two models. Fig. 6.12 depicts the transmural distribution of the action potential at 90% of repolarisation (APD_{90}), generated by the myocytes composing coupled-cells environments. The values of APD_{90} are measured after a 1 Hz electrical stimulation. In the electrophysiological heterogeneous myocardium, the longest APD corresponds to the M cells and the shortest is registered in the subepicardial region. The APD of NM is invariant across the transmural wall.

Fig. 6.13 depicts the simulated transmural ECGs corresponding to myocardial preparations neighbored by bath. The virtual wedges, characterized by equal electrical conductivities present the same ECG profile during the QRS interval. The differences are formed in the T wave region, which corresponds to the repolarisation phase. NM produces a negative T wave. The electrophysiological heterogeneous preparation presents a positive T wave.

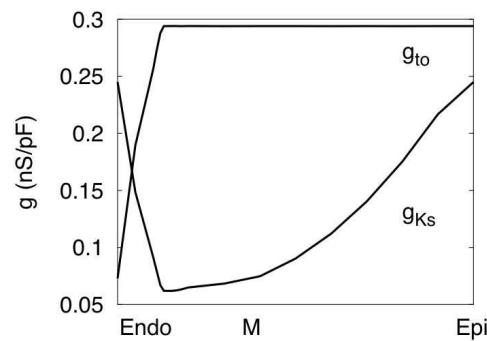
For further enhancement of the reactions induced by electrophysiological differences, the models were simplified for avoiding the occurrence of unnecessary secondary electrical sources. The tissue was not surrounded by bath [84] and it



(a)



(b)



(c)

Figure 6.10: Transmural variation of: a) $\tau_{s,vHalf}$, $\tau_{s,f2}$, $\tau_{s,vHalf1}$, b) $\tau_{s,f1}$, $\tau_{s,slope1}$, c) g_{Ks} , g_{to} , implemented in the electrophysiological heterogeneous model.

was not fragmented by cleavage planes [21]. The electrical stimuli were chosen to produce normal action potential profiles in the excited cells. Therefore,

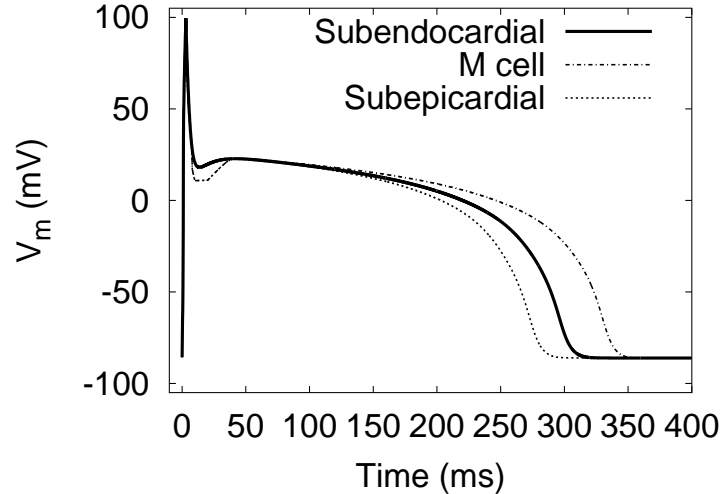


Figure 6.11: The action potential of isolated subendocardial, M and subepicardial human left ventricular myocytes. The profiles were generated with the Tusscher-Noble-Noble-Panfilov model.

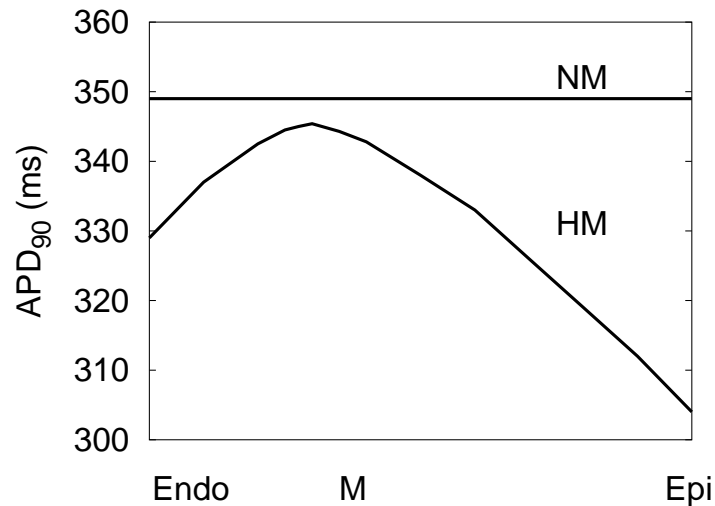


Figure 6.12: The action potential duration at 90% of repolarisation specific to human left ventricular myocytes incorporated in the coupled-cells environment.

the model did not include the electroporation formalism neither cell uncoupling [85].

The parameters of the electrical stimulation The results of the simulations done by Clayton et al., suggest that the fibrillation patterns formed in an electrophysiological homogeneous tissue differ from the ones developed in an electrophysiological heterogeneous myocardium [86]. It also has been shown experimentally that heart failure can lead to nonexcitable gap reentry [87] and to development of early afterdepolarisations. The latter can trigger arrhythmia [88]. Therefore, the failing heart conditions induce fibrillation patterns, different

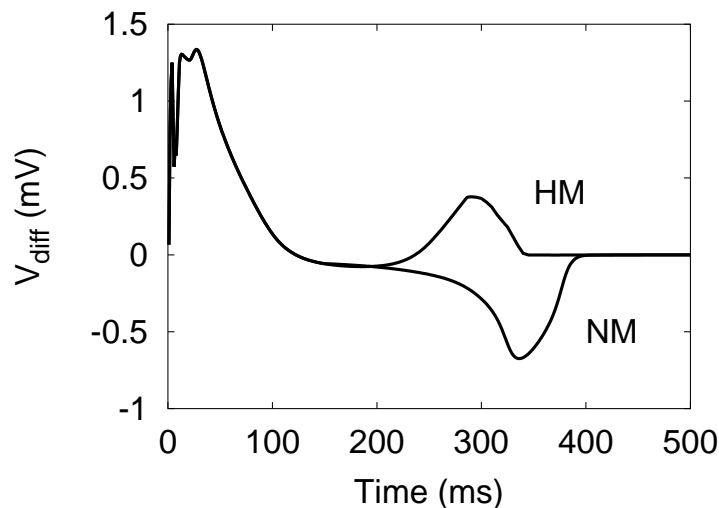


Figure 6.13: The simulated transmural ECG specific to an electrophysiologically homogeneous and a heterogeneous myocardial preparation. The profile of the T wave indicates the formation of realistic data, when the electrophysiologically heterogeneous myocardial preparation is utilized.

to the electrophysiological normal heart. Since fibrillation characteristics would not be similar in the myocardial preparations it was decided to set the tissue completely in the resting phase at the initiation of the electrical stimulation.

The results gathered during a cardiac cycle formed the data set used to compare the electrical responses of the myocardial preparations. The research was extended to several types of electrical stimulation configurations (Table 6.2).

Results Due to the characteristics of the electrical stimulations and the features of the myocardial preparations, Y is a symmetry axis for the V_m spatial distribution. Therefore, the results will be presented in the form of sections through the middle of the tissues, at constant Y .

The response of myocardial preparations to electrical stimulation configuration 1 The variation of V_m produced by the virtual electrodes, in the subepicardial zone, was not strong enough to induce a depolarisation front. Therefore, the excitation was initiated exclusively by the primary electrical sources. In the depolarisation phase and while the myocytes were in the plateau phase, V_m presented a similar distribution in NM and HM. The differences in the responses of the models culminated during the T wave interval. The following presentation of the results is focused on comparisons between the reactions of the myocardial preparations during the T wave interval.

At 330 ms, approximately 20% of the HM was already in the resting phase (Fig. 6.15 a). At the same time, no section of NM reached the resting phase completely (Fig. 6.15 b). The longest V_m interval was formed in NM. The prolongation of the width of V_m interval corresponded to the dispersion of the T wave of NM and the extension of the vulnerable window.

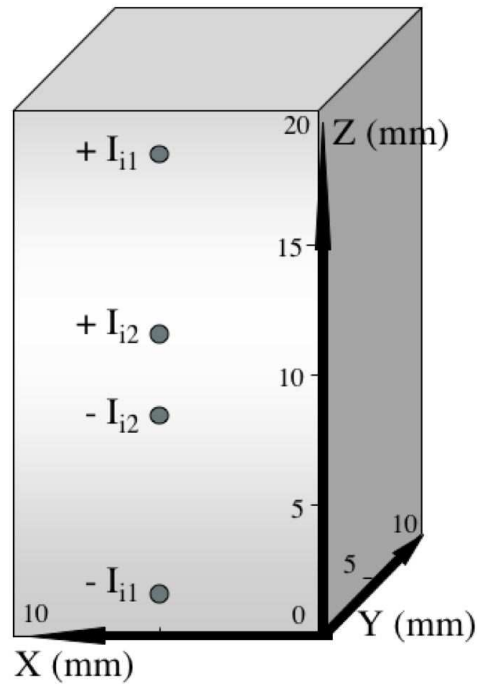


Figure 6.14: The position and the geometrical characteristics of the needle electrodes utilized for stimulating the tissue.

The response of myocardial preparations to electrical stimulation configuration 2 In NM, the inversion of the polarities of the monophasic impulse produced vertically flipped distributions of the isopotential surfaces (Fig. 6.15 c). The time corresponding to the end of refractory phase in NM was identical for both monophasic electrical stimulations.

The inclusion of physiologic heterogeneity implied a distinct response to each monophasic shock. The efficiency of the electrical stimulation depended on the location of the depolarisation front initiation. When the cathode was placed near to the epicardium, HM needed 28 ms more for reaching the complete resting phase. The temporal difference was approximately equal to the APD of subendocardial myocytes minus the APD of the subepicardial myocytes plus the activation delay. 330 ms after the start of the stimulation approximately 43% of the tissue was already resting (Fig. 6.15 d), but the V_m interval was enlarged by 15 mV.

The response of myocardial preparations to electrical stimulation configuration 3 During the first half of the biphasic stimulation the cathode was near to the endocardium. The tissue included in the spatial interval (19, 20) mm of the Z-axis was depolarized during the first 5 ms. During the second half the polarity was inversed and a depolarisation front was initiated at the opposite end of the tissue. At 330 ms a nearly symmetric distribution of V_m can be observed in NM. The axis of symmetry was displaced by 1 mm in the direction of the endocardium (Fig. 6.16). The displacement was more pronounced in the HM (Fig. 6.16) due to electrophysiological heterogeneity. 330 ms after

Number	Electrodes characteristics	Electrical stimuli
1	-10 mm x 10 mm paddle electrodes (Fig. 6.3) -cathode and anode localized near to endo- and epicardium, respectively	-type: monophasic -amplitude: ± 500 mV -duration: 10 ms
2	-10 mm x 10 mm paddle electrodes (Fig. 6.3) -cathode and anode localized near to epi- and endocardium, respectively	-type: monophasic -amplitude: ± 500 mV -duration: 10 ms
3	-10 mm x 10 mm paddle electrodes (Fig. 6.3) -electrodes positioned at the ends of the longest axis of the tissue	-type: biphasic -amplitude: ± 500 mV -duration: 10 ms
4	-0.2 mm x 10 mm needle electrodes (Fig. 6.14) -electrical sources placed at $Z = 1$ mm and $Z = 19$ mm	-type: monophasic -amplitude: ± 110 mA -duration: 10 ms
5	-0.2 mm x 10 mm needle electrodes (Fig. 6.14) -electrical sources placed at $Z = 9$ mm and $Z = 11$ mm	-type: monophasic -amplitude: ± 110 mA -duration: 10 ms

Table 6.2: List of the electrical stimulation configurations utilized in the study of electrophysiological heterogeneity.

the initiation of the stimulation, 60% of HM was already in the resting phase, in contrast to NM, which was mostly refractory. The V_m interval was (-60, -85) mV and (-45, -75) mV for HM and NM, respectively. The variance of V_m and the distribution of the isopotential surfaces corresponding to this moment reflected a stronger dispersion of the T wave in NM than in HM. The virtual wedges were faster completely repolarized after biphasic than after monophasic stimulation.

The response of myocardial preparations to electrical stimulation configuration 4 When the myocardium was stimulated with needle electrodes (Fig. 6.14) the differences between the responses of the tissue models, formed during the repolarisation phase underlined the influence of electrophysiological heterogeneity. Monophasic stimulation produced symmetric patterns of excitation dispersion due to the appearance of virtual electrodes.

The isopotential surfaces in NM presented almost a complete symmetry towards the centre of the tissue all along the simulation. The curvature of the wave fronts was an effect of the fiber twist combined with local electrical conductivity anisotropy. After NM was excited by I_{i1} (Fig. 6.14) the repolarisation was completed first in the core of the tissue and finally at the ends (Fig. 6.17 a).

In HM, the patterns of V_m distribution were strongly influenced by the electrophysiological heterogeneity. At 330 ms the isopotential lines were approxi-

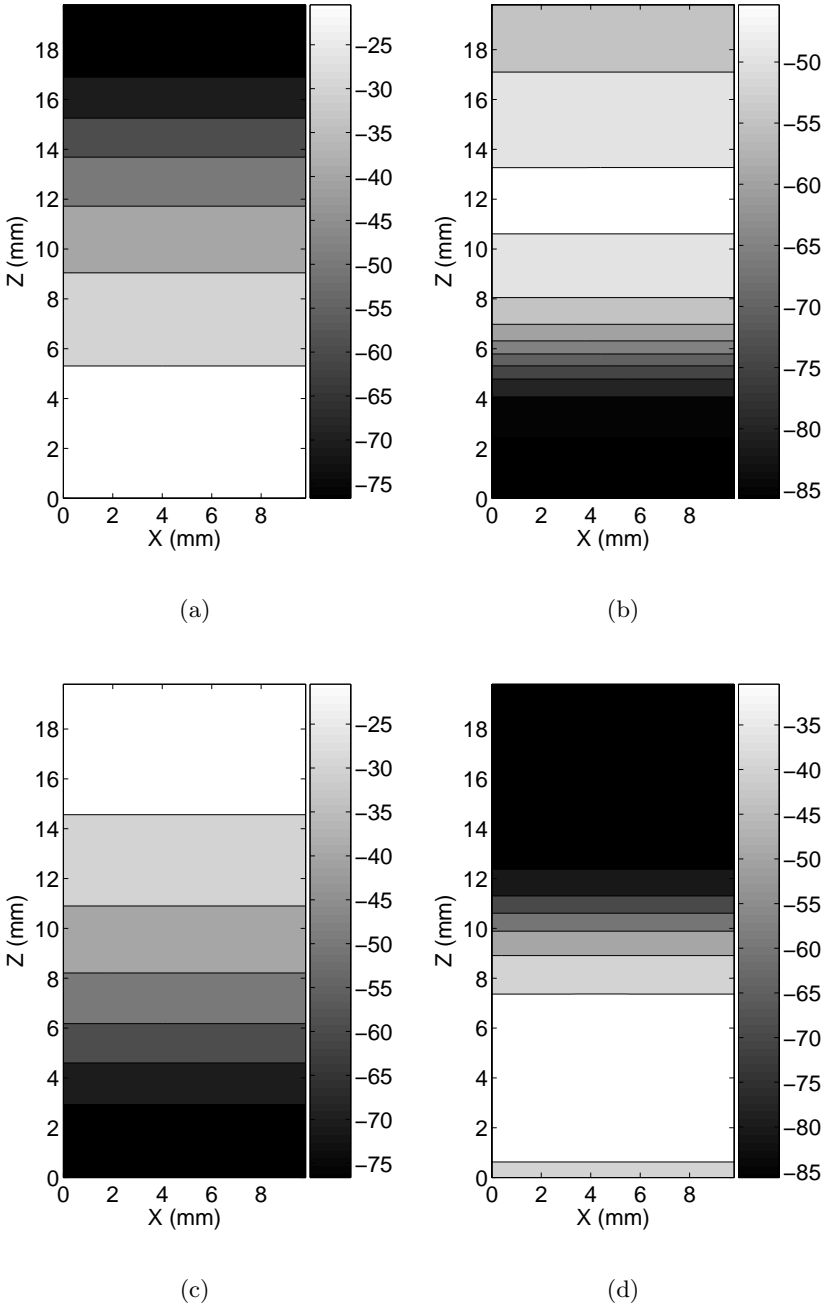


Figure 6.15: Distribution of V_m 330 ms after the first (a, b) and second (c,d) configuration of the electrical stimulation in a section through the: NM (a,c), HM (b,d). The grey bar indicates the value of V_m .

mately parallel (Fig. 6.17 b). The refractory part of the tissue was localized in the interval (4, 12) mm of the Z-axis, corresponding to the M cells region. After 353 ms all myocytes compounding HM were in the resting phase.

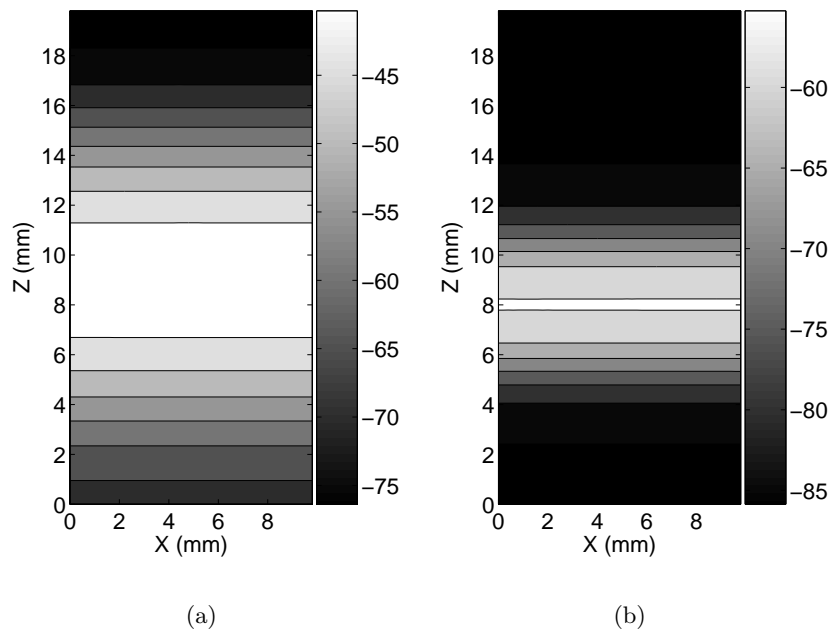


Figure 6.16: Distribution of V_m in NM a and HM b 330 ms, after biphasic external electrical stimulation.

The response of myocardial preparations to the electrical stimulation configuration 5 At 330 ms the most refractory myocytes of NM were localized in the subendocardial and subepicardial regions (Fig. 6.17 c). The interval in which V_m varied remained invariant to the displacement of the needle electrodes. 357 ms after the start of the excitation NM was in the resting phase.

Fig. 6.17 reflects that when the needle electrodes were placed near to the centre of the tissue, the electrophysiological heterogeneity dominated the formation of the electrical response of the myocardium. In HM the distribution of V_m along the Z-axis corresponded to the variation of APD in the tissue (Fig. 6.17 d). In contrast to NM (Fig. 6.17 c) the last part of the myocardium, which went into the resting phase was located not near the extremes, but between endocardium and M cells zone. The distinction between the results underlines that the electrophysiological heterogeneity can drastically modify the response of a cardiac tissue. The entire tissue was re-excitabile after 330 ms and after 349 ms it was completely resting.

Discussion The results of the simulations were gathered after stimulating the tissue with electrical shocks delivered by paddles and needles electrodes. During the T wave interval were formed clear distinctions between the response of NM and HM. The repolarisation following the excitation initiated through paddles illustrated the shift of the most refractory region towards the M cells. During the T wave interval, post-stimulation through needles the distribution patterns of the reexcitable and refractory myocytes was oppositely formed in NM and HM. The difference between the responses underlines the necessity of including

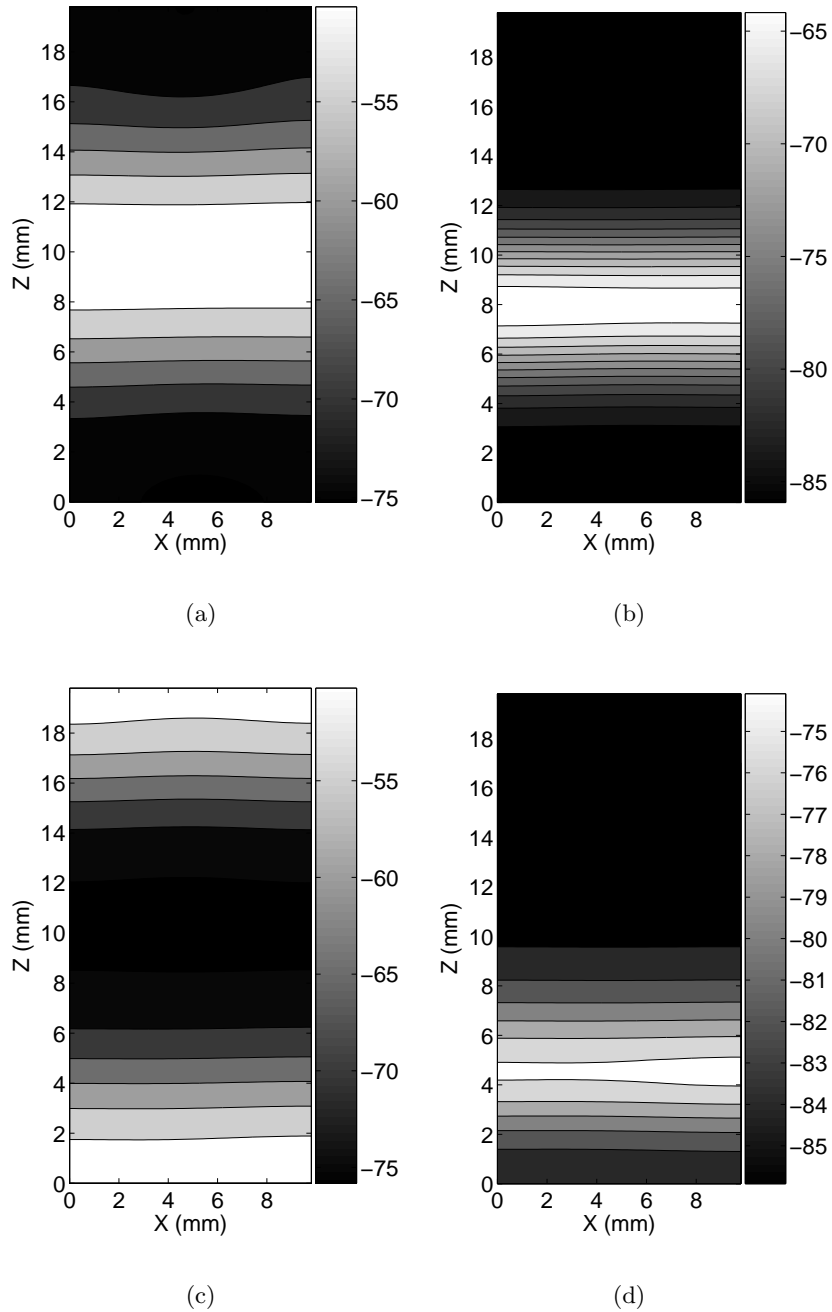


Figure 6.17: Temporal evolution of V_m , as a function of X and Z in a virtual section in NM (a,c) and HM (b,d), 330 ms after the fourth (a, b) and fifth (c,d) configuration of the electrical stimulation. The grey bar indicates the value of V_m .

electrophysiological heterogeneity in the description of the virtual myocardium.

The evaluation of V_m variation in HM reflected that the most effective monophasic stimulation was the one in which the cathode was localized near to the endocardium. The myocardium excited by a biphasic stimulation was at

rest faster than after a monophasic stimulation. In agreement with previously obtained results [89], the biphasic stimuli proved to be more efficient.

6.3 Myocardial Fiber Orientation

The reconstruction of the path of the electrical current in the virtual myocardium is based on the diffusion tensor, incorporated in bidomain formalism. The parameter includes the anisotropic distribution of the electrical conductivity (Table 6.1) and the myocardial fiber orientation. In the myocardium the average conductivity is greater along fibers than across fibers. Extracellular conductivity is greater than the intracellular one. This indicates that a variation of the fiber orientation angle involves a change in the electrical anisotropy of the tissue. Experimental measurements revealed that the orientation of ventricular myocytes varies across the transmural wall [22]. The fiber orientation throughout the ventricular wall can be modeled as a general helix, utilizing simple differential equations. The position vector x of a point on a helix inscribed on an ellipsoidal surface is symmetric about the z axis (represented in Fig. 6.18). In the human left ventricular epicardium the angle of the myocardial fiber orientation is equal to -75° , it is 0° in the midwall and 70° in the endocardial area.

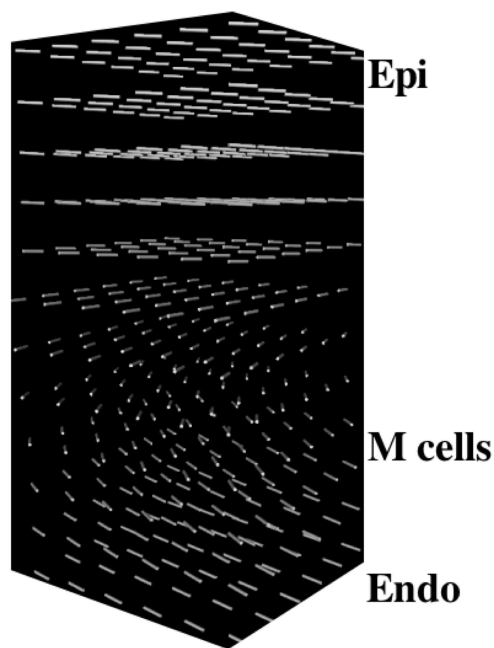


Figure 6.18: The fiber orientation across the transmural wall. In the human left ventricular epicardium the angle of the myocardial fiber orientation is equal to -75° , it is 0° in the midwall and 70° in the endocardial area.

Previous theoretical investigations of animal hearts, indicated that the fiber orientation is influencing the occurrence of secondary electrical sources, termed virtual electrodes [90]. The aim of the research presented in this section, was

to identify the effects of fiber orientation variation on the electrical current diffusion in a human virtual myocardium.

The study is parted in two sections: two-dimensional and three-dimensional model simulations. In both cases the attention is focused on the occurrence of secondary electrical sources and features that induce and influence their appearance.

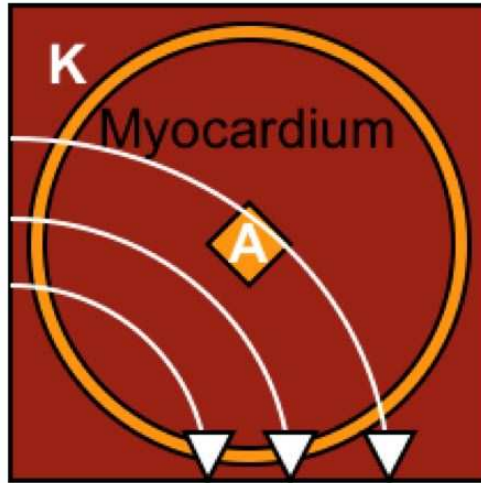


Figure 6.19: Configuration used for the study of the influence of fiber orientation on a two dimensional myocardial preparation. The white curved arrows indicate the myocardial fibers. The anode was placed in the centre and it was surrounded by a circular cathode.

The two-dimensional sheet was represented by 100 x 100 voxels, with a side length of 0.2 mm. A square anode was placed in the center of the tissue. The cathode had a circular form with a radius of 10 mm and it symmetrically surrounded the anode (Fig. 6.19). The duration of the electrical signal was 1 ms. The magnitude of the electrical impulse varied from case to case between 0.1 V and 0.4 V. The angle of the fiber orientation varied from model to model between 30° and 150°.

For the three-dimensional simulations two models were used. The myocardial preparations were 50 x 50 x 100 cubic voxels, large. The length of the sides of the cubic voxels was equal to 0.2 mm. In one case the fiber orientation was set constant throughout the tissue at 70°. The other model included realistic myocardial fiber orientation.

The myocardium was completely surrounded by a 1 mm thick blood layer. The paddle electrodes were placed in bath at the ends of the longest axis. The size of each electrode was 1 x 1 mm². The myocardium was excited by 5 ms long stimuli, which had an amplitude of 0.5 V. The propagated response of the tissue was recorded through time until the volume was fully repolarized. The time necessary for the reestablishment of the resting phase was approximately equal to 400 ms.

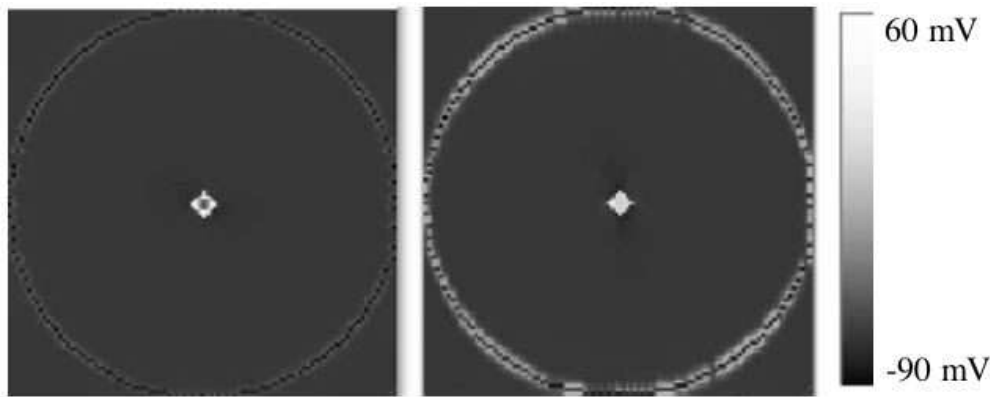


Figure 6.20: left: Transmembrane voltage in a tissue with 30° fiber orientation 1 ms after the $(-0.4V, +0.2V)$ electrical signal is applied; right: Lattice with 110° fiber orientation 1 ms after the $(-0.4V, +0.2V)$ electrical signal is applied. The pictures indicate the correlation between the virtual electrodes polarization magnitude and the fiber orientation.

Results The first effect of the applied electrical shock, that could be observed in all cases, is the hyperpolarization of the area where current was injected and depolarisation of the area in which current was withdrawn. Experiments also reported this type of cardiac excitation [91]. Around the hyperpolarized region cells were depolarized. The value of the transmembrane voltage in these regions varied from case to case.

The two-dimensional model with 30° fiber orientation showed the existence of virtual electrodes depolarisation (VEP) after the electrical signal was applied. The intensity of the secondary electrical source was very low (see Fig. 6.20) therefore its effects were completely extinguished in the following two seconds. In the cases with the fiber orientation higher than 30° and the applied electrical signal larger than 0.2 V the VEP was distributed elliptically (see Fig. 6.21) and the entire tissue was depolarized in 20 ms. When the VEP did not occur the entire tissue was depolarized in around 90 ms. After the tissue with 70° fiber orientation was stimulated with $(-0.2 V, +0.1 V)$ the effects of the VEP focused around the intersection of the cathode with the diameter parallel to the fibers (see Fig. 6.21).

The comparison between the registered results indicate the important role of the virtual electrodes in the depolarisation of the tissue. The cases in which the VEP appeared, the entire tissue got in the rest phase in less than 400 ms. In the other situations or when the VEP vanished fast (two-dimensional tissue with a fiber orientation of 30°) more than 450 ms were needed for the entire tissue to get in the resting phase.

In three-dimensional myocardial preparations, for identifying the relationship between the occurrence of VEP and the orientation of the myocardial fiber various arrangements of the myocytes were considered.

The model based on a realistic orientation of the myocardial fibers presented the formation of VEP near to all corners. In the subepicardial region, near the cathode the secondary electrical sources were more intense than in the

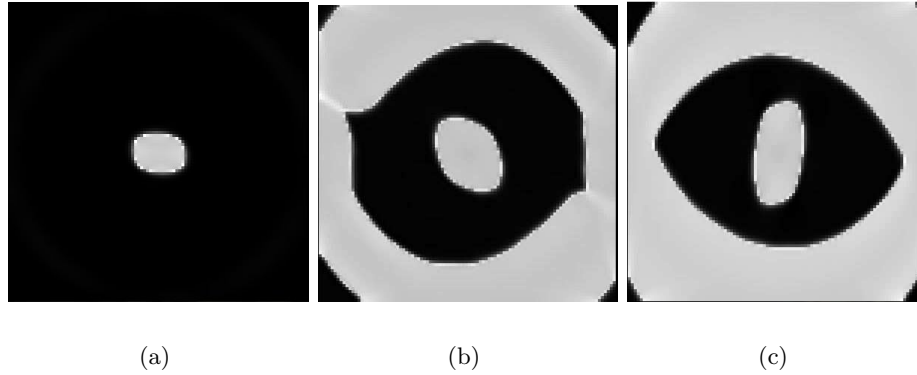


Figure 6.21: The distribution of V_m in a 2D myocardium with a fiber angle equal to a) 30° , b) 70° and c) 110° , 15 ms after the $(-0.4V, +0.2V)$ electrical signal was applied. The pictures illustrate the influence of the fiber orientation on the excitation propagation. Color code as in Fig. 6.20.

subendocardial zone (Fig. 6.22). The immediate effect was that at 10 ms the number of the excited myocytes in the subepicardial part was more than 10 times higher than the numbers of the excited myocytes localized in the subendocardial part. In 20 ms the myocardium was completely depolarized. In 380 ms the tissue was again at rest, the corresponding value of V_m being -80 mV.

In the myocardial preparations characterized by constant fiber orientation VEP occurred only near the cathode and their intensity was lower than in the myocardium with realistic fiber orientation. Therefore, the depolarisation front was propagating only from one side of the subepicardial zone (Fig. 6.23). As an effect, the time to complete depolarisation was drastically increased. The myocardium was at rest after 425 ms.

Discussion The findings of the simulations presented in this section are in agreement with experimental studies with animal hearts [55] indicate the significant impact of the fiber orientation on the process of defibrillation. The large gradient of extracellular current, caused by the non-uniformity of fiber orientation, results in the formation of virtual electrodes in the tissue, away from the defibrillation electrodes. These virtual electrodes play a major role in the time needed for depolarizing the entire myocardium. Only if complete depolarisation is achieved, arrhythmia or fibrillating waves are extinguished. The secondary electrical sources were related to make and break phenomena, which render the tissue refractory. In contrast the straight fibers, reduce the formation of secondary electrical sources in a uniform electric field. In this case the depolarisation front, which spreads from the region neighboring the cathode could lead to an unsuccessful defibrillation. In conclusion, this study determines the role that cardiac microstructure plays in ventricular fibrillation and defibrillation.

In all simulations the time course of the transmembrane voltage was followed until it touched the value of -80 mV in all cells of the tissue. This is indicating

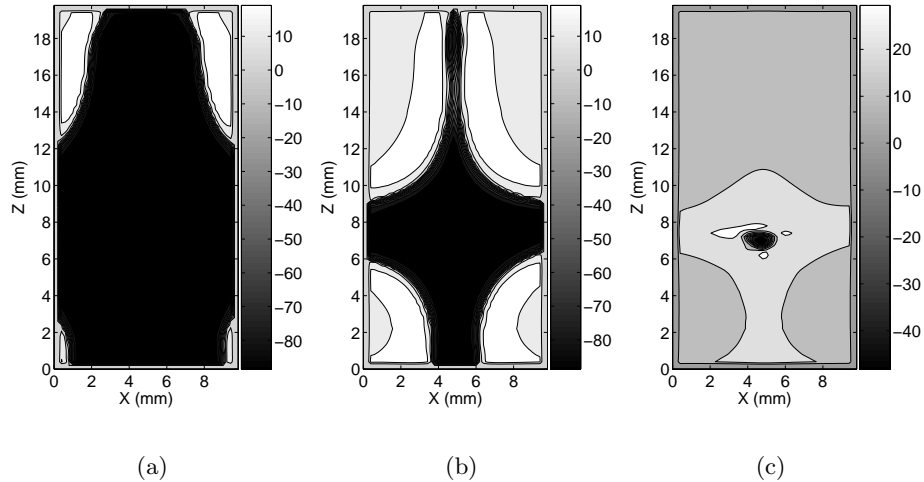


Figure 6.22: The distribution of V_m in a section through the model, which contains a 3D myocardium incorporated in bath. The resting tissue, composed of twisted fibers, was stimulated by paddles (Fig. 6.3). The duration of the monophasic electrical shock was 10 ms and the amplitude was 1V. The electrical response was registered at: a) 10ms, b) 15 ms and c) 19 ms. Secondary electrical sources occurred near to the corners of the tissue, with a higher intensity in the subepicardium.

the resting state of the myocardial bulk. The time needed by the tissue to be again at rest depends both on the depolarisation phase and on the electrophysiological features. The resting state was firstly restored in the myocardial preparations with the most intense secondary electrical sources. Practically, this specific time interval has to be known, because it indicates how fast a heart can be "reset".

6.4 Tissue-Bath Volumes Ratio

The blood is the natural volume conductor, bathing the myocardium. In addition, most experiments done for measuring the variation of V_m induced by electrical shocks, use paddles placed in perfuseate. The physical formalism utilized in computer simulations indicates that the influence of the bath on tissue activation is determined by the resistance of the current flow paths through the bath and the tissue and also the space constants of the tissue.

For studying the direct influence of the blood bath on the electrical reaction of the human left ventricle three types of myocardial preparations had been used. The cellular electrophysiology was simulated with TNNP model (Sect. 4.4.2).

The geometry of each myocardial preparation was parallelepipedic. The distinction between the three utilized types was constituted by the ratio between the volume of the blood and of the myocardium. The size of the entire wedge was equal to $10 \times 10 \times 20 \text{ mm}^3$. For the research was utilized first a model, with a 0.2 mm thick blood layer surrounding the myocardium. The second used

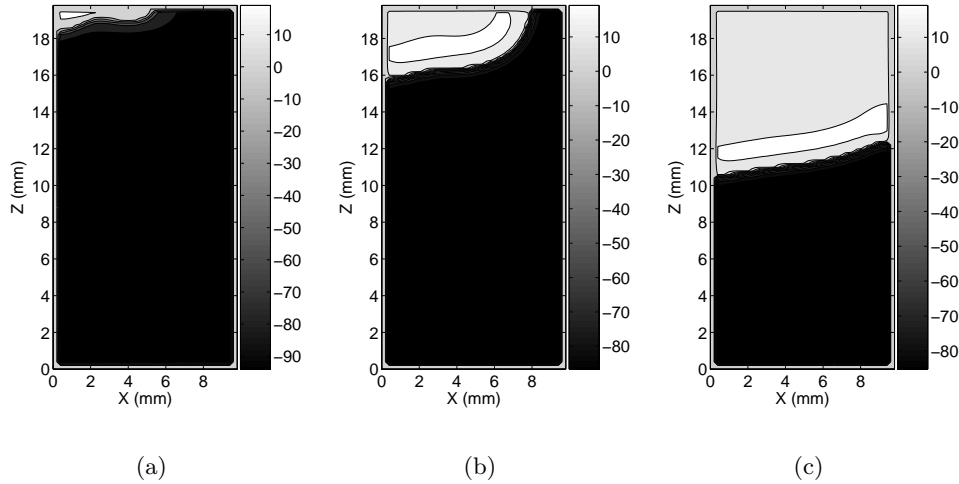


Figure 6.23: The distribution of V_m in a section through the model, which contains a 3D myocardium incorporated in bath. The resting tissue, composed of straight fibers (70°), was stimulated by paddles (Fig. 6.3). The duration of the monophasic electrical shock was 10 ms and the amplitude was 1V. The electrical response was registered at: a) 5ms, b) 10 ms and c) 20 ms. Secondary electrical sources occurred only in subepicardial region.

model contained a larger volume of blood, in which was centered a myocardial tissue with the size $4 \times 4 \times 19 \text{ mm}^3$. The third model comprised the largest blood volume and the myocardium had the size equal to $1 \times 1 \times 19 \text{ mm}^3$. The thinnest myocardium was composed of straight fibers, while in the other two models the realistic orientation of the myocytes was reconstructed.

The polarization of the tissue was induced by one of the three types of the selected stimulation configurations. In one of the simulation sets the monophasic electrical impulse was delivered through rectangular paddles localized in bath. The anode was placed near the endocardium and the cathode near the epicardium. The size of the electrodes was equal to the side of the model parallel to XY plane. The duration of the electrical shock was equal to 10 ms and the amplitude was 1V.

For a further research of the influence of the bath surrounding the tissue, needle electrodes were applied (Fig. 6.14). The duration of the monophasic stimulation delivered through the needle electrodes was equal to 10 ms and the amplitude was 75 mA.

It was observed that the modifications of the bath or the electrodes locations altered the patterns of membrane polarization. The physics, inducing the modifications is presented below.

During stimulation, a part of the electrical current delivered to the tissue by the two electrodes reaches the low resistance perfusion bath, characterized by the same conductivity as the extracellular space. From the bath, the current reenters the myocardium through the tissue-bath interface. The total current that propagated in bath is parted between the intra- and the extracellular domain. In this way secondary electrical sources can be created at the tissue-bath

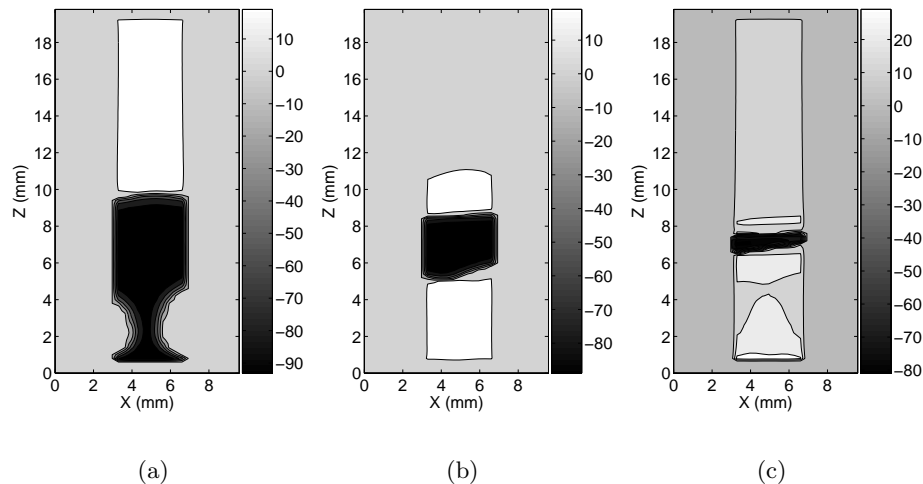


Figure 6.24: The distribution of V_m in a section through the model, composed of a medium sized myocardium incorporated in bath. The resting tissue, composed of twisted fibers, was stimulated by rectangular paddles, localized in bath, near the endocardium, respectively the epicardium. The duration of the monophasic electrical shock was equal to 5 ms and the amplitude was 1V. The electrical response was registered at: a) 5 ms, b) 7 ms and c) 10 ms.

interface.

The study was focused on the occurrence of primary and secondary electrical sources. The phase of interest started with excitation initiation and it was finalized with the complete depolarisation of the tissue.

Results The simulations showed that the modification of the tissue/bath volumes ratio induces strong variations in the response of the myocardium to electrical stimuli. At 10 ms, the preparation, containing the largest myocardial volume presented depolarisation near to the cathode and the manifestation of secondary electrical sources near to the anode. The excitation near the cathode was stronger than in the neighborhood of the anode. The volume of the depolarized tissue, near to epicardium was approximately equal to 130 mm^3 . The volume of the subendocardial excited region was approximately equal to 20 mm^3 . The shape of the depolarisation fronts indicates that the electrical conductivity is higher along the fiber than across the fiber. Before complete depolarisation, reached 10 ms after the end of electrical stimulation no additional secondary electrical sources formed.

At 5 ms, more than half of the medium sized myocardium was already depolarized. Due to cathodal stimulation, the tissue comprised in between $Z=10 \text{ mm}$ and $Z=20 \text{ mm}$ was excited (Fig. 6.24). The secondary electrical sources, occurring at the corners neighboring the anode excited a smaller volume of the tissue. They were characterized by a smaller magnitude than the pair of secondary electrical sources, which occurred at the top. The depolarisation spread only until $Z=4 \text{ mm}$. The curvature of the depolarisation fronts, due to the value of the electrical conductivity and to the fiber orientation could be ob-

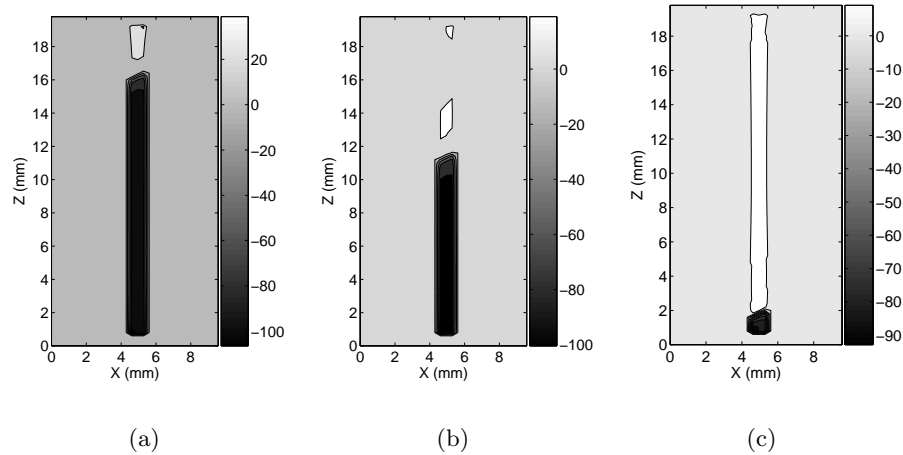


Figure 6.25: The distribution of V_m in a section through the model, which contains a very small myocardial volume incorporated in bath. The resting tissue, composed of straight fibers, was stimulated by rectangular paddles, localized in bath, near the endocardium, respectively the epicardium. The duration of the monophasic electrical shock was equal to 5 ms and the amplitude was 1V. The electrical response was registered at: a) 5 ms, b) 10 ms and c) 21 ms.

served in the lower part of the myocardium, until the 7th ms. The myocardium was entirely depolarized 1 ms after the end of the electrical stimulation.

The preparation with the smallest myocardial volume presented initiation of depolarisation only in the region, near to the cathode (Fig. 6.25). The excitation spread from top to the bottom of the tissue and in 22 ms the entire tissue was depolarized.

The simulations with needle electrodes indicated that the secondary electrical sources are influencing the myocardium stronger than the primary electrical sources even though they have a lower magnitude (Fig. 6.26). The response of the myocardium to electrical sources placed in the sub-endocardial and sub-epicardial regions was similar to the reaction of the preparation stimulated by paddles placed in perfusion. The only distinction was formed by the elevated value of V_m of the myocytes near to the needle cathode.

The placement of the primary electrical sources 1 mm above and below the centre of the tissue presented an additional distinction to the myocardium stimulated exclusively by secondary electrical sources. At 5 ms, the myocytes surrounding the anode, placed 1 mm below the centre of the tissue were depolarized due to the occurrence of a virtual electrode. The additional secondary electrical source reduced the time needed to complete depolarisation of the whole myocardium with 1 ms.

The magnitude of the secondary electrical sources depended on how much current entered the bath medium. By shifting the position of the electrodes towards the center of the tissue the intensity of the electrical sources decreased.

Discussion The data of Spach et al are cited widely as evidence for secondary electrical sources in cardiac tissue [92]. A part of the hypothesis presented by

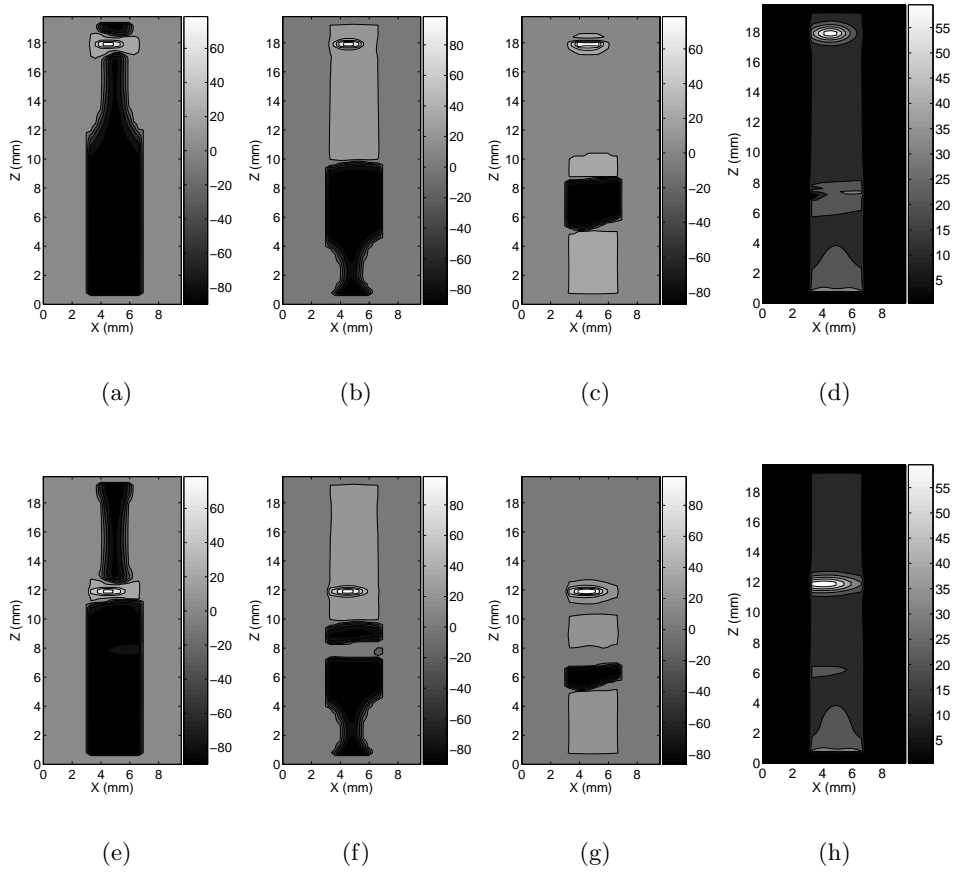


Figure 6.26: The distribution of V_m in a section through the model, which contains a medium sized myocardium incorporated in bath. The resting tissue, composed of twisted fibers, was stimulated by needle electrodes, localized inside the tissue, 1 mm away from the endo- and epicardial wall (top) and 1 mm above and below the centre on the tissue. The duration of the monophasic electrical shock was 10 ms and the amplitude was 1V. The electrical response was registered at: a), e) 3ms, b), f) 5 ms, c), g) 7 ms and d), h) 11 ms.

Spach et al was based on the supposition that excitation propagation in a tissue is 1-dimensional. In contrast, the theoretical research indicated that excitation propagation is three dimensional. In the three-dimensional myocardium, immersed in perfusion, V_m gradients exist not only in the direction of propagation, but also in the direction perpendicular to the tissue surface. Reasoning based on the 1-dimensional cable model presented by Spach et al, is not always applicable.

The effects of primary and secondary electrical sources are additive. It can be observed that the transmembrane voltage of the cells near to the tissue-bath interface is dramatically altered, but there are also modifications near to the center of the tissue predominantly induced by the variation of the magnitude of the primary sources.

In several theoretical studies [93], [94], [95] it has been shown that the pres-

ence of the perfusing bath may account for the acceleration of depolarisation that was observed by Spach et al. The high-conductivity bath causes the wave-front to be curved (surface leading bulk) and the surface excitation rate to be slowed. This effect is more dramatic for longitudinal propagation than for transverse propagation because of the unequal anisotropy ratios of the tissue. For longitudinal propagation, the intracellular and interstitial conductivities are approximately the same, so large interstitial potentials exist in the bulk, although the potential in the high-conductivity bath is small. For transverse propagation, the interstitial conductivity is 4 times greater than the intracellular conductivity. Therefore, the extracellular potentials are small both at the tissue surface and deep in the bulk. The smaller gradients of the extracellular potential result in smaller gradients in the transmembrane potential during transverse propagation compared with longitudinal propagation. Our calculated changes in excitation propagation are qualitatively consistent with previous numerical models [93], [94], [95] and with experimental data [92].

The results in Sect. 6.22 show that the influence of the perfusing bath extends at least 0.1 mm below the tissue surface. These results agree qualitatively with the recent experimental data of Spach et al [96].

Quantitatively, the biggest discrepancy between our calculations and the experimental data of Spach et al [96] lies in maximum size of the virtual electrodes. The reason for the discrepancy could be due to the fragmentization of the myocardium by cleavage planes or blood vessels.

One way to distinguish between the two mechanisms (capillaries versus perfusing bath) would be to repeat the simulations including cleavage planes (Sect. 6.5).

6.5 Cardiac Microstructure-Cleavage Planes

The exogenous current traverses the myocardium along convoluted intracellular and extracellular domains. The redistribution of the current in the two media induces changes in V_m distribution: regions of membrane hyper- and depolarisation of extent larger than a single cell are induced in the myocardium by the defibrillation shock. Tissue inhomogeneities also contribute to local membrane depolarisation in the myocardium, superimposed over the large-scale depolarisation associated with the fiber orientation of the myocardium.

Consider what would happen if the conducting myocardial region is bounded by an isolating medium and an electrical source is suddenly introduced. The bidomain model predicts an initial current flow into the boundary, but no current can escape into the nonconducting surrounding region. We must consequently have a transient during which charge piles up at the boundary. The process continues until the field from the accumulating charges brings the net normal component of electric field to zero at the boundary. To characterize a steady-state condition with no further increase in charge requires satisfaction of the boundary condition: $\frac{\partial\Phi}{\partial n} = 0$ at the surface (within the tissue). The source that develops at the bounding surface is secondary to the initiation of the primary field; it is referred to as a secondary source. The secondary electri-

cal source is essential for satisfaction of boundary conditions and it contributes to the total field everywhere else.

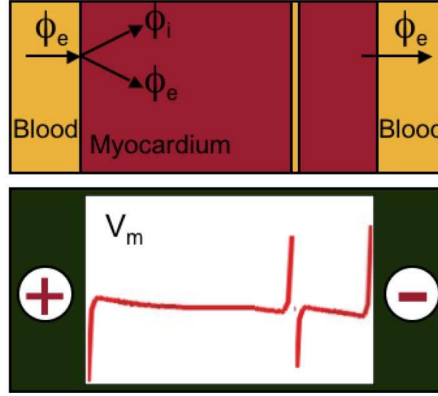


Figure 6.27: The formation of secondary electrical sources, due to tissue inhomogeneities, e.g. cleavage planes, according to the bidomain theory.

The same phenomena arise if the region would be bounded by a medium with a different electrical conductivity. In this case, when the primary source is applied the current flowing into the boundary is not equal to the current flowing away from the boundary. The gradient induces an accumulation of charge and a secondary source will develop satisfying the boundary condition:

$$-\sigma'_k \frac{\partial \Phi_1}{\partial \mathbf{n}} = -\sigma''_k \frac{\partial \Phi_2}{\partial \mathbf{n}} = J_n \quad (6.2)$$

The two neighboring regions are denoted by prime and double-prime superscripts. The vector $\vec{\mathbf{n}}$ is oriented from the prime to double-prime region. The accumulated single source density is given by:

$$K_s = J_n \left(\frac{1}{\sigma'_k} - \frac{1}{\sigma''_k} \right) \sigma$$

The magnitude of the steady-state secondary source for the scalar function $\Psi = \Phi \sigma$ can be described as an equivalent double layer:

$$\vec{K}_k^i = \Phi_k (\sigma''_k - \sigma'_k) \vec{\mathbf{n}} \quad (6.3)$$

The secondary potential field generated by \vec{K}_k^i is given by:

$$\Psi_p^s = \sigma_p \Phi_p^s \frac{1}{4\pi} \sum_k \int_k \Phi_k (\sigma''_k - \sigma'_k) \vec{\mathbf{n}} \nabla (1/r) dS \quad (6.4)$$

The superscript s denotes exclusively the secondary field component. Solving the equation (6.4) one obtains:

$$\Phi_p^s = \frac{1}{4\pi\sigma_p} \sum_k \int_k \Phi_k (\sigma''_k - \sigma'_k) \vec{\mathbf{n}} \nabla (1/r) dS \quad (6.5)$$

The total electrical potential can be calculated by adding the primary field. Assuming that all applied currents lie in a region with conductivity σ_a , we have:

$$\Phi_p^s = \frac{1}{4\pi\sigma_a} \int \vec{j}^i \cdot \nabla(1/r)dv + \frac{1}{4\pi\sigma_p} \sum_k \int_k \Phi_k(\sigma_k'' - \sigma_k') \vec{n} \cdot \nabla(1/r) dS \quad (6.6)$$

The physical formalism indicates theoretically how the appearance of secondary electrical sources depends on the intensity of the stimulus. For the enlargement of the understanding of the phenomena correlated to the cleavage planes the electrical behaviour of a virtual myocardium intersected by interlaminar clefts was simulated.

Constructional aspects of the models The research presented in this section was based on investigations of the influence of cleavage planes on the electrical behaviour of the human left ventricle. The electrophysiology was described by the Priebe-Beuckelmann electrophysiological model (Sect. 4.4.1). For observing the influence of the cleavage planes on the reaction of the myocardium to electrical stimulation two cases were considered. Firstly, the tissue was initially at rest. Secondly, the tissue presented an arrhythmic behavior while the electrical shock of interest was applied.

For the case in which the myocardium was resting the applied three-dimensional structure was $1 \times 1 \times 2 \text{ cm}^3$ in size. It included 0.1 cm blood bath medium at both sides. The intracellular myocardial bulk was twice intersected by isolating half filled grids. The extracellular domain remained continuous. The intracellular domain contained planes with uniformly distributed voxels of zero conductivity. The geometrical pattern of the cleavage planes reproduced the anatomical cardiac features. The cleavage planes comprised in the myocardium are intersecting each other due to the varying angles. A pair of planar electrodes, $1 \times 1 \text{ cm}^2$ large, were placed in the immediate vicinity of the bath at the ends of the z axis. The electrical sources are not placed directly on the myocardium for obtaining more precise spatial distribution of membrane polarization in the cardiac tissue during the initial phase of electrical stimulation. The duration of the $(-5, +5) \text{ V}$ biphasic electrical stimulation was 10 ms.

The size of the arrhythmic myocardium was $4 \times 0.5 \times 4 \text{ cm}^3$ ([76], [77]). The tissue was intersected by three cleavage planes centrally localized. The rectangular paddles, placed near endo- and epicardium were $4 \times 0.5 \text{ cm}^2$ large. The myocardium was stimulated with monophasic electrical impulses. The duration of the applied electrical shock was 10 ms. The amplitude of the electrical stimuli was 5 V.

The spatial discretization was set equal to 0.2 mm. The calculation time step was 10 μs .

Results The results of the simulations indicated that the inclusion of interlaminar clefts between layers of cardiomyocytes induces the appearance of secondary electrical sources far away from the location of the electrodes.

The stimulation of a resting myocardium through paddle electrodes induced the excitation of the entire region neighboring the cleavage planes. The first

depolarisation front was formed by the primary electrical source. After 2 ms the secondary electrical sources also induced a depolarisation front. A characteristic of the response of the myocardium illustrated in the results is that the cleavage planes nearest to the anode induce more intense secondary electrical sources (Fig. 6.28). The inversion of the polarity of the primary electrical source intensified the excitation of the myocytes neighboring the farthest away cleavage plane.

The depolarisation phase was temporally reduced by the occurrence of secondary electrical sources in the middle of the transmural wall. Since the M cells were excited few ms after the application of the electrical stimuli, the time needed by the tissue to be completely at rest was drastically reduced.

The investigation of the influence of cleavage planes existence on the response of an arrhythmic human myocardium brought important information for understanding of defibrillation phenomena. 5 ms after the application of the external electrical field the subepicardial region was depolarized, while the myocytes forming the subendocardium were hyperpolarized (Fig. 6.29 a, b).

Few ms later, in the tissue containing an on-going arrhythmia, sections of the cleavage planes induced the appearance of secondary electrical sources (Fig. 6.29 c). Only one of the three cleavage planes, intersecting the myocardium induced a depolarisation front with a surface equal to $4 \times 1 \text{ cm}^2$. A part of the myocytes near the middle cleavage plane were excited by the secondary electrical source, while the refractory cells were not depolarized. Most of the myocytes localized between the cathode and the centre of the myocardium were depolarized by the arrhythmic wave. Therefore, the influence on the distribution of V_m , of the cleavage plane localized near to the primary electrical source was neglectable.

The formation of secondary electrical sources in the middle of the myocardium modified the depolarisation patterns and increased the number of excited cells.

Discussion The study reports observations on the influence of left ventricle lamination on the response of myocardium to cardiac electric stimulation and defibrillation.

In agreement with the data published by Hooks et al., [21], the simulations with human three-dimensional cardiac preparations reflect that structural discontinuities induce the occurrence of secondary electrical sources. In particular it was observed that interlaminar cleavage planes play a very important role in the spatio-temporal distribution of V_m . Therefore a good representation of the myocardium must take into consideration that the tissue is not continuous.

The investigations of the arrhythmic preparations reflected that the cleavage planes are partly activated post-defibrillation. The electrical sources formed in the middle of the myocardial bulk increased the portion of the depolarized tissue. Considering the critical mass theory (Sect. 4.7.2), the formation of supplementary depolarisation fronts decreases the probability of a reentry appearance.

The experimental measurements indicate that the left ventricular my-

ocardium is intersected by isolating regions in average after each 4 to 6 cells. The orientation of the cleavage planes varies across the transmural wall (Fig. 3.4). In future studies a realistic description of the laminar cardiac features will have to be implemented in the models.

6.6 Inferences

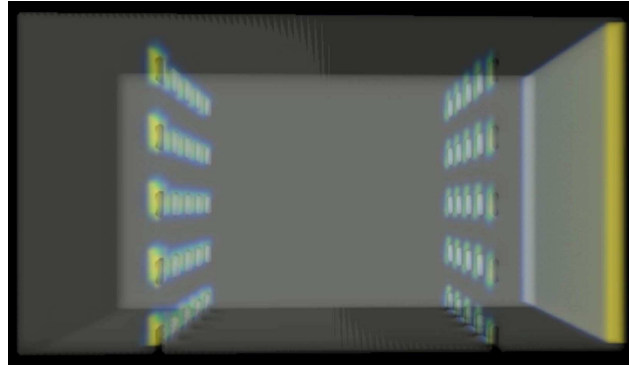
In this chapter the influence of the cardiac features, which can be incorporated in a virtual human left ventricular myocardium was investigated.

The study presented in the first subchapter indicate the necessity of the incorporation of variant tissue curvature and wall thickness for theoretical investigations of internal defibrillation. A tissue with parallelepipedic geometry can be used in fundamental studies of transmurally propagating processes. A large slice of myocardium manifests an electrical behaviour similar to the parallelepipedic section and it can be used in studies of arrhythmias.

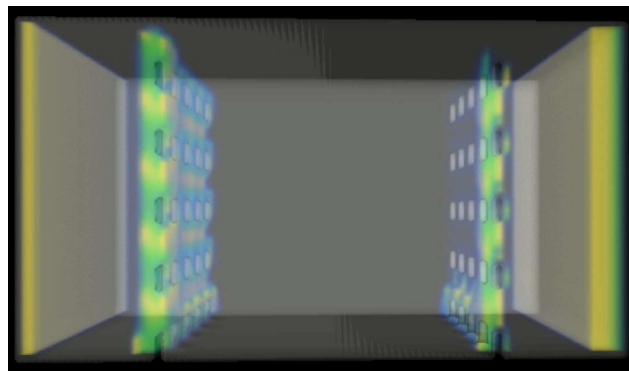
The differences in electrophysiological characteristics of epi-, M- and endo-cells are reflected mainly during the repolarisation phase. The distinctions between the results found with an electrophysiological heterogeneous and an homogeneous tissue reflect the necessity of including the physiologic transmural variation.

The orientation of the myocardial fiber together with the existence of a blood pool and of the cleavage planes influence the distribution of V_m during the depolarisation phase. The anatomical cardiac fiber twist must be represented in the model for a realistic simulation of the tissues electrical behaviour. The muscle/blood volume ratio strongly influences the occurrence of secondary electrical sources. A model without blood pool reacts as a cardiac wedge immersed in a large bath. The cleavage planes may induce the formation of secondary electrical sources in the centre of the transmural wall, resulting in a reduction of the depolarisation phase. In the theoretical studies of the identification of the defibrillation success the cleavage planes must be included in the myocardium.

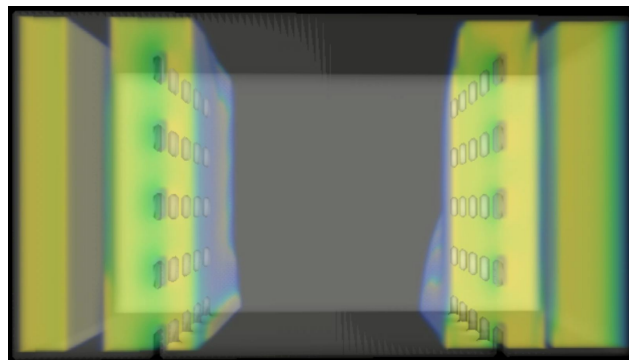
Therefore, for a most accurate study of the left ventricle electrical activity 3D myocardial preparations based on heterogeneous electrophysiology with anisotropic electrical conductivity, realistic fiber twist and cleavage planes are necessary.



(a)



(b)



(c)

Figure 6.28: Transmembrane voltage in a tissue with realistic fiber orientation and two cleavage planes, after (+5V, -5V) biphasic electrical signal is applied, at different moments after the excitation initiation: a) 6 ms, b) 11 ms and c) 20 ms. Same color code as in Fig. 6.6. The interlaminar clefts are represented by half filled grids, intersecting the intracellular space. The results indicate that the secondary electrical sources, which occur near the cleavage planes present different intensities. During the first phase of stimulation secondary electrical sources occur near the cleavage plane furthest away from the cathode. The inversion of the polarity induces secondary electrical sources in the neighborhood of the other cleavage plane.

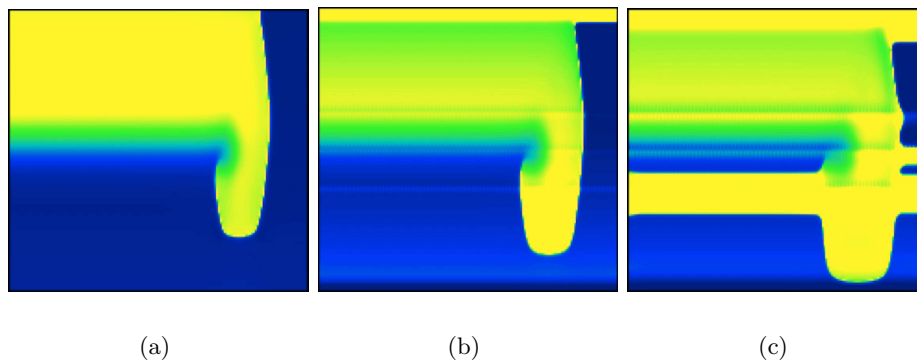


Figure 6.29: The distribution of V_m in a section through the tissue with realistic fiber orientation and 3 interlaminar clefts after (+5V, -5V) monophasic electrical signal is applied, at different time steps: a) 1 ms before the electrical stimulation, b) 5 ms and c) 15 ms after the defibrillation. Same color code as in Fig. 6.6. The results indicate that the central cleavage plane is only partly inducing secondary electrical sources. The modification of V_m created by the upper cleavage plane is neglectable. The secondary electrical source formed near the lowest cleavage plane excited a large fraction of the myocardium.

7 Influence of Electrical Stimulation Characteristics

Presently, many types of electrical stimulation configurations are utilized in cardiac therapies. The aim of the defibrillator producers is to improve the existent products for enhancing the therapeutical efficiency.

In this chapter the features of the electrical stimulation configurations and their influences on human myocardium are theoretically investigated. The first subchapter describes the characteristics of the electrical stimuli. The data were gathered from studies of the impact between a single cell or a myocardial wedge and electrical stimuli with various phases, amplitudes and frequencies.

The second subchapter sums up the results of simulations with human myocardial wedges excited by electrical impulses delivered by various types of electrodes. A part of the study is focused on the modifications in the cardiac behaviour implied by the variation of the location of the electrodes. In the following subchapter a new therapeutical procedure is introduced.

In the last section is discussed the optimal timing for applying the defibrillation shock.

The results of the theoretical investigations are addressed mainly to the scientists who are engaged in experimental investigations of the human heart.

7.1 Features of the Electrical Stimuli

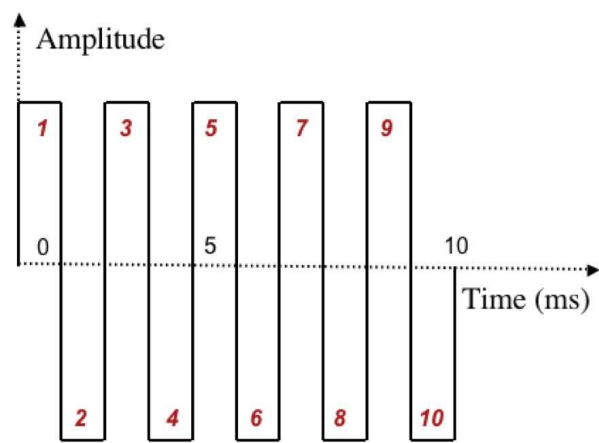
7.1.1 Microscopic Level

Defibrillation efficiency depends on the activation of the cardiomyocytes. A cell stimulated by an extracellular field is depolarized at one end and hyperpolarized at the other [97]. If the electrical impulse is sufficient in amplitude and duration the depolarisation will not disappear with the interruption of the stimulus. The excitation threshold strongly depends on the way depolarisation influences the activation and inactivation sodium currents. If the stimulus is large and rapid, the membrane depolarizes quickly and activates the sodium current (opens the m gate) before sodium inactivation variables, h and j can substantially change. Further, the process is described in detail.

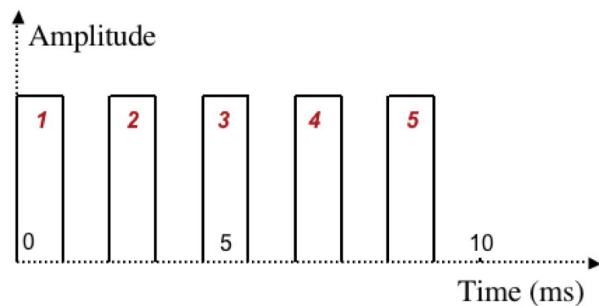
Quantitative information on the phenomenon was gathered from the excitation of a virtual human ventricular myocyte. The electrophysiological characteristics were simulated with TNNP model (Sect. 4.4.2). The cell was stimulated by monophasic and biphasic impulses, with various frequencies and amplitude (Fig. 7.1).

The main purpose of the research was to identify the necessary strength of an impulse with a specific frequency and duration to induce the formation of an action potential (AP). The lowest intensity of the electrical impulse leading to the occurrence of an AP is termed excitation threshold.

Another objective of the research was the identification of membrane processes corresponding to the excitation threshold. The sum of these informations enables the scientist to draw a conclusion on the stimulation efficiency.



(a)



(b)

Figure 7.1: Wave forms utilized for stimulating the cell: a) biphasic and b) monophasic stimulation. Examples given for 500 Hz. The numbers written in red indicate the number of the pulses, which can be odd or even for each frequency. The waveforms are similar to the "chopped" pulses of Schiller and Metrax.

Biphasic Electrical Stimuli The research started with the injection into the cell of a biphasic stimulus with a 100 Hz, 10 ms duration (Fig. 7.3 and Fig. 7.4). As presented in Sect. 5, these are at present the most common characteristics of a defibrillation stimulus.

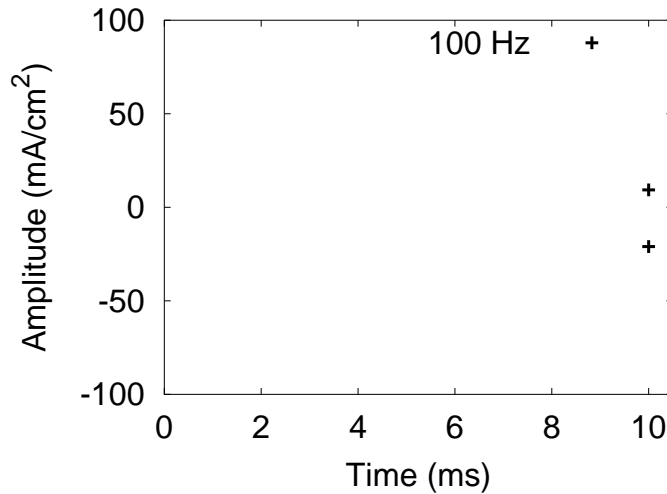


Figure 7.2: The excitation thresholds for a 10 ms long biphasic 100 Hz cellular stimulation. The intensity of the electrical stimulus necessary to depolarize the human ventricular myocyte is smaller if the amplitude is positive during the first 5 ms.

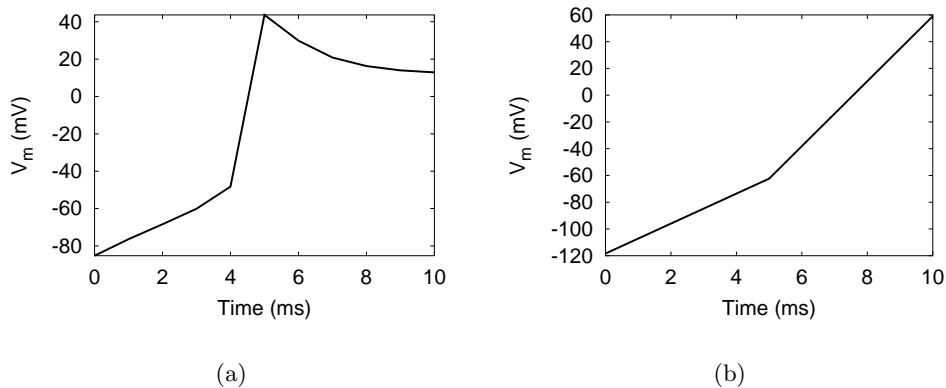


Figure 7.3: AP profile during a successful excitation with a biphasic 100 Hz and 10 ms long stimulus. The amplitude of the first pulse was a) positive, b) negative. The success of the biphasic stimulation depends on two factors. First the positive amplitude must be high enough for creating a positive V_m . Secondly, the current must be withdrawn from the cell at the beginning of the early repolarisation or its amplitude must be small enough for facilitating the start of the plateau phase.

Initially was investigated a resting single cell activated by a biphasic electrical impulse having a positive amplitude during the first 5 ms. V_m varied slowly from -85 mV to -40 mV (Fig. 7.3 a). The electrophysiological phenomenon was mainly coordinated by the j gate which presented a stronger variation than m and h (Fig. 7.4 left column). The -40 mV transition moment depended on the amplitude of the electrical stimulus. A higher amplitude decreases the time needed by V_m to reach the threshold. For the minimal successful amplitude, the transition occurred at 4 ms. After $V_m > -40$ mV m and h gate variables

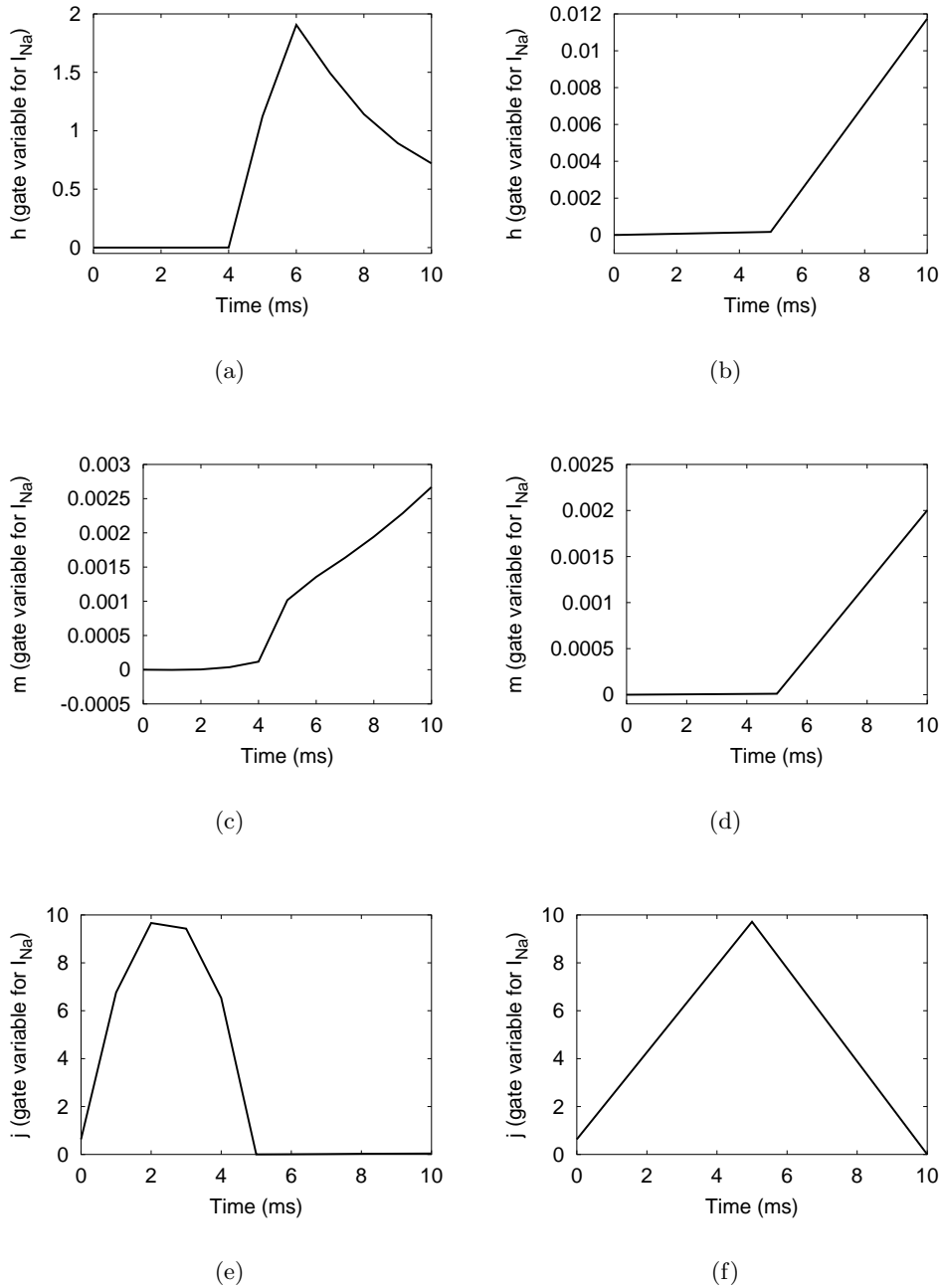
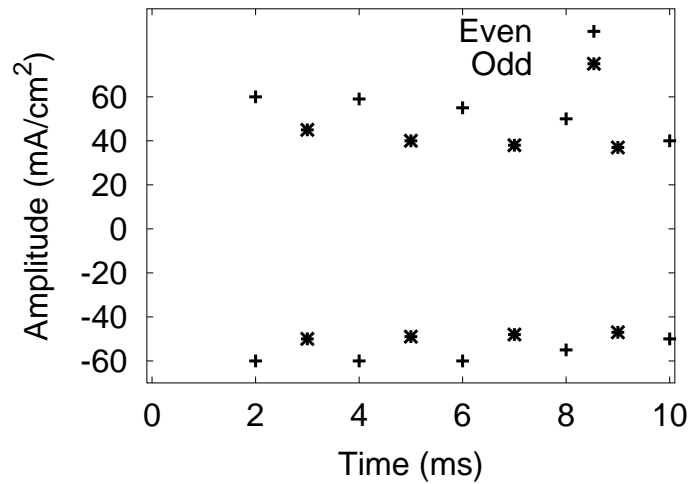
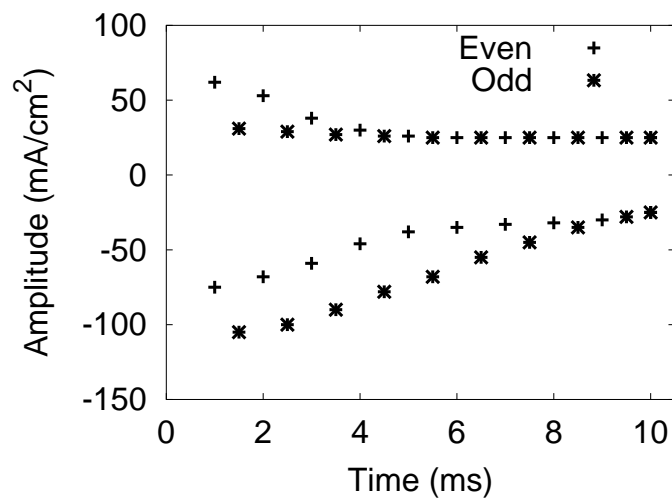


Figure 7.4: The gate variables for I_{Na} during a successful excitation with a biphasic 100 Hz and 10 ms long stimulus having a positive (left column) or a negative (right column) amplitude in the first half of the stimulation interval.

presented strong modifications (Fig. 7.4 a, c). During the second phase the m continued to increase, while h was decreasing and j was almost equal to zero. The reduction of the inactivation current, h - j simultaneous with the amplification of the activation current facilitated the initiation of the plateau phase.



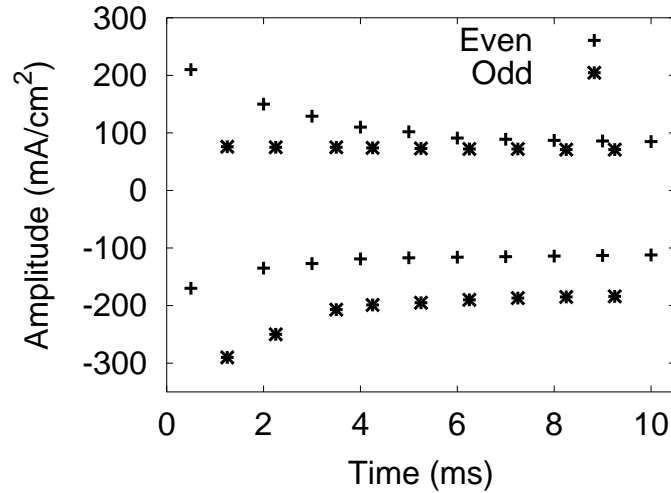
(a)



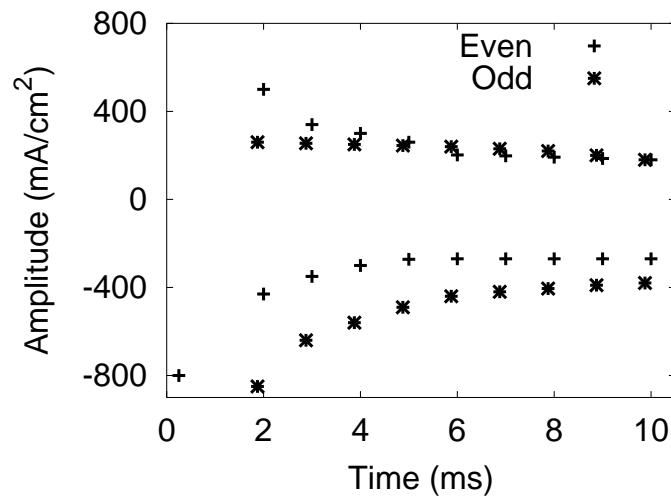
(b)

Figure 7.5: Excitation threshold of myocytes for a) 500 Hz and b) 1 kHz, of biphasic stimulation. The results present different excitation threshold values for distinct parities of the pulse numbers. The difference is higher for initial negative amplitude.

The phenomena corresponding to initial positive-secondary negative electrical stimulation were further researched with pulses of various amplitudes. The results reflected the dependence of the stimulation success on two factors. First the positive amplitude must be sufficiently high for creating a positive V_m . Secondly, the current must be withdrawn from the cell at the beginning of the early repolarisation or its amplitude must be small enough for facilitating the start



(a)



(b)

Figure 7.6: Excitation threshold of myocytes corresponding to a) 2 kHz, b) 4 kHz, of biphasic stimulation. The graphs illustrate the exponential variation with the duration of the stimuli for odd and even numbers of pulses. The sign of the amplitude corresponds to the value of the first pulse.

of the plateau phase. If the absolute value of the negative pulse is lower than the positive amplitude the successful excitation range is higher. For example, the impulses with equal amplitudes during both phases induced the occurrence of an action potential profile in the interval (9, 17) mA/cm². The biphasic stimuli with a negative amplitude equal to 50% of the positive amplitude were successful in the interval (8.3, 29) mA/cm².

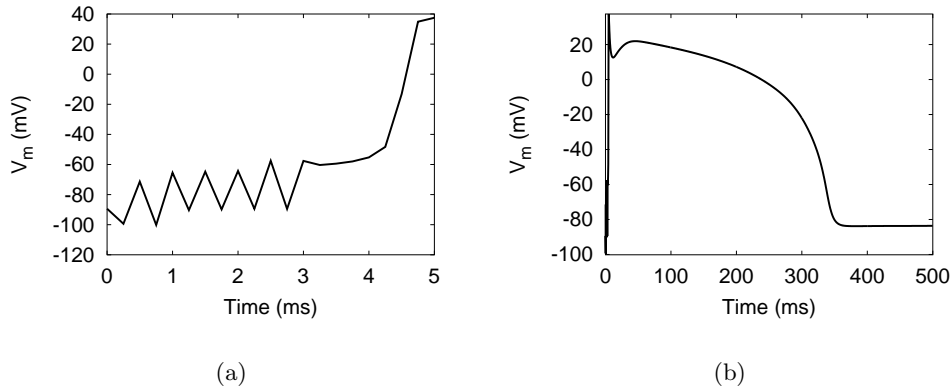


Figure 7.7: AP profile corresponding to a successful excitation with a 2 kHz and 5 ms long biphasic stimulus, during a) the first 5 ms and b) 500 ms.

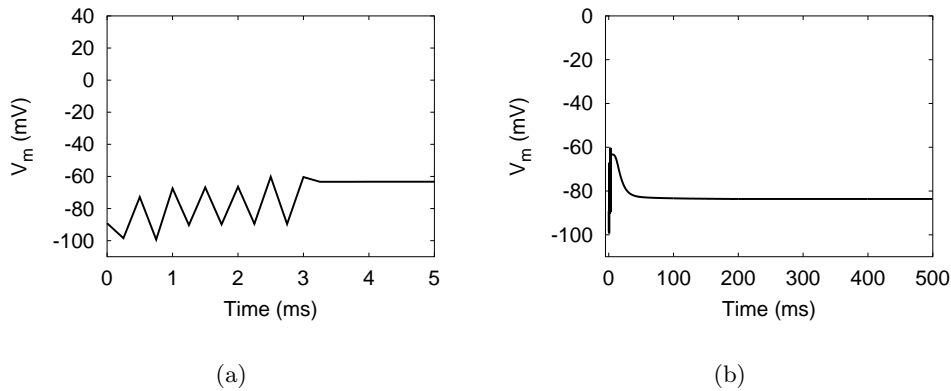


Figure 7.8: V_m evolution after a failing stimulation corresponding to a 2 kHz and 5 ms long biphasic stimulus, during a) the first 5 ms and b) 500 ms.

The inversion of the polarity modified both the temporal variation of V_m and I_{Na} gate variables. The resting cell was hyperpolarized by the negative electrical stimulus. In the first 5 ms, the cell membrane tended to regain the normal resting state. During the second phase of the stimulation the variation of V_m leading to a positive value became faster. The -40 mV threshold could not be observed in V_m profile or in the variation of I_{Na} gate parameters.

Comparing the values of the I_{Na} gate variables corresponding to the two biphasic electrical stimuli it was observed the formation of different temporal evolutions. The strongest contrast was formed by the j gate. The parabolic curve, characteristic to the cell excited from the resting state (Fig. 7.4 e) was substituted by a triangular variation (Fig. 7.4 f). The results of the simulations also indicated that the excitation threshold was increased from 9 to 21 mA/cm² if the cell was first hyperpolarized and then depolarized (Fig. 7.2).

The investigation of cellular stimulation was further extended to higher frequencies: 500 Hz, 1 kHz, 2 kHz and 4 kHz. The research included even and

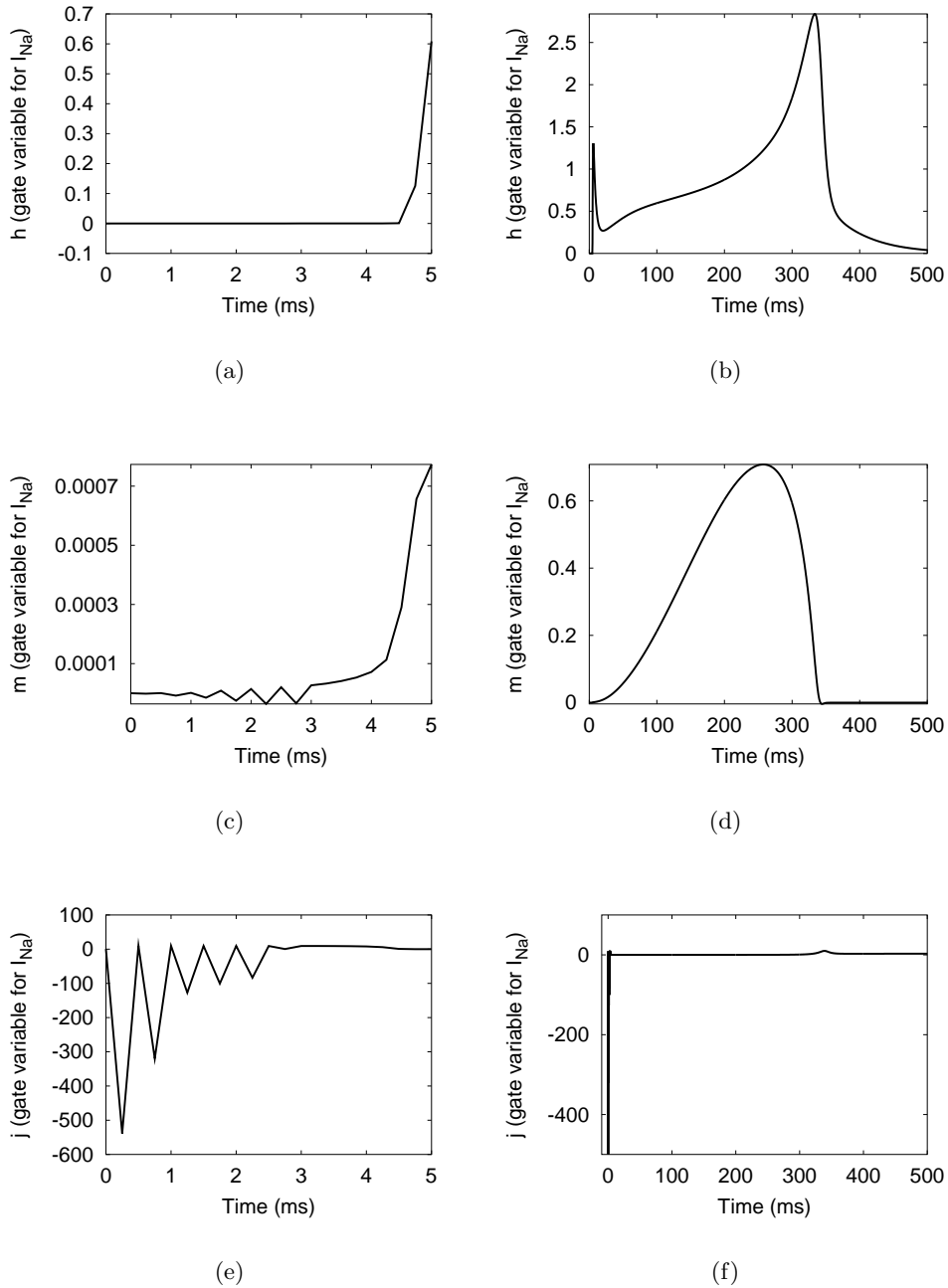
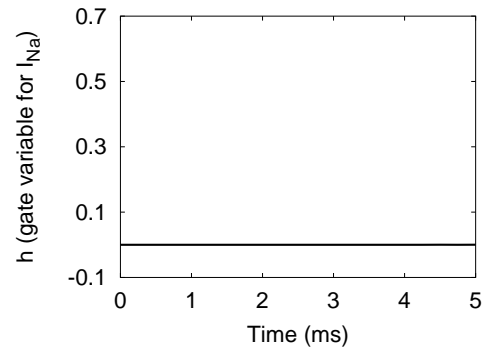
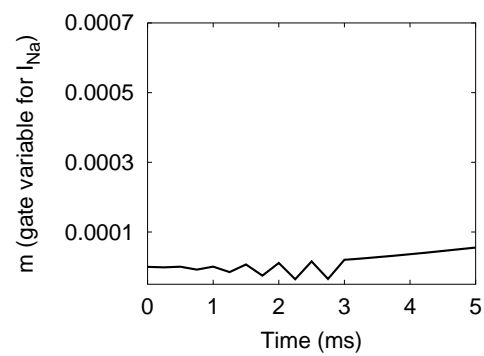


Figure 7.9: The gate variables for I_{Na} corresponding to a successful excitation with a 2 kHz and 5 ms long biphasic stimulus, during the first 5 ms (left column) and 500 ms (right column).

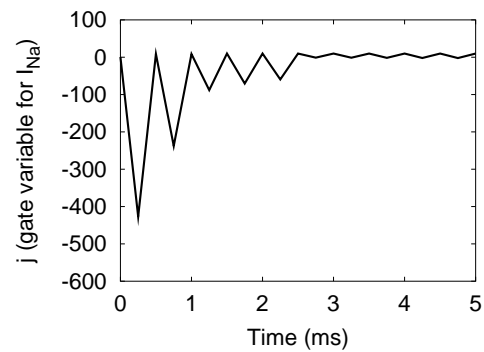
odd number of pulses. Both electrical stimuli starting with a positive or a negative amplitude were studied. The excitation thresholds corresponding to 500 Hz electrical stimuli varied very little with the impulse duration remaining in the $\pm(40, 60)$ mA/cm² interval. The excitation thresholds for 1 kHz varied



(a)



(b)



(c)

Figure 7.10: The variation of the gate parameters for I_{Na} during a failing excitation with a 2 kHz and 5 ms long biphasic stimulus.

according to parity of the number of pulses and to the sign of the initial amplitude. For odd numbers of pulses with positive initial amplitude the excitation threshold was invariant with the impulse duration. The change of the pulses

number parity induced a variation of the threshold with the stimulation duration. For impulses shorter than 4 ms the excitation threshold increased with the reduction of the stimulation duration. The dependence was enhanced by the inversion of the polarity of the signal. For even stimuli the variation of the excitation thresholds was manifested in the interval (0, 5) ms and for odd stimuli the interval was equal to (0, 8) ms. The entire spectrum of excitation thresholds corresponding to 1 kHz biphasic electrical stimuli was included in the interval (-150, 100) mA/cm².

For 2 and 4 kHz the excitation threshold interval was broadened to (-350, 300) mA/cm² and (-900, 800) mA/cm², respectively. The dependence on impulse duration was more clearer formed in the interval (0,6) ms than it was for smaller frequencies.

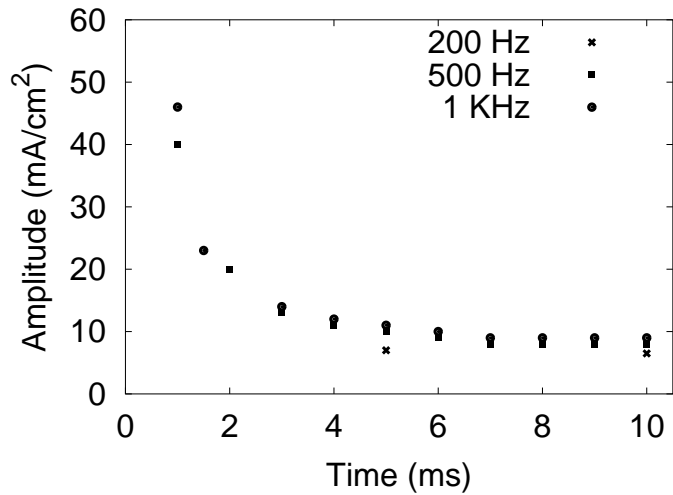
The study was extended to the understanding of the gating processes associated to high stimulation frequency. As an example is described the reaction of the human left ventricle myocyte excited with a 2 kHz, 5 ms long stimulus. The reaction of the cell to the threshold intensity is illustrated in Fig. 7.7 and Fig. 7.9. In the first 3 ms V_m had a sawtooth evolution, corresponding to the waveform of the stimulus. In this period the mean value of V_m was slowly increasing. At 3 ms, the cell entered a new regime in which V_m increased rapidly without reflecting any more the waveform of the applied stimulus. The variation of m and j gates also reflected the waveform of the stimulus during the first 3 milliseconds. Afterwards, the evolution of I_{Na} gate parameters was independent of the waveform of the electrical stimulus. Their variation during the APD is typical for the successful activation of the myocyte.

In Fig. 7.8 and Fig. 7.10 is shown the reaction of the cell stimulated with a 2 kHz, 5 ms long electrical impulse having an amplitude a fraction smaller than the excitation threshold. During the first 3 ms, V_m formed a sawtooth profile. Due to the intensity of the impulse the amplitude and the temporal augmentation of the mean value of V_m were not big enough to lead to a depolarisation. Simultaneously, the h gate remained opened, as its value was constantly equal to zero (Fig. 7.10 a). The oscillations of the m and j gates were similar to the ones induced by the more intense stimulus. The main difference was the reduction of the amplitude, finally leading to failure of the cell excitation.

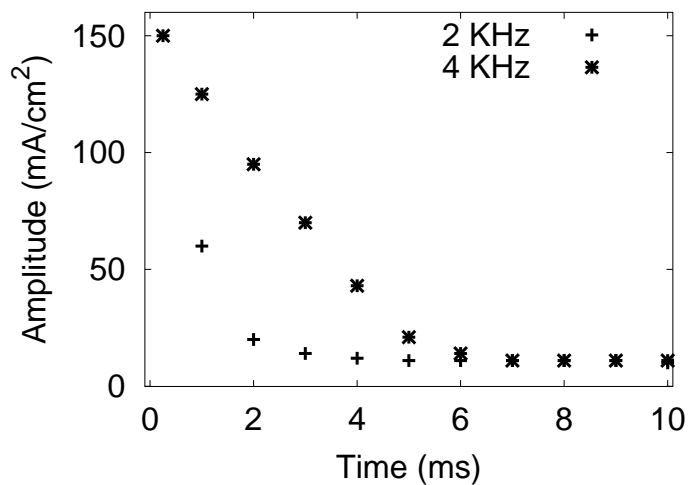
Monophasic Electrical Stimuli The investigation of cellular stimulation was continued with monophasic stimuli of various frequencies. The utilized waveform is presented in Fig. 7.1.

The plots of excitation thresholds as functions of impulse duration indicate an exponential variation in the interval (0, 5) ms and invariance with time for stimuli longer than 5 ms (Fig. 7.11). The rheobase varies with the frequency. The rheobase of 200 Hz was 15% smaller than for 500 Hz. The rheobase of 2 KHz was almost equal to the one of 4 kHz. The simulations indicated that the excitation threshold is strongly increased for small numbers of pulses in the 4 kHz case.

The excitation of the cell with a high frequency monophasic impulse produced a linear increment of V_m in time (Fig. 7.12 a). The variation was mainly



(a)



(b)

Figure 7.11: Excitation threshold of myocytes for various frequencies: a) 200 Hz, 500 Hz and 1 kHz, b) 2 kHz and 4 kHz, of monophasic stimulation. The graphs illustrate the variation with the duration of the stimuli.

dictated by the j gate, which had a strong fluctuation. After the -40 mV threshold was reached, V_m slope became steeper. At the same time h gate closed and m opened.

In the Fig. 7.13 are shown the excitation thresholds as functions of frequency for both mono- and biphasic impulse trains. The picture indicates a small difference between the mono- and biphasic amplitude thresholds for low frequencies, like 500 Hz. The difference was enlarged with the frequency, being

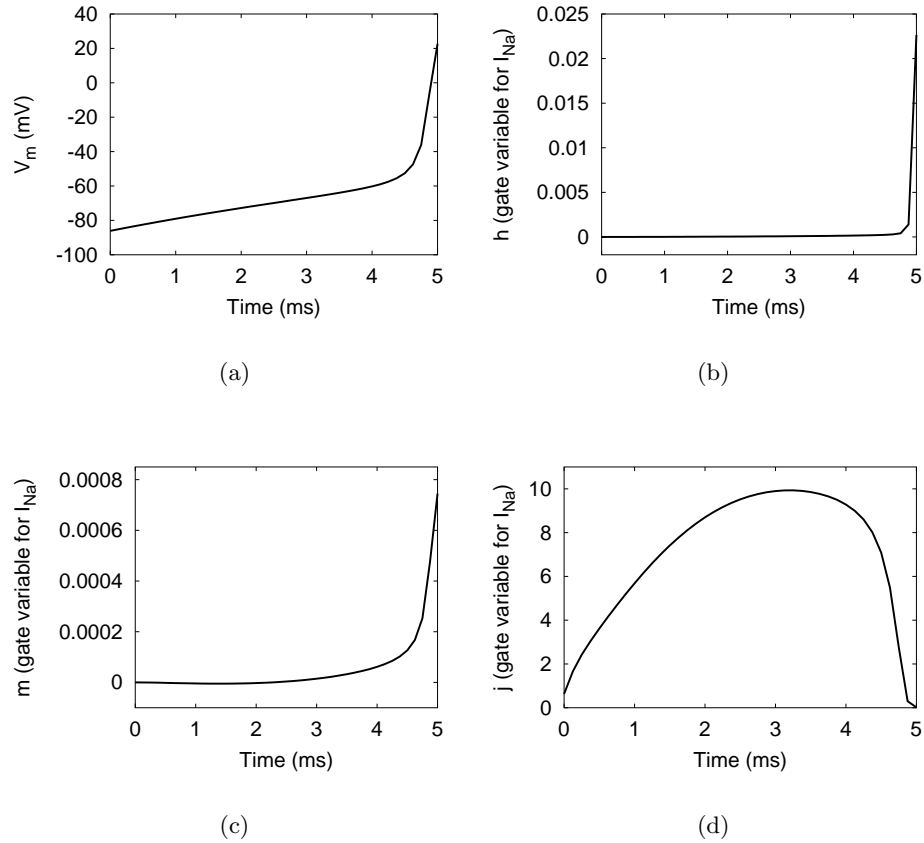


Figure 7.12: V_m and the gate variables for I_{Na} after a successful excitation with a 2 kHz and 5 ms long monophasic stimulus.

35 times larger for 4 kHz.

In the research was included a comparison between the excitation thresholds corresponding to two distinct monophasic wave forms. First was considered a rectangular impulse. Secondly was used a truncated exponential, having the maximum amplitude equal to the amplitude of the other wave type. The two wave form types are illustrated in Fig. 7.14. The investigation domain included impulses with lengths in between 1 and 7 ms. The results indicated that the excitation thresholds were smaller for rectangular stimuli than for truncated exponential. The difference was larger for longer electrical stimuli than for short impulse durations.

The Matlab's fitting toolbox was used for fitting the curves of the excitation thresholds corresponding to monophasic rectangular and truncated exponential stimuli with Weiss-Lapicque and Blair laws (Fig. 7.15). The comparison between the fitting results indicated that Blair law was more accurate in the description of the variation than Weiss-Lapicque law and both mathematical equations described better the excitation thresholds curves for truncated exponential than for rectangular stimuli. Blair law overestimated near chronaxie and underestimated the rheobase.

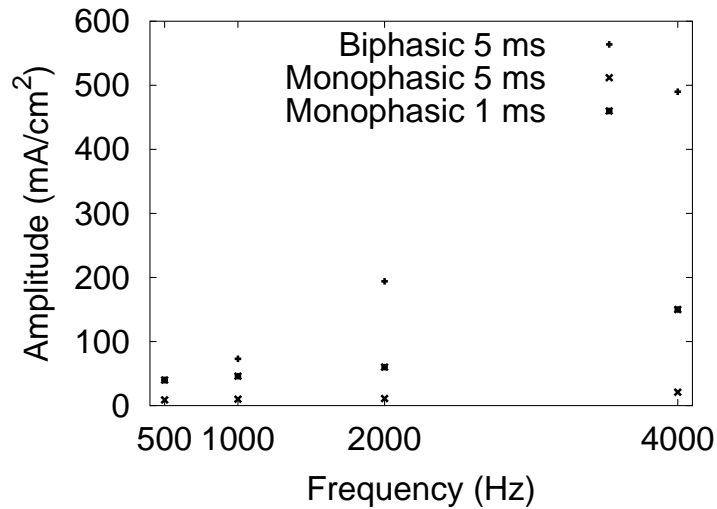


Figure 7.13: Comparison between monophasic and biphasic cellular stimulation. The results indicate higher excitation threshold for biphasic stimuli. The difference increases with the frequency.

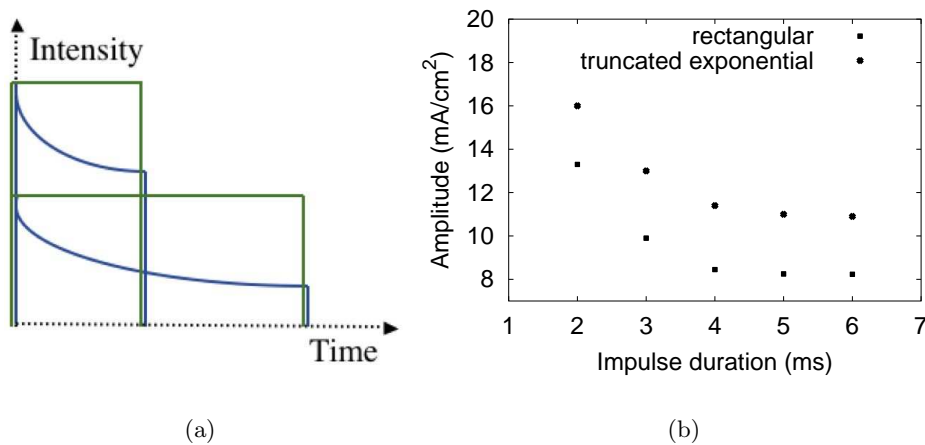


Figure 7.14: a) Rectangular and truncated exponential monophasic stimulation wave forms. b) Comparison between the excitation thresholds for the two stimulation wave forms. The results indicate a reduction of the difference between the thresholds with the impulse duration.

Blair formalism is based on a condenser theory. The charging of a capacitor is described by the expression:

$$V_C(t) = V_{C,Max} \cdot (1 - e^{-\frac{t}{\tau}}) \quad (7.1)$$

For simplifying the comparison it is presumed that the cell crossed a steady state evolution from the resting to the end of depolarisation phase. The formula describing the process is the equation (4.28) for m_∞ (Sect. 4.4.2).

Even though both functions contain an exponential dependence, the profiles of the curves are different. The existence of a maximum limit above which the

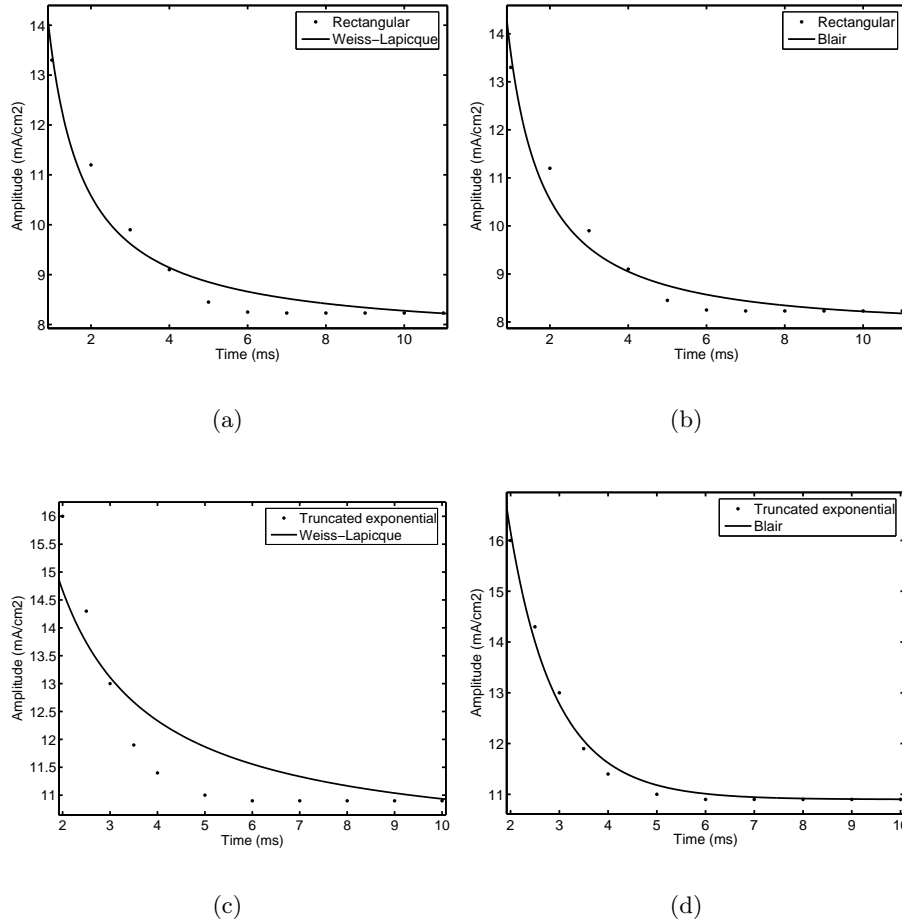


Figure 7.15: Excitation thresholds of monophasic rectangular and truncated exponential stimuli fitted by Weiss-Lapicque and Blair laws.

outcome of the function is constant implies a good fit in the short duration pulses range.

7.1.2 Macroscopic Level

Recently, studies were done to evaluate cardiac rhythms following the first defibrillation shock, comparing biphasic truncated exponential, monophasic damped sinusoidal and monophasic truncated exponential waveforms in patients experiencing out-of-hospital ventricular fibrillation cardiac arrest [89]. The results of this research illustrated the defibrillation chances through a statistical method. The impacts of specific electrical shock characteristics can also be studied with computer models, which could actually bring a more detailed look over the phenomena.

This subsection reports the influence of electrical shock features on the behavior of the human ventricular myocardium. For the investigation a three-dimensional computer model of human cardiac tissue was used. The myocardial

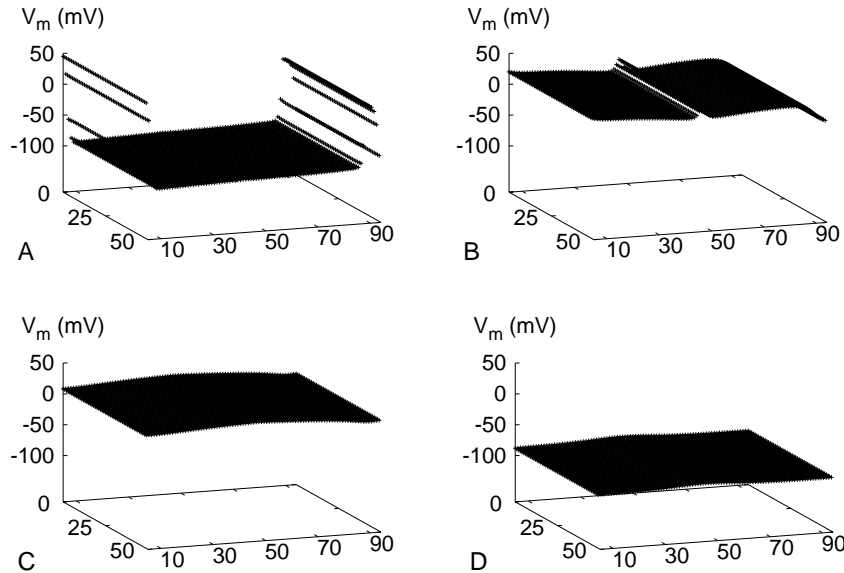


Figure 7.16: Biphasic stimulation of a continuous wedge of myocardium. The transmembrane voltage distribution is presented at: a) 5 ms, b) 25 ms, c) 60 ms, d) 350ms.

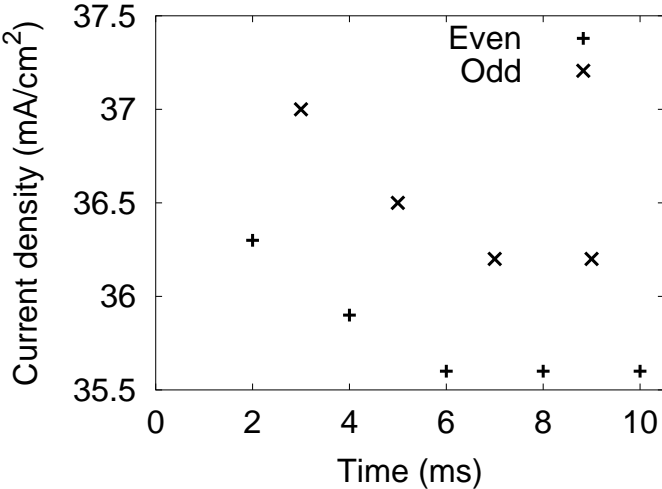
preparations were described in detail in Sect. 6.1.1 and Sect. 6.5. The cellular electrophysiology utilized for both models was based on the TNNP model (Sect. 4.4.2).

Quadratic planar electrodes ($1 \times 1 \text{ cm}^2$ in size), were placed in bath medium, at the ends of the longest axis ($Z=0$, $Z=2 \text{ cm}$). Because of the conditions chosen, the applied electric signal had to cross 1 mm of the bath medium before entering the myocardial area. In this way the extracellular potential was homogeneously distributed to the myocytes placed on the boundary surfaces.

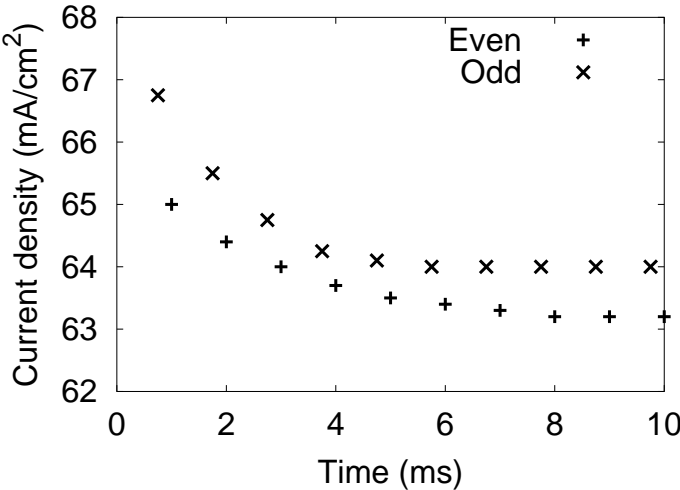
Biphasic Stimulation of Continuous Myocardium The first objective was to study the cardiac tissue reaction to different types of biphasic signals given by planar electrodes. Past studies revealed that cleavage planes are reducing the time needed for the entire tissue to be depolarized after an electrical shock [74]. Firstly a cardiac wedge, which was not fragmented by cleavage planes was used. In this way the differences between the obtained results were enhanced. A continuous medium needs more time for passing from one phase to another, especially when the depolarisation front is planar.

Considering experimental data we decided to initiate the investigation using 100 Hz exponentially decaying, sinusoidal and rectangular signals with magnitudes varying from 0.1 to 5 V. The two phases of the applied electric signal were temporally symmetric and equal to 5 ms.

The first reaction of the myocardium after the biphasic impulse was the appearance of depolarisation fronts at both ends. The most interesting feature of this phase was the magnitude of V_m near to the border of the bath medium. A



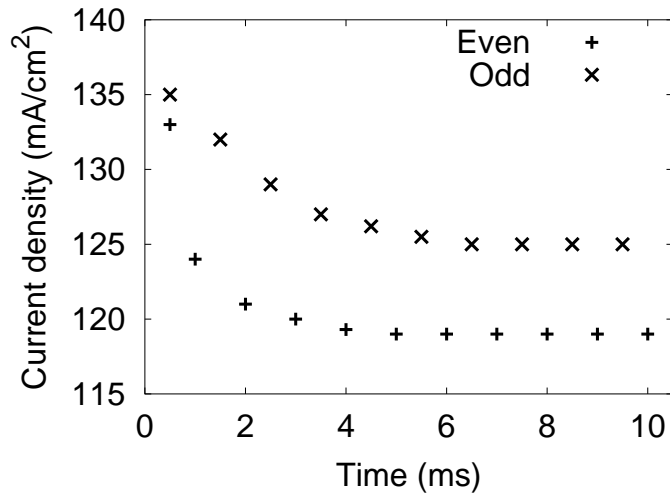
(a)



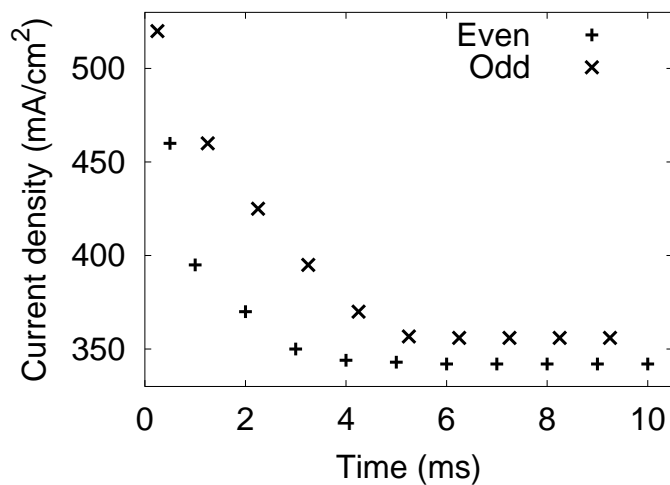
(b)

Figure 7.17: Excitation thresholds for biphasic stimulation of a continuous wedge of myocardium corresponding to a) 500 Hz and b) 1 kHz

strongly hyperpolarization was induced in the cases with a too high magnitude of the second phase. The depolarisation front was not able to annihilate it. In the other cases the tissue reached the isopotential state after approximately 150 ms. The time course of the transmembrane voltage was followed until complete repolarisation. For identifying further differences between various signals, the time needed in each case for the tissue to get from one state (resting, depolarized, repolarized) to another was recorded and compared. The time intervals corresponding to complete depolarisation and total repolarisation can



(a)



(b)

Figure 7.18: Excitation thresholds for biphasic stimulation of a continuous wedge of myocardium corresponding to a) 2 kHz and b) 4 kHz.

give a measure whether a defibrillation shock will be successful or not.

For sinusoidal and exponentially decaying signals always less time was needed for achieving complete depolarisation and total repolarisation in comparison to the rectangular ones. The time intervals could be further decreased by increasing the ratio between the magnitudes of the first and second phase of the electric signal. For example, a rectangular signal of ± 1 V in both phases induced the complete depolarisation in 90 ms and total repolarisation in 450 ms. A rectangular signal of ± 2 V in first phase and ± 1 V in the second one induced

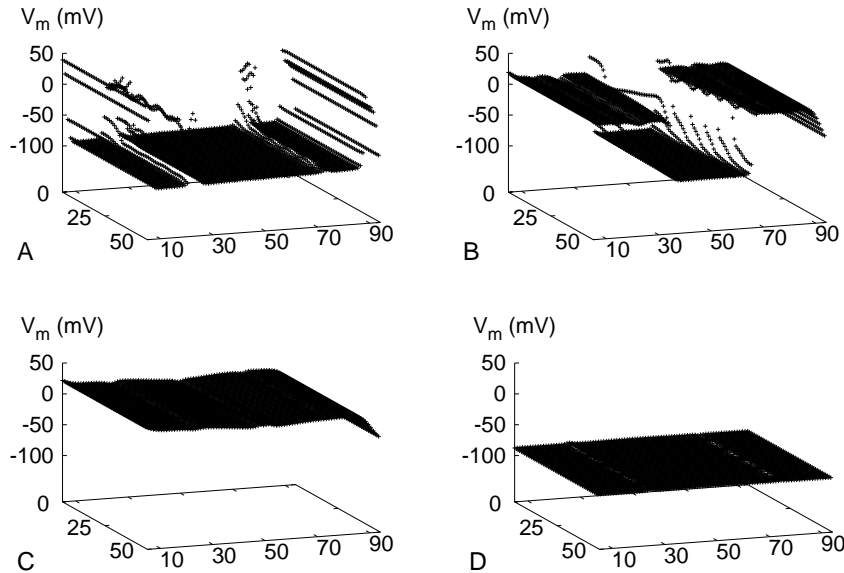


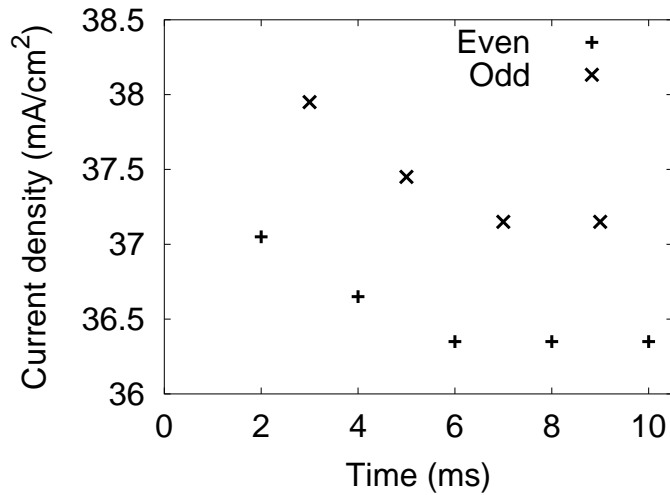
Figure 7.19: Biphasic stimulation of a fragmented wedge of myocardium. The transmembrane voltage distribution is presented at: a) 5 ms, b) 15 ms, c) 37 ms, d) 342 ms.

the complete depolarisation in 85 ms and total repolarisation in 440 ms. The shortest myocardial phases corresponded to the exponentially decaying signal with the magnitudes maxima fixed at ± 3 V and ± 1 V.

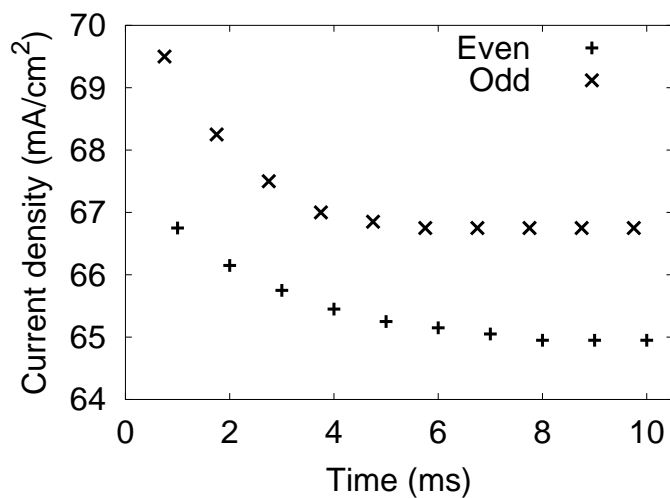
The research was continued with the stimulation of the myocardium with biphasic impulses of higher frequencies: 500 Hz, 1 kHz, 2 kHz and 4 kHz. The myocardium was repeatedly stimulated with electrical impulses of various intensities until the excitation thresholds were identified. For 500 Hz stimuli for both even and odd numbers of pulses the values of the excitation thresholds varied in a range of (36, 38.5) mA/cm² (Fig. 7.20 a). The interval was broader for higher frequencies. For 1 kHz, 2 kHz and 4 kHz excitation thresholds were included in the interval (63, 67) mA/cm², (117, 135) mA/cm² and (330, 520) mA/cm², respectively (Fig. 7.20 b, Fig. 7.18 a, b).

Biphasic Stimulation of Myocardium Fragmentized by Cleavage Planes Another objective of the biphasic stimulation study was to understand the phenomena related to tissue discontinuities. For the research, the model with interlaminar clefts between layers of cardiomyocytes was used.

After the application of ± 1 V, 100 Hz biphasic stimuli with rectangular waveform, the intramural myocardium was depolarized by secondary sources created near to the cleavage planes. The side area closest to the anode was depolarized, while the opposite one was hyperpolarized (Fig. 7.19). The myocytes depolarized by secondary electrical sources presented a lower V_m than the myocardial layer beneath the cathode. When the entire tissue was depolarized, the section that was initially hyperpolarized presented the lowest V_m ,



(a)



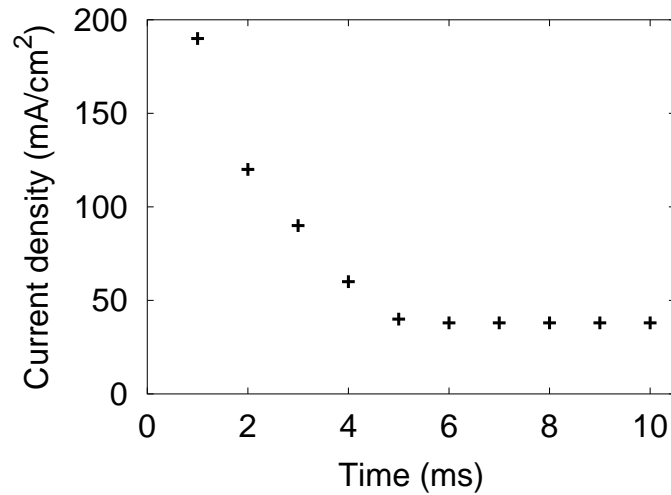
(b)

Figure 7.20: Excitation thresholds for biphasic stimulation of a wedge of myocardium containing interlaminar clefts corresponding to a) 500 Hz and b) 1 kHz

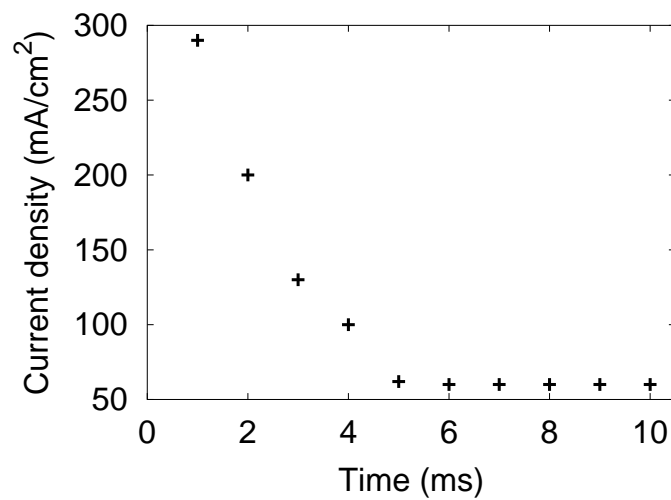
even though it had a positive value. The formation of additional depolarisation fronts simultaneously with primary electrical sources, implied a reduction of the temporal length of the myocardial phases.

Inverting the polarity of the electrical impulse did not modify the electrical behavior of the intramural region.

The excitation threshold of an impulse for the fragmentized myocardium was the weakest electrical stimulus inducing secondary electrical sources near



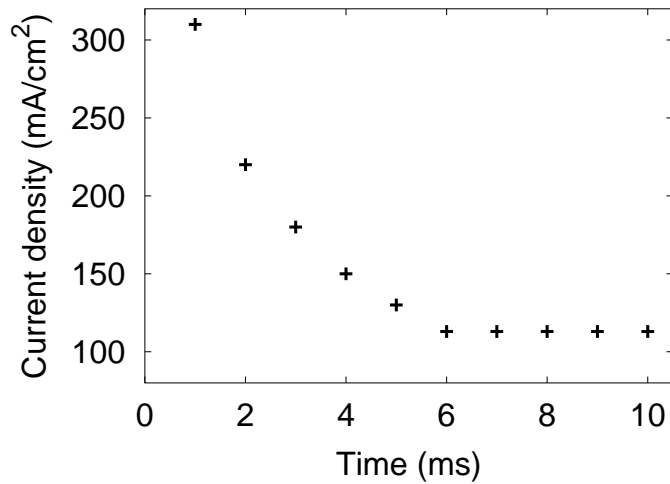
(a)



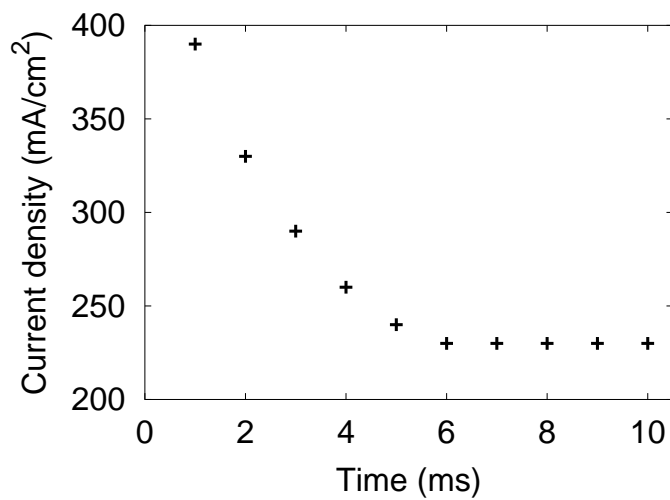
(b)

Figure 7.21: Excitation thresholds for monophasic stimulation of a continuous wedge of myocardium corresponding to a) 500 Hz and b) 1 kHz

to both cleavage planes. The excitation thresholds of the tissue intersected by cleavage planes were theoretically recorded for 500 Hz and 1 kHz. Fig. 7.20 a, b is shown that the excitation thresholds are included in the intervals (36.3, 38) mA/cm² and (65, 69.8) mA/cm² for 500 Hz and 1 kHz. The differences between the rheobases of even and odd numbers of pulses were equal to 0.95 and 1.75 mA/cm² for 500 Hz and 1 kHz.



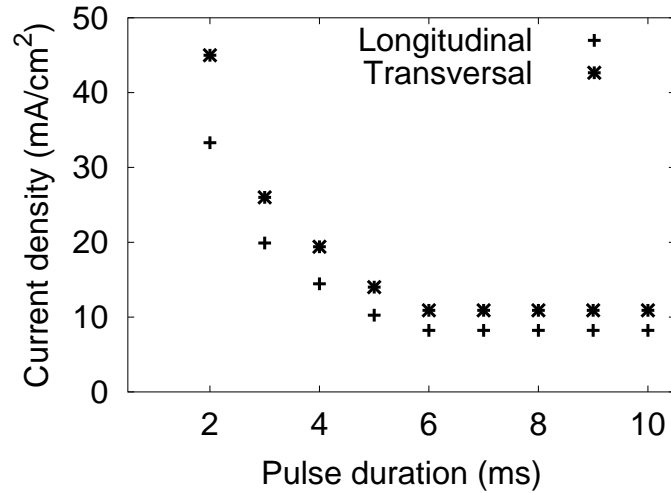
(a)



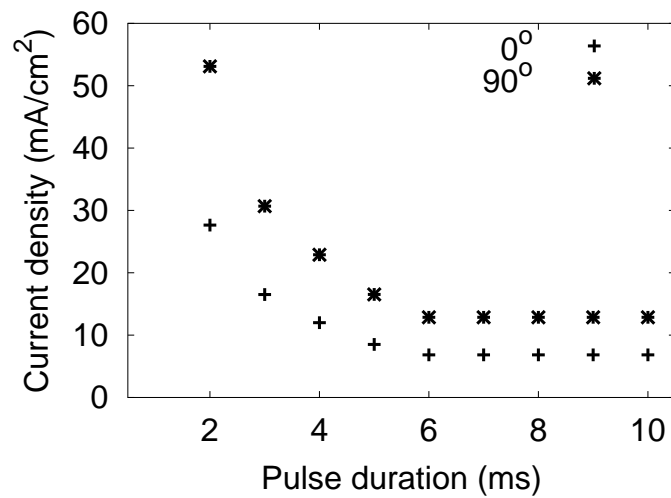
(b)

Figure 7.22: Excitation thresholds for monophasic stimulation of a continuous wedge of myocardium corresponding to a) 2 kHz and b) 4 kHz

Monophasic Stimulation of the Myocardium During the investigation of the reaction of the continuous myocardium to monophasic electrical stimuli, the wave form illustrated in Fig. 7.1 b) was utilized. The rheobase corresponding to 500 Hz was equal to 43 mA/cm² (Fig. 7.21 a). For stimulations shorter than 5 ms the excitation threshold increased inversely proportional with the duration. The maximum value (192 mA/cm²) was recorded for 1 ms stimulus duration. For 1 kHz, the rheobase was equal to 52 mA/cm² (Fig. 7.21 b). The maximum excitation threshold value, corresponding to the frequency of 1 kHz was of 291



(a)



(b)

Figure 7.23: Excitation thresholds for monophasic transversal and longitudinal stimulation of a continuous wedge of myocardium with a) realistic fiber twist, b) straight fibers. The differences between the strength-duration curves indicate the dependencies on the excitation path. The lowest values were recorded for 0° , a nonexistent type of myocardium in reality. In the tissue with realistic fiber twist the longitudinal stimulation was lower than the transversal variation.

mA/cm^2 . At 2 kHz, the value of the rheobase was almost the double of the one specific to 1 kHz (Fig. 7.22 a). The excitation threshold started to increase stronger for stimuli shorter than 6 ms and for the stimulus with 1 ms duration and 2 kHz frequency it had the value equal to $309 \text{ mA}/\text{cm}^2$. For 4 kHz the excitation threshold varied in the interval $(219, 395) \text{ mA}/\text{cm}^2$ (Fig. 7.22 b).

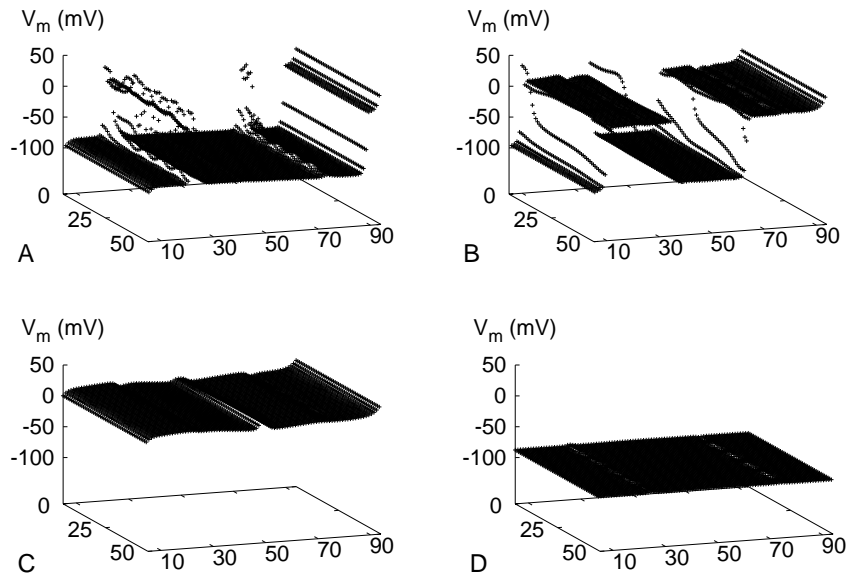


Figure 7.24: Monophasic stimulation of a fragmented wedge of myocardium. The transmembrane voltage distribution is presented at: a) 5 ms, b) 20 ms, c) 45 ms, d) 360 ms. The pictures show that the cleavage plane farthest away from the cathode induces the strongest secondary electrical source.

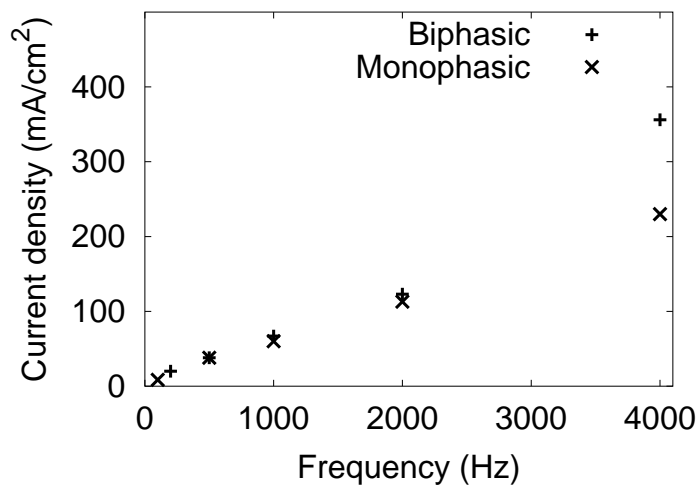


Figure 7.25: Comparison between excitation thresholds of 5 ms long biphasic stimulations of different frequencies for a continuous wedge of myocardium.

In Fig. 7.23 are illustrated the excitation thresholds for single-pulse monophasic transversal and longitudinal stimulation. The myocardial preparations used in the investigation were composed of realistically rotating or straight fibers. The differences between the strength-duration curves indicate the dependencies on the excitation path. The lowest values were recorded for 0° , a nonexistent type of myocardium in reality. The nearest to the minimal exci-

tation thresholds were obtained by stimulating longitudinally the tissue with realistic fiber twist. For pulse durations longer than 6 ms, the excitation thresholds corresponding to longitudinal stimulation were only 30% smaller than for transversal configuration. At 2 ms the difference is of 50%.

The next investigated problem was the influence of the cleavage planes on the excitation thresholds. The stimulation of the fragmented myocardium with various frequencies can induce the formation of secondary electrical sources near the cleavage planes (Fig. 7.24 a). The excitation spread from the centre of the tissue towards the exterior and vice-versa leading to complete depolarisation at 45 ms (Fig. 7.24 b, c). At 360 ms the entire tissue was resting.

Fig. 7.25 illustrates the variation of the rheobase with frequency for both mono- and biphasic electrical stimulations of the continuous myocardium. The excitation thresholds of monophasic stimuli are lower than for biphasic signals. Even though the difference was almost neglectable for low frequencies, at 4 kHz it was approximatively equal to 100 mA/cm^2 .

Discussion The investigation of the influence of electrical stimuli characteristics on the formation of the cardiac response started at the microscopic level. The variation of the gate parameters of I_{Na} presented distinct profiles for biphasic and monophasic stimulation. The value of the m gate parameter presented fluctuations around the time average increasing slope. The temporal length of the fluctuations corresponded to the frequency of the applied stimulus. Once the V_m was higher than -40 mV the oscillations disappeared and the slope of V_m became steeper. The reaction of the cell demonstrates that the theory presented by Roberts et al. [98], according to which the biphasic shocks higher than 200 Hz would not be efficient due to the capacitive behavior of the membrane is false. The application of monophasic stimuli induced a continuous enhancement of V_m and m during the application of the electrical shock, even while the amplitude of the signal was zero. The success of the stimulation depended mainly on the velocity of the V_m and m variation.

The excitation thresholds of monophasic stimuli were lower than the ones of biphasic impulses, for each studied frequency. Nevertheless, experiments have proven that biphasic stimulation is more efficient [99]. Keener and Lewis, suggested that the biphasic stimulus is successful because the activation threshold is lowered by an initial hyperpolarization [100]. The simulations with the virtual human myocyte indicated a faster variation of V_m post-hyperpolarization than the one associated to the resting cell. But the excitation threshold corresponding to the biphasic stimulus with an initial negative amplitude is higher than for the case with inverted polarities. Since the monophasic stimulations indicated that the velocity of V_m variation is strongly dependent on the intensity of the impulse, we conclude that the theory presented by Keener and Lewis is not sustained by the simulations done with a human ventricular myocyte. The investigations of frequencies up to 4 kHz also indicated that the excitation threshold must be higher if the first pulse is negative.

The stimulation of the cell with rectangular and truncated exponential pulses indicated that the waveforms corresponding to the higher energy present

the lowest excitation threshold.

The outcomes of the fitting of the simulations results with Weiss-Lapicque and Blair laws are very similar to the ones obtained by Mouchawar et al., who compared the strength duration curves with experimentally obtained data from the dog heart [101]. In conclusion, both Weiss-Lapicque and Blair fits are better for short duration stimulation and they underestimate the rheobase. From the two laws Blair's relation proved to be the most accurate one.

For a better understanding of the differences between monophasic and biphasic stimulations the investigation was continued on virtual sections of the human left ventricle.

All along the study the reaction of resting tissue to an electrical shock was shown. The results reflect the way a healthy tissue reacts, therefore it is helpful for getting a general fundamental understanding of the phenomena. Information gathered in this section is used in following sections, presenting the effects of the electrical shocks on fibrillating tissue.

The data obtained from our simulations showed that the sinusoidal and the exponentially decaying signals were more efficient in exciting a tissue than the rectangular ones, due to a lower hyperpolarization induced during the first phase. It was observed that a very strong hyperpolarization induced through the second phase of the electrical shock may lead to a failure of the therapy. The result indicates that the magnitude of the second phase of the electrical shock has to be smaller than the magnitude of its first phase. Nevertheless, the magnitude has to be high enough to produce depolarisation fronts at both ends. The excitation threshold was for all studied frequencies higher when the number of the pulses was odd than for even numbers. The strength-duration curves for monophasic stimuli was lower than for any kind of biphasic stimuli. The comparison of the reactions of the myocardium to the two types of stimuli reflects some of the causes that can lead to the failure of complete depolarisation when monophasic impulses are applied. The results indicate that it is recommended to create depolarisation fronts uniformly distributed in space for producing secondary electrical sources in the intramural region. A planar depolarisation front is activating the areas near to the cleavage planes much easier. Normally, a fibrillating tissue has already some refractory regions, so a depolarisation produced at both ends would increase the chance of the entire tissue to be depolarized. Therefore, a biphasic stimulus can induce the formation of more secondary electrical sources than a monophasic one.

In conclusion, the results indicate that the biphasic stimuli are more efficient than the monophasic ones due to the myocardial structure.

7.2 Electrode Characteristics

The average current density increases inversely with the area for a constant total current of the electrode. At the same time a smaller electrode could be correlated to a decreased amount of excited tissue during the stimulation duration.

Even though the electrode characteristics have been intensively researched,

Configuration number	Electrodes size (mm ²)	Position of anode	Position of cathode	Corresponding figure
1	1310.4	top	apical border	Fig. 7.26 a
2	80	bottom left endocardium	top right epicardium	Fig. 7.26 b
3	840	y=maximum	y=minimum	Fig. 7.26 c
4	80	y=maximum, bottom	y=minimum, top	Fig. 7.26 d
5	1080	x=maximum top	x=minimum bottom	Fig. 7.26 e
6	1080	centred, parallel to epicardium	centred, parallel to endocardium	Fig. 7.26 f
7	40	x=minimum z=0	x=maximum z=0	Fig. 7.26 g

Table 7.1: Configurations used in the investigation of electrode characteristics

a unified theory does not exist to predict the effect of the electrode area on the excitation/defibrillation thresholds. Such a theory could not be formulated until present because the corresponding phenomena have not been completely identified. The results presented in this section present an insight on the influence of electrode characteristics on internal defibrillation.

Materials and methods For the investigations a curved section of the human left ventricle was utilized. The characteristics of the myocardial preparation were described in detail in Sect. 6.1.3.

As a selected condition, the myocardium was in the resting phase before it was activated by the electrical shock. A pair of rectangular electrodes were placed in the immediate vicinity of the myocardium. Their orientation and area varied from case to case. The chosen configurations of the electrodes are described in Table 7.1 and illustrated in Fig 7.26.

The duration of the applied electrical shock was 10 ms. For the investigation of the correlation between the excitation patterns and the electrodes locus the amplitude of the electrical impulse was 200 mV. For the study of the dependence of the excitation thresholds on paddles positions 1 kHz and 2 kHz stimuli with various intensities were applied.

The calculation time step is 10 μ s. The simulations were performed on a 2 GHz Power Mac G5. The average time needed for each computation was 150 hours.

Results The simulations revealed that virtual electrode polarization (VEP) plays an important role. The surface of the tissue immediately depolarized after the start of the electrical shock was larger than the surface beneath the cathode. If the subendocardial or subepicardial region was not directly excited

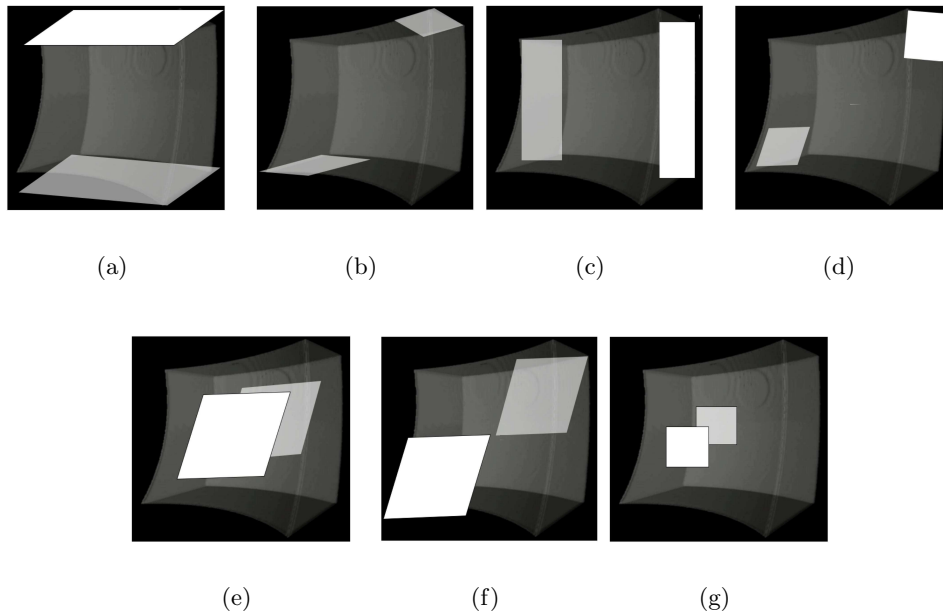


Figure 7.26: Models of the chosen configurations of electrodes for the study.

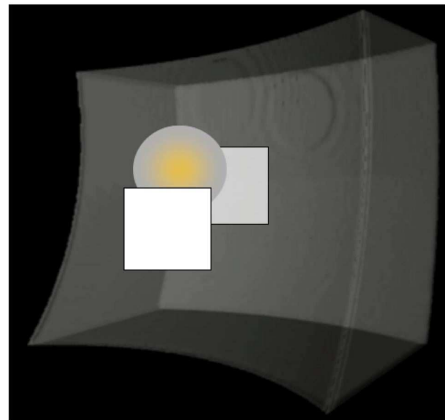


Figure 7.27: Schematic representation of the displacement of the most affected area by electrical stimulation. Due to the varying tissue curvature and fiber orientation the center of the most affected region (marked with yellow) appears above the median of the paddles.

by the stimulus originated from the cathode, then secondary electrical sources were formed. The further evolution of the myocardium was described in detail in Sect. 6.1.3. Immediately after the stimulation, even though all the myocytes composing the subendocardium and the subepicardium were depolarized, a part of the cells presented a higher V_m than the rest. When the electrodes were parallel to the endo- and epicardial surfaces, the cells with the highest V_m , were localized in the subendocardial and subepicardial regions. Due to the varying tissue curvature and fiber orientation the center of the most affected region by the electrical stimulation did not intersect the median of the paddles. For

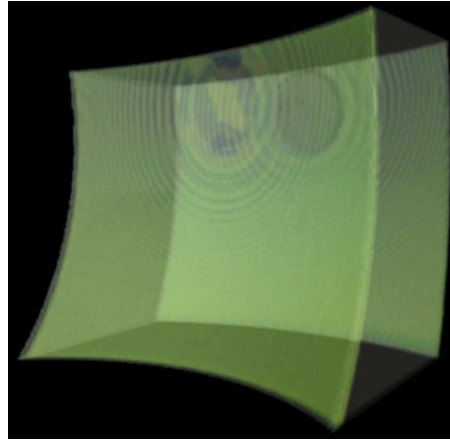


Figure 7.28: Displacement of the area most affected by the electrical stimulation. The enlargement of the electrodes size amplified the transmembrane voltage differences and the distance between the centre of the most affected region and the median of the paddles. Same colour code as in Fig. 6.6.

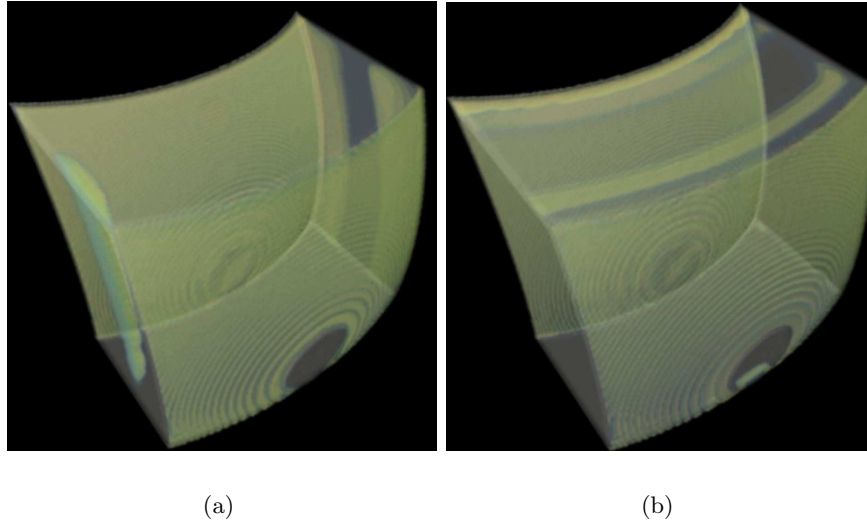
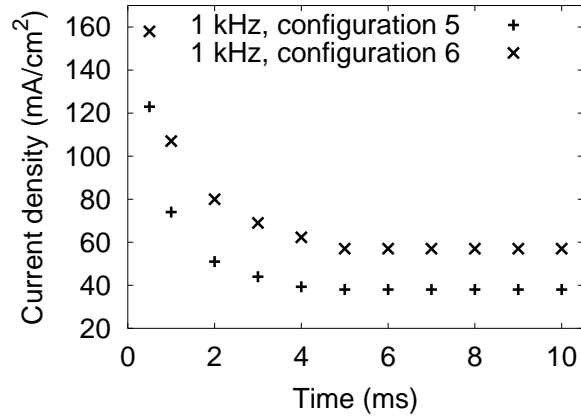
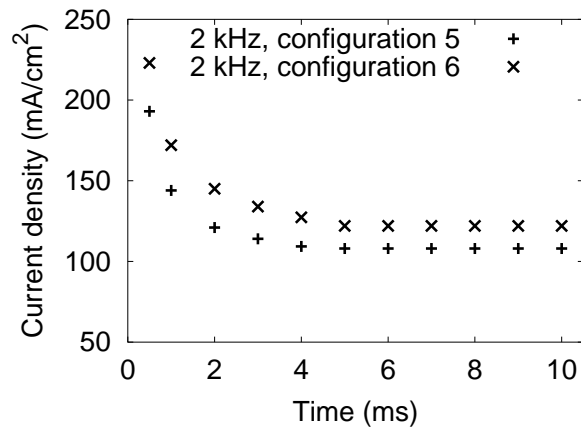


Figure 7.29: Distribution of the transmembrane voltage at 5 ms, in a heterogeneous left ventricle myocardium beneath the electrodes oriented perpendicular on endo- and epicardial surfaces. Same colour code as in Fig. 6.6.

the 7th configuration, the centre of the myocytes with the highest V_m was 3.2 mm above the median of the two electrodes (Fig. 7.27). The difference between the highest V_m and the average value of V_m corresponding to the rest of depolarized myocytes was equal to 7 mV. For the 5th configuration, in which larger electrodes were applied, the V_m difference was equal to 23 mV and the displacement was of 4.8 mm (Fig. 7.28). The centre of the most affected area had an oval form, with the same orientation as the myocytes forming the region where it appeared and it was surrounded by hyperpolarization. At the frontier between the hyperpolarized and normally depolarized myocytes in four small



(a)



(b)

Figure 7.30: Excitation thresholds corresponding to 1 and 2 kHz stimulation for stimulation applied along (configuration 5) and across (configuration 6) the fibers. For both frequencies the excitation threshold were elevated when the stimulation was not along the fibers. The difference increased for stimuli with short durations.

areas, the myocytes presented a V_m higher than average. The more intense depolarisations corresponded to the corners of the rectangular electrodes.

In the configurations with paddles perpendicular on the endo- and epicardium (Fig. 7.26 a, b, c, d), the most affected myocytes were localized beneath the electrodes. The vertically placed electrodes induced both hyperpolarization and depolarisation beneath both primary electrical sources (Fig. 7.29 a). In the central region under the cathode, the tissue was depolarized and it was surrounded by hyperpolarization. Beneath the anode, the distribution of positive

and negative V_m was inverted. The stimulation of the tissue through horizontally placed electrodes induces similar hyperpolarization-depolarisation patterns as in the cases with vertically oriented electrodes. The differences occurred at 3 ms, when the depolarisation, that was surrounded by hyperpolarization was extinguished. The depolarisation formed at the extremes spread further together with the excitation initiated in the subendocardial and subepicardial regions (Fig. 7.29 b). The variation of the electrodes sizes modified the ratios between the depolarized and hyperpolarized regions and also the V_m of the myocytes corresponding to these areas.

The study of the excitation thresholds for the electrodes placed in bath as described in configurations 5 and 6 indicated differences in the reaction of the myocardium connected to the shift of the electrodes (Fig. 7.30). Both for 1 and 2 kHz the excitation thresholds were lower when the stimulation was along the fiber. The differences induced by the shift of the electrodes were stronger for the higher frequency and shorter impulse durations.

Discussion The study showed that the initiation of depolarisation near to endocardium and epicardium is invariant to the position in which the bath electrodes were placed. Supplementary regions from which depolarisation spread were observed when one of the electrodes was placed at the apical border of the myocardium while the other one was fixed at its top. The additive effect implied the shorting of the time needed until the myocardium was overall depolarized. According to this aspect such electrodes configuration can increase the defibrillation efficiency.

In all cases, the most excited cells appeared next to hyperpolarized myocytes. The distribution of depolarized-hyperpolarized areas depended on the size and the orientation of the paddles. Similar types of results were experimentally obtained by Knisley et al. [78].

7.3 New Defibrillation Procedure: Electrodes Array

In the previous sections was shown that the excitation threshold is higher for biphasic than for monophasic shocks. Nevertheless, the biphasic shocks present the advantage that they induce the occurrence of depolarisation fronts at two sides of the cardiac wedges. Considering the disadvantages correlated to the high electrical shocks therapy, like cells uncoupling and electroporation, a new defibrillation procedure was proposed [76].

The nominated method consists of the utilization of spatially alternated electrodes polarity. The efficiency of the proposed technique was investigated on a virtual wedge of human myocardium. The characteristics of the utilized preparation are presented in Sect. 6.1.1.

The electrodes were placed at the ends of the longest (Z) axis (Fig. 7.31). We studied both the case in which the electrodes were placed directly on the tissue and the case in which the electric signal had to pass through a blood medium before reaching the myocardium. The electrical shock was applied to

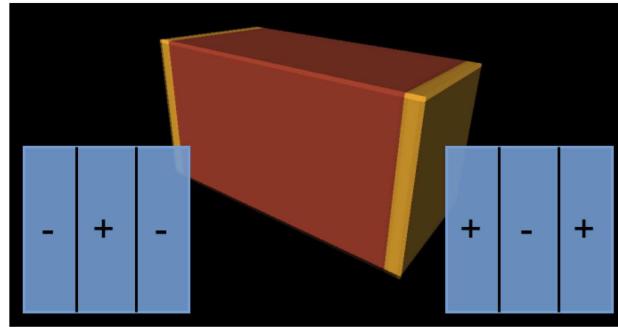


Figure 7.31: Electrodes array configuration. The arrangement presents a spatial alternation of the electrodes polarity, inversely configures at the opposite end. At the left end were placed more electrodes with negative polarities than at the right one.

the myocardium through rectangular electrodes, having alternating polarities. The number of electrodes was odd and varied between 3 and 49. At the left end were placed more electrodes with negative polarities than at the right one. The absolute value of the electric signal was the same all along the XY surface, but the polarity was changed.

The magnitude of the electric impulse was included in the interval (0.01, 7) V. The defibrillation shock was always applied for 1 ms. The temporal evolution of V_m was followed in all cases for 500 ms. This time interval is 100 ms longer than the action potential duration, meaning that we were able to gather data from all tissue phases.

An optimal excitation range was searched by varying the number of the alternating electrodes and the magnitude of the electrical signal.

Results The numerical simulations indicated that both too intense and too weak stimuli cause side effects. When the amplitude of the electrical defibrillation shock was too low the depolarizing front did not advance towards the centre of the cardiac muscle. The depolarisation threshold increased with the number of alternating electrodes.

When the magnitude of the defibrillation shock was too high the hyperpolarized areas remained unexcited.

According to the geometrical features of the myocardial preparation and the selected stimulation configuration XZ was a symmetry plane for the V_m spatial distribution. The following pictures, illustrating the variation of V_m correspond to the mediator plane of Y axis.

First was investigated the case with 3 electrodes placed at the ends of the Z axis of the myocardium (Fig. 7.32, Fig. 7.33).

1 ms after stimulation, the configuration with the electrodes placed directly on myocardium presented the depolarisation of the myocytes neighboring the cathodes and hyperpolarization near the anodes (Fig. 7.32 a). The electrical signal propagated in the tissue like light, which passes through slots. Hence the depolarized areas were larger than the surfaces of the cathodes. At 5 ms, the hyperpolarized myocytes were depolarized (Fig. 7.32 b). The initial nonuniform

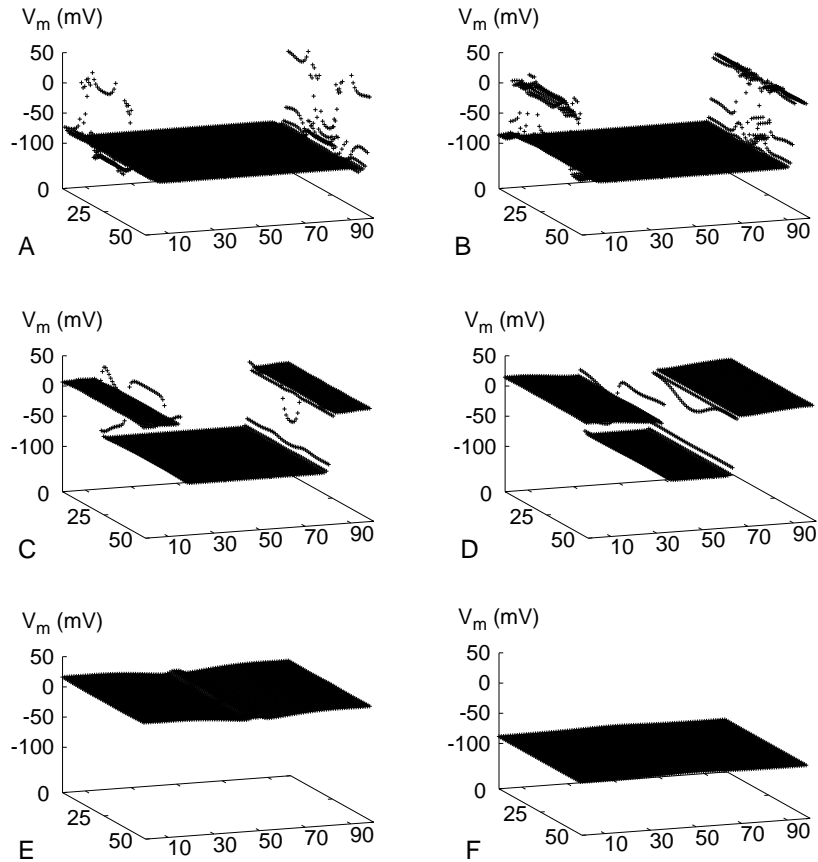


Figure 7.32: Transmembrane voltage, V_m as a function of distance, measured in voxels, in a cardiac tissue after a (± 0.2 V) electric signal is applied through a 3 electrode array: A) 1 ms; B) 5 ms; C) 25 ms; D) 55 ms; E) 80 ms; F) 445 ms;

distribution of the depolarisation front diminished with time (Fig. 7.32 c, d). At 80 ms the two depolarisation fronts reached the centre of the myocardium (Fig. 7.32 e) and at 445 ms all the myocytes were in the resting phase (Fig. 7.32 f). The optimal impulse had the amplitude of 0.2 V.

When the electrodes were placed in bath the extracellular potential was redistributed. In the first 5 ms a larger percentage of myocytes was depolarized at the left than at the right end of the preparation (Fig. 7.33 a, b). At both ends of the longest axis depolarisation fronts appeared (Fig. 7.33 c, d). The excited surfaces were smaller than the areas of the cathodes. At 85 ms the myocardium was completely depolarized (Fig. 7.32 e) and at 450 ms V_m had the resting phase value (Fig. 7.33 f). The optimal strength of the electrical stimulus was 5 V for this configuration.

The studied case with the largest number of alternating stimuli applied a 49 electrode array. At the right end 25 electrodes with negative polarity and 24 with positive polarity were placed. At the left end the arrangement was

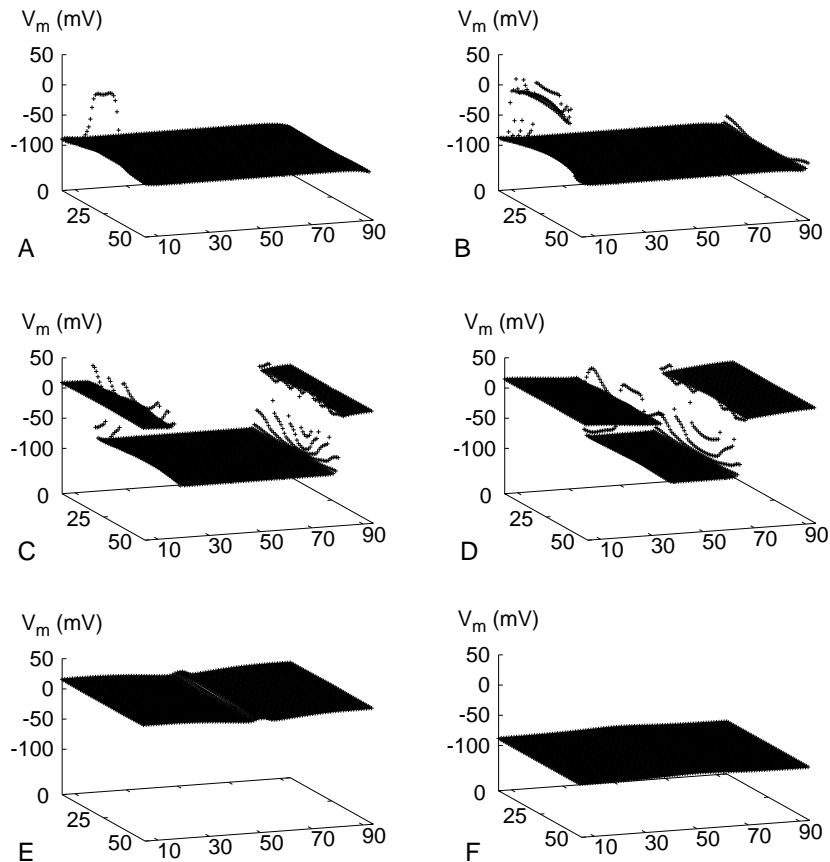


Figure 7.33: Transmembrane voltage, V_m as a function of distance, measured in voxels, in a cardiac tissue, which is incorporated in blood medium after a (± 5 V) electric signal is applied through a 3 electrode array: A) 1 ms; B) 5 ms; C) 25 ms; D) 55 ms; E) 85 ms; F) 450 ms.

inverted.

When the electrodes were placed directly near to the myocardium the optimal value for the extracellular potential was 0.3 V. 1 ms after the defibrillation shock was applied depolarizing fronts were produced at both ends of Z axis (Fig. 7.34 A, B). The depolarisation spread in the tissue with same velocity from both directions (Fig. 7.34 C, D). After 85 ms the complete depolarisation phase was reached (Fig. 7.34 E). The time necessary for the tissue to regain the resting phase was 445 ms (Fig. 7.34 F).

The spatial gradient of the electrical signal, passing through blood medium was decreased. Because the depolarizing front was spreading only from the right side, where a higher number of positive stimuli was delivered (Fig. 7.35 a, b). Under these circumstances the time needed for the entire tissue to be entirely depolarized was 155 ms. This prolonged the time needed by the tissue to get into the resting phase to 480 ms. The optimal value for the extracellular potential was in this case 6 V.

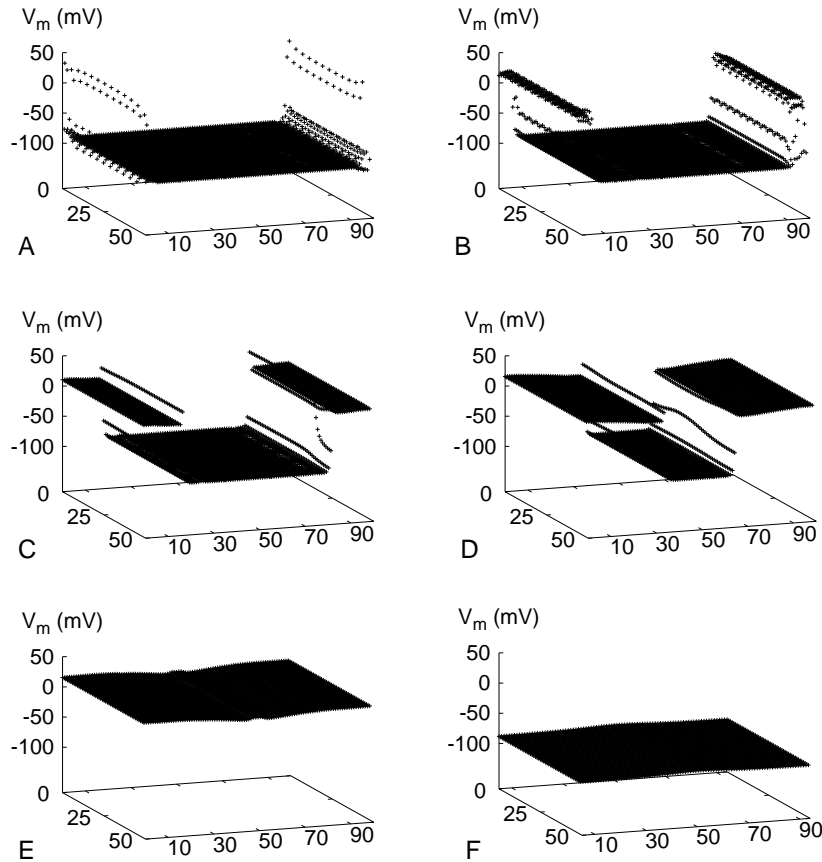


Figure 7.34: Transmembrane voltage, V_m as a function of distance, measured in voxels, in a cardiac tissue after a (± 0.3 V) electric signal is applied through a 49 electrodes array: A) 1 ms; B) 5 ms; C) 25 ms; D) 55 ms; E) 85 ms; F) 450 ms.

Figure 7.36 indicates that the excitation thresholds was almost constant as long as the number of electrodes was smaller than 20 and afterwards it increased faster and faster with the number of the electrodes. The values of the excitation thresholds were 10 times larger when placed in bath than when located near to the tissue.

Discussion The simulations done on the three-dimensional myocardial tissue showed that using an electrode array, depolarisation fronts in the neighbourhood of both electrically stimulated areas can be induced. In this way at least 5 ms, which are the typical period after which the polarity of the biphasic defibrillation shock is inverted, are saved.

The decisive differences between the models were formed in the first 5 ms. The evolution of the myocardium was continuously observed, until the magnitude of the transmembrane voltage in all cardiac myocytes had the value -80 mV. The limit is showing the beginning of the resting phase. The comparison

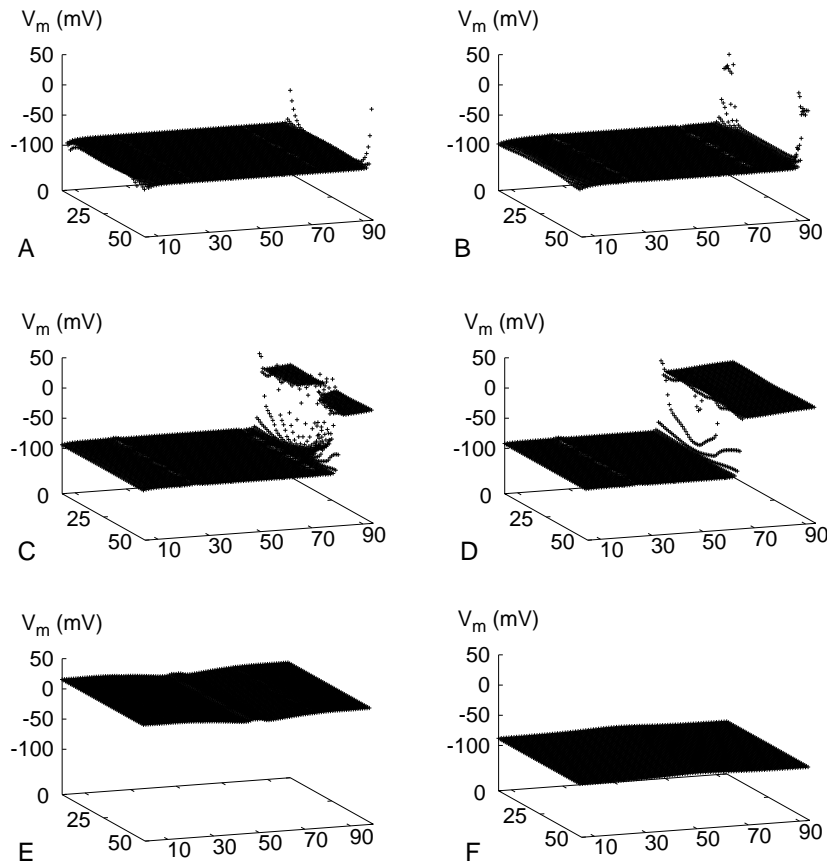


Figure 7.35: Transmembrane voltage, V_m as a function of distance, measured in voxels, in a cardiac tissue, incorporated in blood medium, after a (± 6 V) electric signal is applied through a 49 electrode array: A) 1 ms; B) 5 ms; C) 25 ms; D) 55 ms; E) 155 ms; F) 480 ms.

done between cases with different numbers of electrodes revealed that if the size of the electrode is too small the chance of the electric signal to penetrate the myocardium is decreased. According to the obtained results, an arrangement with a small number of electrodes with alternating polarities could increase the defibrillation chance.

7.4 Electrical Stimulation Moment

This section is concerned with the influence of defibrillation moment on a fibrillating human ventricular myocardium. Presently, both the external and the internal defibrillators deliver the electrical shocks at a moment independent of the fibrillating patterns. In an ICD is integrated an ECG recorder and interpreter necessary for determining whether an electrical shock must be applied or not. This component of the ICD can be adapted to identify if the fibrillation presents a periodicity. This would enhance the possibility of delivering the

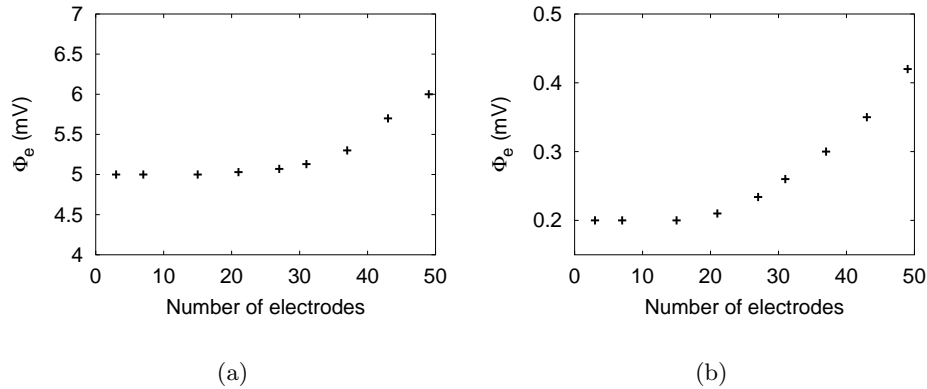


Figure 7.36: Variation of excitation threshold with the number of electrodes. The primary electrical sources are placed a) directly near to myocardium, b) in blood medium. The excitation thresholds increase with the number of the electrodes and are 10 times larger when placed in bath than when located near to the tissue.

defibrillation shock at the most efficient moment.

The proposed setup was tested on a large three-dimensional virtual wedge of the human left ventricular myocardium. The constructional aspects were described in detail in Sect. 6.1.2. Comparisons between continuous and laminar cardiac muscles (Sect. 6.5) are made.

In order to obtain a good view on the influence of the moment in which the defibrillation is applied, the amplitude of the electrical shock was kept constant at ± 3 V. At selected moments the effects of cathodal-anodal arrangements were investigated (Fig. 7.37).

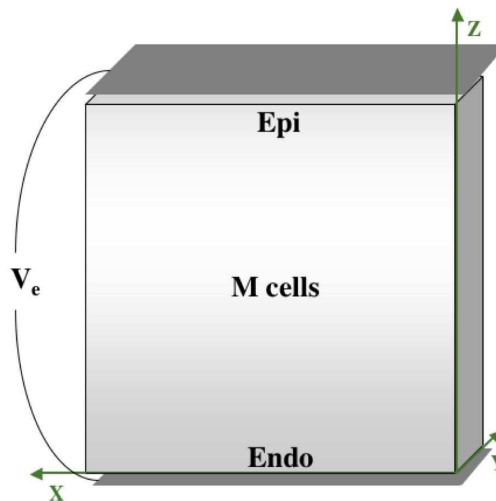


Figure 7.37: The placement of defibrillation paddles used in the investigation of electrical stimulation moment. In half of the cases the cathode was placed near to epicardium and the anode near to endocardium. In the other half the arrangement of the electrodes was inverted.

Simulation Parameters For gaining the derived results, 24 simulations with a three-dimensional virtual wedge of cardiac tissue were done. In half of them continuous myocardial media were used and otherwise tissues fragmented by cleavage planes were utilized. In each case 500 ms of the post defibrillation electrocardiac behavior were simulated. The numerics were performed on a 2 GHz dual processor Power Mac G5. The average time needed for each computation was 95 hours.

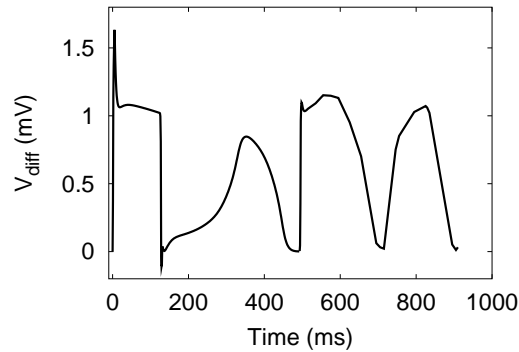


Figure 7.38: The simulated ECG of the fibrillating human ventricular myocardium.

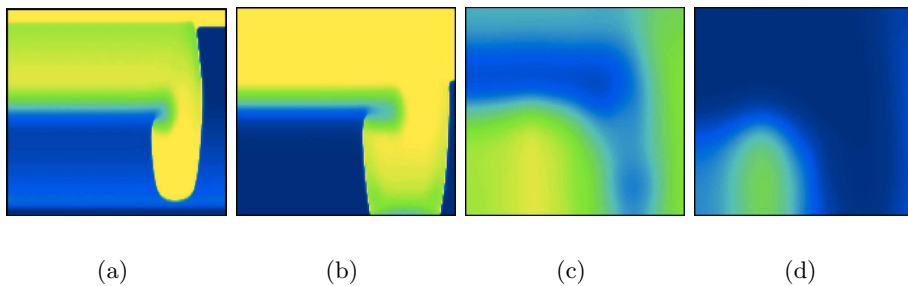


Figure 7.39: Variation of transmembrane voltage in a continuous myocardium after the 450 ms defibrillation. Distribution corresponding to a) 458 ms, b) 480 ms, c) 700 ms, d) 790 ms. The pictures reflect the utilized electrodes configuration: cathode top and anode bottom. The electrical shock modifies the excitation pattern is a small percentage, sufficient for a successful defibrillation. Same colour code as in Fig. 6.6.

Results In the study fibrillating cardiac preparations were utilized. A spiral wave was induced in the myocardium with two electrical stimuli: a baseline driving stimulus (delivered in the first ms of the simulation) and a premature stimulus (390 ms) (Fig. 6.6). The procedure is known under the term $S_1 - S_2$ protocol. The parameters of the spiral remained constant in time. Therefore, the simulated ECG presented a periodical pattern (Fig. 7.38). The fibrillation frequency was 5 Hz. Furthermore, a chaotically fibrillating state can be further induced in the human left ventricle myocardium by delivering a weak electrical

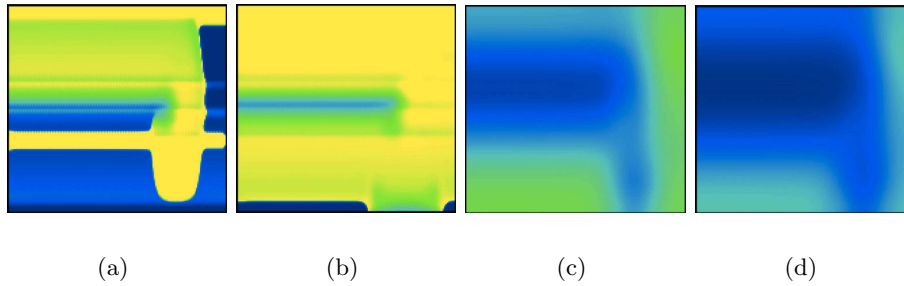


Figure 7.40: Variation of transmembrane voltage in a myocardium fragmented by 3 cleavage planes, after the 450 ms defibrillation. Distribution corresponding to a) 458 ms, b) 480 ms, c) 700 ms, d) 730 ms. The pictures reflect the utilized electrodes configuration: cathode top and anode bottom. The electrical shock induces the occurrence of secondary sources near the cleavage planes, thus strongly modifying the excitation pattern, leading to a successful defibrillation. Same colour code as in Fig. 6.6.

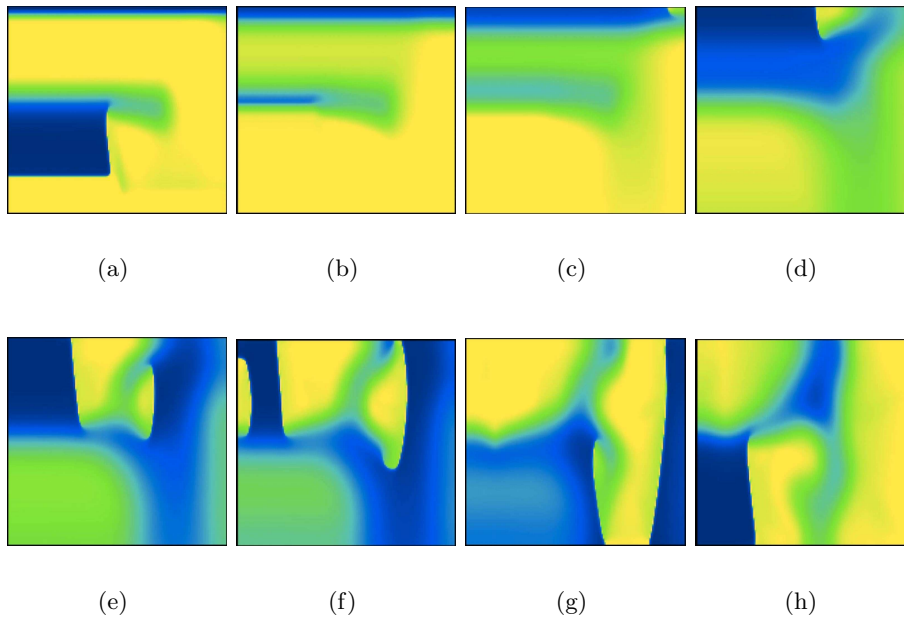


Figure 7.41: Variation of transmembrane voltage in a continuous myocardium after a 500 ms defibrillation. Distribution corresponding to a) 500 ms, b) 545 ms, c) 588 ms, d) 665 ms, e) 733 ms, f) 763 ms, g) 800 ms, h) 900 ms. The pictures reflect the utilized electrodes configuration: anode top and cathode bottom. The electrical shock induces a depolarisation front that propagates from the bottom towards the centre and a strong hyperpolarization at the top. At 588 ms the first reentry occurs at the right top corner. At 800 ms the second reentry is observable. At 900 ms the activity of the tissue is chaotic, marking the unsuccessful defibrillation. Color code similar to Fig. 6.6.

shock to the tissue. The effect of the additional impulse is that it forces the single spiral wave to split in more waves.

In a fibrillating myocardium, it is of high interest to observe the volume ratio

Defibrillation moment (ms)	Polarity	Number of reentries	Outcome of defibrillation	Resting moment (ms)
450	-+	0/0	success	870/ 790
450	+ -	1/1	success	800/800
500	-+	1/1	failure	-
500	+ -	3/1	failure	-
600	-+	2/1	failure	-
600	+ -	0/0	success	940/940
650	-+	0/0	success	980/ 1030
650	+ -	1/1	success	960/990
700	-+	1/1	failure	-
700	+ -	1/1	failure	-
800	-+	2/0	success	1200/1100
800	+ -	1/0	success	1180/1130
900	-+	1/1	failure	-
900	+ -	2/2	failure	-

Table 7.2: The reaction of human ventricular myocardium (continuous model/fragmentized model) to defibrillation.

of the tissue, which is immediately affected by defibrillation. Thus, the areas forming depolarisation fronts were identified. Some of the muscle discontinuities like blood vessels, collagenous septa and cleavage planes induce the appearance of secondary electrical sources. As it was previously predicted [102], when the distribution of the electrical current is not uniform (as in a fibrillating tissue case) only a part of the cleavage planes neighborhood is activated.

For better visualization, slices through the three-dimensional tissues are shown.

Fig. 7.39 illustrates the evolution of a continuous myocardium after a successful defibrillation. The electrical shock was applied at 450 ms. The cathode was placed at the top of the tissue and the anode was near the bottom. As an effect a supplementary excitation front propagated from the top towards the opposite end of the tissue (Fig. 7.39 a, b). 400 ms after the defibrillation the spiral wave is totally extinguished and the myocytes are resting.

The reaction of a myocardium fragmentized by cleavage planes after a defibrillation with the same characteristics as in the previously described case is illustrated in Fig. 7.40. Immediately after the deliverance of the electrical shock, secondary sources occurred near to parts of the cleavage planes (Fig. 7.40 a). 35 ms after defibrillation the entire tissue was depolarized (Fig. 7.40 b). Since no reentry appeared in the myocardium, at 730 ms the myocytes were resting (Fig. 7.40 c, d).

In Fig. 7.41 is shown the spatial distribution of V_m after an unsuccessful defibrillation applied at 500 ms. The anode was localized near the top and the cathode at the bottom. The myocytes under the anode were hyperpolarized. From the bottom propagated a depolarisation front towards the centre of the

tissue (Fig. 7.41 a, b). At 588 ms was observed the occurrence of a reentry (Fig. 7.41 c). The new excitation wave travelled towards the centre of the myocardium (Fig. 7.41 d, e). After the intersection with a refractory area the excitation wave splinted in two (Fig. 7.41 e, f). At 763 a second reentry was visible (Fig. 7.41 f). The propagation of excitation was limited by the refractory myocardial section (Fig. 7.41 g). 500 ms after the defibrillation of the tissue the excitation waves propagated chaotically in the tissue, marking the defibrillation failure.

The outcomes of the investigated cases are presented in Table 7.2.

Discussion The cleavage planes are an anatomical feature of the left ventricular myocardium. The cardiac wedges fragmented by cleavage planes manifest different reaction to electrical stimulation even if the tissue is fibrillating. When only a small part of the myocardium was depolarized by the fibrillating waves, a big part of the cleavage planes produced secondary sources. Under these circumstances, 100 ms difference was registered between the resting phase of the fragmented and of the continuous myocardium. These results underline that the existence of the cleavage planes significantly increases the defibrillation chances.

The results of the investigations illustrate that the number of the reentries varies with defibrillation moment and type of the chosen model. Just a part of the occurring reentries were strong enough to reinduce fibrillation. The rest was extinguished in time, leading to a successful defibrillation.

The defibrillation statistics together with the ECG fibrillation pattern indicate the optimal moments for the application of the therapy. The highest success was registered when the electrical shock was applied at the peak of the ECG up to 50 ms later. The defibrillation applied when V_{diff} presented the lowest value led to a substitution of the regular with a chaotic fibrillation.

7.5 Inferences

In this chapter the characteristics of electrical therapy were summed. Starting with an investigation on the features of the stimuli, the superiority of biphasic over monophasic signals for frequencies varying from 100 Hz to 4 kHz was shown. The higher efficiency of the biphasic impulses is not due to electrophysiology, but is connected with the temporal inversion of polarity. Based on this result a new defibrillation method was proposed. The utilization of a spatial alternation of the polarities can be more efficient than the standard biphasic therapy. When using an electrodes array the amplitude of the monophasic impulse can be lower and the stimulus duration shorter than it is necessary for a successful biphasic therapy. The comparisons made with monophasic impulses reflect some of the causes why standard biphasic stimulation can lead to the failure of complete depolarisation, like the effects of the induced hyperpolarization.

The study of the electrodes position yielded results, which are in concordance with experiments and reflected that beneath the electrode both hyperpo-

larized and depolarized regions exist. The ratio between these strongly depends on the size of the electrodes. The transmembrane voltage distribution in the layer beneath the electrodes is more homogeneous for circular paddles.

The modeling of defibrillation showed that a certain stimulus applied 50 ms or 100 ms later post-optimum moment may lead to a failure of the therapy. According to the importance of defibrillation moment it is concluded that the statistics formed from data of a limited number of animal experiments may be inaccurate.

The simulations were done in three-dimensional human ventricular myocardium, including a realistic fiber orientation and cleavage planes. All these features, put together form a very complex representation of the cardiac muscle. The clefts constitute one of the most important features of the left ventricular model. In the past they have been poorly studied from the electrical point of view [21]. Therefore it was necessary to understand the basic role of the cardiac microstructure in the response to electrical stimulation. If a fibrillation would be ongoing in the virtual myocardium an electrically chaotic behavior would be present. In such circumstances it would be very difficult to identify the exact influence of the cleavage planes. This information is needed in order to take a good decision if the clefts should or not be included in the defibrillation simulation of the fibrillating cardiac human heart.

The chances of the defibrillation success depend on many factors. This is why this chapter not only focused on the total excitation time of the modeled tissue, but also included identification of the depolarisation sources and excitation thresholds. These combined informations give a measure of how fast the myocardium can be brought in an electrically equivalent state.

8 Factors Modifying the Vulnerability to Electrical Shocks

One fundamental purpose of the cardiac research is the development of therapeutic methods. Defibrillation is one of the most studied cardiac therapies. The investigation of electrical shocks therapy must be extended to the factors modifying the vulnerability of the heart to the stimulation. Various circumstances can induce dysfunctionalities of the cardiac response. In the first section a new formalism describing in detail the electroporation is introduced. The second section summarizes different degrees of heart failure.

8.1 Electroporating Membrane

The enlargement of knowledge about electrical stimulation phenomena is essential for the development of cardiac interventional therapy. Electroporation defines the formation of pores in the cellular membrane under exposure to high electrical currents. The process constitutes a biotechnological tool, that can be applied for modifying the inner part of a cell. More explicitly, electroporation is used in the insertion of proteins, plasmids or foreign DNA into living cells, fusion of cells, improving drug delivery and hence effectiveness in chemotherapy of cancerous cells, activation of membrane transporters and enzymes, and alteration of genetic expression in living cells.

The phenomenon additionally occurs as a side-effect in e.g. electric injury, electrocution, and cardiac procedures involving electric shocks. Due to its manifestation characteristics, electroporation was studied by scientists working in various research fields.

Experimental research has been done on different types of living cells ([103], [104]) and also for artificial vesicles [105]. Electroporation has been observed also in myocytes with the aid of voltage-sensitive dyes ([106], [85]). Initiation of electroporation in such experiments is generally achieved by applying electrical stimuli higher than 100 mV for 1 to 10 ms.

An accurate model for defibrillation should include electroporation. In 1999, Wanda and Krassowska published a formalism for electroporation [107]. The theory was further developed by the research group of N. Trayanova, which added a hypothetical outward current to the electroporation current [108], as proposed by Cheng et al. [109]. The theoretical model does not consider long-term damage effects and it does not present the transition between phases.

Based on the experimental data published by Cheng et al. [109] and Al-Khadra et al. [85] it is presented a formulation, illustrating the physics of all

phases of electroporation.

8.1.1 Physical Properties of Electroporation

The physical properties of electroporation are connected to the characteristics of the cell membrane, which is the medium where the phenomenon may occur.

The cell membrane of a cardiomyocyte (sarcolemma) consists of a semi-permeable phospholipid bilayer. The lipids of the membrane halves are oriented in such a way that the hydrophobic tails are connected to each other. The hydrophilic heads are grouped to the outer side and are in contact with the aqueous solution of the intracellular and the extracellular space. The thickness of the sarcolemma ranges between 4 and 5 nm [110].

The cell membrane forms intrusions at certain distances spreading at the z-discs along the junctional part of the sarcoplasmic reticulum into the cell (Fig. 4.1). The activation of the cell can be conducted near to the sarcoplasmic reticulum through the so-called transversal tubuli (T tubules). The T tubule surface is between 10 % and 50 % of the whole sarcolemmal area [111].

Various pore forming proteins are included in the sarcolemma. These proteins are mainly specific to distinct ion types e.g. sodium, potassium and calcium. Also exchanger and pump proteins are located in the membrane. Specific calcium channels are located in the membrane of the transversal tubuli to trigger the calcium release of the sarcoplasmic reticulum into the intracellular domain (cytoplasm). In contrast to membrane ion channels, the low resistance ohmic coupling pore between adjacent cells, so-called gap junctions, do not show ion selectivity.

When the cell is in a very strong electrical field additional pores are formed in the phospholipid bilayer. Once electroporation starts, the cell membrane passes through several phases before regaining the normal behavior. The formation of the pores is followed by the enlargement of the radius of the pores, while the stress is first released in the membrane and secondly in the fluid surrounding the pores. Then the pores with the smaller radius start to close while the ones with a bigger radius are enlarged. In this period the total opening of the electropores is almost constant. While the number of the pores decreases, the tension in the membrane becomes smaller.

First Phase The capacitive nature of the membrane will trigger the build up of oppositely signed charges on either side of the membrane. This involves the local alignment of the dipole moments existing in the normal conditions.

Immediately after the initiation of electrical stimulation the behavior of the cells is modified. For understanding the formation of pores, the molecules forming the cell membrane are treated as dipoles.

In the presence of an electrical field, E , an additional force F and a torque \mathcal{T} are exercised on the molecules. The force is expressed by:

$$F = (p\nabla)E \quad (8.1)$$

The torque tends to align p parallel to E as it is reflected in the following equation:

$$\mathcal{T} = \mathbf{p} \times \mathbf{E} \quad (8.2)$$

These two factors dictate the rotation of the phospholipids into the interior of the membrane. If the effect of the torque is stronger than the attraction force existing between the hydrophilic heads and the aqueous solution the dipoles rotate, electropores characterized by a specific radius r_0 are formed.

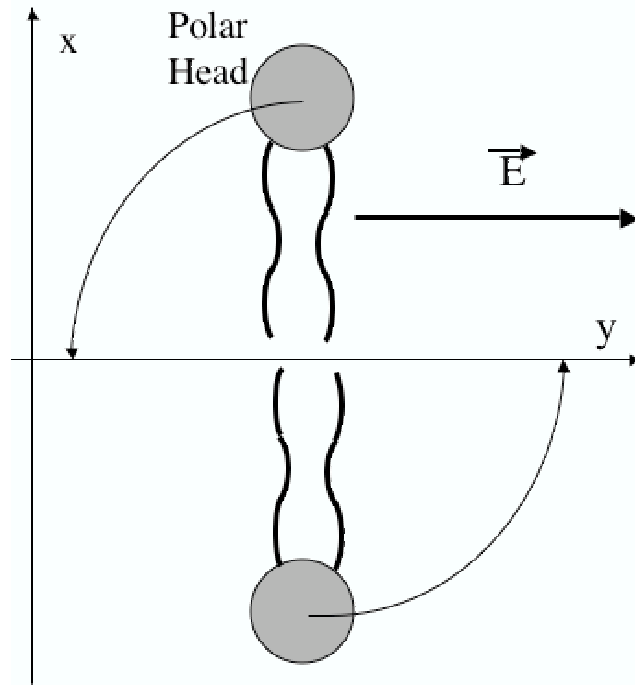


Figure 8.1: The bipolar molecule is rotating under the influence of external electrical fields.

For obtaining the right physical description of the molecules rotation, the moment of inertia, with an effect opposite to the torque is included. The moment of inertia reads:

$$I = \frac{\hbar}{4\pi B} \quad (8.3)$$

B is a rotational energy coefficient, which can be obtained spectroscopically. The rotational constants define the coordinate system in which the inertia matrix for the molecule is strictly diagonal.

The physics describing the kinematic gives the temporal evolution of the angle θ and the angular velocity ω of the phospholipid:

$$\omega = \omega_0 + \alpha t \quad (8.4)$$

$$\theta = \theta_0 + \omega_0 t + \frac{1}{2} \alpha t^2 \quad (8.5)$$

The parameter α is the rotation damping coefficient and it depends on the moment of inertia, on the viscosity of the medium [112] and on the semi-axes of the phospholipids.

While the dipoles are rotating, the conductivity of the cell membranes is modified. Experiments indicated that the conductivity of the tissue varies during electroporation. The mean value of the membrane conductance is time dependent, and follows an exponential law([113]):

$$\sigma_m = A(1 - e^{-\frac{t}{\tau_i}}) \quad (8.6)$$

The parameter A can be determined from fitting the equation with the experimental data. The value of $\tau_{i=1,5}$ is the temporal length of the i -th electroporation phase.

The maximal conductance of the membrane depends on the intensity and the duration of the external electrical stimuli.

The time derivative of the membrane conductance is equal to:

$$\sigma_m' = \frac{A}{\tau_i} e^{-\frac{t}{\tau_i}} \quad (8.7)$$

Second Phase In the investigation of defibrillation phenomena, the parameter of interest is the transmembrane voltage, V_m . We start by expressing the pore energy in two ways. Equalizing the mathematical expressions is determined the formula describing V_m .

First the energy from the calculation of the field around a closed loop in the region of the pore is derived [114].

The electrical field in spherical coordinates is:

$$\hat{E} = E_r \hat{r} + E_\theta \hat{\theta} \quad (8.8)$$

Considering the symmetry of the cell $E_\phi=0$. The components of the electrical field can be expressed in terms of cartesian coordinates:

$$E_r = E_{r0} \cos(90 - \theta) \hat{x} + E_{r0} \sin(90 - \theta) \hat{y} \quad (8.9)$$

$$E_\theta = E_{\theta0} \cos(\theta) \hat{x} + E_{\theta0} \sin(\theta) \hat{y} \quad (8.10)$$

According to the Maxwell's equations E_r and E_θ can be written as:

$$E_r = \left[\frac{3\sigma_i r (1 - \frac{2d}{r})}{3r\sigma_m + 2d\sigma_i} \right] E_0 \cos(\theta) \quad (8.11)$$

$$E_\theta = \left[\frac{-3\sigma_i r (\frac{\sigma_m}{\sigma_i} + \frac{d}{r})}{3r\sigma_m + 2d\sigma_i} \right] E_0 \cos(\theta) \quad (8.12)$$

where σ_i denotes the electrical conductivity of the aqueous fluid. The constant d expresses the thickness of the membrane. The parameters E_0 and r are the extracellular energy and the radius of the pore, respectively.

Substituting the last two relations in equation 8.8 one obtains an equation describing the energy in the pore.

$$E \cong \frac{3\sigma_i r \left(1 - \frac{4d}{r}\right)^{\frac{1}{2}}}{3r\sigma_m + 2d\sigma_i} E_0 \cos(\theta) \quad (8.13)$$

The value of the extracellular energy, E_0 and the radius of the pore, r are functions of time. If the electrical stimulation ceases, the extracellular energy decreases with time.

$$E_0 = E_M - \frac{E_M - E_m}{\tau_2} (t - \tau_1) \quad (8.14)$$

With E_M and E_m the extracellular energy at the beginning and at the end of the second phase, with the length τ_2 are denoted. In case without interruption E_0 remains constant.

In the next step, an expression for the energy in the pores considering the mechanical stress in the membrane is derived. During the expansion of the pores radius, the mechanical stress in the membrane is decreasing. Γ_{ini} denotes the initial surface tension,

$$\Gamma_{ini} = K_s \frac{n\pi r_\infty^2}{S} \quad (8.15)$$

where K_s is the Young modulus, n is the number of pores, S the area of the initial surface and the nominator the maximum possible area the membrane surface can extend to. The elastic stretching modulus of the cell membrane K_s is approximatively equal to 0.2 J/m^2 [115]. The parameter r_∞ expresses the value of the radius, which the pores would eventually reach if the line tension would decrease slowly.

The second phase has a duration of approximatively 100 ms. The exact value can be calculated when Γ_{ini} is known.

$$\tau_2 = \frac{d \cdot \eta_m}{\Gamma_{ini}} \quad (8.16)$$

The viscosity of the membrane has a typical value of $\eta_m = 5 \times 10^{-1} \text{ Pa}\cdot\text{s}$ [115]. The membrane is significantly more viscous than the intra- and extracellular domains (η_i and η_e) [116]. The differences in the viscosities of the media imply the radial dissipation of the surface tension inside the membrane around each pore of increasing radius $r(t)$ [117].

$$r(t) \cong \frac{r_\infty r_0}{\sqrt{r_0^2 + (r_\infty^2 - r_0^2) e^{-\frac{2t}{\tau_2}}}} \quad (8.17)$$

Following is the derivative of r with respect to time which will appear in the expression of transmembrane voltage time derivative.

$$r' = \frac{r_\infty r_0}{\tau_2} [r_0^2 + (r_\infty^2 - r_0^2) e^{-\frac{2t}{\tau_2}}]^{-\frac{3}{2}} (r_\infty^2 - r_0^2) e^{-\frac{2t}{\tau_2}} \quad (8.18)$$

Given the equations (8.15) and (8.17), it is possible to express the surface tension in a perforated finite membrane:

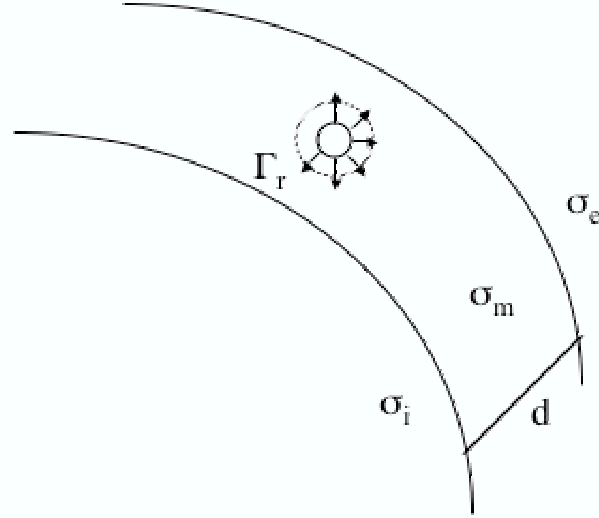


Figure 8.2: The work done by the tension $\Gamma(r)$ per unit time is dissipating radially around each pore of increasing radius $r(t)$.

$$\Gamma(r) = \Gamma_{ini} \frac{r_\infty^2 - r^2}{r_\infty^2} \quad (8.19)$$

Knowing r and $\Gamma(r)$, the pore energy in a finite membrane under initial tension, in the presence of V_m [118], [119] reads:

$$E = 2\pi\gamma r - \int_0^r \Gamma(r) \cdot 2\pi r \cdot dr - \pi a_p V_{m,ep}^2 r^2 \quad (8.20)$$

where γ is the energy of the pore boundary. The coefficient a_p is equal to [120]:

$$a_p = \frac{1}{2d} (k_w - k_m) \epsilon_0 \quad (8.21)$$

The terms k_w and k_m are the dielectric constants of water and membrane and ϵ_0 is the permittivity of vacuum. After calculating the integral in (8.20) and using (8.19) the energy of the pore is given by:

$$E = 2\pi\gamma r - \Gamma_{ini} \pi \left(r^2 - \frac{r^4}{2r_\infty^2} \right) - \pi a_p V_{m,ep}^2 r^2 \quad (8.22)$$

This energy leads to an unstable local maximum at r_{uns} and an apparently stable pore radius, r_{eq} . In the case of strong initial tension and small pore line tension ($r_\infty \gg \frac{\gamma}{\Gamma_{ini}}$) we have $r_{uns} \cong \frac{\gamma}{\Gamma_{ini}}$ and $r_{eq} \cong r_\infty \left[1 - \frac{\gamma}{2\Gamma_{ini} r_\infty} \right]$.

Based on these results from literature it is calculated in this work the value of V_m as a function of time. Equalizing the equations (8.13) and (8.22) it follows:

$$\left[\frac{3\sigma_i r \left(1 - \frac{4d}{r} \right)^{\frac{1}{2}}}{3r\sigma_m + 2d\sigma_i} \right] \left[E_M - \frac{E_M - E_m}{\tau_2} (t - \tau_1) \right] \cos(\theta) = 2\pi\gamma r - \Gamma_{ini} \left(r^2 - \frac{r^4}{2r_\infty^2} \right) - \pi a_p V_{m,ep}^2 r^2 \quad (8.23)$$

It follows that V_m is equal to:

$$V_{m,ep} = \sqrt{\frac{2\gamma}{ra_p} - \frac{\Gamma_{ini}}{\pi a_p} \left(1 - \frac{r^2}{2r_\infty^2}\right) - \left(\frac{3\sigma_i}{ra_p\pi}\right) \left[\frac{\left(1 - \frac{4d}{r}\right)^{\frac{1}{2}}}{3r\sigma_m + 2d\sigma_i}\right]} \cdot E_0(t) \cdot \cos(\theta) \quad (8.24)$$

In many experiments dV_m/dt is measured [85]. Considering that V_m is a function of r and σ_m , which are variables of time, the derivative of V_m with respect to time is given by:

$$\begin{aligned} \frac{dV_{m,ep}}{dt} = & \left\{ \frac{-2\gamma}{r^2 a_p} r' + \frac{\Gamma_{ini}}{\pi a_p} \left(\frac{rr'}{r_\infty^2}\right) - \frac{3\sigma_i}{r^2 a_p \pi} r' \left[\frac{\left(1 - \frac{4d}{r}\right)^{\frac{1}{2}}}{3r\sigma_m + 2d\sigma_i} \right] \cdot E_0(t) \cdot \cos(\theta) \right. \\ & - \left(\frac{3\sigma_i}{ra_p\pi} \right) \left[\frac{-2dr'}{r^2 \left(1 - \frac{4d}{r}\right)^{\frac{1}{2}} (3r\sigma_m + 2d\sigma_i)} \right] \cdot E_0(t) \cdot \cos(\theta) \\ & - \left(\frac{3\sigma_i}{ra_p\pi} \right) \left[\frac{\left(1 - \frac{4d}{r}\right)^{\frac{1}{2}}}{(3r\sigma_m + 2d\sigma_i)^2} \right] \cdot (3r'\sigma_m + 3r\sigma_m') E_0(t) \cdot \cos(\theta) \\ & \left. - \left(\frac{3\sigma_i}{ra_p\pi} \right) \left[\frac{\left(1 - \frac{4d}{r}\right)^{\frac{1}{2}}}{3r\sigma_m + 2d\sigma_i} \right] \cdot \left(-\frac{E_M - E_m}{\tau_2} \right) \cos(\theta) \right\} \\ & \frac{1}{2\sqrt{\frac{2\gamma}{ra_p} - \frac{\Gamma_{ini}}{\pi a_p} \left(1 - \frac{r^2}{2r_\infty^2}\right) - \left(\frac{3\sigma_i}{ra_p\pi}\right) \left[\frac{\left(1 - \frac{4d}{r}\right)^{\frac{1}{2}}}{3r\sigma_m + 2d\sigma_i}\right]}} \cdot E_0(t) \cdot \cos(\theta) \end{aligned} \quad (8.25)$$

Rearranging the terms the expression reduces to:

$$\begin{aligned} \frac{dV_{m,ep}}{dt} = & \frac{1}{2V_m} \left\{ \frac{-2\gamma}{r^2 a_p} r' + \frac{\Gamma_{ini}}{\pi a_p} \left(\frac{rr'}{r_\infty^2}\right) - \frac{3\sigma_i}{r^2 a_p \pi} r' \left[\frac{\left(1 - \frac{4d}{r}\right)^{\frac{1}{2}} E_0 \cos(\theta)}{3r\sigma_m + 2d\sigma_i} \right] \right. \\ & + \left(\frac{3\sigma_i}{ra_p\pi} \right) \left\{ \left[\frac{2dr' E_0 \cos(\theta)}{r^2 \left(1 - \frac{4d}{r}\right)^{\frac{1}{2}} (3r\sigma_m + 2d\sigma_i)} \right] - \left[\frac{\left(1 - \frac{4d}{r}\right)^{\frac{1}{2}} E_0 \cos(\theta)}{(3r\sigma_m + 2d\sigma_i)^2} \right] \right. \\ & \left. \left. \left[(3r'\sigma_m + 3r\sigma_m') - \left(\frac{E_M - E_m}{\tau_2} \right) \cos(\theta) \right] \right\} \right\} \end{aligned} \quad (8.26)$$

Third Phase If $\eta_i r_\infty > \eta_m$ one finds that the dynamic regime crosses over to a third one dominated by the dissipation of the stress in the surrounding fluid. The time scale of this phase is between 150-200 ms. It can be precisely determined from:

$$\tau_3 \cong \frac{\eta_i \Gamma_\infty}{\gamma_{ini}}. \quad (8.27)$$

During this period the pore opening obeys:

$$r(t) \cong r_\infty \frac{1 - a \cdot e^{-\frac{2t}{\tau_3}}}{1 + a \cdot e^{-\frac{2t}{\tau_3}}} \quad (8.28)$$

where

$$a = (r_\infty - r_c) / (r_\infty + r_c) \quad (8.29)$$

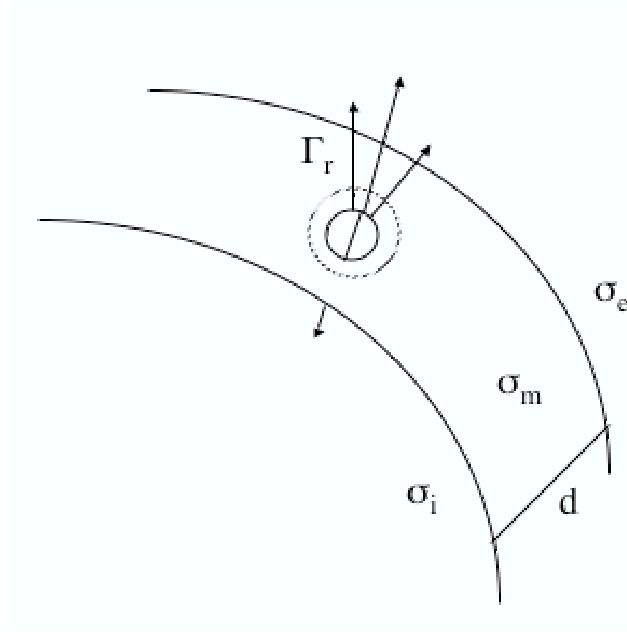


Figure 8.3: The work done by the tension $\Gamma(r)$ per unit time dissipates in the surrounding fluid.

and r_c denotes the critical value of the radius, which leads to catastrophic bursting of the membrane. Its value can be determined experimentally.

The derivative of the radius with respect to time is in this case:

$$r'(t) \cong \frac{4r_\infty a \cdot e^{-\frac{2t}{\tau_3}}}{\tau_3 (1 + a \cdot e^{-\frac{2t}{\tau_3}})^2} \quad (8.30)$$

The temporal variation of the V_m is described by eq. (8.24), to which the appropriate value of the radius and its time derivative will be fitted. The main difference between the reversible and the irreversible electroporation process occurs at the cross over to the third dynamic regime. The break of the membrane could be easily misinterpreted as the occurrence of pore nucleation after the end of the electric pulse. The phenomenon was observed by Wilhem et al. [121].

Fourth Phase At the beginning of the fourth phase the pores are fairly equal. The slight differences in the size is inducing small oscillations of the pores edges. When the line tension of the small pores is not balanced by the average surface tension in the relaxed membrane the smaller pores are contracting while the bigger ones increase their radius. Therefore, a quasi-stable state is created and the average electroporation opening is almost constant. With time the smaller pores will start to close. The smaller the number of the pores, the faster the average electroporation radius decreases. The final closure of the pores is most probably controlled by the cytoskeleton dynamics and possibly by other biological regulation mechanisms, which directly influence the ionic currents flow.

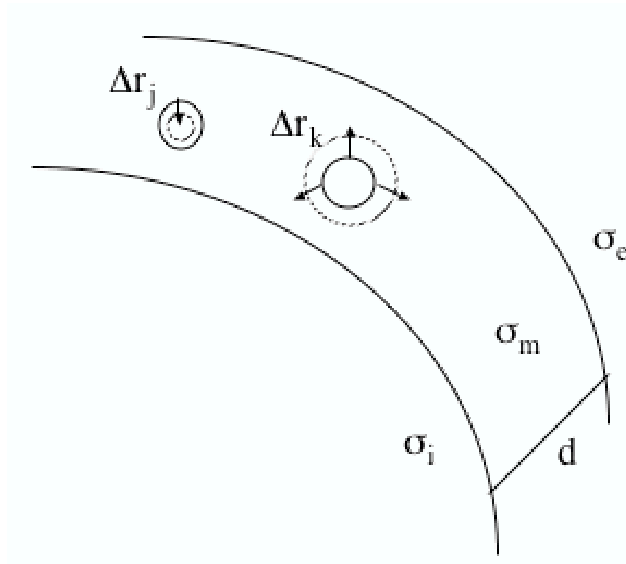


Figure 8.4: When the line tension of the small pores is not balanced by the average surface tension in the relaxed membrane the small pores are closing while the bigger one increase their radius.

The predominant event in the fourth phase is the exponential disappearance of the pores. This phenomenon is described by:

$$r(t) \cong r_3 - C_{41} e^{-\frac{t \cdot C_{42}}{\tau_4}} \quad (8.31)$$

The parameter r_3 denotes the value of the radius at the end of the third phase. The constants C_{41} and C_{42} can be determined by fitting the model to experimental data. The derivative of the radius with respect to time is in this case:

$$r'(t) \cong -\frac{C_{41} C_{42}}{\tau_4} \cdot e^{-\frac{t \cdot C_{42}}{\tau_4}} \quad (8.32)$$

The duration of the fourth phase can be calculated by considering the liquid volume displaced during the closure of the pores ΔV . The sealing of the pores ends in few seconds, therefore it can be precisely measured from the experimental point of view.

$$\tau_4 \cong \frac{\eta \Delta V}{K_s} \quad (8.33)$$

$$\tau_4 \cong \frac{4\pi\eta_m \cdot r_{4i}^2 \cdot d}{K_s} \quad (8.34)$$

The term r_{4i} represents the value of the radius at the beginning of the fourth phase.

Fifth Phase This phase corresponds to the final state of tissue regeneration. After the closure of the pores, the maximum value of V_m increases very slow in time, regaining the normal value after tens of minutes.

$$\lim_{t \rightarrow 1s} \frac{dV_{m,max}}{dt} = 0 \quad (8.35)$$

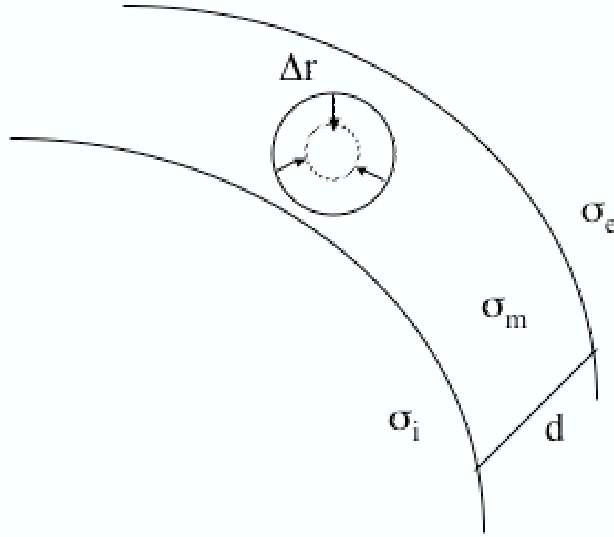


Figure 8.5: When the line tension of the pores decreases to a certain limit, the cytoskeleton dynamics induces the final closure of the pores.

Compared to the variation corresponding to the previous phases the maximum value of V_m , is approximately constant.

8.1.2 Application of the Electroporation Formalism to a Specific Electrophysiological Cell Model

TNNP electrophysiological model (Sect. 4.4.2) was used for observing the changes induced in human myocardium, by electroporation in response to high electrical stimuli. Using Euler-Cromer time-domain integration method one can simulate the creation of the pores. This method was proposed for satisfying the law of energy conservation. The process involving the pores creation lasts less than a μs . For numerical simulations a time step of the order of ns would be needed. For simulating the reaction of the myocardium to electrical stimuli we need the temporal evolution of the transmembrane voltage during an interval longer than the action potential duration (400 ms). Because of the computational constraints (time step is of the μs order) this phase was skipped in the simulation.

For the second, third and fourth phase of electroporation the equation (4.26) is substituted by:

$$\frac{\partial V_m}{\partial t} = -\frac{1}{C_{m,ep}}(I_{mem} + I_{pore}) + \frac{\partial V_{m,ep}}{\partial t} \quad (8.36)$$

The leak current passing through the pore is proportional with the myoplasm volume V_{myo} , with the ionic valence (Z) and the ionic flux. It is inverse proportional with the geometric membrane area, A_{geo} . The constant of proportionality

is the Faraday's constant F .

$$I_{\text{pore}} = -\frac{V_{\text{myo}} \cdot F}{A_{\text{geo}}} (Z_{\text{Ca}j\text{Ca}} + Z_{\text{K}j\text{K}} + Z_{\text{Na}j\text{Na}}) \quad (8.37)$$

The ion flux through the pore can be calculated by using Goldman-Hodgkin-Katz equation [122]. For the fifth phase of electroporation the equation (4.26) is used and C_m is kept at a constant value, 10% bigger than normally. As an effect, the action potential duration will have the normal value, but the amplitude will be reduced with 10%. The value of the pores radius at the end of each phase must be equal to the value of the radius of the pores in the beginning of the following phase.

$$r_i = r_{i+1} \quad (8.38)$$

This condition implies a continuous variation of the V_m trough phases. Fig. 8.6 shows how the action potential varies in time due to electroporation. The variation of V_m indicates that electroporation does not follow time symmetry. The modifications of the action potential due to pores formation is stronger than the changes, appearing during the restoration of the normal membrane functions. The obtained results resemble the experimental data published by Al-Khadra et al. [85].

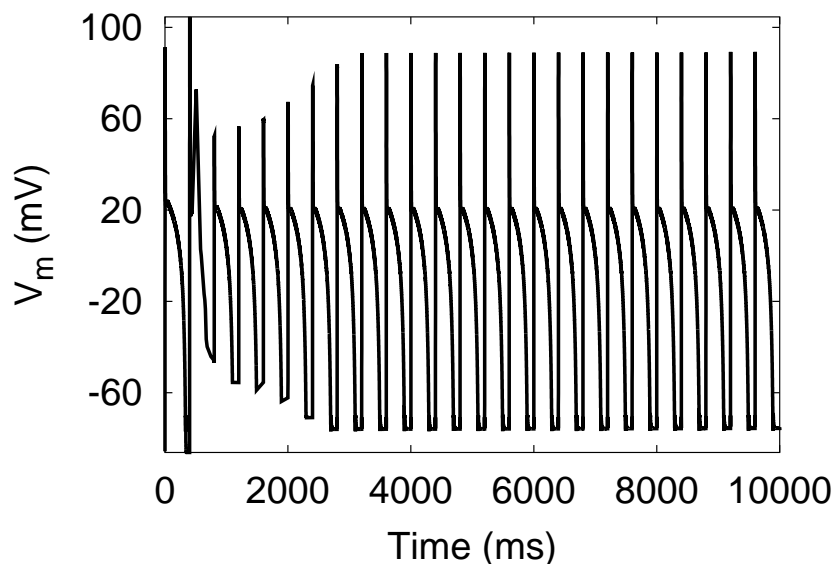


Figure 8.6: The variation of transmembrane voltage after electroporation of the membrane.

The influence of electroporation was then studied at the tissue level. The size of the used virtual myocardial wedge was $1 \text{ cm} \times 1 \text{ cm} \times 2 \text{ cm}$. The tissue was electrophysiologically heterogeneous in the direction of the longest axis. The arrangement of the myocytes corresponded to the realistic fiber orientation. The electrical current was injected in the myocardium through two punctual electrodes. The sources were centred inside the tissue, 0.2 cm from the ends of the longest axis. A monophasic electrical stimulus with the amplitude of 130 A

was applied for 5 ms. Two sets of data were generated: one included electroporation, the other yielded the control data. The distribution of V_m , 1 ms after the end of the stimulation is illustrated in Fig. 8.7 and 8.8. The myocardium neighboring both electrodes is excited, due to the appearance of virtual electrodes. The spread of depolarisation is strongly influenced by fiber orientation. The comparison of the two sets of pictures indicates that electroporation reduces the transmembrane voltage variation interval. As a consequence, the distribution of V_m is more homogeneously around the electrodes location. The introduction of electroporation also slightly modifies the depolarisation front.

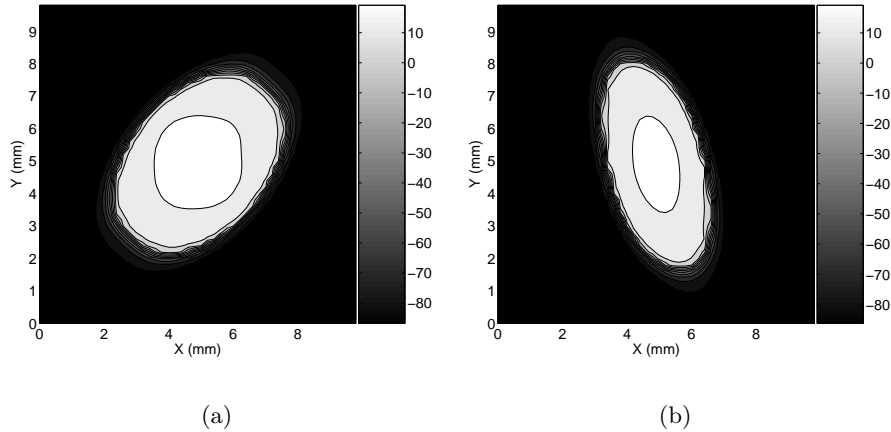


Figure 8.7: The distribution of isopotential surfaces after an electrical stimulation of 5 ms, applied through needle electrodes. The anode was localized in the subendocardial volume (a), while the cathode was placed in subepicardial region (b). The pictures illustrate the data obtained with a model, which does not contain electroporation.

Discussion The novelty of the formalism is that it describes both the electrophysiological and mechanical properties of membrane during each electroporation phase. Presently still exist discrepancies between experimental and theoretical results, which can be redissolved by using more accurate mathematical models.

The change in the distribution of the transmembrane voltage induced by the inclusion of the new electroporation formalism are similar to the results obtained by Ashihara and Trayanova, 2004 [108].

Even though momentary the scientists involved in the research of defibrillation phenomena are interested in the cardiac activity of approximately 1 s, the investigation interval will be extended in the future. The prolongation of the researched cardiac interval will enhance the need of more accurate mathematical model.

The formalism presented in this section constitutes just a start of an accurate description of electroporation. The model must be developed in future to include the distribution of the pores in the membrane according to the distance between the cell and the electrode. Another investigation necessary for the de-

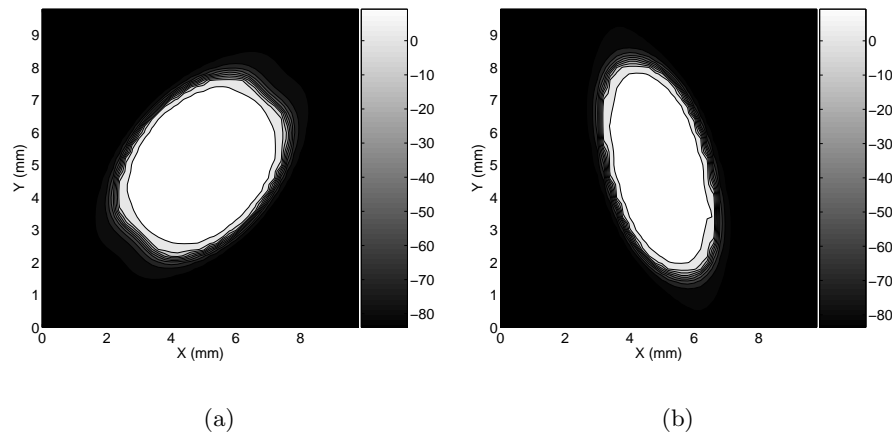


Figure 8.8: The distribution of isopotential surfaces after an electrical stimulation of 5 ms, applied through needle electrodes. The anode was localized in the subendocardial volume (a), while the cathode was placed in subepicardial region (b). The subfigures show the results delivered by the model which includes the mathematical formalism of electroporation.

velopment of the model is the determination of the constants included in the equations, for fitting properly the reaction of human myocytes.

8.2 Heart Failure

The study of electrophysiological heterogeneity is often associated with the study of factors, which are inducing a distortion in the AP. An example of the case is the human tissue with terminal heart failure, which presents a prolonged action potential duration [123]. The major currents responsible for repolarisation (I_{to} , I_{Ks} , the rapid delayed rectifier potassium current, I_{Kr} and the inward rectifier potassium current, I_{K1}) together with the electrical conductivity were reduced in this pathology [124]. During heart failure also the intracellular sodium concentration is elevated due to the alteration of the Na^+ - Ca^{2+} exchange function (NCX) [125]. Although expression of numerous ion channels is altered in heart failure, the mechanisms leading to electrophysiological dysfunction and to arrhythmias are not completely known.

The aim of this work was to identify the influence of the modification of the transmural electrophysiological variation on the fundamental reaction of the myocardium to electrical stimulation. Simulations were performed on four types of myocardial preparations representing electrophysiological heterogeneous human ventricular wedge adapted to various degrees of heart failing conditions.

Common characteristics of the myocardial preparations The cellular electrophysiology of the cardiac preparations used in the study, was described with the ten Tusscher-Noble-Noble-Panfilov model of a human ventricular myocyte (Sect. 4.4.2). The orientation of the myocardial fibers was adapted to measurements of human ventricular cells (Sect. 6.3). The geometry of the vir-

tual cardiac wedges is shown in Fig. 6.2 a. The size of the tissues was 10 mm x 10 mm x 20 mm. The grid was composed of cubic voxels with a side length of 0.2 mm.

Differences between the myocardial preparations The research was carried out using four different myocardial preparations: a control heart failing model (HFM), a model with increased NCX (HFM_{NCX}) and two models with reduced intra- and extracellular electrical conductivities ($\text{HFM}_{\sigma 1}$, $\text{HFM}_{\sigma 2}$). The sum of their characteristics is presented in Table 8.1.

The electrophysiological modifications imply the change of the APD profile. Fig. 8.9 depicts the transmural distribution of the action potential at 90% of repolarisation (APD_{90}), generated by the myocytes composing coupled-cells environments. The values of APD_{90} are measured after a 1 Hz electrical stimulation. In the electrophysiological heterogeneous myocardium, the longest APD corresponds to the M cells and the shortest is registered in the subepicardial region. The APD of HFM presents an elevation of the mean value and a reduction of the gradient compared to HM. To HFM_{NCX} corresponds an even stronger prolongation of the APD. The variation of the electrical conductivity induces a negligible variation of APD.

Name of the model	Notation	Distinctive Characteristics
Heart failing control model	HFM	Normal electrical conductivity (Table 6.1) Heterogeneous distribution of electrophysiological properties I_{to} , I_{Ks} and I_{K1} reduced by 25%
Heart failing model with 25% increased NCX	HFM_{NCX}	Normal electrical conductivity (Table 6.1) Heterogeneous distribution of electrophysiological properties I_{to} , I_{Ks} and I_{K1} reduced by 25% $\text{Na}^+ - \text{Ca}^{2+}$ exchange function increased by 25%
Heart failing model with 25% decreased electrical conductivity	$\text{HFM}_{\sigma 1}$	Electrical conductivity reduced by 25% Heterogeneous distribution of electrophysiological properties I_{to} , I_{Ks} and I_{K1} reduced by 25% $\text{Na}^+ - \text{Ca}^{2+}$ exchange function increased by 25%
Heart failing model with 50% decreased electrical conductivity	$\text{HFM}_{\sigma 2}$	Electrical conductivity reduced by 50% Heterogeneous distribution of electrophysiological properties I_{to} , I_{Ks} and I_{K1} reduced by 25% $\text{Na}^+ - \text{Ca}^{2+}$ exchange function increased by 25%

Table 8.1: The description of the myocardial preparations constructed for the investigation of heart failure.

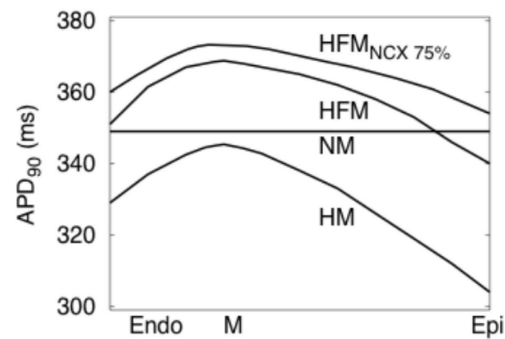


Figure 8.9: Comparison between simulated APDs of healthy and failing heart with normal electrical conductivities.

For further enhancement of the reactions induced by electrophysiological differences, the models were simplified for avoiding the occurrence of unnecessary secondary electrical sources. The tissue was not surrounded by bath [84] and it was not fragmented by cleavage planes [21]. The electrical stimuli were chosen to model normal action potential profiles in the excited cells. Therefore, the model did not include the electroporation formalism neither cell uncoupling [85].

The parameters of the electrical stimulation The results of the simulations done by Clayton et al., suggest that the fibrillation patterns formed in an electrophysiological homogeneous tissue differ from the ones developed in an electrophysiological heterogeneous myocardium [86]. It also has been shown experimentally that heart failure can lead to nonexcitable gap reentry [126] and to development of early afterdepolarisations. The latter can trigger arrhythmia [88]. The failing heart conditions induce fibrillation patterns, different to the electrophysiological normal heart. Since fibrillation characteristics would not be similar in the myocardial preparations it was decided to set the tissue completely in the resting phase at the initiation of the electrical stimulation.

The results gathered during a cardiac cycle formed the data set used to compare the electrical responses of the myocardial preparations. The research was extended to several types of electrical stimulation configurations (Table 6.2).

Myocardial reaction after monophasic electrical stimulation applied through external paddles Due to the characteristics of the electrical stimulations and the features of the myocardial preparations, y is a symmetry axis for the V_m spatial distribution. Therefore, the results will be presented in the form of sections through the middle of the tissues, at constant y (Fig. 8.10, 8.11, 8.13).

The variation of V_m produced by the virtual electrodes, in the subepicardial zone, was not strong enough to induce a depolarisation front. Therefore, the excitation was initiated exclusively by the primary electrical sources. In the depolarisation phase and while the myocytes were in the plateau phase, V_m presented a similar distribution in HFM and HFM_{NCX} (Fig. 8.10 a, b, e, f).

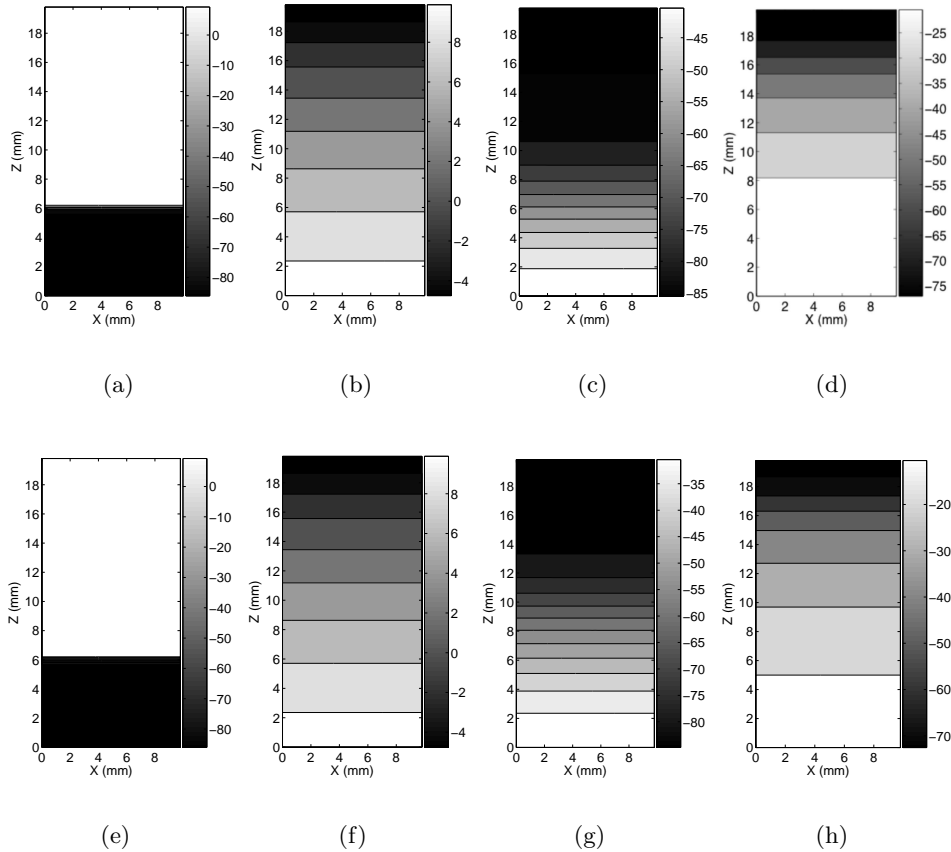


Figure 8.10: Distribution of V_m in the heart failing models with normal electrical conductivities after 10 ms long monophasic stimulation at: a), e) 50 ms, b), f) 150 ms, c), g) 250 ms, d), h) 350 ms.

The distinctions between the behaviours of the tissues with equal electrical conductivities were formed during the repolarisation phase. At 250 ms and also at 330 ms V_m interval (the range in which V_m varies at a certain moment) of HFM was shorter than in HFM_{NCX} and the mean value of V_m was nearest to the resting phase. HFM_{NCX} was completely repolarized at 369 ms, 9 ms later than HFM.

The reaction of HFM _{σ_1} and HFM _{σ_2} to monophasic stimulation reflected the dependence of the depolarisation phase duration on the value of the electrical conductivity (Fig. 8.11 a, e). The temporal modification of the depolarisation phase induced the broadening of the V_m interval, from the start of the repolarisation phase. At 250 ms, when all myocytes were still refractory, the preparation characterized by a reduction of the electrical conductivity by 25%, presented a distribution of V_m in a 16 mV long interval (Fig. 8.11 b). The reduction to 50% enlarged the V_m interval by 4 mV (Fig. 8.11 f). At 350 ms, when the top of the preparation was already in the resting phase and the bottom was still refractory the difference between the length of the V_m intervals was enlarged to 20 mV (Fig. 8.11 c, g). While the tissue comprises refractory, partly excitable, and

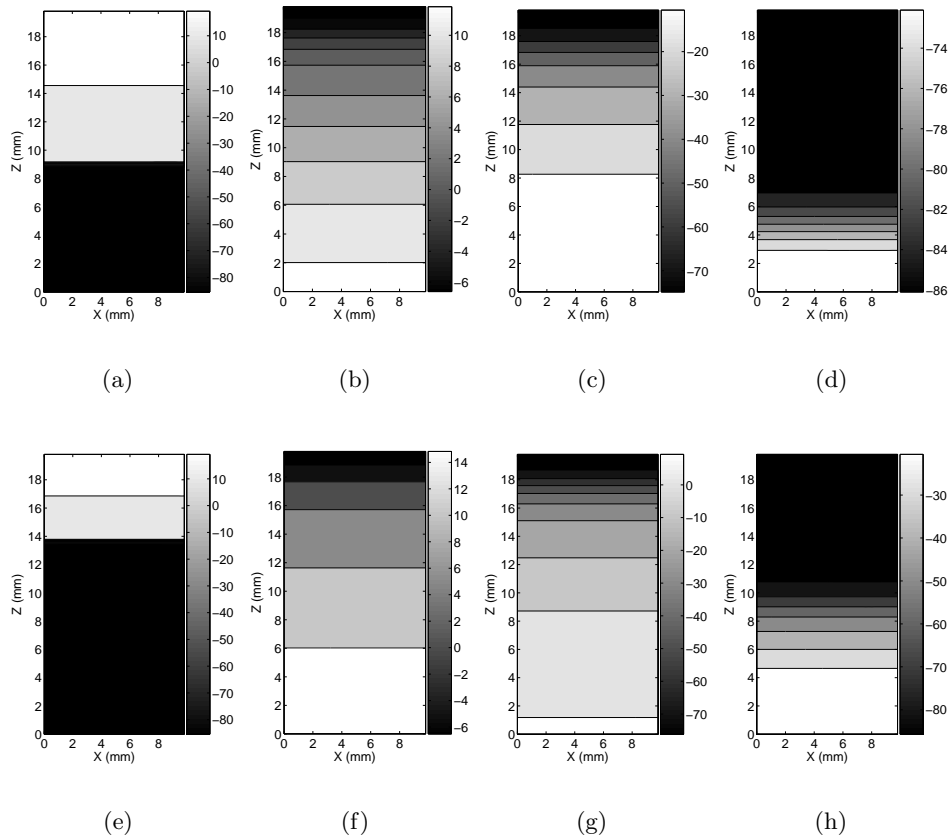


Figure 8.11: Distribution of V_m in the heart failing models with 25% (top) and 50% (bottom) electrical conductivities after 10 ms long monophasic stimulation at: a), e) 50 ms, b), f) 250 ms, c), g) 350 ms, d), h) 420 ms.

excitable parts, arrhythmias can develop if an additional electrical stimulus is applied [127]. The time, during which refractory, partly excitable, and excitable cells coexist in the myocardium is termed vulnerable window. A prolongation of the V_m interval indicates the enlargement of the vulnerable window.

Figure 8.12 depicts the simulated transmural ECGs corresponding to myocardial preparations after monophasic stimulation. The virtual wedges, characterized by equal electrical conductivities present the same ECG profile during the QRS interval. The differences are formed in the T wave region, which corresponds to the repolarisation phase. The electrophysiological heterogeneous preparations present positive T waves, which have different amplitudes and the peaks are located in different positions on the time axis. The heart failing conditions produce a dispersion of the T wave and a temporal delay in the appearance of the peak. The modification of the electrical conductivities induce a change in the QRS complex associated with a temporal shift of the T wave.

As illustrated in Fig. 8.10 and Fig. 8.12 the differences in the responses of the models characterized by equal electrical conductivities culminated during the T wave interval. Therefore, the presentation of the following results is focused

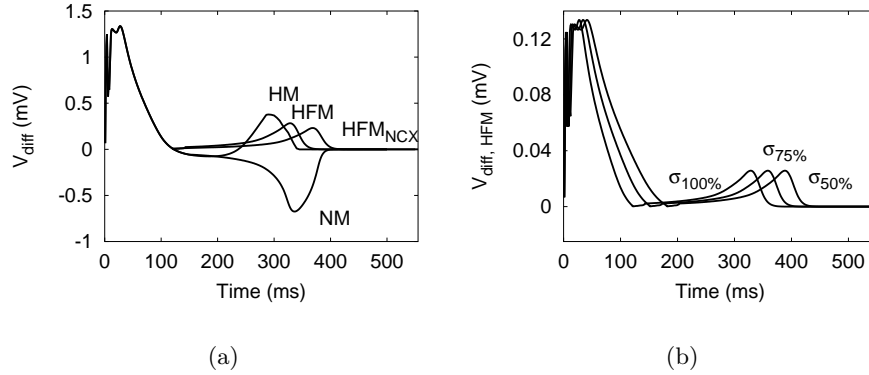


Figure 8.12: Comparison between simulated ECGs of healthy and failing heart with a) normal and b) reduced electrical conductivities. The electrophysiological heart failing characteristics affect mainly the T wave, implying a reduction of the amplitude and a displacement on the temporal axis. The modification of the electrical conductivities induce a change in the QRS complex and a temporal shift of the T wave.

on comparisons between the reactions of HFM and HFM_{NCX} during the end of the repolarisation phase.

The response of HFM and HFM_{NCX} to biphasic electrical stimulation applied through external paddles During the first half of the biphasic stimulation the cathode was near to the endocardium. The tissue included in the spatial interval (19, 20) mm of the Z-axis was depolarized during the first 5 ms. During the second half the polarity was inversed and a depolarisation front was initiated at the opposite end of the tissue. At 330 ms V_m axis of symmetry was displaced in the direction of the endocardium both in HFM (Fig. 8.13 a) and HFM_{NCX} (Fig. 8.13 d). The V_m interval was (-35, -75) mV and (-30, -70) mV for HFM and HFM_{NCX} , respectively. The virtual wedges were completely repolarized faster in the case of biphasic than after monophasic stimulation.

The response of HFM and HFM_{NCX} to monophasic electrical stimulation applied through internal needle electrodes When the myocardium was stimulated with needle electrodes the differences between the responses of the tissue models, formed during the repolarisation phase underlined the influence of electrophysiological heterogeneity. Monophasic stimulation produced symmetric patterns of excitation dispersion due to the appearance of virtual electrodes.

After the symmetrical propagation of depolarisation from the extremes of the tissue towards the centre, the repolarisation patterns were asymmetrical (Fig. 8.13 b, e). The median of the most refractory part of the tissue was placed between the centre of the tissue and the M cells zone. At 330 ms, 50% of HFM were completely repolarized (Fig. 8.13 b). At the same moment, even though V_m interval was the same in HFM_{NCX} , the percentage of completely repolarized tissue was smaller (Fig. 8.13 e).

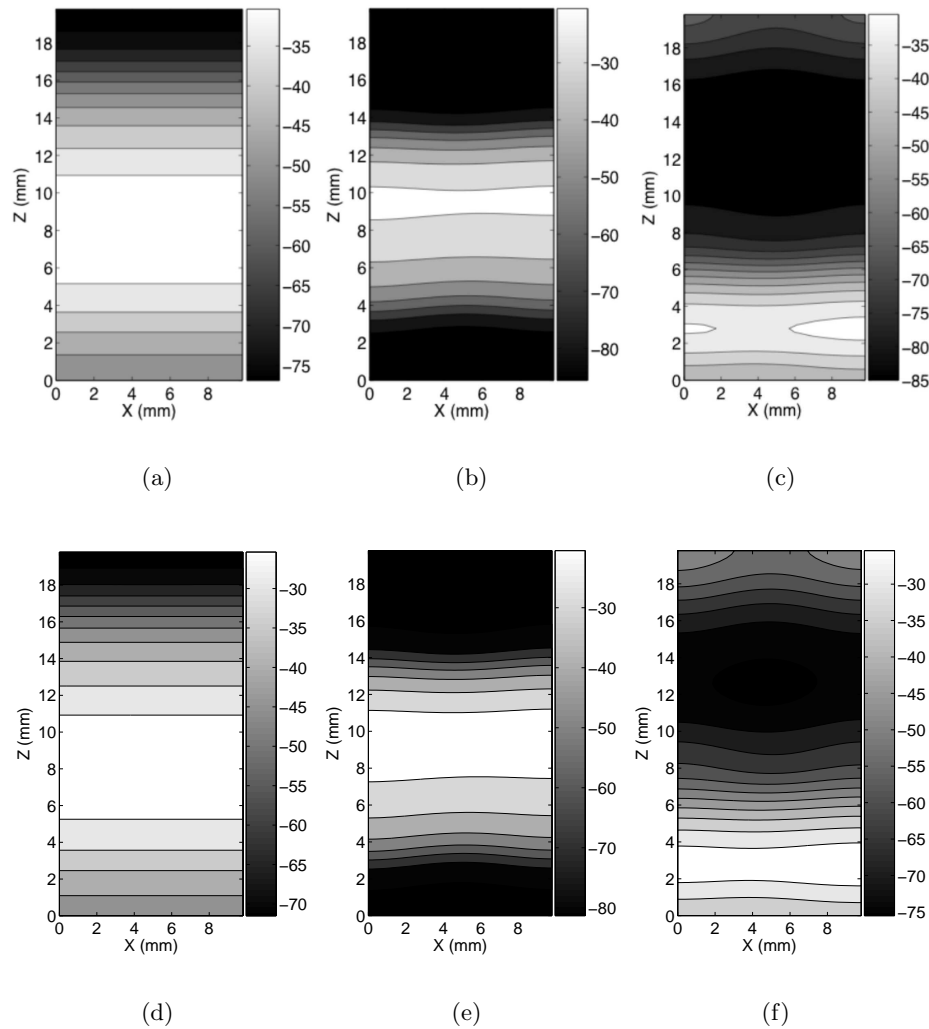


Figure 8.13: Distribution of V_m in HFM (top) and HFM_{NCX} (bottom) at 330 ms after: a), d) biphasic external stimulation and monophasic stimulation applied through needle electrodes placed 1 mm away from b), e) the centre, c), f) extremes of the longest axis.

The shift of the electrodes towards the centre of the virtual wedge reduced the time needed by HFM and HFM_{NCX} to achieve the complete resting state by 11 and 9 ms, respectively. The temporal reduction was induced by the faster excitation of the M cells, presenting the longest APD. 330 ms after the simulation initiation the refractory zone was located mainly in the M cells region (Fig. 8.13 c, f). Compared to HFM, the most refractory region of HFM_{NCX} was spatially more extended and the average value of V_m was farther away from the resting value. The modifications of V_m illustrate that the upregulation of NCX implies an extension of the vulnerable window.

Discussion The various heart failing conditions were gradually implemented in the myocardial preparations. This enhanced the possibility to identify the corresponding influence on the response to electrical stimulation. Initially, I_{K1} , I_{to} and I_{Ks} were homogeneously reduced by 25%. Then, $Na^+ - Ca^{2+}$ exchange function was increased and finally the electrical conductivities were decreased. The simulations indicated that each heart failing feature is modifying the spatio-temporal evolution of V_m in a specific way.

In contrast to canine cells [124] the reduction of I_{to} , I_{Ks} and I_{K1} in a human electrophysiological cellular model did not modify the early repolarisation and the plateau phase. A comparison of the gained data showed no substantial differences between the responses of the virtual wedges with equal electrical conductivities during the depolarisation phase. The results reflected that the differences in electrophysiology induce distinctive changes during the T wave interval. The responses differed in the formation of the isopotential surfaces, the interval in which V_m varied and the moment corresponding to the full repolarisation.

The modification of I_{to} and I_{K1} induced a prolongation of APD, which was stronger in the subepicardial and subendocardial regions than in M cells area. As a result the APD gradient showed a general decrease. The heterogeneous prolongation of APD in the failing heart has been previously noticed by Akar and Rosenbaum [128].

Experimental comparisons between failing and non-failing human cardiomyocytes indicated that during heart failure the $Na^+ - Ca^{2+}$ exchange function is increased [125]. The up-regulation of NCX induced a further prolongation of the APD.

The results also indicated that despite the prolongation of the APD the heart failing preparations conserved the effects related to electrophysiological heterogeneity. The centre of the most refractory region presented a shift towards the M-cells, exclusively manifested in the electrophysiological homogeneous cardiac preparations. The influence of heart failure was most obvious after the electrical stimulation through needle electrodes placed near the centre of transmural wall. In NM the most refractory region was localized near the extremes of the tissue, while in the other preparations it was centred in the M-cells area.

QT-interval prolongation is a well-recognized feature of human heart failure [129]. In concordance with previous results, the ECG of HFM and HFM_{NCX} presented a displacement of the T wave peak together with a reduction of the amplitude. The dispersion of the T wave could also be observed in the obtained results. At 330 ms HFM and HFM_{NCX} comprised a larger refractory zone than HM. As a consequence, medical doctors can utilize the characteristics of the T waves for identifying how much the electrophysiology was affected by heart failing conditions.

During heart failure the myocytes tend to be more electrically uncoupled than in the healthy myocardium because of fibrosis between cells [130]. Experiments also pointed out that increased intracellular $[Ca^{2+}]$ and $[H^+]$ amplify the resistance of the gap junctions [131, 132]. For researching the influence of fibrosis the electrical conductivity was homogeneously decreased by 25% and 50%. The results were in agreement with previous experimental data, indicating the

extension of the vulnerability window.

Experiments showed that during heart failure, a down regulation and redistribution of gap junction proteins exists in addition to the alterations in ion channel expression [133]. Considering experimental data on gap junction distribution, in future models the homogeneous reduction of the electrical conductivity will be replaced by a heterogeneous modification.

The evaluation of V_m variance in HM, HFM and HFM_{NCX} reflected that the most effective monophasic stimulation is the one in which the cathode was localized near to the mid-myocardium. The myocardium excited by a biphasic stimulation was at rest faster than after a monophasic stimulation. In agreement with previously obtained results [89], the biphasic stimuli proved to be more efficient.

8.3 Inferences

In this chapter two distinct factors that modify the vulnerability of the tissue to electrical shocks: electroporation and heart failure were presented.

The first section was mainly focused on presenting a new mathematical formalism meant to describe more accurately the membrane reaction after application of intense electrical stimuli. The model is more accurate than the other existing methods used in the study of defibrillation. Nevertheless, the electroporation modeling must be in future associated with cell uncoupling.

In the second part of the chapter different degrees of heart failure were described. Another factor influencing the vulnerability to electrical shocks in a similar way is the ischemia. Since both modify the T wave, a parallel investigation of heart failure and ischemia must be completed in order to be able to draw correct conclusions about the process denaturing the electrocardiogram.

9 Summary and Conclusions

Modeling the reaction of the human left ventricle to electrical stimuli is a promising approach to support the understanding of the complex mechanisms specific to the cardiovascular system. Due to the enormous investigation of the topic, the knowledge about the micro and macro cardiac structure is very vast. The apparent contradiction between experimental results of research sustained at various cardiac levels (cell, tissue, organ), indicates the existence of uncovered gaps. This thesis demonstrates that theoretical investigation based on multidisciplinary tools, like biophysics, medicine and engineering can be combined to resolve the phenomenological dilemma.

The variation of the characteristics of the human left ventricular model indicated the importance of including realistic anatomical structures, fiber orientation combined with realistic heterogeneous electrophysiology and anisotropic electrical properties in order to reproduce the normal excitation pattern observed experimentally. The outcomes of the simulations with electrophysiological transmural heterogeneous distribution underlined a correct reconstruction of the electrocardiograms and repolarization patterns inversely distributed as in the homogeneous tissue. The experimentally recorded positive T-wave can only be correctly reconstructed when including the transmural electrophysiological heterogeneities. The inclusion of the cleavage planes, which are an anatomic feature of the left ventricle, modify the overall reaction of the model, due to the occurrence of secondary electrical sources. The variation of the tissue-surrounding bath volumes ratio imply a modification of the magnitude of the virtual electrodes polarization, explaining the cause of different magnitudes experimentally reported. The simulated ventricular fibrillation has the frequency measured in vivo.

After the identification of the most appropriate features for cardiac modeling the characteristics of the electrical therapy were researched. The investigation of both cellular and tissue electrical behaviors reflected that the electrophysiology is not the only determinant in the success of defibrillation. The results proved that the hypotheses exclusively based on the capacitive nature of the membrane are rough approximations, possibly leading to false conclusions. The simulations with three-dimensional tissues indicated that the most efficient stimulation configuration is the one producing the highest amount of depolarization fronts. Accordingly, from the present days standard therapies the biphasic stimuli are the most efficient. The same amount of depolarization fronts could be induced with electrode arrays. The method presents the advantage that the stimulation interval can be reduced by half and the intensity of the pulses can be lowered, since the excitation thresholds corresponding to monophasic stimuli are lower

than for biphasic ones. The defibrillation of the human myocardial preparation also indicated the importance of applying the shock in the right moment. The identification of the optimum interval being possible by studying the electrocardiogram.

The thesis also includes a new formalism describing electroporation more accurately than the models presently used in defibrillation simulation. The method incorporates the physics of each electroporation phase. The evolution of the simulated transmembrane voltage is very similar to the produced experimental data. The implementation of heart failure modified the electrocardiogram and the action potential profile as the experiments indicated.

The models utilized during the research present different limitations. The implemented anatomical features are mainly based on the Visible Female data set. The heart of this person was not completely healthy and the geometry and shape have changed until the data acquisition. The rule-based system to set the ventricular fiber orientation needs to be enhanced by a technique to measure its orientation e.g. with diffusion tensor MRI. The modeling of the left ventricle can also be enhanced by describing in addition to the transmural also the apico-basal heterogeneity. Furthermore, the orientation of the cleavage planes and their intramural distribution was neglected. The constants incorporated in the electroporation formalism must be adapted to fit human data.

The methods described in this thesis offer the opportunity to state in future work the interaction of anatomy, electrophysiology and excitation propagation more precisely. The model provides insights into the phenomena correlated to the cardiac response to electrical stimuli in such a detailed way that currently cannot be achieved experimentally. All parameters during normal and abnormal excitation can be traced and analyzed.

To validate the presented models, experimentally recorded ECGs on heart and body surfaces have to be compared to simulated ECGs in physiological, pathological, and pacing cases. Furthermore, a detailed model can consider individual human anatomy to get more information about the influence of varying anatomical architecture on excitation conduction and its role in the initiation of arrhythmia.

If the computing power and the availability of human measured data will continue to increase as fast as in the past decades, it is expected that electrical models of the full torso will soon become standard tools in clinical work. These models will reconstruct physiological cases as an idealized representation of humans and pathological cases of individual patients for personalized therapy planning.

Bibliography

- [1] A. Vulpian, "Note sur les effets de la faradisation directe des ventricules du coeur le chien.," no. 975, 1874.
- [2] J. A. MacWilliam, "Fibrillar contraction of the heart," vol. 8, no. 296, 1887.
- [3] C. Beck, W. Pritchard, and H. Feil, "Ventricular fibrillation of long duration abolished by electric shock," vol. 135, no. 985, 1947.
- [4] A. Pullan, "A high-order coupled finite element/boundary element human torso model," *IEEE Transactions on Biomedical Engineering*, vol. 43, pp. 292–298, Mar. 1996.
- [5] K. A. T. and J. Hunter and A. J. Pullan, "A finite element method for an eikonal equation model of myocardial excitation wavefront propagation," *SIAM Journal on Applied Mathematics*, vol. 63, no. 1, pp. 324–350, 2002.
- [6] J. M. Rogers and A. D. McCulloch, "A collocation-Galerkin finite element model of cardiac action potential propagation," *IEEE Transactions on Biomedical Engineering*, vol. 41, pp. 743–757, Aug. 1994.
- [7] E. J. Woo, S. Tungjitkusolmun, H. Cao, J.-Z. Tsai, J. G. Webster, V. R. Vorperian, and J. A. Well, "A new catheter design using needle electrode for subendocardial rf ablation of ventricular muscles: Finite element analysis and in vitro experiments," *IEEE Transactions on Biomedical Engineering*, vol. 47, pp. 23–31, Jan. 2000.
- [8] H. I. Saleheen and K. T. Ng, "New finite difference formulations for general inhomogeneous anisotropic bioelectric problems," *IEEE Transactions on Biomedical Engineering*, vol. 44, Sep. 1997.
- [9] D. M. Sullivan, D. T. Borup, and O. P. Gandhi, "Use of the finite-difference time-domain method in calculating EM absorption in human tissues," *IEEE Transactions on Biomedical Engineering*, vol. 34, pp. 148–157, Feb. 1987.
- [10] L. Wang and R. Patterson, "Multiple sources of the impedance cardiogram based on 3-d finite difference human thorax models," *IEEE Transactions on Biomedical Engineering*, vol. 42, pp. 141–148, Feb. 1995.
- [11] A. J. Pullan, C. P. Bradley, and P. J. Hunter, "A high order coupled finite element/boundary element torso model," in *Proc. Computers in Cardiology*, vol. 20, pp. 309–312, 1993.

- [12] H. Veister, J. Loejoenen, and T. Katila, "Creating 3D boundary element models of the heart from 2D projections," *Proc. Biomag2000*, pp. 821–824, 2000.
- [13] K. S. Yee, "Numerical solution of initial boundary value problems involving maxwell's equations in isotropic media," *IEEE Trans. Antennas Propagat.*, vol. AP-17, pp. 585–589, 1966.
- [14] M. L. James, *Applied Numerical Methods for Digital Computation*. New York: Harper and Row, 3 ed., 1985.
- [15] W. Bargmann, "Bau des Herzens," in *Das Herz des Menschen* (W. Bargmann and W. Doerr, eds.), pp. 88–164, Stuttgart: Georg Thieme Verlag, 1963.
- [16] R. H. Anderson and A. E. Becker, *Anatomie des Herzens*. Stuttgart: Georg Thieme Verlag, 1982.
- [17] H. Gray and W. H. Lewis, *Anatomy of the human body*. Philadelphia: Lea & Febiger, 20 ed., 1918.
- [18] J. Sobotta, *Atlas der Anatomie des Menschen*, vol. 1. Urban & Schwarzenberg, 20 ed., 1993.
- [19] M. Kutryk, S. Kassam, and D. Stewart, "Angiogenesis: An emergency technology for the treatment of coronary artery disease," *Cardiology Rounds*, vol. 6, pp. 102–109, 2001.
- [20] J. Schrader, "Das Herz," in *Lehrbuch der Physiologie* (R. Klinke and S. Silbernagl, eds.), ch. 7, pp. 109–144, Stuttgart, New York: Thieme, 2001.
- [21] D. A. Hooks, K. A. Tomlinson, S. G. Marsden, I. J. LeGrice, B. H. Smaill, A. J. Pullan, and P. J. Hunter, "Cardiac microstructure: implications for electrical propagation and defibrillation in the heart," *Circ Research.*, vol. 91, no. 331, 2002.
- [22] D. D. Streeter, "Gross morphology and fiber geometry of the heart," in *Handbook of Physiology: The Cardiovascular System* (B. Bethesda, ed.), vol. I, pp. 61–112, American Physiology Society, 1979.
- [23] A. A. Young, L. J. LeGrice, M. A. Young, and B. H. Smaill, "Extended confocal microscopy of myocardial laminae and collagen network," *J. Microscopy*, vol. 192, pp. 139–150, Nov. 1998.
- [24] A. F. Grimm, K. V. Katele, and H.-L. Lin, "Fiber bundle direction in the mammalian heart," *Basic Res. Cardiol.*, vol. 71, pp. 381–388, 1976.
- [25] J. W. Papez, "Heart musculature of the atria," *Am. J. Anatomy*, vol. 27, pp. 255–286, 1920.

- [26] D. K. Racker, "The av junction region of the heart: A comprehensive study correlating gross anatomy and direct three-dimensional analysis. part i. architecture and topography," *The Anatomical Record*, vol. 256, pp. 49–63, 1999.
- [27] R. H. Anderson and S. Y. Ho, "The architecture of the sinus node, the atrioventricular conduction axis, and the internodal atrial myocardium," *J. Cardiovasc. Electrophysiol.*, vol. 9, pp. 1233–1248, 1998.
- [28] D. Chiras, *Human Biology*. Colorado College: Jones and Bartlett, 4 ed., 202.
- [29] G. W. Beeler and H. Reuter, "Reconstruction of the action potential of ventricular myocardial fibres," *J. Physiol.*, vol. 268, pp. 177–210, 1977.
- [30] C.-H. Luo and Y. Rudy, "A model of the ventricular cardiac action potential," *Circ. Res.*, vol. 68, no. 6, pp. 1501–1526, 1991.
- [31] M. Courtemanche, R. J. Ramirez, and S. Nattel, "Ionic mechanisms underlying human atrial action potential properties: insights from a mathematical model," *Am. J. Physiol.*, vol. 275, no. 44, pp. H301–H321, 1998.
- [32] A. Nygren, C. Fiset, L. Firek, J. W. Clark, D. S. Lindblad, R. B. Clark, and W. R. Giles, "Mathematical model of an adult human atrial cell," *Circ. Res.*, vol. 82, pp. 63–81, 1998.
- [33] L. Priebe and D. J. Beuckelmann, "Simulation study of cellular electric properties in heart failure," *Circ. Res.*, vol. 82, pp. 1206–1223, 1998.
- [34] O. Bernus, R. Wilders, C. W. Zemlin, H. Vershelde, and A. V. Panfilov, "A computationally efficient electrophysiological model of human ventricular cells," *Am. J. Physiol.*, vol. 282, pp. H2296–H2308, 2002.
- [35] K. H. W. J. ten Tusscher, D. Noble, P. J. Noble, and A. V. Panfilov, "A model for human ventricular tissue," *Am. J. Physiol.*, vol. 286, pp. H1573–H1589, 2004.
- [36] V. Iyer, R. Mazhari, and R. L. Winslow, "A computational model of the human ventricular myocyte," *Biophys. J.*, vol. 87, pp. 1507–1525, 2004.
- [37] A. L. Hodgkin and A. F. Huxley, "A quantitative description of membrane current and its application to conduction and excitation in nerve," *J. Physiol.*, vol. 177, pp. 500–544, 1952.
- [38] M. Näbauer, D. J. Beuckelmann, P. Überfuhr, and G. Steinbeck, "Regional differences in current density and rate-dependent properties of the transient outward current in subepicardial and subendocardial myocytes of human left ventricle," *Circ.*, vol. 93, pp. 168–177, 1996.
- [39] G.-R. Li, J. Feng, L. Yue, M. Carrier, and S. Nattel, "Evidence for two components of delayed rectifier K^+ current in human ventricular myocytes," *Circ. Res.*, vol. 78, pp. 689–696, 1996.

- [40] T. Nagatomo, Z. Fan, B. Ye, G. S. Tonkovich, C. T. January, and J. C. Makielski, "Temperature dependence of early and late currents in human cardiac wild-type and long q-t δ KPQ Na⁺ channels," *Am. J. Physiol.*, vol. 275, pp. H2016–H2024, 1998.
- [41] J. Malmivuo and R. Plonsey, *Bioelectromagnetism*. New York; Oxford: Oxford University Press, 1995.
- [42] M. S. Spach, J. F. Heidlage, and P. C. Dolber, "The dual nature of anisotropic discontinuous conduction in the heart," in *Cardiac Electrophysiology. From Cell to Bedside* (D. P. Zipes and J. Jalife, eds.), ch. 25, pp. 213–222, Philadelphia: W. B. Saunders Company, 3 ed., 1999.
- [43] A. G. Kléber, V. G. Fast, and S. Rohr, "Continuous and discontinuous propagation," in *Cardiac Electrophysiology. From Cell to Bedside* (D. P. Zipes and J. Jalife, eds.), ch. 24, pp. 213–222, Philadelphia: W. B. Saunders Company, 3 ed., 1999.
- [44] H. J. Jongsma and M. B. Rook, "Biophysics of cardiac gap junction channels," in *Cardiac Electrophysiology. From Cell to Bedside* (D. P. Zipes and J. Jalife, eds.), ch. 14, pp. 119–125, Philadelphia: W. B. Saunders Company, 3 ed., 1999.
- [45] S. Verheule, M. J. A. van Kempen, P. H. J. A. te Welscher, B. R. Kwak, and H. J. Jongsma, "Characterization of gap junction channels in adult rabbit atrial and ventricular myocardium," *Circ. Res.*, vol. 80, pp. 673–681, 1997.
- [46] V. M. Unger, N. M. Kumar, N. B. Gilula, and M. Yeager, "Three-dimensional structure of a recombinant gap junction membrane channel," *Science*, vol. 283, pp. 1176–1180, 1999.
- [47] A. Noma and N. Tsuboi, "Dependence of junctional conductance on proton, calcium and magnesium ions in cardiac paired cells of guinea-pig," *J. Physiol.*, vol. 382, pp. 193–211, 1987.
- [48] S. P. Thomas, J. P. Kucera, L. Bircher-Lehmann, Y. Rudy, J. E. Saffitz, and A. G. Kléber, "Impulse propagation in synthetic strands of neonatal cardiac myocytes with genetically reduced levels of connexin43," *Circ. Res.*, vol. 92, pp. 1209–1216, 2003.
- [49] R. H. Hoyt, M. L. Cohen, and J. E. Saffitz, "Distribution and three-dimensional structure of intercellular junctions in canine myocardium," *Circ. Res.*, vol. 64, pp. 563–574, 1989.
- [50] J. P. Keener and A. V. Panfilov, "The effects of geometry and fibre orientation on propagation and extracellular potentials in myocardium," in *Computational Biology of the Heart* (A. V. Panfilov and A. V. Holden, eds.), pp. 235–258, Chichester: John Wiley & Sons, 1997.

- [51] A. V. Panfilov, "Three-dimensional wave propagation in mathematical models of ventricular fibrillation," in *Cardiac Electrophysiology. From Cell to Bedside* (D. P. Zipes and J. Jalife, eds.), ch. 31, pp. 271–277, Philadelphia: W. B. Saunders Company, 3 ed., 1999.
- [52] J. M. Rogers, "Modeling the cardiac action potential using b-spline surfaces," *IEEE Transactions on Biomedical Engineering*, vol. 47, pp. 784–791, June 2000.
- [53] R. A. FitzHugh, "Impulses and physiological states in theoretical models of nerve membran," *Biophys. J.*, vol. 1, pp. 445–466, 1961.
- [54] J. Rogers, M. Courtemanche, and A. McCulloch, "Finite element methods for modelling impulse propagation in the heart," in *Computational Biology of the Heart* (A. Panfilov and A. V. Holden, eds.), ch. 7, pp. 217–234, Chichester: John Wiley & Sons, 1997.
- [55] C. S. Henriquez, A. L. Muzikant, and C. K. Smoak, "Anisotropy, fiber curvature and bath loading effects on activation in thin and thick cardiac tissue preparations: Simulations in a three-dimensional bidomain model," *J. Cardiovasc. Electrophysiol.*, vol. 7, pp. 424–444, May 1996.
- [56] B. Surawicz, "Brief history of cardiac arrhythmias since the end of the nineteenth century," *Journal of Cardiovascular Electrophysiology*, vol. 14, no. 12, pp. 1365–1372, 2003.
- [57] E. J. Ciaccio, "Premature excitation and onset of reentrant ventricular tachycardia," *Am J Physiol Heart Circ Physiol*, vol. 283, no. 4, pp. H1703–H1712, 2002.
- [58] I. M. Popp, G. Seemann, and O. Dössel, "A simulation study of biphasic defibrillation shocks," *BioMed Central Cardiovascular Disorders*, 2004. accepted.
- [59] N. Wiener and A. Rosenblueth, "The mathematical formulation of the problem of conduction of impulses in a network of connected excitable elements, specifically in cardiac muscle," *Arch. Del. Instit. De Cardiologia De Mexico*, vol. 16, pp. 205–265, 1946.
- [60] W. Garrey, "The nature of fibrillary contraction of the heart: its relation to tissue mass and form," *Am J Physiol.*, vol. 33, pp. 397–414, 1914.
- [61] K. Younossi, H. J. Rudiger, K. Haap, and H. Antoni, "Experimental studies on the threshold for fibrillation produced by direct or sinusoidal alternating current in the isolated guinea-pig heart," *Basic Res Cardiol.*, vol. 68, no. 6, pp. 551–568, 1973.
- [62] R. Brugada, T. Tapscott, G. Z. Czernuszewicz, A. J. Marian, A. Iglesias, L. Mont, J. Brugada, J. Girona, A. Domingo, L. L. Bachinski, and R. Roberts, "Identification of a genetic locus for familial atrial fibrillation," *N. Engl. J. Med.*, vol. 336, no. 13, pp. 905–911, 1997.

- [63] W. Irrnich, "Optimal truncation of defibrillation pulses," *Pacing and Clinical Electrophysiol.*, vol. 18, no. 4, pp. 673–688, 1995.
- [64] "www.stanfordhospital.com," 2005.
- [65] K. F. Kwaku and S. M. Dillon, "Shock-induced depolarization of refractory myocardium prevents wave-front propagation in defibrillation," *Circulation Research.*, vol. 79, pp. 957–973, 1996.
- [66] W. T. Baxter, S. F. Mironov, A. V. Zaitsev, J. Jalife, and A. M. Pertsov, "Visualizing excitation waves inside cardiac muscle using transillumination," *Biophys J*, vol. 80, no. 1, pp. 516–530, 2001.
- [67] H. A. Blair, "On the measure of excitability," *The Journal of General Physiology*, 1932. <http://www.jpg.org>.
- [68] W. A. H. Rushton, "Blair's "condenser theory" of nerve excitation," *The Journal of General Physiology*, 1933. <http://www.jpg.org>.
- [69] K. Nanthakumar, V. J. Plumb, A. E. Epstein, G. D. Veenhuyzen, D. Link, and G. N. Kay, "Resumption of electrical conduction in previously isolated pulmonary veins rationale for a different strategy?," *Circulation.*, vol. 109, pp. 1226–1229, 2004.
- [70] M. Valderrabano, J. Yang, C. Omichi, J. Kil, S. T. Lamp, Z. Qu, S.-F. Lin, H. S. Karagueuzian, A. Garfinkel, P.-S. Chen, , and J. N. Weiss, "Frequency analysis of ventricular fibrillation in swine ventricles," *Circ. Res.*, vol. 90, no. 2, pp. 213 – 222, 2002.
- [71] D. Noble, A. Varghese, P. Kohl, and P. Noble, "Improved guinea-pig ventricular cell model incorporating a diadic space, I_{Kr} and I_{Ks} , and length- and tension-dependend processes," *Can. J. Cardiol.*, vol. 14, pp. 123–134, Jan. 1998.
- [72] N. Trayanova and K. Skoubine, "Modeling defibrillation: Effects of fiber curvature," *J. Electrocardiol.*, vol. 31, pp. 23–29, 1998.
- [73] A. T. Sambelashvili, V. P. Nikolski, and I. R. Efimov, "Virtual electrode theory explains pacing threshold increase caused by cardiac tissue damage," *Am J Physiol Heart Circ Physiol.*, vol. 286, no. 6, pp. H2183–94, 2004.
- [74] I. M. Popp, G. Seemann, and O. Dössel, "Investigation of the influence of electric fields on human ventricular myocardium including realistic fibre orientation: A simulation study," in *Proc. CinC*, vol. 30, pp. 213–216, 2003.
- [75] R. Plonsey, "The use of bidomain model for the study of excitable media," *Lect. Math. Life Sci.*, vol. 21, pp. 123–149, 1989.

- [76] I. M. Popp, G. Seemann, and O. Dössel, "The influence of heterogeneity of external applied fields on human ventricular myocardium," in *Proc. MEDICON*, 2004. accepted.
- [77] I. M. Popp, G. Seemann, and O. Dössel, "Investigation of electrical defibrillation of chaotically fibrillating human ventricular myocardium in a computer model," in *Proc. ICE*, 2004. accepted.
- [78] X. Zhou and S. B. Knisley, "Effects of defibrillation shocks on the transmembrane potentials," *American Heart Association*, no. NC-93-GS-19,, 1994.
- [79] T. Furukawa, R. J. Myerburg, N. Furukawa, A. L. Bassett, and S. Kimura, "Differences in transient outward currents of feline endocardial and epicardial myocytes," *Circ. Res.*, vol. 67, pp. 1287–1291, 1990.
- [80] P. G. Volders, K. R. Sipido, E. Carmeliet, R. L. Spatjens, H. J. Wellens, and M. A. Vos, "Repolarizing K^+ currents ITO1, and IKS are larger in right than left canine ventricular myocardium," *Circ.*, vol. 99, pp. 206–210, 1999.
- [81] W. Shimizu and C. Antzelevitch, "Sodium channel block with mexiletine is effective in reducing dispersion of repolarization and preventing torsade de pointes in LQT2 and LQT3 models of the long-QT syndrome," *Circ.*, vol. 96, pp. 2038–2047, 1997.
- [82] F. Sachse, G. Seemann, K. Chaisaowong, and D. Weiss, "Quantitative reconstruction of cardiac electromechanics in human myocardium: Assembly of electrophysiological and tension generation models," *J. Cardiovasc. Electrophysiol.*, vol. 14, no. S10, pp. S210–S218, 2003.
- [83] G. Seemann, F. B. Sachse, D. L. Weiß, and O. Dössel, "Investigating heterogeneity in human heart with simulated transmural electrocardiograms," *Int. J. Bioelectromagnetism*, 2003.
- [84] B. J. Roth, "Influence of a perfusing bath on the foot of the cardiac action potential," *Circulation Research*, vol. 86, no. 19, 2000.
- [85] A. Al-Khadra, V. Nikolski, and I. R. Efimov, "The role of electroporation in defibrillation," *Circulation Research*, vol. 87, no. 797, 2000.
- [86] R. H. Clayton and A. V. Holden, "Dispersion of cardiac action potential duration and the initiation of re-entry: A computational study," *BioMedical Engineering*, vol. 4, no. 11, 2005.
- [87] C. Antzelevich and S. Sicouri, "Clinical relevance of cardiac arrhythmias generated by afterdepolarisations: Role of m-cells in the generation of u waves, triggered activity and torsade de pointes," *J. Am. Coll. Cardiol.*, vol. 23, pp. 259–277, 1994.

- [88] J. R. Sommer and R. B. Jennings, "Ultrastructure of cardiac muscle," in *The Heart and Cardiovascular System* (H. A. Fozzard, E. Haber, R. B. Jennings, A. M. Katz, and H. E. Morgan, eds.), ch. 1, pp. 3–50, New York: Raven Press, Ltd., 2 ed., 1992.
- [89] J. Carpenter, T. D. Rea, J. A. Murray, P. J. Kudenchuk, and M. S. Eisenberg, "Defibrillation waveform and post-shock rhythm in out-of-hospital ventricular fibrillation cardiac arrest," *Resuscitation*, vol. 59, no. 2, pp. 189–96, 2003.
- [90] N. Trayanova, "Far-field stimulation of cardiac tissue," *Herzschrittmacher Therapie und Elektrophysiologie*, vol. 10, pp. 137–148, 1999.
- [91] S. Weidmann, "Electrical constants of trabecular muscle for mammalian heart," *J. Physiol.*, vol. 210, pp. 1041–1054, 1970.
- [92] M. S. Spach, W. T. M. III, D. B. Geselowitz, R. C. Barr, J. M. Kootsey, and E. A. Johnson, "The discontinuous nature of propagation in normal canine cardiac muscle: evidence for recurrent discontinuities of intracellular resistance that affect the membrane currents," *Circ. Res.*, vol. 48, pp. 39–45, 1981.
- [93] R. Plonsey, C. Henriquez, and N. Trayanova, "Extracellular (volume conductor) effect on adjoining cardiac muscle electrophysiology," *Med. Biol. Eng. Comput.*, vol. 26, no. 1, pp. 126–129, 1988.
- [94] B. J. Roth, "Action potential propagation in a thick strand of cardiac muscle," no. 68, pp. 162–173, 1991.
- [95] C. S. Henriquez, "Simulating the electrical behaviour of cardiac tissue using the bidomain model," *Critical Reviews in Biomedical Engineering*, vol. 21, no. 1, pp. 1–77, 1993.
- [96] M. S. Spach, P. C. Dolber, J. F. Heidlage, and R. C. Barr, "Extracellular discontinuities in cardiac muscle: evidence for capillary effects on the action potential foot," *Circ. Res.*, vol. 83, pp. 1144–1164, 1998.
- [97] M. Apkon and J. M. Nerbonne, "Characterization of two distinct depolarization-activated K^+ currents in isolated adult rat ventricular myocytes," *J. of General Physiology*, vol. 97, pp. 757–767, 1991.
- [98] S. Roberts, D. Guan, and R. Malkin, "The defibrillation efficacy of high frequency alternating current sinusoidal waveforms in guinea pigs," *PACE*, vol. 26, pp. 559–604, 2003.
- [99] S. Roberts, D. Guan, and R. Malkin, "Comparison of six clinically used external defibrillators in swine," *Resuscitation*, vol. 57, no. 1, pp. 73–83, 2003.
- [100] S. Roberts, D. Guan, and R. Malkin, "The biphasic mystery: why a biphasic shock is more effective than a monophasic shock for defibrillation," *J. Theor Biol.*, vol. 200, no. 1, pp. 1–17, 1999.

- [101] G. A. Mouchawar, L. A. Geddes, J. D. Bourland, and J. A. Pearce, "Ability of the lapicque and blair strength-duration curves to fit experimentally obtained data from the dog heart," *IEEE Trans Biomed Eng.*, vol. 36, no. 9, pp. 971–974, 1989.
- [102] I. M. Popp, G. Seemann, and O. Dössel, "Computer modeling of virtual electrodes in human ventricular myocardium," in *Proc. IASTED*, 2004, accepted.
- [103] T. R. Gowrishankar, U. Pliquett, and R. C. Lee, "Dynamics of membrane sealing in transient electroporation of skeletal muscle membranes," *Ann. N.Y. Acad. Sci.*, vol. 30, no. 888(1), pp. 195 – 210, 1999.
- [104] M. H. Wu, S. L. Smith, and M. E. Dolan, "High efficiency electroporation of human umbilical cord blood cd34+ hematopoietic precursor cells," *Stem Cells*, vol. 19, no. 6, pp. 492 – 499, 2001.
- [105] K. A. Riske and R. Dimova, "Electro-deformation and poration of giant vesicles viewed with high temporal resolution," *Biophys. J.*, vol. 88, no. 2, pp. 1143 – 1155, 2005.
- [106] S. Knisley, B. Hill, and R. Ideker, "Virtual electrode effects in myocardial fibers," *Biophysical Journal*, vol. 66, pp. 719–728, 1994.
- [107] K. A. DeBruin and W. Krassowska, "Modeling electroporation in a single cell. i. effects of field strength and rest potential," *Biophys. J.*, vol. 77, no. 3, pp. 1213–1224, 1999.
- [108] T. Ashihara and N. Trayanova, "Asymmetry in membrane responses to electric shocks: insights from bidomain simulations," *Biophys. J.*, vol. 87, pp. 2271–2282, 2004.
- [109] D. K. L. Cheng, L. Tung, and E. Sobie, "Nonuniform responses of transmembrane potential during electric field stimulation of single cardiac cells," *Am J Physiol Heart Circ Physiol*, vol. 277, pp. H351–H362, 1999.
- [110] J. Dudel, "Grundlagen der Zellphysiologie," in *Physiologie des Menschen* (R. F. Schmidt, G. Thews, and F. Lang, eds.), ch. 1, pp. 3–19, Berlin, Heidelberg, New York: Springer, 2000.
- [111] D. M. Bers, *Excitation-Contraction Coupling and Cardiac Contractile Force*. Dordrecht, Netherlands: Kluwer Academic Publishers, 1991.
- [112] M. Ciofalo, M. W. Collins, and T. R. Hennessy, "Nanoscale fluid dynamics in physiological processes: A review study," *WIT Press, Boston*, vol. MA, 1999.
- [113] G. C. Troiano, L. Tung, V. Sharma, and K. J. Stebe, "The reduction in electroporation voltages by the addition of a surfactant to planar lipid bilayers," *Biophys. J.*, vol. 75, no. 2, pp. 880–888, 1998.

- [114] W. Hercules, J. Lindsay, A. Coble, and R. Schmukler, "Electroporation of biological cells embeded in polycarbonate filter," 2003.
- [115] M. Bloom, E. Evans, and O. G. Mouritsen *Q. Rev. Biophys.*, vol. 24, p. 293, 1991.
- [116] G. Debregeas, P. Martin, and F. Brochard-Wyart *Rev. Lett.*, vol. 6, p. 3, 1995.
- [117] K. Luby-Phelps *Curr. Opin. Cell Biol.*, vol. 75, p. 3886, 1995.
- [118] I. G. Abidor, V. B. Arakelyan, Y. A. C. L.V. Chernomordik, V. Pastushenko, and M. R. Tarashevich, "Electric breackdown of bilayer lipid membranes. i. main experimental facts and their qualitative discussion," *Bioelectrochem. Bioeng.*, vol. 6, pp. 37–52, 1979.
- [119] J. C. Weaver and R. A. Minzer, "Decreased bilayer stability due to transmembrane potential," *Phys. Lett.*, vol. 86, no. A, pp. 57–59, 1981.
- [120] R. W. Glaser, S. L. Leikin, L. V. Chernomordik, V. F. Pastushenko, and A. I. Sokirko, "Reversible electrical breakdown of lipid bilayers: formation and evolution of pores," *Biochem. Biophys. Acta.*, vol. 940, pp. 275–287, 1988.
- [121] U. C. Wilhelm, M. Winterhalter and R. Benz *Biophys. J.*, vol. 64, p. 121, 1993.
- [122] K. Ohuchi, Y. Fukui, I. Sakuma, N. Shibata, H. Honjo, and I. Kodama, "A dynamic action potential model analysis of shock-induced aftereffects in ventricular muscle by reversible breakdown of cell membrane," *IEEE Trans. Biomed. Eng.*, vol. 49, no. 1, pp. 18–30, 2002.
- [123] M. Näbauer, D. J. Beuckelmann, and E. Erdmann, "Characteristics of transient outward current in human ventricular myocytes from patients with terminal heart failure," *Circ. Res.*, vol. 73, pp. 386–394, 1993.
- [124] G. R. Li, C. P. Lau, A. Ducharme, J. C. Tardif, and S. Nattel, "Transmural action potential and ionic current remodelling in ventricles of failing canine hearts," *J. Physiol. Heart Circ. Physiol.*, vol. 283, no. 3, pp. H1031–H1041, 2002.
- [125] C. R. Weber, V. Piacento, S. R. Houser, and D. M. Bers, "Dynamic regulation of sodium/calcium exchange function in human heart failure," *Circulation Research*, vol. 108, no. 2224, 2003.
- [126] C. Antzelevitch and S. Sicouri, "Clinical relevance of cardiac arrhythmias generated by afterdepolarizations: Role of M-cells in the generation of U waves, triggered activity and torsade de pointes," *J. Am. Coll. Cardiol.*, vol. 23, pp. 259–277, 1994.

-
- [127] R. R. Alievand and A. V. Panfilov, "Multiple responses at the boundaries of vulnerability window in the bz reaction," *Phys. Rev. E*, vol. 52, no. 3, pp. 2287–2293, 1995.
- [128] F. G. Akar and D. S. Rosenbaum, "Transmural electrophysiological heterogeneities underlying arrhythmogenesis in heart failure," *Circ. Res.*, vol. 93, no. 7, pp. 638–645, 2003.
- [129] S. Kaab, H. B. Nuss, N. Chiamvimonvat, B. O'Roukre, P. Pak, D. Kaas, E. Marban, and G. Tomaselli, "Ionic mechanism of action potential prolongation in ventricular myocytes from dogs with pacing-induced heart failure," *Circ. Res.*, vol. 78, pp. 262–270, 1996.
- [130] S. M. Factor, E. H. Sonnenblick, and E. S. Kirk, "The histologic border zone of acute myocardial infarction-islands or peninsulas?," *Am. J. Pathol.*, vol. 92, pp. 111–124, 1978.
- [131] W. C. D. Mello, "Effect of intracellular injection of calcium and strontium on cell communication in the heart," *J. Physiol.*, vol. 250, pp. 231–245, 1975.
- [132] P. Maurer and R. Weingart, "Cell pairs isolated from adult guinea pig and rat hearts: effects of $[ca^{2+}]_i$ on nexal membrane resistance," *Pflügers Arch*, vol. 409, pp. 394–402, 1987.
- [133] W. Peters, P. Kowallik, K. Wilhelm, and M. Meesmann, "Evolution of late potentials during the first 8 hours of myocardial infarction treated with thrombolysis," *Pacing Clin. Electrophysiol.*, vol. 19, pp. 1981–22, 1996.

Curriculum Vitae

Name Iulia-Mihaela Graf

Born 09.12.1979 in Bistrita, Romania.

Education and Academic Grades

2002–2005	Scientific employee at the Institute of Biomedical Engineering at the University Karlsruhe (TH), Karlsruhe, Germany
July, 2002	Diploma in Theoretical Physics, University of Bucharest, Romania, grade 8.92
March–June, 2002	Sokrates student, University of Tuebingen, Germany
1998 – 2002	Faculty of Physics at the University of Bucharest, Romania
July, 1998	Bacalaureat (High School Diploma), Bistrita, Romania, grade 8.79
May, 1998	Professional attestation for English-Romanian translations
1994 – 1998	The National College <i>Liviu Rebreanu</i> , Bistrita, Romania
1986 – 1994	Primary School Number 3, Bistrita, Romania

Participation to Contests and Scholarships

2002–2005	PhD scholarship from German Research Foundation (DFG)
March–June, 2002	Sokrates scholarship
1998–2002	scholarship from University of Bucharest for the obtained degrees
1998	nominated the best pupil of district Bistrita-Nasaud (scholarship from townhall of Bistrita for superior studies)

- 1998 National Science Contest (3rd place)
 1998 National Physics Contest
 1998 Transilvanian Inter-District Contest Physics *Top – Fiz*
 1997 National Science Contest (5th place)
 1997 National Physics Contest
 1997 Transilvanian Inter-District Contest Physics *Schwartz*
 1996 National Physics Contest
 1996 Transilvanian Inter-District Contest Physics *Top – Fiz*
 1995 Transilvanian Inter-District Contest Physics *Top – Fiz*

Scientific and Work Experience

- 2002–2005 Ph.D. student at the Graduate Research Center "Mixed Fields and Nonlinear Interactions", University Karlsruhe (TH); name of research project: "The Influence of External Electrical Fields on Human Heart", supervisor: Prof. Dr. Olaf Dössel
- Since March, 2005 supervision of diploma student, Yu Cao
- Jan., 2005 organizing for GKMF members the technical week at the Institute of Light Technology, University Karlsruhe (TH)
- 2002–2004 attendance of the circular lectures organized for GKMF members
- Oct., 2004 organizing visit to research groups from ETH and ETZ, Zuerich
- Sept., 2004 oral presentation at CinC international conference (USA)
- Aug., 2004 oral presentation at MEDICON international conference (Italy)
- July, 2004 oral presentation at ICE international conference (Japan)
- June, 2004 re-elected spokesperson of GKMF
- May, 2004 organizing for GKMF members the technical week at the Institute of Microtechnology, Research Centre Karlsruhe
- April, 2004 organizing visit to Infineon Technologies-Muenchen for GKMF members

Feb., 2004	oral presentation at IASTED international conference (Austria)
Nov., 2003	oral presentation <i>Elektromechanische Modellierung des Herzens</i> for <i>Mdchen Technik Tag</i>
Oct., 2003	organizing the lecture of Prof. Biermann for GKMF members
Sept., 2003	oral presentation at CinC international conference (Grece)
Winter semester 2003-2004	tutor in Electromagnetics and Numerical Calculations
July., 2003	organizing visit to the radio telescope from Effelsberg for GKMF members
Summer semester 2003	<i>Filtering ECG data with Matlab</i> research project
March, 2003	oral presentation "Application of Bioinformatics to Functional Modeling of the Heart" at Bioinformatics workshop in Research Centre Karlsruhe
Oct., 2003	organizing the lecture of Prof. Biermann for GKMF members
Winter semester 2002-2003	Lectures with exams in: Materials and Devices, Electromagnetics and Numerical Calculations, Integrated Systems of Signal Processing
Sep., 2002	elected spokesperson of Research Training Group 786 "Mixed Fields and Nonlinear Interactions" (GKMF)
March–June, 2002	work on Diploma thesis "Competition between isoscalar and isovector pairing in nuclei $N=Z$ "; supervisor: Prof. Dr. A. Faessler, Institute of Theoretical Physics, Tuebingen
2001–2002	collaboration with Prof. Dr. D. Grecu, Romanian National Institute of Theoretical Physics IFINHH
2001– 2002	specialization on theoretical physics (special chapters in quantum mechanics, collision theory, quantum electrodynamics)
2001	participation to astrophysics lectures at MEF (Module d' Etudes Francophones) organized by French Astrophysics professors from Paris-Meudon
2001	physics lecturer in Bucharest's National College, Mihai Eminescu
2000–2001	co-operation with faculty's newspaper, <i>Tabu</i>
1998	English-Romanian translator for Sophia publisher

Publications

Per-review journals

- I. M. Graf, G. Seemann, D. L. Weiß, and O. Dössel, “Influence of electrophysiological heterogeneity in human healthy and failing heart on electrical stimulation,” *MBEC*, 2005, submitted.
- I. M. Popp, G. Seemann, and O. Dössel, “A simulation study of biphasic defibrillation shocks,” *BMC Cardiovascular Disorders*, vol. 4, no. 1, pp. 9, 2004

Per-review Conferences

- I. M. Graf, G. Seemann, and O. Dössel, “Theoretical Research on the Influence of Defibrillator Paddle Position on the Human Ventricular Myocardium,” in *Proc. Computers in Cardiology*, vol. 31, pp. 97–100, 2004
- I. M. Popp, G. Seemann, and O. Dössel, “Computer modeling of virtual electrodes in human ventricular myocardium,” in *Proc. IASTED*, 2004
- I. M. Popp, G. Seemann, and O. Dössel, “The influence of heterogeneity of external applied fields on human ventricular myocardium,” in *Proc. MEDICON*, 2004
- I. M. Popp, G. Seemann, and O. Dössel, “Investigation of electrical defibrillation of chaotically fibrillating human ventricular myocardium in a computer model,” in *Proc. ICE*, 2004
- I. M. Popp, G. Seemann, and O. Dössel, “The reaction of a fibrillating myocardium to electrical shocks of different durations,” in *Proc. BMT*, vol. 49, no. 2, pp. 376-377, 2004
- I. M. Popp, G. Seemann, and O. Dössel, “Investigation of the influence of electric fields on human ventricular myocardium including realistic fibre orientation: A simulation study,” in *Proc. CinC*, vol. 30, pp. 213–216, 2003.